Tri-Orthogonal Polarisation Diverse Communications

by

Nicholas Paul Lawrence

BSc (Hons.) (Physics),
University of Leicester, UK, 1995

MSc (Microwave Solid State Physics, Distinction),
University of Portsmouth, UK, 1998

MPhil (Brillouin Sensing Optical Fibre Techniques),
University of Southampton, UK, 2002

Thesis submitted for the degree of

Doctor of Philosophy

in

Electrical and Electronic Engineering,
Faculty of Engineering, Computer and Mathematical Sciences
The University of Adelaide, Australia

2017

Supervisors:

Prof. Derek Abbott, School of Electrical & Electronic Engineering

Dr Hedley J. Hansen, School of Electrical & Electronic Engineering

Dr Brian W.-H. Ng, School of Electrical & Electronic Engineering

THE UNIVERSITY *of* ADELAIDE

Contents

Contents iii

Acknowledgments ix

Statement of Originality xiii

Thesis Conventions xv

Abstract xvii

Publications xxiii

List of Figures xxv

List of Tables xxxiii

Chapter 1. Introduction to Thesis Research 1

1.1 Introduction 3

1.1.1 Why is There an Issue Currently Facing Wireless Network Design? 3

1.1.2 What Exactly is Being Done About It? 3

1.1.3 How Can the Research in This Thesis Impact This Issue? 7

1.1.4 Research Motivations and Thesis Objectives 10

1.2 Statement of Original Contributions 16

1.3 Overview of the Thesis 18

1.4 Chapter Summary 21

Chapter 2. Tri-Orthogonal Polarisation Diversity Review and Modelling Critique 23

2.1 Tri-Orthogonal Polarisation Diversity Review 24

2.2 Critique of Applicable Modelling Techniques 34

2.3 Chapter Summary 37

Chapter 3. Tri-Orthogonal Approach Applied to Terrestrial Channel **39**

3.1 Introduction . . . 40

3.2 Methods . . . 49

3.3 Results . . . 60

3.4 Chapter Summary . . . 71

Chapter 4. Faraday Rotation and Path Delay **73**

4.1 Introduction . . . 74

4.2 Methods . . . 80

4.2.1 Link Geometry . . . 80

4.2.2 Latitude, Longitude and Height Determination for Faraday Rotation and Path Delay Simulation . . . 82

4.2.3 Magnetic Field Vector and Total Electron Content . . . 85

4.3 Results . . . 91

4.4 Chapter Summary . . . 97

Chapter 5. Tri-Orthogonal Approach Applied to NGSO Ionospheric Channel **101**

5.1 Introduction . . . 102

5.2 Method . . . 107

5.2.1 Link Geometry . . . 111

5.2.2 Transmitter and Receiver Arrangement . . . 113

5.2.3 Latitude and Longitude Determination for Non-Geosynchronous Satellite Orbit Track . . . 115

5.2.4 The Channel . . . 117

5.2.5 Polarisation . . . 120

5.2.6 Gain . . . 121

5.2.7 Faraday Rotation and Path Delay . . . 122

5.2.8 Doppler Frequency Shift . . . 122

5.2.9 Two State Ionosphere . . . 125

5.2.10 Satellite Channel Matrix . . . 126

5.2.11 Pure LoS Power Transfer . . . 129

5.3 Capacity . . . 146
5.3.1 Consideration of Array Panellisation . . . 148
5.4 Results . . . 153
5.4.1 Application of Total Fading Margin Over the FoV Over a Random Orbital Period . . . 155
5.4.2 No Fading Margin Application Over the FoV Over a Random Orbital Period . . . 155
5.4.3 Statistical Analysis of Channel Capacity With No Application of Fading . . . 159
5.4.4 Analysis of Iridium System Channel According to Empirical Slow and Fast Fading Statistics . . . 162
5.4.5 Effect of Mutual Coupling on System Performance . . . 171
5.5 Chapter Summary . . . 179

Chapter 6. Planar Tri-orthogonal Diversity Slot Antenna 183
6.1 Introduction . . . 184
6.1.1 Tri-Orthogonality . . . 184
6.2 Antenna Design and Feed Network . . . 185
6.2.1 Concept . . . 185
6.2.2 Specific Antenna Design . . . 188
6.2.3 Feed Arrangement for Tri-Orthogonal Operation . . . 189
6.3 Results . . . 193
6.4 Mutual Coupling and Pattern Diversity . . . 203
6.5 Chapter Summary . . . 206

Chapter 7. Slot Antenna with Omnidirectional and Circular Polarisation 207
7.1 Introduction . . . 208
7.2 Antenna Design and Feed Network . . . 210
7.2.1 Concept . . . 210
7.2.2 Specific Antenna Design . . . 211
7.2.3 Feed Arrangement for OLP, CP Operation . . . 211
7.3 Results . . . 217

7.3.1 S-parameters . . . 217
7.3.2 Radiation Characteristics of OLP, CP System . . . 217
7.4 Diversity Characteristics . . . 219
7.4.1 Excitation Port Diversity . . . 222
7.4.2 Excitation Phase Diversity . . . 222
7.4.3 Excitation Magnitude Diversity . . . 223
7.5 Chapter Summary . . . 228

Chapter 8. Wideband Low-Profile Electric Monopole 229

8.1 Introduction . . . 230
8.2 Design . . . 231
8.3 Results . . . 233
8.4 Chapter Summary . . . 236

Chapter 9. Contributions & Future Research Directions 237

9.1 Introduction . . . 238
9.2 Part I: Software-Based Original Contributions . . . 239
9.2.1 Tri-Orthogonal Approach Applied to Terrestrial Channel: (Chapter 3) . . . 239
9.2.2 Faraday Rotation and Path Delay in the Ionosphere: (Chapter 4) . . . 240
9.2.3 Tri-Orthogonal Approach Applied to Non-Geosynchronous Satellite Orbit Ionospheric Channel: (Chapter 5) . . . 240
9.3 Part II: Hardware-Based Original Contributions . . . 241
9.3.1 Planar Tri-Orthogonal Diversity Slot Antenna: (Chapter 6) . . . 241
9.3.2 Multifunction Two-Port Slot Antenna with Omnidirectional and Circular Polarisation: (Chapter 7) . . . 242
9.3.3 Wideband Low-Profile Electric Monopole: (Chapter 8) . . . 242
9.4 Part III: Future Research Directions . . . 243
9.4.1 Wideband Planar Tri-Orthogonal Diversity Slot Antenna . . . 243
9.4.2 Millimetre-Wave Tri-Orthogonal Diversity Slot Antenna . . . 244
9.4.3 Circular Polarisation Operation in Any Link Direction . . . 244
9.5 Part IV: Outlook . . . 245

Appendix A. Fundamentals Relative to this Research 249

A.1 Maxwell's Equations 250

A.1.1 In Vacuo 250

A.1.2 Monochromatic Plane Waves 251

A.1.3 Linear, Circular and Elliptical Polarisation 253

A.1.4 Electromagnetic Waves in Matter 257

A.2 Transmitting and Receiving Antennas 262

A.2.1 Effective Area of an Antenna 262

A.2.2 Antenna Noise Temperature 262

A.3 Effective Length and Polarisation Mismatch 263

Bibliography 267

List of Acronyms 291

Biography 295

Acknowledgments

I begin by thanking those who have shaped my scientific knowledge in RF and microwave design and theory over the years. I start with Dr David Nixon, Mr Colin White, and Dr David Franklin of the University of Portsmouth, UK, who guided me during a MSc in Microwave Solid State Physics, and nurtured my interest in microwave device design. A period of eight years as a RF engineer working in the diverse areas of RF power amplification, DVB-T and RF sensors has given me an excellent grounding in the physical realities of RF and microwave design and measurement techniques. I subsequently became a Chartered Engineer and Member of the IET, formerly the IEE as my experience has grown in this role.

It is true to say that my career has followed a less straight path than most. To this effect, I have performed research in Fibre Optic Sensing Techniques at the University of Southampton, UK, where I obtained a MPhil in Brillouin Sensing Techniques for my work. I am sincerely grateful to Dr Trevor Newson, Dr Peter Waite, Dr Arthur Hartog, Dr Mohamed Alahbabi, and Dr Yuh-Tat Cho for their assistance during this research.

I have spent several years living and working in France, working for a British RF power amplifier design company with a French auxiliary arm, and for a French RF power amplifier design company. I am grateful to my inspiring interlocutors, Mr Bernard Cottereau and Mr Michel Rousselet, during these wonderful years.

In Australia, I would like to convey my deepest gratitude to my supervisors **Prof. Derek Abbott**, **Dr Hedley Hansen** and **Dr Brian Ng** for their guidance and support throughout my PhD candidature. My principal supervisor, Derek Abbott, has advised me with his open view and broad knowledge. His critical and thoughtful comments were always constructive and fruitful to improve the quality of my research. In addition, my co-supervisor, Hedley Hansen, also provided me with his solid knowledge in the field of millimetre-wave systems. Furthermore, I would like to express my gratitude to my second co-supervisor, Brian Ng, who has advised me in regard of signal processing techniques. My sincere thanks go to Prof. Christophe Fumeaux, who has provided constructive analysis of my designs when required, and with whom it has been a pleasure to work.

Acknowledgments

I would like to thank Dr Mihail V. Codrescu of the National Oceanic and Atmospheric Administration in Washington D.C., United States, for his efforts in explaining a method to me for accessing ionospheric data required in my research.

I acknowledge the contributions of the following fellow researchers who have made my time enjoyable and rewarding at the University of Adelaide: Mr Lachlan Gunn, Dr Sam Darvishi, Dr Amir Ebrahimi, Dr Nicoangelo Iannella, Mr Shengjian 'Jammy' Chen, and Mr Peng Wang.

This research has relied on the crafting capabilties and advise of several colleagues in the workshops at the University of Adelaide. My thanks to Mr Brad Pullen, Mr Alban O'Brien, and Mr Pavel Simcik. I also thank the administrators of the Elecrical and Engineering Department, and in particular Ms Rose-Marie Descalzi and Ms Deb Koch.

Finally, I owe the biggest thanks to the support of my family. In particular, to my mother and father, who provided me with the step to reach this academic height, through their committment to me and my brothers.

And to my beloved wife, Margot, and our two children, Alexander and Elizabeth. I thank you all from the bottom of my heart.

Nicholas Paul Lawrence,
February 2017,
Adelaide.

To my dearest wife, Margot
to my children, Alexander and Elizabeth
and to my Mum and Dad,
with all my love.
Finally, I dedicate this thesis to my late brother, James.

Statement of Originality

I certify that this work contains no material, which has been accepted for the award of any other degree or diploma in my name, in any university or other tertiary institution and, to the best of my knowledge and belief, contains no material previously published or written by another person, except where due reference has been made in the text. In addition, I certify that no part of this work will, in the future, be used in a submission in my name, for any other degree or diploma in any university or other tertiary institution without the prior approval of the University of Adelaide and where applicable, any partner institution responsible for the joint-award of this degree.

I give consent to this copy of my thesis when deposited in the University Library, being made available for loan and photocopying, subject to the provisions of the Copyright Act 1968.

The author acknowledges that copyright of published works contained within this thesis resides with the copyright holder(s) of those works.

I also give permission for the digital version of my thesis to be made available on the web, via the University's digital research repository, the Library Search and also through web search engines, unless permission has been granted by the University to restrict access for a period of time.

I acknowledge the support I have received for my research through the provision of an Australian Government Research Training Program Scholarship.

	17/02/2017
Signed	Date

Thesis Conventions

The following conventions have been adopted in this thesis:

Typesetting

This document was compiled using LaTeX2e. Texmaker and TeXstudio were used as text editor interfaced to LaTeX2e. Inkscape and Xcircuit were used to produce schematic diagrams and other drawings.

Referencing

The Harvard style has been adopted for referencing.

System of units

The units comply with the international system of units recommended in an Australian Standard: AS ISO 1000–1998 (Standards Australia Committee ME/71, Quantities, Units and Conversions 1998).

Spelling

Australian English spelling conventions have been used, as defined in the Macquarie English Dictionary (A. Delbridge (Ed.), Macquarie Library, North Ryde, NSW, Australia, 2001).

Terminology

Where applicable, recent terminology is introduced where such terminology is seen to be being used more frequently within an interested community. As a consequence, the

term 'mmWave' is used in this thesis as opposed to the more conventional 'mm-wave' and 'mmwave' forms, as it is more commonly used in the 5G community.

In this thesis, system capacity may be given using a unit of $bps_{(1\ Hz)}$. This term refers to capacity performance for a system operating with a 1 Hz bandwidth. As such, this unit is equivalent to spectral efficiency ($bpsHz^{-1}$).

Spectral efficiency is a useful metric for contrasting performance between systems with non-identical operating bandwidths.

In reviewed literature, the terms of capacity and spectral efficiency are found to be interchanged as system performance is often contrasted with reference to one operating bandwidth.

In this thesis, contrast is made between systems as a function of orthogonal polarisation. In each case, contrast is made using one operating bandwidth, and so differentiation between capacity and spectral efficiency is arbitrary.

For satellite systems, a distinction between the terms 'geostationary' and 'geosynchronous' is often confused in the literature. In this thesis, the term 'geostationary' is applied to a satellite orbit around the Earth at a height above the equator such that the satellite appears stationary as seen from a stationary ground receiver on Earth. In the literature, this orbit height is typically given as 35 786 km. The term 'geosynchronous' is applied to a satellite orbit around the Earth, and irrespective of orbital inclination, whose orbital period is equal to that of a sidereal day, typically given in the literature as 23 hr 56 min 4 sec. As such, the more general term 'geosynchronous' includes the term 'geostationary', but not the other way around.

Abstract

This thesis investigates improving communication link coverage through tri-orthogonal polarisation diversity. Tri-orthogonal polarisation diversity exploits radiated electromagnetic energy transmission and reception in three orthogonal spatial directions with an aim to provide enhanced communication link performance. Original contributions to this branch of diversity are presented in areas of both software and hardware design.

First, simulations are presented highlighting the benefit of tri-orthogonal polarisation diversity at both the transmitter and receiver over a range of terrestrial channel conditions. The results are presented in an easily understandable graphical format that results from a novel model design considering all antenna orientations. Orientation robustness at the antenna is demonstrated as a consequence of a tri-orthgonal polarisation diverse approach.

Second, additional research is performed in order to extend the model into the field of satellite systems. The ionosphere is required to be modelled, and this is performed according to a novel vectorised approach using realtime ionospheric data and terrestrial magnetic field appreciation.

Third, ionospheric modelling is incorporated into a non-geosynchronous satellite orbit channel model that provides an insight into the benefit of applying a tri-orthogonal polarisation diverse approach uniquely at the receiver. Novelty is provided in the form of a vectorised approach to simulation covering all antenna orientations in a field-of-view as observed from a satellite transmitter. This is extended over the orbits of three distinct satellite systems. Output is provided in graphical format and conclusions are drawn form the data which suggest that a tri-orthogonal polarisation diverse approach applied at the receiver provides an increase in reception performance.

Fourth, an antenna is designed, simulated, constructed and tested that provides three orthogonal polarisations in a phase-centred differentially-fed package. Novelty is provided in the design being planar in nature, with three orthogonal modes being able to be transmitted from a single slot. Results emanating from the testing procedure demonstrate the benefits of the design in terms of diversity and extension to beamforming applications.

Fifth, as an extension to the antenna design, a circularly polarised feeding arrangement is used together with an omnidirectional vertically polarised mode feed in an antenna and feed combination. This provides the possibility of a direct comparison with conventional circularly polarised techniques, such as those used in both terrestrial and satellite receive antennas.

Sixth, the operational bandwidth of the omnidirectional vertically polarised mode is extended by adapting the design of the cavity wall resonating slots in a substrate-integrated monopole antenna while maintaining a planar structure. The electric monopole design demonstrates an increase in operating bandwidth from 2.5% to 56%.

In the thesis, a tri-orthogonal polarisation diverse approach is shown to be beneficial to signal reception over a range of channels, both in the areas of terrestrial and satellite communications. The concept is demonstrated to be feasible in a planar structure. Tri-orthogonal polarisation diversity is likely to play an increasing role in the future as systems look to cope with an ever increasing data flow.

The demand for content on mobile devices has forced massive growth in mobile data over the past two decades. This growth has recently reached saturation point, and so new avenues for extending growth have to be considered. A search for available bandwidth has lead research to focus on the mmWave section of the electromagnetic spectrum. The advent of the next generation of wireless connectivity, dubbed fifth generation or 5G, is now upon us (Rappaport *et al.* 2013b). With data traffic set to multiply by up to one thousand fold by 2020 (Qualcomm Inc. Accessed: 2014b, Qualcomm Inc. Accessed: 2014a, Li *et al.* 2014, Chin *et al.* 2014), as The Internet of Things (Ashton 2009, Cisco Inc. Accessed: 2014, Gubbi *et al.* 2013) enters into the fray, an overhaul of wireless design is somewhat overdue. For static point-to-point, or LoS systems, challenges exist according to the channel environment and temporal changes that may occur within. For any network that has a mobile component built in, where spatial position and alignment of transmitter and receiver change over time, signal propagation is additionally influenced by link geometry. In an increasingly mobile world, this presents challenges as increased coverage, one of the main focus points of the 5G system, will require efficient use of radiated electromagnetic energy.

Conventional techniques for improving data rate have typically aimed at increasing performance at the transmitter. For terrestrial networks, a transmitter is typically stationary. Performance outweighs size constraints and so power amplification and combination may be used to excite antennas that flood a network cell with a strong linearly

polarised transmitted signal. For commercial providers, this has proved a very successful technique, mainly as a result of the majority of wireless subscribers living in dense urban environments. For a linearly polarised wave, operating at conventional operating frequencies around 2 GHz, and transmitted with relatively high power, the urban environment typically provides assistance for signal reception at the receiver through diversity brought about by reflection, refraction and scattering or multipath due to the presence of buildings. Small misalignments in transmit and receive antennas are mitigated as the propagating signal wavelength is large and a relatively high transmit power establishes a relatively high signal-to-noise ratio, providing useful multipath effects over the channel. At certain receive positions, channel fading may occur when superposition of received multipath components effectively cancel each other. This may be mitigated through additional transmitters that are spaced appropriately; a concept known as spatial diversity that has been cited at mmWave frequencies (Smulders 2002, Park and Pan 2012). Diversity of signal is important in that it offers a greater possibility of a signal being received due to individuality of uncorrelated channel propagation for each diverse signal component.

As more content is demanded by subscribers within an ever shrinking timeframe, a higher frequency of operation is typically required for a carrier wave capable of providing this service. Add in the context of mobility, and issues quickly appear. Beneficial effects on a linearly polarised signal operating at conventional low gigahertz frequencies arising from reflection, refraction, and scattering or multipath effects, assist signal reception. Relatively long wavelengths are subjected to many scatterers, and due to the relatively high transmit power involved, scattering effects provide diversity at the receiver in the form of many smaller receivable diverse signal components. These signal components are superpositioned either constructively or destructively, after diverse individual propagation through the channel, at the receiver to provide signal reception.

At mmWave frequencies, due to a shrinking wavelength, the following issues arise:

- increased path loss over a defined range due to spreading loss (Pozar 2011), and increased atmospheric absorption (Liebe *et al.* 1989). An obvious solution is to provide more transmit power at the transmitter. At higher frequencies, miniaturisation of devices limits this possibility as heat sinking becomes problematic. Amplifier non-linearity and unwanted third order intermodulation impact on system performance (Niknejad and Hashemi 2008, Hashemi and Raman 2016)

- the beneficial effect of multipath fading may not exist in a mmWave terrestrial channel (Pi and Khan 2011), as a smaller wavelength typically implies a reduced beamwidth and less scatterers available for the LoS signal to scatter into useful smaller diverse signal components. Due to a relatively low transmit power involved, any scattering of a LoS signal into smaller, weaker diverse signal components may result in no received signal. As a result, cell range is reduced and more transmitters are required to provide coverage over a network

- with a shrinking wavelength, relatively lower transmit power, and increased mobility, antenna misalignment becomes problematic. A drive for radiated power efficiency is paramount in providing the next generation of wireless networks. An ability to transmit signals into and receive signals from all angles is necessary (Rappaport *et al.* 2013b).

The terahertz range, for example, offers extremely high transfer rates, although any small misalignment greatly affects rate. The use of dielectric mirrors is required to effectively steer the transmitted signal to its destination. Mitigation of misalignment becomes important in maintaining system performance.

For the next generation of mobile wireless systems to operate within the mmWave section of the electromagnetic spectrum, a solution to extend range is to increase radiated energy in a direction of propagation, through beam steering techniques. Within a mobile context, this poses challenges, not least as the link geometry is variable. For terrestrial networks, conventional transmitted waveforms are mainly vertically polarised, or circularly polarised, and as such are mainly one dimensional, or two dimensional at best, in performance. To provide the next generation of wireless networks, a third dimension needs to be considered to provide efficient use of radiated electromagnetic energy. Frequency bands of interest for 5G systems differ from country to country. According to the US Federal Communications Commission (FCC), the mmWave region that will be studied ranges from 24–80 GHz (Rappaport *et al.* 2013b, Rappaport Accessed: 2014, Above Ground Level Media Group Accessed: 2015).

One of the aims of 5G is to improve coverage (Rappaport *et al.* 2013b). One method that is being considered is the joining of terrestrial and satellite services into one seamless network that may be readily accessed by the subscriber at the receiver (Evans *et al.* 2005, Evans *et al.* 2015, Federal Communications Commission Accessed: 2016). Satellite

networks provide their own specific challenges, as transmit power is limited to payload specifications, and coverage typically requires a satellite that is moving relative to the Earth's surface. Once again we find ourselves facing the same three issues that we encountered within the terrestrial context of a mmWave channel. If we are to increase link performance in a satellite channel to complement any improvement in terrestrial channels then the following points need to be considered:

- propagation using higher operating frequencies typically suffers from higher path losses (Liebe *et al.* 1989, Pozar 2011). In some circumstances this can be mitigated by higher transmit power, but not all. A satellite payload is subject to a strict payload capacity and this restricts the size of transmit power devices and hence available transmit power that can be launched into orbit
- a lack of beneficial reflectors, refractors, and scatterers is observed during channel propagation as the signal is typically LoS, narrow in beamwidth, and weak due to higher path loss and lower transmit power (Pi and Khan 2011). Multipath effects may degrade system performance as signals are weak
- an evolving link geometry that affects antenna alignment. Linear and circular polarised signals are only two dimensional in nature. Three dimensions need to be considered, and beam steering of radiated power to provide the required range is a requirement (Evans *et al.* 2005, Hong *et al.* 2014b).

To ensure that the next generation of mobile systems are fully mobile, while providing increased data rate, we need to consider diversity in three dimensions. Beam steering of a transmitted signal with high gain in the direction of a receiver is one viable option, and in the context of full mobility, three dimensional signal transmission and reception appears a logical step to achieving this (Hong *et al.* 2014a). While at a terrestrial transmitter, it is suggested that size is not a constraint, it remains so for a satellite transmitter, as it is at a mobile receiver. This rules out spatial diversity as an approach to increasing system performance. One approach of increasing diversity within a confined volume is through polarisation techniques (Vaughan 1990).

In this thesis, we investigate the benefit of a subset of this approach—tri-orthogonal polarisation diversity (Andrews *et al.* 2001). In effect, the concept provides at least one additional degree of freedom or layer of diversity over conventional techniques such as circular polarisation. Due to orthogonality in three directions, this approach has a

wide field of view, and potentially offers diversity and improved system performance through beam steering in any unit direction. Tri-orthogonal polarisation diversity may be applied either at the transmitter, at the receiver, or at both.

In Chapter 1 of the thesis, both novel software and hardware aspects of the research are highlighted. Overall, the research outcomes of this thesis from both simulation and measured results suggest that the concept of tri-orthogonal polarisation diversity is:

- beneficial to wireless performance over a majority of antenna orientations
- plausible for implementation within typical antenna volume constraints.

Publications

Note: Articles with an asterisk (*) are directly relevant to this thesis.

Journal Articles

- *Lawrence, N. P., Ng, B. W.-H., Hansen, H. J. and Abbott, D., "5G terrestrial networks: Mobility and coverage—solution in three dimensions," *IEEE Access*, April 2017. doi: 10.1109/ACCESS.2017.2693375

- *Lawrence, N. P., Fumeaux, C. and Abbott, D., "Planar slot antenna with circular and vertical polarization diversity," *Microwave and Optical Technology Letters*, 2017. (in review)

- *Lawrence, N. P., Fumeaux, C., Abbott, D., "Planar triorthogonal diversity slot antenna," *IEEE Transactions on Antenna and Propagation*, vol. 65, no. 3, pp. 1416–1421, 2017. doi: 10.1109/TAP.2016.2647719

- *Lawrence, N. P., Hansen, H., Abbott, D., "Tri-orthogonal polarization diversity reception for non-geosynchronous satellite orbit ionospheric channels," *International Journal of Satellite Communications and Networking*, 2016. doi: 10.1002/sat.1203

- *Lawrence, N. P., Fumeaux, C. and Abbott, D., "Wideband substrate-integrated monopole antenna," *Microwave and Optical Technology Letters*, 58(8), pp. 1855–1857, 2016. doi: 10.1002/mop.29925

- *Lawrence, N. P., Hansen, H. and Abbott, D., "Triorthogonal polarization diversity for 5G networks," *Transactions on Emerging Telecommunications Technologies*, 2016, pp. 992–999. doi: 10.1002/ett.3042

- *Lawrence, N. P., Ng, B. W.-H., Hansen, H. J. and Abbott, D., "Analysis of millimetre-wave polarization diverse multiple-input multiple-output capacity," *Royal Society Open Science*, vol. 2, no. 12, art. no. 150322, 2015. doi: 10.1098/rsos.150322

- *Lawrence, N. P., Hansen, H. J. and Abbott, D., ”3-D low earth orbit vector estimation of Faraday rotation and path delay,” *IEEE* Access, vol. 3, pp. 1684–1694, 2015. doi: 10.1109/ACCESS.2015.2479247

- Alahbabi, M., Lawrence, N., Cho, Y. T. and Newson, T. P., ”High spatial resolution microwave detection system for Brillouin-based distributed temperature and strain sensors,” *Measurement Science and Technology*, 2004. doi: 10.1088/0957-0233/15/8/019

Conference Articles

- *Lawrence, N. P., Hansen, H. and Abbott, D., ”Implications of polarization impurity for 5G networks,” *41st International Conference on Infrared, Millimeter, and Terahertz Waves* (IRMMW-THz), Copenhagen, Denmark, 2016, doi: 10.1109/IRMMW-THz.2016.7758493

- *Lawrence, N. P., Ng, B. W.-H., Hansen, H. J. and Abbott, D., ”Analysis of millimeter-wave polarization diverse MIMO capacity,” *39th International Conference on Infrared, Millimeter, and Terahertz Waves* (IRMMW-THz), Tucson, AZ, 2014. doi: 10.1109/IRMMW-THz.2014.6956121

- *Lawrence, N. P., Ng, B. W.-H., Hansen, H. J. and Abbott, D., ”Analysis of polarization diversity at terahertz frequencies,” *39th International Conference on Infrared, Millimeter, and Terahertz Waves* (IRMMW-THz), Tucson, AZ, 2014. doi: 10.1109/IRMMW-THz.2014.6956120

- Lawrence, N., Davis, L. M. and Haley, D., ”A polarimetric line-of-sight channel model for MIMO satellite communications,” *Communications Theory Workshop* (AusCTW), Adelaide, Australia, 2013, pp. 99–104. doi: 10.1109/AusCTW.2013.6510052

- Alahbabi, M., Lawrence, N., Cho, Y. T. and Newson, T. P., ”High spatial resolution microwave detection system for long range Brillouin-based distributed sensors,” *16th International Conference on Optical Fiber Sensors* (OFS-16), Nara, Japan, 13–17 Oct 2003. oai: eprints.soton.ac.uk:41622

List of Figures

1.1 In countries around the world, an unlicensed 60 GHz bandwidth regulation exists with a large ultrawide bandwidth, typically of 7 GHz 6

1.2 A view of the shift towards total wireless connectivity 8

1.3 Driverless vehicles and remote surgery are offered through wireless total connectivity 9

1.4 The various possibilities of polarisation misalignment and subsequent mismatch loss 12

1.5 Thesis outline and original contributions 19

1.6 Frames of reference 21

2.1 The mmWave region of the electromagnetic spectrum 24

2.2 Millimetre wave beamwidth 26

2.3 Colocated tri-orthogonal antenna arrangement 28

2.4 Slot radiator version of the MIMO cube 30

2.5 A tri-orthogonal antenna constructed using FR4 material 31

2.6 A cross-shaped dielectric resonator antenna (DRA) structure, operating at 4.7 GHz with a 6.8% overlapping bandwidth 32

3.1 Tri-orthogonal arrangement of half-wavelength dipole modes 43

3.2 The benefit of a tri-orthogonal arrangement of polarisation modes 44

3.3 Terrestrial channel link geometry 51

3.4 System according to specific location in the terrestrial FoV 53

3.5 Gain (G) (dB) profiles of the six half-wavelength dipole modes over the terrestrial channel FoV 55

3.6 Polarisation mismatch (e_{pol}) (dB) profiles for each unit dipole mode pair 56

3.7 Simulated capacity ($\text{bps}_{(1\text{ Hz})}$), or spectral efficiency, at the FoV centre of uni-polarised, dual-polarised, and tri-orthogonal arrangements at 2.55 GHz 61

3.8 Simulated capacity ($bps_{(1\ Hz)}$), or spectral efficiency, at the FoV centre of uni-polarised, dual-polarised, and tri-orthogonal arrangements at 60 GHz 62
3.9 Channel parameters over the FoV 62
3.10 Tri-orthogonal, or 3 × 3, AWGN fading channel capacity ($bps_{(1\ Hz)}$), or spectral efficiency 63
3.11 Capacity advantage ($bps_{(1\ Hz)}$), or spectral efficiency advantage, of a tri-orthogonal, or 3 × 3, system over that of a dual-polarised, or 2 × 2, system in an AWGN fading channel 64
3.12 Tri-orthogonal, or 3 × 3, Rayleigh fading channel capacity ($bps_{(1\ Hz)}$), or spectral efficiency 65
3.13 Capacity advantage ($bps_{(1\ Hz)}$), or spectral efficiency advantage, of a tri-orthogonal, or 3 × 3, system over that of a dual-polarised, or 2 × 2, system in a Rayleigh fading channel 66
3.14 Rayleigh fading channel capacity ($bps_{(1\ Hz)}$), or spectral efficiency, profile at $\theta_T = 0°$ for uni-polarised, dual-polarised and tri-orthogonal systems 68
3.15 Rayleigh fading channel capacity ($bps_{(1\ Hz)}$), or spectral efficiency, profile at $\theta_T = 90°$ for uni-polarised, dual-polarised and tri-orthogonal systems 69
3.16 Capacity advantage ($bps_{(1\ Hz)}$), or spectral efficiency advantage, of a rich scattering environment such as a Rayleigh fading channel over that of a AWGN fading channel 70

4.1 Ionospheric channel link geometry 81
4.2 System according to specific location in NGSO ionospheric FoV 82
4.3 Typical ionospheric layer profile at low latitudes according to sun activity and diurnal effect 89
4.4 Height parameter within the ionospheric channel model 90
4.5 Path delay (m) estimates over the FoV (28th May 2014, frequency: 1.616 GHz, orbit height: 780 km) 93
4.6 Faraday rotation (°) estimates over the FoV (15th January 2010, frequency: 1.616 GHz, orbit height: 780 km) 94

5.1 Commercial patch antenna providing L1 GPS and Iridium satellite signal reception 106

5.2 Transmit gain profile of L1 GPS system . . . 132
5.3 Orbcomm LEO satellite system Tx and Rx gains at the satellite, T . . . 133
5.4 Satellite system providing conventional CP mode wave transmission to the nadir location in the NGSO ionospheric channel FoV . . . 134
5.5 Iridium system FoV dimensional metrics, according to orbital parameters in Table 5.1 . . . 135
5.6 Orbcomm system FoV dimensional metrics, according to orbital parameters in Table 5.1 . . . 136
5.7 GPS system FoV dimensional metrics, according to orbital parameters in Table 5.1 . . . 137
5.8 Determination of the NGSO FoV according to latitude (L) and longitude (l) . . . 138
5.9 Iridium system gains (dB) . . . 139
5.10 Iridium system polarisation mismatches (dB) without the effect of Faraday rotation, (operating frequency: 1616 MHz; (L,l): (0°,0°)) . . . 140
5.11 Iridium system polarisation mismatches (dB) with the effect of Faraday rotation, (operating frequency: 1616 MHz; (L,l): (0°,0°)) . . . 141
5.12 Doppler shift (Hz) for an Iridium satellite tracking west to east while passing over a stationary ground receiver at any (L,l) position within the NGSO FoV . . . 142
5.13 Doppler frequency shift of a NGSO satellite system . . . 142
5.14 Three dimensional Doppler shifts (Hz) for the Iridium LEO satellite travelling in an orbit inclined at $\theta_{\text{inc}} = 86.4°$ and five distinct ground receiver vectors . . . 143
5.15 Diurnal ionospheric scaling factors . . . 144
5.16 Ionospheric profiling as a function of longitudinal position, or (l) and Coordinated Universal Time, or UTC . . . 145
5.17 Simulated Iridium system style capacity ($\text{bps}_{(1\text{ Hz})}$), or spectral efficiency, over a FoV centred at (0,0) and according to orbital parameters . . . 147
5.18 Phased Array Panellisation . . . 149
5.19 Simulated Iridium system style capacity ($\text{bps}_{(1\text{ Hz})}$), or spectral efficiency, using a method of array panellisation, over a NGSO ionospheric FoV centred at (0,0) and according to orbital parameters . . . 150

5.20 Iridium orbit track lasting 6027s over the globe, with FoV measurements made every 600s . . . 153
5.21 Orbcomm orbit track lasting 6021s over the globe, with FoV measurements made every 600s . . . 154
5.22 GPS track lasting 23h 57m 24s over the globe, with FoV measurements made every hour . . . 154
5.23 Simulated percentage improvement in Iridium system capacity, over a NGSO ionospheric FoV according to Iridium orbital parameters and a total fading margin of 16 dB, as a result of implementing a third orthogonal polarisation mode at the receiver . . . 156
5.24 Simulated percentage improvement in Orbcomm system capacity, over a NGSO ionospheric FoV according to Orbcomm orbital parameters and a total fading margin of 16 dB, as a result of implementing a third orthogonal polarisation mode at the receiver . . . 157
5.25 Simulated percentage improvement in GPS system capacity, over a NGSO ionospheric FoV according to GPS orbital parameters and a total fading margin of 22 dB, as a result of implementing a third orthogonal polarisation mode at the receiver . . . 158
5.26 Simulated percentage improvement in Orbcomm system capacity, over a NGSO ionospheric FoV according to Orbcomm orbital parameters and a deterministic complex LoS voltage transfer with no fading, as a result of implementing a third orthogonal polarisation mode at the receiver . . . 159
5.27 Simulated percentage improvement in GPS system capacity, over a NGSO ionospheric FoV according to GPS orbital parameters and a deterministic complex LoS voltage transfer with no fading, as a result of implementing a third orthogonal polarisation mode at the receiver . . . 160
5.28 Simulated percentage improvement in Iridium system capacity, over a NGSO ionospheric FoV according to Iridium orbital parameters and suburban LoS shadowing statistical fading, as a result of implementing a third orthogonal polarisation mode at the receiver . . . 168
5.29 Simulated percentage improvement in Iridium system capacity, over a NGSO ionospheric FoV according to Iridium orbital parameters and suburban intermediate shadowing statistical fading, as a result of implementing a third orthogonal polarisation mode at the receiver . . . 169

5.30 Simulated percentage improvement in Iridium system capacity, over a NGSO ionospheric FoV according to Iridium orbital parameters and suburban deep shadowing statistical fading, as a result of implementing a third orthogonal polarisation mode at the receiver 170
5.31 Simulated percentage improvement in Iridium system capacity, over a NGSO ionospheric FoV according to Iridium orbital parameters and urban LoS shadowing statistical fading, as a result of implementing a third orthogonal polarisation mode at the receiver 171
5.32 Simulated percentage improvement in Iridium system capacity, over a NGSO ionospheric FoV according to Iridium orbital parameters and urban intermediate shadowing statistical fading, as a result of implementing a third orthogonal polarisation mode at the receiver 172
5.33 Simulated percentage improvement in Iridium system capacity, over a NGSO ionospheric FoV according to Iridium orbital parameters and urban deep shadowing statistical fading, as a result of implementing a third orthogonal polarisation mode at the receiver 173
5.34 Average capacity performance of the 3×2 arrangement over an orbit . . 174
5.35 Average capacity performance of the 3×2 tri-orthogonal receiver and 2×2 conventional CP mode receiver system arrangement over an orbit 176
5.36 Simulated increase in diversity gain (dB) 179

6.1 Antenna design with port referencing 187
6.2 The two fundamental modes of operation of the proposed antenna . . . 188
6.3 Tri-orthogonal feed design with port referencing 190
6.4 Simulated and measured port reflection coefficients of the LP system . . 192
6.5 Simulated and measured port isolation coefficients of the LP system . . 193
6.6 Radiation characteristics of the tri-orthogonal antenna and feed design . 194
6.7 Simulated 3D OLP radiation pattern when the antenna is driven through port 5 196
6.8 Simulated 3D (a) L3X (b) L3Y radiation patterns when the antenna is driven through port 6 197
6.9 Simulated 3D (a) L3Y (b) L3X radiation patterns when the antenna is driven through port 7 198

6.10 Mean effective gains (MEGs) for the three orthogonal polarisation modes 198
6.11 Cross correlation of the antenna 203
6.12 The tri-orthogonal design, due to low mutual coupling between the three orthogonal polarisation modes, provides pattern diversity through phased feeding techniques 205

7.1 Antenna design with port referencing. A symmetrical design about the z axis includes a common radiative slot through which CP and OLP modes radiate 214
7.2 Mode radiation characteristics 215
7.3 OLP, CP feed design with port referencing 216
7.4 Simulated and measured port reflection coefficients and isolation coefficients of the OLP, CP antenna and feed system 218
7.5 Radiation characteristics of the OLP, CP antenna and feed design 224
7.6 Measured and simulated axial ratio, showing CP performance over a bandwidth about the design frequency of 5.89 GHz 225
7.7 Mean effective gains (MEGs) for the OLP and CP modes 225
7.8 Measured and simulated envelope correlation coefficients (ECCs) of the OLP, CP mode antenna and feed system 226
7.9 Port diversity operation of the antenna in the main orthogonal ϕ axes directions, according to antenna port excitations of cases I to IV in Table 7.5226
7.10 Phase and power diversity operation of the antenna 227

8.1 The antenna design 232
8.2 Reflection coefficient of the proposed antenna 233
8.3 Antennna realised gain patterns 235

A.1 An electromagnetic wave consists of a sinusoidal electric field distribution and associated sinusoidal magnetic field distribution 252
A.2 The direction of polarisation of an electromagnetic wave is described according to the electric field vector 254

A.3 Circular polarisation 255
A.4 Linear and circular polarisations are the extreme forms of the more general case of elliptical polarisation 257
A.5 The effect of relative phase on two orthogonal polarisation modes 258
A.6 Resultant polarisation through circular polarisation combination 259
A.7 Resultant polarisation through linear polarisation combination 260

List of Tables

1.1 Unlicensed wireless communication bands 6

5.1 Commercial system information on three distinct NGSO satellite systems considered in this thesis 111
5.2 Orbital parameters for the three distinct NGSO satellite systems considered in this thesis 112
5.3 Iridium style channel capacity ($\text{bps}_{(1\text{ Hz})}$), or spectral efficiency, minima, maxima, and range over the NGSO ionospheric FoV centred at (0,0) . . . 148
5.4 Narrowband fading statistics (suburban area, handheld antenna, 1.82 GHz) 162
5.5 Narrowband fading statistics (urban area, handheld antenna, 1.82 GHz) 163

6.1 Antenna Dimensions 189
6.2 Feed Dimensions 191
6.3 Mean effective gains (MEGs) for the three orthogonal polarisation modes 199
6.4 Envelope correlation coefficients (ECCs) (from simulated 3D radiation patterns) 199
6.5 Real and imaginary electric field components in specific radiating directions (from simulated 3D radiation patterns) 201
6.6 Antenna cross correlation in specific radiating directions (from simulated 3D radiation patterns) 201
6.7 Antenna cross correlation at various values of elevation given by θ along a constant azimuthal angle of $\phi = 45^\circ$ (from simulated 3D radiation patterns) 202

7.1 Feed Dimensions 213
7.2 Mean effective gains (MEGs) for the OLP and CP modes 219
7.3 Real and imaginary electric field components in specific radiating directions (from simulated 3D radiation patterns) 221
7.4 Antenna cross correlation in specific radiating directions (from simulated 3D radiation patterns) 221

7.5 Diversity Feeding 223

8.1 Antenna Dimensions 231

Chapter 1

Introduction to Current Challenges Facing Continued Mobile Data Growth

THIS chapter provides an introductory background on the current challenges facing continued mobile data growth. It highlights proposed wireless network solutions, while suggesting that radiation efficiency may benefit from polarisation diversity in three orthogonal directions. Indeed, the next generation of wireless systems, aiming to provide for a massive increase in mobile data traffic due to a rapid increase in subscriber numbers and connected devices, must be developed on the basis of exploration, expansion, and enhancement of current engineering techniques. In order to deliver high quality wireless connectivity, a concerted effort to improve network performance is required by all organisations involved. Material is provided according to the following criteria:

- why is there an issue currently facing wireless network design?
- what exactly is being done about it?
- how can the research in this thesis impact this issue?
- what are the outcomes of the research in this thesis?

In light of this material, objectives and motivations behind the presented research are given. The original contributions of this thesis are then highlighted, followed by the structural organisation of the thesis.

1.1 Introduction

1.1.1 Why is There an Issue Currently Facing Wireless Network Design?

Mobile data growth has reached a tipping point (Rappaport *et al.* 2013b). The rapid explosion in wireless services over the past couple of decades has presented numerous challenges and solutions in order to provide the wireless subscriber with content. Diversity techniques coupled with coding techniques now provide wireless communications for a growing mobile population. The introduction of smartphones, enabling various data forms to be transferred wirelessly at the touch of a screen, has revolutionised personal communication. Systems are constantly evolving in order to provide the user with improved content. To provide higher end content to the wireless subscriber, more data is typically required to be transferred. This requires higher data transfer rates, or a wireless subscriber who is willing to wait longer for data to be transferred to them. With the latter option not being credible, data transfer rates must increase. Available bandwidth at operating frequencies used in current systems is limited, and this is driving the next generation of wireless design.

1.1.2 What Exactly is Being Done About It?

Engineers are agreed that higher operating frequencies will be required to advance mobile data growth and expectations. The metric of capacity may be used to gauge wireless system development that aims to meet this increase in mobile data traffic. Capacity may be defined as the theoretical limit for the amount of information that may be transferred via a communication channel with a given noise characteristic and bandwidth (Shannon 1948, Shannon 1949). If the transmission information rate, typically denoted as R, is less than the system capacity, typically denoted as C, then coding techniques may be employed to reduce data transmission error probabiliites down to arbitrarily small values. To achieve the lowest values of error probability, coding must work on longer blocks of signal data, requiring longer time delays and higher computer processing requirements.

The theoretical limit of capacity is now in sharp focus if mobile technology is to meet performance requirements over the next decade.

1.1 Introduction

The introduction of fifth generation, or 5G, regulations aims to provide systems that may deliver data transfer rates or capacity two to three orders of magnitude higher than those currently available (Rappaport *et al.* 2013b). To achieve this, we may consider Shannon's theorem on the capacity C of a channel in bits/sec with additive white Gaussian noise. This is given by the Shannon-Hartley equation,

$$C = B \log_2 \left(1 + \frac{S}{N}\right) \tag{1.1}$$

where B is the channel bandwidth in Hertz and S and N are the average power of the received signal and noise over the bandwidth in Watts, respectively. In order to provide multi-gigabit/sec data transfer rates, the theorem suggests that the capacity of a channel requires a commensurate large bandwidth and large signal power. The Shannon-Hartley equation is based on two important concepts, namely that:

- in principle, a trade-off between SNR and bandwidth is possible
- the information capacity depends on both SNR and bandwidth.

When considering Equation 1.1, it is useful to note that:

- the bandwidth of the system limits how fast information symbols may be sent over the communications channel
- the SNR limits the amount of information that may be placed in each transmitted symbol
- an increase in SNR provides increased transmission robustness against noise. In effect, SNR provides us with a proxy for signal quality, signal power and channel characteristics
- capacity is measured at the receiver front end
- in order to increase the information rate, the SNR and allocated bandwidth need to be traded against each other to find the best combination of these two parameters
- in the instance of no noise, the SNR becomes infinite. An infinite information rate is theoretically possible within a very small bandwidth.

The search for methods to increase data transfer capacity to satisfy future mobile traffic demands stems from an initial decision in December 1995 by the US Federal Communications Commission to allocate a 5 GHz band for unlicensed applications in the mmWave region around 60 GHz. A subsequent modification to this allocation resulted in the band being extended to 7 GHz (57–64 GHz) (Van Tuyl 1996). Many other countries, including Australia, opted for similar frequency band allocation for high data rate unlicensed communications at mmWave frequencies, and this is shown in Figure 1.1. At 60 GHz, strong attenuation caused by the resonance of oxygen molecules exists, and so this band is in principle not suitable for long-range wireless communication of the order of a few kilometres. This range limitation permits spectrum reuse by multiple systems within close proximity of one another. Furthermore, as well as a larger available bandwidth at higher frequencies resulting in higher capacity data transfer, operation at mmWave frequencies allows both antenna sizes and spacing in multiple-antenna systems to be reduced. This offers the possibility of compact systems that are affordable (Niknejad and Hashemi 2008) and able to be integrated into areas such as textiles (Werner and Jiang 2016), potentially offering an unprecedented access to wireless communications.

In many parts of the world, research into 5G technologies is not confined to a single frequency band around 60 GHz. In the UK, a portion of the mmWave region of the electromagnetic spectrum between 28–80 GHz is being investigated (Quotient Associates Ltd Accessed: 2015) to provide an increase in data transfer capacity. In the US, the frequency bands of interest are given below in what is known as the Spectrum Frontiers Proposal (Rappaport *et al.* 2013b, Rappaport Accessed: 2014, Above Ground Level Media Group Accessed: 2015, Qualcomm Technologies Inc. Accessed: 2016, Cellular Telephone Industries Association Accessed: 2016, Federal Communications Commission Accessed: 2016):

- 24 GHz Bands (24.25–24.45 GHz and 25.05–25.25 GHz)
- Local Multipoint Distribution Service Band (27.5–28.35 GHz, 29.1–29.25 GHz, and 31–31.3 GHz)
- 39 GHz Band (38.6–40 GHz)
- 37/42 GHz Bands (37.0–38.6 GHz and 42.0–42.5 GHz)
- 60 GHz Bands (57–64 GHz and 64–71 GHz)

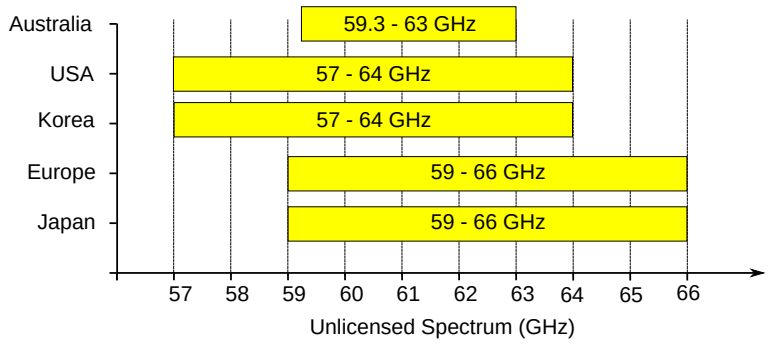

Figure 1.1. In countries around the world, an unlicensed 60 GHz bandwidth regulation exists with a large ultrawide bandwidth, typically of 7 GHz. The allocation of an unlicensed ultrawide bandwidth at 60 GHz, in the mmWave region, has paved the way for exploring the possibility of high capacity data transfer methods for fifth generation, or 5G applications.

Table 1.1. Unlicensed wireless communication bands. A comparison of the different features of some of the in-use license-free wireless communication bands and those at 60 GHz in the mmWave spectrum.

	802.11b	Bluetooth	802.11a	UWB	60 GHz
Cell radius (m)	100	10	50	10	10
Information rate per channel (Mbps)	11	1	54	50	500
Number of channels	3	10	12	6	10
Capacity (Mbps/m^2)	0.001	0.03	0.1	1	16

- 70/80 GHz Bands (71–76 GHz and 81–86 GHz).

In the US, interest in increasing data transfer rate was initially placed on technologies operating in the frequency band of 3.55–3.65 GHz, only slightly higher than those conventionally used, as frequencies beyond 24 GHz were perceived as unsuitable for signal propagation due to physical and technical limitations (Federal Communications Commission Accessed: 2015). However, it is now understood that multiple ricochets providing multiple reflections and hence multiple copies of a signal transmitted at 24 GHz or above are available after channel propagation at the receiver (Sun *et al.* 2014, MacCartney and Rappaport 2014). These processes provide diversity. Disparate signals resulting from these processes may be received by MIMO antennas and subsequently built into an intelligible data signal potentially offering multi-gigabit data transfer rates (Rappaport *et al.* 2013b, Alkhateeb *et al.* 2014).

The allocation of a 7 GHz bandwidth for the next generation or fifth generation of license-free communication devices operating at 60 GHz offers the possibility of enhanced transfer rates. Such data rates are far higher than those encountered at conventional low microwave frequencies (Smulders 2002). In Table 1.1, a comparison is made between different features of current in-use license-free wireless communication bands and those in the 60 GHz band.

The move to the mmWave spectrum is in anticipation of up to a thousand fold increase in mobile traffic by 2020. While mobile subscriber numbers are saturated in many developed countries, it is expected that content is likely to increase requiring greater network capacity. This traffic is to be driven primarily by the rapid spread of mobile networks into developing countries, as well as the integration of smart goods on to wireless networks, known as the Internet of Things (Ashton 2009). To summarise, the rollout of 5G is looking to provide:

- increased coverage (Rappaport *et al.* 2013b)
- integration of networks including satellite and terrestrial networks (Mak *et al.* 2014, Evans *et al.* 2015, Federal Communications Commission Accessed: 2016), and the Internet of Things (Gubbi *et al.* 2013).

Proposed concepts of the next generation of wireless interconnectivity are highlighted in Figures 1.2 and 1.3.

1.1.3 How Can the Research in This Thesis Impact This Issue?

The rollout of 5G is currently little more than a concept, with a fully fledged industry standard yet to be agreed upon. Standardisation of the concept is urgently required. Multiple groups are working on standards regarding interoperability and backward compatibility issues (Institute of Electrical and Electronics Engineers Accessed: 2016, European Union Accessed: 2016, Federal Communications Commission Accessed: 2016). Improved coverage is one aspect that is targeted in the 5G rollout. This statement is ambiguous as coverage is nominally applied to spatial position alone. If networks are to perform as required, the challenges of operating at mmWave frequencies need to be considered (Rappaport *et al.* 2013b). These challenges are brought about as a consequence of:

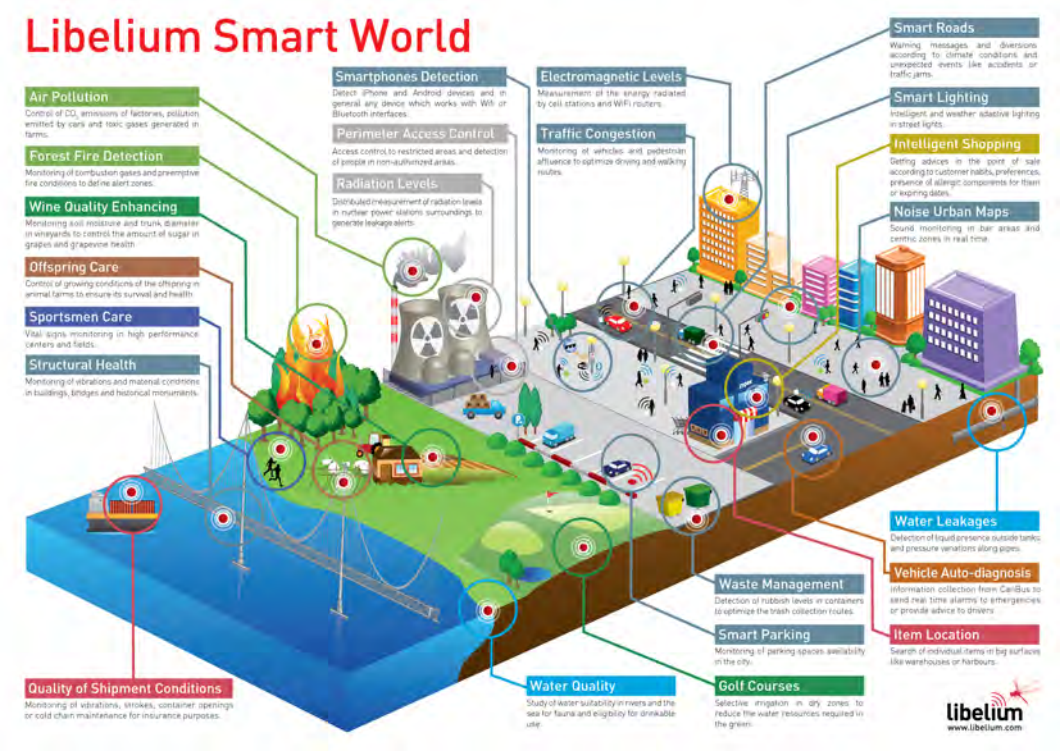

Figure 1.2. A view of the shift towards total wireless connectivity. The next generation of wireless networks aims to offer connectivity to up to a thousand fold more devices, but many questions remain as to how to progress to a target that has been set for 2020. After Libellium Comunicaciones Distribuidas (Accessed: 2014).

- higher transmit power being required to combat free space path loss effects over the channel
- higher transmit and receive antenna directivity being required to focus power, typically along boresight
- nonlinearity and intermodulation effects increasing as a function of frequency, restricting linear power transmission
- smaller component size creating issues for component heatsinking and effective aperture area.

In addition to these challenges, the effect of polarisation mismatch, or antenna misalignment, may drastically reduce system performance. To mitigate antenna alignment issues, circular polarisation (CP) is used as a *de facto* signal propagation technique (Toh *et al.* 2003). In effect, the transmitted electric vector tip may be considered as rotating about the direction of propagation (Balanis 2005). As a result, a component of the

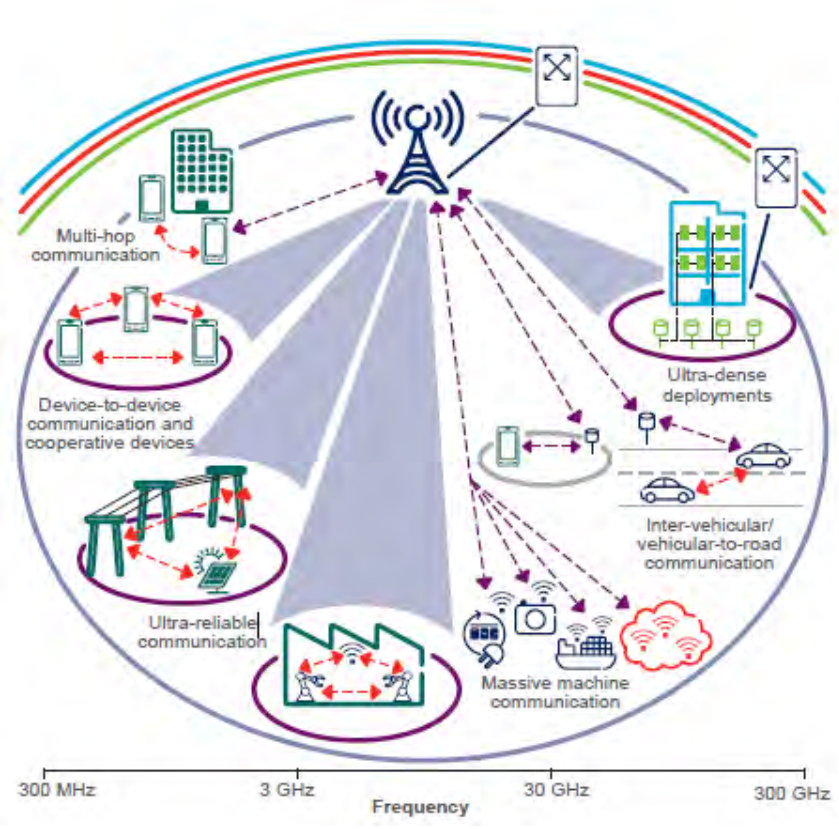

Figure 1.3. Driverless vehicles and remote surgery are offered through wireless total connectivity. Wireless connectivity for all devices offers the possibility of wireless control and optimisation of a majority of household appliances and industrial equipment in what is known as the Internet of Things. After Ericsson (Accessed: 2015).

propagated signal is always received, and for identically left or right-handed CP mode transmit and receive antennas that are perfectly aligned along a direction of propagation a CP wave is received provided that a CP wave is transmitted and that the channel affects the orthogonal linear components of the CP wave in an identical manner. Deviation of alignment of an antenna at either end of the channel, a transmitted signal with axial ratio that is not 0 dB, or channel effects which affect one linear component of the CP wave more than the other, develop an elliptically polarised (EP) wave. In the extreme case, the EP wave may become linearly polarised (LP), and this may severely degrade link propagation. In Rappaport *et al.* (2013b), the notion of beam steering is highlighted as a solution to misalignment issues.

This thesis investigates improving coverage through polarisation diversity in three orthogonal directions, otherwise known as tri-orthogonality. Diversity offers alternative signal propagation paths, and in so doing offers link possibilities in channels

that would otherwise prove impenetrable. Polarisation diversity uses orthogonality of polarisations to provide a compact solution that has been researched considering polarisation in two orthogonal dimensions (Lee and Yeh 1972, Turkmani *et al.* 1995). Extending polarisation diversity to three orthogonal dimensions effectively provides a colocated solution that theoretically may provide enhanced diversity, and the potential to beam steer to increase radiated electromagnetic energy in any link direction. In so doing, the angular range of coverage is expanded. However, physical antenna solutions no longer remain planar in nature, and acquire volume (Chiu *et al.* 2007b). Therefore, compactness of the solution is hitherto unavailable.

In Andrews *et al.* (2001), a tripling of capacity is suggested for a tri-polarised orthogonal arrangement at the antenna. The experiment is conducted at a frequency and in an environment that produces a rich scattering environment. In effect, this does not provide a full picture of the tri-orthogonal arrangement as misalignment issues are mitigated by such an environment. A similar environment is presented in Chiu *et al.* (2007b).

With these issues raised, the thesis aims to provide the following:

- an improved understanding of the effects of misalignment and its mitigation by a tri-orthogonal antenna arrangement over a range of channel environments
- a compact antenna solution for a tri-orthogonal polarisation diverse arrangement.

1.1.4 Research Motivations and Thesis Objectives

Wireless subscribers are predominantly concerned with ubiquitous, ever increasing amounts of content. In order to provide this, data rates need to be consistently augmented (Qualcomm Inc. Accessed: 2014a, Qualcomm Inc. Accessed: 2014b). At this point in time, conventional wireless propagation techniques have been more than adequate providers of content. Systems have made the best use of a signal wavelength that is often longer than objects found in the channel environment. Propagated signals have been able to reflect from and refract around objects to provide reception in places where no LoS signal propagation is possible. Strong reception signals have been a direct consequence of this effect. Where deadspots have occurred where no reception is possible, be it as a result of signal blockage or superpositioned cancellation of

signals at the receiver, a solution has been to add an additional transmit antenna. At the terrestrial level and in an environment where it makes economic sense to do so, this policy has been extremely useful. Furthermore, to increase rate, and so provide greater content, signal processing methods have been able to code signals to increase rate. Higher levels of complexity in coding typically rely on higher signal-to-noise ratios. Wireless network systems' architects have been able to squeeze as much rate as possible out of conventional networks. In environments where it is not economically viable to perform such measures, or in environments where it is just not feasible to do so, content has not evolved to the same extent.

The growth of mobile data in recent years has now reached a point where it has saturated networks. Additional bandwidth is required if this growth is to continue. But there is also a need to make systems more efficient if we are to reap the benefits of the next generation of wireless design.

When engineers highlight data rate, several points need to be made. Firstly, a maximum rate is often quoted (Samsung Electronics Inc. Accessed: 2014). Secondly, the conditions in which network performance is measured may be optimal (University of Surrey Accessed: 2015). Like-for-like comparisons become difficult. Thirdly, perfect antenna alignment of transmitter and receiver is the norm. After all, what would be the point of measuring rate using a misaligned system? Crucially, the third of these points is very much in focus if 5G is to deliver on what it promises. The concept of ubiquitous coverage has been mentioned as a goal of the rollout 5G networks. The definition remains rather vague, however. Coverage as a function of spatial positioning of antennas and as a function of relative angular alignment of antennas are not the same, and it can be argued that the latter is of more relevance as engineers look to use radiated power efficiently (Rappaport *et al.* 2013b).

This thesis considers a definition of coverage in terms of antenna alignment. A misalignment of incoming electromagnetic signal and receive antenna reduces link performance, and in the most extreme case may render the link inoperable. Figure 1.4 highlights the effect of polarisation misalignment. For terrestrial wireless systems, polarisation is defined by the orientation of the electric field vector relative to the plane of the Earth.

Polarisation mismatch is typically observed as a signal drop at the receiver due to a misalignment of electric field vectors of an incoming signal and of the receive antenna. The misalignment may result from incorrect alignment of the transmit antenna with

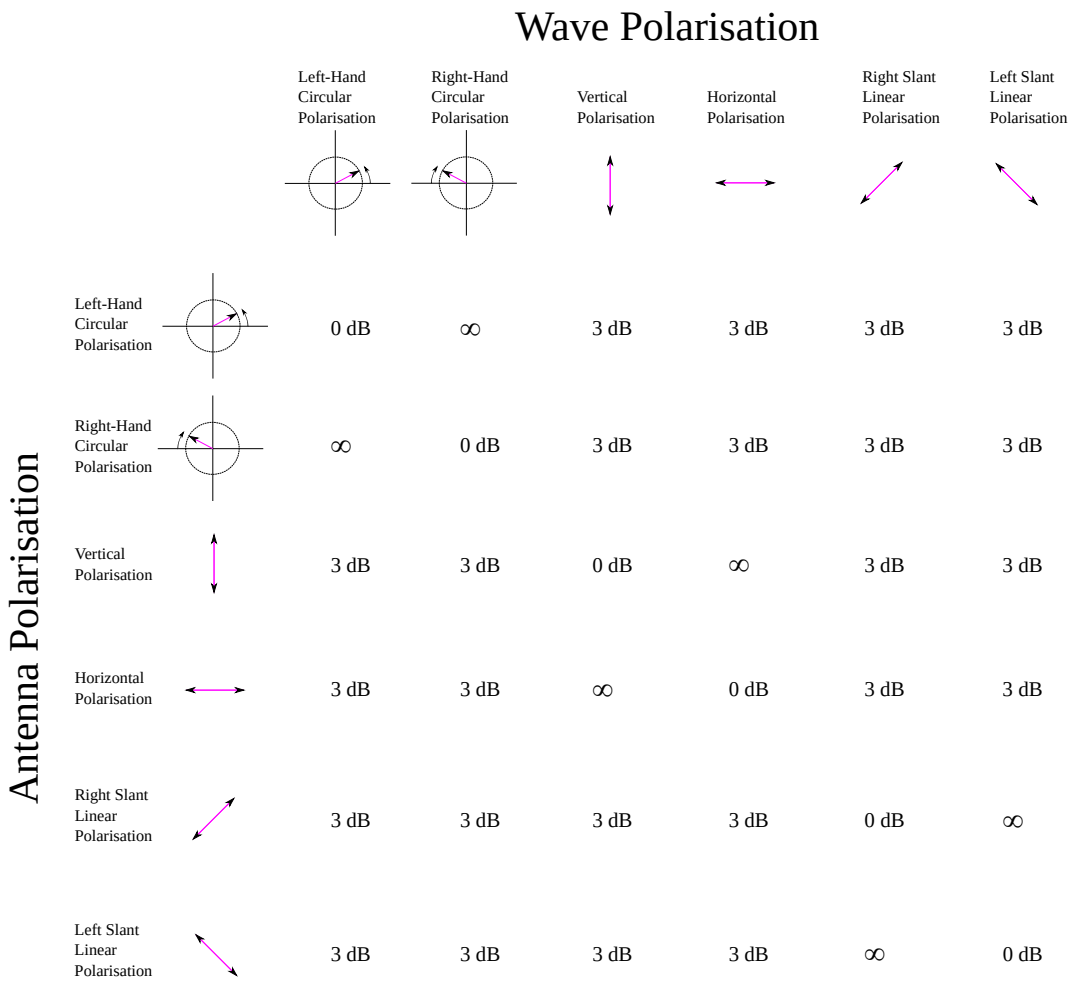

Figure 1.4. The various possibilities of polarisation misalignment and subsequent mismatch loss. Polarisation is defined by the orientation of the electric field vector relative to the plane of the Earth. The effect of polarisation misalignment between an incoming electromagnetic signal and a receive antenna may render links inoperable in the most extreme cases.

respect to the receive antenna to begin with, or the propagating signal experiencing depolarising effects in the channel, or a combination of both. Conventional techniques to combat such issues have included an increase of power at the transmitter, spatial diversity through provision of additional antennas spaced apart from each other, and signal propagation using circular polarisation techniques. In the latter, a component of the rotating electric vector tip of a propagating waveform is always received. However, a circularly polarised waveform may only be transmitted in one direction, and any deviation of a receiver away from this direction typically results in elliptically polarised reception. In the extreme case, reception may become linearly polarised which may result in a drop in system capacity. Deviation from a case of perfect reception of

a circularly polarised waveform may be exacerbated when the effects of specular reflection and multipath are also considered. Specular reflections of a signal provide a 180° shift in phase between propagating vertical and horizontal components of a circularly polarised signal. In an extreme case, a right-hand circularly polarised network may provide no reception at the receiver as the signal has become left-hand circularly polarised as a result of such a reflection.

In the case of multipath fading, received signal components may effectively cancel each other out at the receiver, providing reduced range or spatial positions of impaired or indeed no reception. Such fading may affect reception of a signal with purely LoS components, or that with stochastic components introduced through propagation over the channel. Signal scatterers may scatter a signal to the extent that all resulting diverse signal components are too weak for reception. The benefit of multipath is dependent on a high SNR at the receiver, together with a limited cancellation effect of superpositioned received signal components. These components provide diversity at the receiver as a result of propagating along uncorrelated individual subchannel paths. With increasing path loss, or reduced transmit power, multipath effects degrade signal reception more readily, as received signal strength begins to fall consistently below the receiver noise floor. The ability to provide an increased signal strength at the receiver becomes crucial in mitigating specular reflective effects and in providing beneficial multipath fading effects.

Fifth generation or 5G networks are looking to provide greater content in a unit time period through higher operating frequencies in the mmWave region of the electromagnetic spectrum. With new horizons appear new issues:

- higher operating frequencies are subject to increased free space path or spreading loss due to a smaller wavelength of operation (Pozar 2011)
- signal absorption at higher operating frequencies is higher than that encountered at conventional terrestrial network operating frequencies (Liebe *et al.* 1989)
- mmWave signals are not scattered to the same extent as conventional high power low gigahertz signals, as narrow beamwidths are required to focus transmit power. Multipath effects are typically not as beneficial (Pi and Khan 2011). Instead, a LoS signal tends to dominate. All of this suggests a higher power requirement

- higher power amplifiers at mmWave operating frequencies are typically inefficient smaller devices than those at low gigahertz frequencies (Niknejad and Hashemi 2008). Inefficiency leads to increased heat energy that must be dissipated effectively

- as operating frequency increases, solid state power devices typically become less efficient and are subject to non-linear effects (Hashemi and Raman 2016). Third order intermodulation, where an unwanted signal becomes dominant in an operating bandwidth, restricts transmit power. While not necessarily a problem in a terrestrial environment at the transmitter, where power amplifiers may be banked together to provide the required output power without producing an unwanted third order intermodulated signal, it is indeed a problem for a mobile handheld receiver where mass and volume are restricted. The same criteria equally applies to a satellite payload providing communications coverage to thousands of subscribers.

For static systems, such as a fixed point-to-point terrestrial network or geostationary satellite providing a service within a fixed field of view, or FoV, the alignment issue can be managed to provide adequate gain and power to subscribers. We however live in a mobile world, and so for subscribers to terrestrial networks using handheld devices, and for subscribers to satellite services where global coverage is proposed, requiring satellites that move relative to the Earth's surface, the issue of alignment becomes crucial. One of the aims of 5G is to combine terrestrial and satellite services to improve coverage (Mak *et al.* 2014, Evans *et al.* 2015), and this will require consideration of efficient antenna design. In this context, conventional techniques are no longer adequate. We need to think in three dimensions, and to provide mechanisms in which we may efficiently radiate electromagnetic energy through compact design.

Diversity, or the ability to provide additional paths of signal propagation is possible in many forms. If space is no problem, spatial diversity, such as telecommunications providers use in urban centres where antennas are placed on numerous rooftops to provide maximum coverage, is considered as a conventional solution. When space is constrained, one technique of providing additional diversity is through polarisation.

In this thesis, we consider the technique of tri-orthogonal polarisation diversity. By introducing three orthogonal polarisations at an antenna, we are in effect providing a three dimensional aspect to signal transmission and reception which, as alluded to

above, is what we require. The benefit of a third orthogonal polarisation, or additional polarisation beyond that of the linear components of the conventional techniques of circular or dual polarisation (Balanis 2005), is that it provides antenna performance that is less dependent of transmit or receive angle.

The concept of tri-orthogonality and antenna design has been highlighted in previous research (Andrews *et al.* 2001, Chiu *et al.* 2007b). However, tri-orthogonal antennas and subsequent analysis have typically been demonstrated in environments that facilitate propagation. A rich scattering environment (Andrews *et al.* 2001) is demonstrated to provide a tripling in capacity when compared to a linearly polarised system. In effect, a rich scattering environment provides the possibility for an arbitrarily polarised signal to be transmitted and subsequently received. This is fine in such an environment, but what about in channels that are not rich scattering environments? This may be the case for a 5G mmWave channel, or a satellite channel. In both, a LoS signal may typically dominate. Add movement of the receiver relative to the transmitter into the mix, and angle of transmission and reception become critical in the ability to propagate a signal.

Through a metric of system capacity, we consider the following scenarios as a means to analysing the performance of tri-orthogonal polarisation:

- a short-range terrestrial link operating at 60 GHz, providing tri-orthogonal polarisation diversity at both transmitter and receiver. Simulation of a AWGN fading channel where only a line-of-sight signal exists is performed, as well as simulation of a Rayleigh fading channel. Both simulations are conducted over a transmit field-of-view covering all possible orientations at the receiver. The simulations suggest that in a AWGN fading channel, the tri-orthogonal system provides orientation robustness above that of a conventional dual-polarised system, while in a Rayleigh fading channel, capacity is significantly increased over the majority of the FoV

- a non-geosynchronous satellite channel based on three conventional *in situ* satellite payloads. Tri-orthogonal polarisation diversity is provided at the receiver only. The simulations are based on line-of-sight channel metrics, fading margin applications and stochastics. For all three systems, the addition of a third orthogonal polarisation at the receiver provides a significant increase in capacity over that provided by conventional techniques.

Simulations cover extreme channel conditions in both cases, and suggest that a tri-orthogonal approach is beneficial in both cases. Ideally, we once again require capacity to be independent of propagation angle, and tri-orthogonal polarisation diversity is shown through a fundamental physical approach to provide an improvement in this respect.

Of course, the benefit of tri-orthogonal polarisation diversity cannot be implemented unless an appropriate design can be demonstrated. Previous designs (Andrews *et al.* 2001, Chiu *et al.* 2007b) have increased the third dimension of any design, and so have made the design more bulky with obvious implications where size is a constraint. In this context, research has been conducted leading to a planar design that fulfills the criteria of tri-orthogonal polarisation diversity. In addition, a sequential feeding network has been applied to the antenna design that adds a polarisation orthogonal to the antenna surface to a circularly polarised system. The antenna provides a high level of symmetry and orthogonality, providing the possibility of three dimensional beam steering. Such a possibility provides the ability to steer a radiation pattern, and so increase gain, of an antenna in a particular direction, and so mitigate to a certain degree the limitation of transmit power at mmWave frequencies.

Finally, we extend the concept providing an electric monopole, or signal polarisation, orthogonal to the antenna surface, by extending the operational bandwidth of such a design.

In summation, this thesis provides consideration of tri-orthogonality through a fundamental vectorised approach, and highlights the benefits of three dimensional design through tri-orthogonal polarisation diversity over all possible antenna orientations. An antenna solution is provided that provides three orthogonal polarisations within a conventional planar volume, demonstrating that three dimensional design in planar form is achievable. The concept of three dimensional beam steering is introduced, and may be further enhanced to cover a wider bandwidth. This is suggested by a wideband monopole design that provides polarisation orthogonal to the antenna surface, once again in a conventional planar volume.

1.2 Statement of Original Contributions

This dissertation involves several contributions in the area of tri-orthogonal polarisation diverse simulation and measurement in the RF and microwave frequency range.

These contributions can be generally categorised into a software, or simulation-based, section, and a hardware, or physical design-based, section. The two sections are self-contained, yet linked through the tri-orthogonal approach.

The software section of the thesis is concerned with the design of a model incorporating a fundamental vectorised approach providing analysis of the benefits of a tri-orthogonal approach to next generation wireless propagation. Propagation is considered over all antenna orientations in a FoV format at the transmitter, as rich scattering environments in which arbitrary signal polarisations are typically received are not always the case. The model is associated with two contrasting channel cases: a mmWave channel environment, with a comparison of a tri-orthogonal antenna and a conventional antenna arrangement being made; a non-geosynchronous satellite channel with time dependent link geometry, and the implementation of a third signal polarisation orthogonal to a conventional receive antenna surface. Three existing satellite channels are considered.

The hardware section of the thesis provides a tri-orthogonal polarisation diverse design within the constraints of conventional design requirements. A frequency specific novel planar design is designed through simulation, constructed and subsequently tested. The antenna design is subsequently fed to provide both an omnidirectional vertical signal polarisation mode, orthogonal to the antenna surface, and a circular signal polarisation mode. The design is used to highlight the possibility of three dimensional beam steering. Finally, an addition to this hardware section concerns an operational bandwidth broadening applied to a vertical electric monopole through a readily manufacturable redesign of a resonant cavity.

In summary, novel aspects of this thesis suggest that, through a tri-orthogonal polarisation diverse approach, there is a significant benefit to system capacity:

- in terrestrial wireless (Lawrence *et al.* 2014a, Lawrence *et al.* 2014b) and non-geosynchronous satellite channel environments (Lawrence *et al.* 2013, Lawrence *et al.* 2015a, Lawrence *et al.* 2016d)
- in AWGN fading channels where orientation robustness is provided, and in Rayleigh fading channels where additional capacity is provided (Lawrence *et al.* 2015b, Lawrence *et al.* 2016c)
- in channels where tri-orthogonal polarisation diversity is applied at both the transmitter and receiver, or indeed just at the receiver (Lawrence *et al.* 2016b).

Novel aspects of the thesis also demonstrate that:

- a planar antenna and feed design providing three orthogonal signal polarisations is possible (Lawrence *et al.* 2017b)
- the feed component of the design may be altered to provide circular and vertical signal polarisations. Three dimensional beam steering is highlighted (Lawrence *et al.* 2017a)
- the operational bandwidth of a vertical electric monopole, with signal polarisation orthogonal to the antenna surface, may be significantly increased within the confines of a planar design (Lawrence *et al.* 2016a).

1.3 Overview of the Thesis

As outlined in Fig. 1.5, this thesis encompasses four sections; a background including an appendix, two sections of original contribution and a conclusion that motivates future research directions. Together, these sections form nine thesis chapters in total that are supplemented by an appendix. A detailed description for each part of the thesis is presented as follows. At all times, system comparison is performed on a unit basis through a vectorised approach based on a fundamental approach. In other words, the inclusion of an additional polarisation for transmission requires a rescaling of transmitted power of each polarised signal. Conventionally, propagation is considered in a direction of propagation. In a direction of propagation, we may describe any waveform as elliptically polarised. Elliptical polarisation has two extreme subsets: linear polarisation and circular polarisation, and looking back along the direction of propagation any form of elliptical polarisation may be described by two linear orthogonal components (Balanis 2005). In this thesis, this idea is expanded to three dimensions, and consideration of the impact of a tri-orthogonal arrangement in all propagation directions in a FoV as seen by the transmitter is made. Indeed, in certain directions only two polarisations, rather than three, may be of use and if so the model will demonstrate this in its simulated output.

Background [Introduction to Current Challenges Facing Continued Mobile Data Growth (Chapter 1) & Review of Tri-Orthogonal Polarisation Diversity and Critique of Applicable Modelling Techniques (Chapter 2)] provide the background

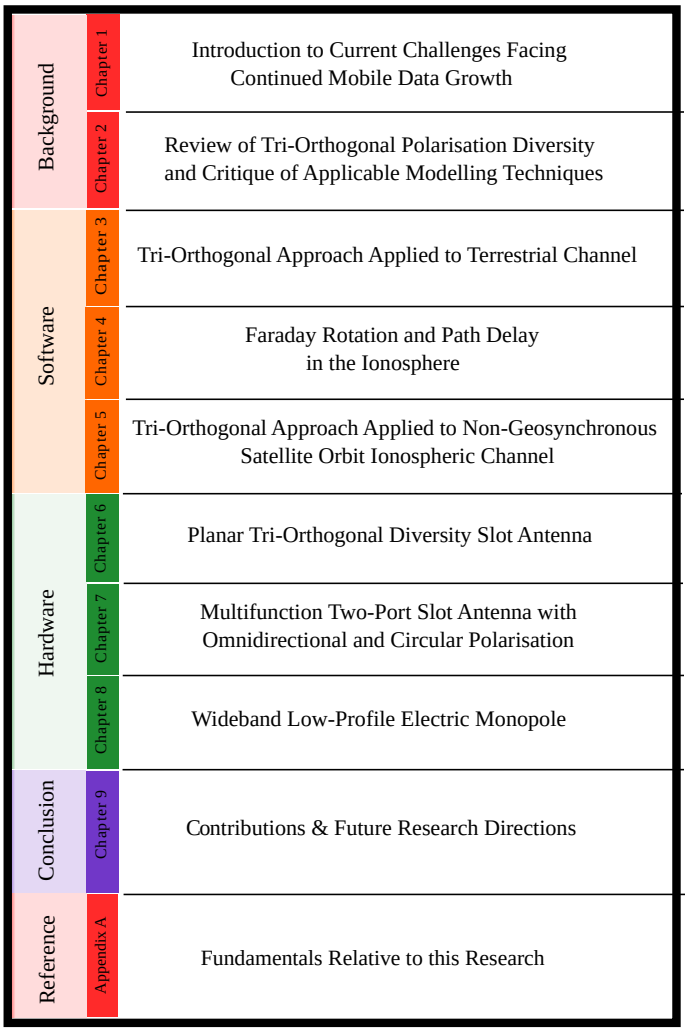

Figure 1.5. Thesis outline and original contributions. This dissertation is composed of nine chapters in total, which are supplemented by an appendix. The original contributions are distributed in two sections: a software section including model design, and providing simulation results through application of the model to terrestrial and non-geosynchronous satellite channels; a hardware section including three antenna designs that demonstrate that polarisation diversity may be enhanced within the confines of conventional planar structures. All of the thesis chapters are virtually self-contained.

information and introduction required for the thesis. In Chapter 1 of this thesis, the challenges facing the next generation of wireless communications are given, as well as the role that tri-orthogonal polarisation may play in mitigating these challenges. In Chapter 2, a review of tri-orthogonal polarisation diversity is presented, together with a critique of modelling techniques applicable to this research.

Software [Tri-Orthogonal Approach Applied to Terrestrial Channel (Chapter 3) & Faraday Rotation and Path Delay in the Ionosphere (Chapter 4) & Tri-Orthogonal Approach Applied to Non-Geosynchronous Satellite Orbit Ionospheric Channel (Chapter 5)] present data output from our model and subsequent interpretation for two system cases that consider a tri-orthogonal arrangement. The simulations use real parameters taken from academic study, and these are used to provide easily understandable two dimensional output for all antenna orientations in a FoV. The advantage of a tri-orthogonal arrangement is made evident in both cases.

Hardware [Planar Tri-Orthogonal Diversity Slot Antenna (Chapter 6) & Multifunction Two-Port Slot Antenna with Omnidirectional and Circular Polarisation (Chapter 7) & Wideband Low-Profile Electric Monopole Antenna (Chapter 8)] are focussed on the hardware design of antennas that are of significance in enhancing polarisation diversity, and so in the implementation of a physical tri-orthogonal system.

Conclusion [Contributions & Future Research Directions (Chapter 9)] summarises the results and contributions in this dissertation and outlines possible future research work and improvements.

Appendix [Fundamentals Relative to this Research (Appendix A)] provides additional reading on the physical fundamentals used throughout this research.

Within this thesis, the Frames of Reference in Figure 1.6 are used, unless otherwise specified.

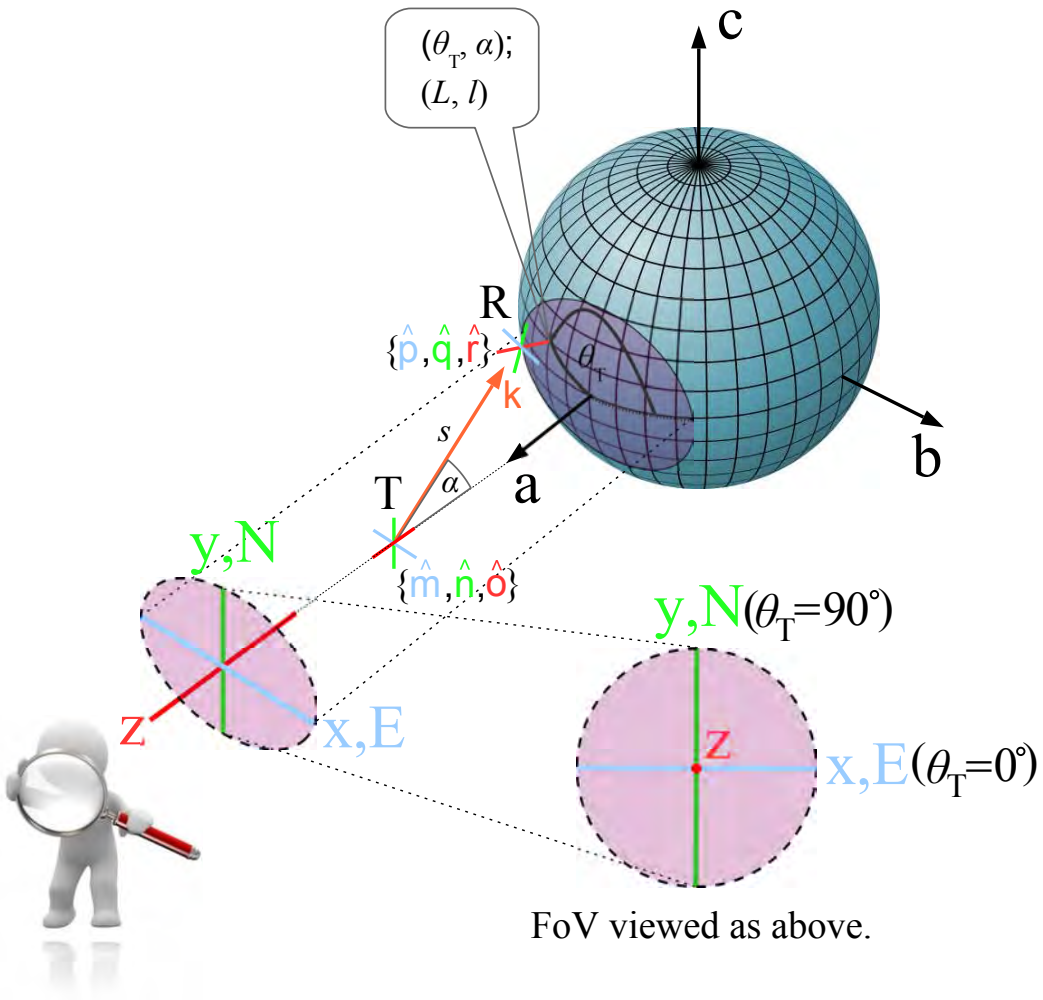

Figure 1.6. Frames of reference. In this thesis, a field-of-view (FoV) is seen from the perspective of the transmitter T, with the receiver R moving over the sphere, covering all antenna orientations. The nomenclature in this figure is used throughout this thesis.

1.4 Chapter Summary

In this chapter, the reader is introduced to the issues regarding the next generation of wireless networks. These issues are significant, given the timeline that is required to be followed if the growth in mobile data is to continue. Suggestions are proposed with regard to the role that the research undertaken in this thesis might play in helping to solve these issues. Original contributions in this thesis are highlighted, together with a structural organisation of the thesis.

In Chapter 2, a review is undertaken of tri-orthogonal polarisation diverse methods applied to terrestrial design. As one of the aims of 5G is to provide improved wireless coverage, including through interconnection of terrestrial and satellite systems, a

critique of channel modelling is presented. This critique provides a basis for a channel model that considers tri-orthogonal polarisation diversity applied to a terrestrial channel that is presented in Chapter 3. In addition, the critique forms a basis for a channel model that considers tri-orthogonal polarisation diversity applied to a non-geosynchronous satellite channel that is presented in Chapters 4 and 5.

Chapter 2

Review of Tri-orthogonal Polarisation Diversity and Critique of Applicable Modelling Techniques

THIS chapter presents a review of tri-orthogonal polarisation diversity, focussing on the lucrative terrestrial market. This market will be augmented by satellite systems. In order to propagate electromagnetic energy effectively, to maintain range in channels devoid of scatterers, tri-orthogonal polarisation diversity is applicable to both terrestrial and satellite channels. An insight into current designs making use of this approach and their limitations is given.

2.1 Tri-Orthogonal Polarisation Diversity Review

The next generation of wireless networks is set to handle up to a thousand times more traffic than current levels by 2020. Higher operating frequencies in the mmWave region of the electromagnetic spectrum are being considered as a lack of available bandwidth currently exists at conventional operating frequencies (Rappaport *et al.* 2013b). The mmWave region extends from 30–300 GHz (Nanzer 2012), sitting between the microwave region (3–30 GHz) (Nanzer 2012) while overlapping the lower region of terahertz frequencies (100 GHz–30 THz) (Tonouchi 2007). The mmWave region is shown in Figure 2.1, together with frequency bands of interest for the next generation of wireless networks.

As the drive to develop new networks is pursued, a compelling argument exists that wireless radiated energy needs to be used efficiently if designs are to be effective. Networks operating in the microwave region make use of several advantages that may not necessarily exist in the mmWave region. These typically include:

- high transmit power due to reduced intermodulation and non-linear effects
- low spreading loss and atmospheric absorption

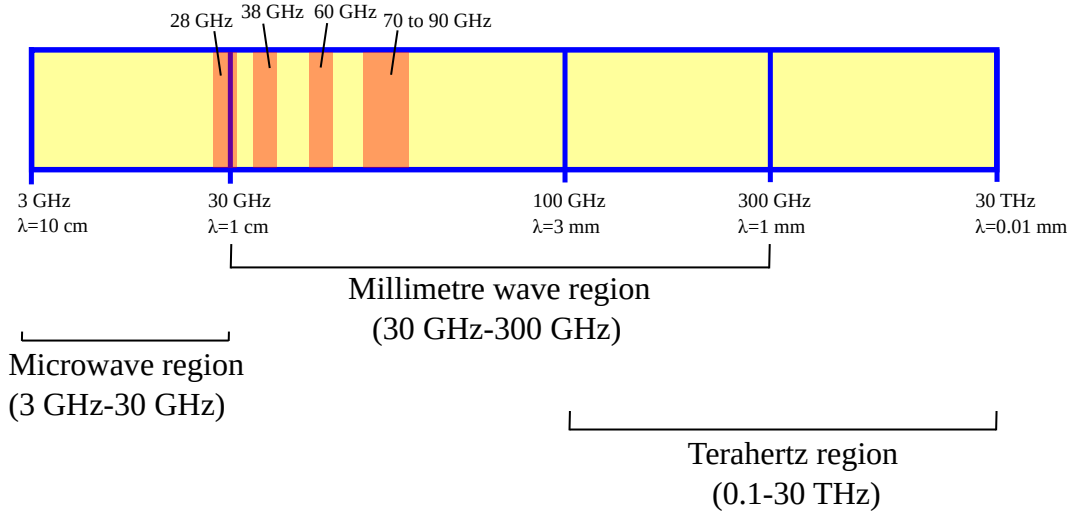

Figure 2.1. The mmWave region of the electromagnetic spectrum. The mmWave region extends over a region of 270 GHz, from 30–300 GHz. Frequency bands of interest for the next generation of wireless networks are shown. Note that there is no standardised definition of the terahertz band. Whilst terahertz spectroscopists loosely define the band as the 0.1 THz to 10 THz range, another common alternative loose definition is 0.1 THz to 30 THz.

- good coverage due to a wide beamwidth
- multipath fading providing diversity, particularly in dense urban environments.

In the mmWave region of the electromagnetic spectrum, signal propagation is typically subject to:

- lower transmit power due to increased intermodulation and non-linear effects
- higher spreading loss and atmospheric absorption
- reduced coverage due to a narrow beamwidth.
- reduced beneficial multipath fading, due to a reduction of scattering mechanisms at higher frequencies and lower transmit power.
- reduced range coverage, due to unwanted multipath fading, and lower transmit power.

Coupled with a lower transmit power due to non-linear effects, a reduced beamwidth at mmWave frequencies, as seen in Figure 2.2, provides a reduced probabilty of multipath fading. Multipath fading in a rich scattering environment provides several copies of a propagated signal through a channel, as a consequence of the signal being divided into multiple lower power copies of itself. This provides several resolvable signals which propagate along distinct subchannel paths to a receiver, increasing the possibility of reception (Goldsmith 2005). Broadly speaking, to increase capacity across a channel, narrowband signals should be used in place of wideband or spread spectrum signals, with the number of resolvable signals kept low while providing diversity (Telatar and Tse 2000).

Polarisation diversity offers the possibility of transmitting distinctly polarised signals that may be subjected to individual subchannel path effects. At mmWave operating frequencies where signals may be more line-of-sight due to narrower beamwidths, such an arrangement provides diversity and resolvable signals at the receiver. A similar argument holds for satellite channels, which are typically LoS in nature, and are proposed to be integrated into new fifth generation, or 5G, networks (Evans *et al.* 2005, Li *et al.* 2009, Mak *et al.* 2014, Evans *et al.* 2015).

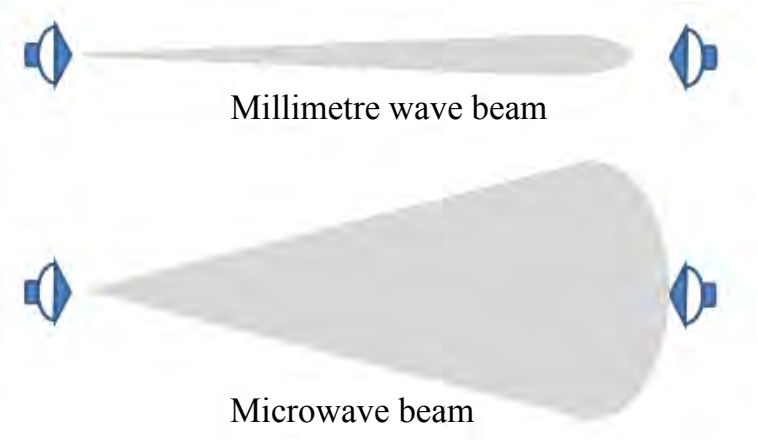

Figure 2.2. Millimetre wave beamwidth. Due to increased free space path loss, mmWave beamwidths are narrow in order to focus radiated energy in the direction of propagation. A consequence of this is a more LoS channel when compared to those operating at microwave frequencies, requiring beam steering of radiated energy. The LoS channel is also typical of satellite channels, which are proposed to be integrated into new fifth generation, or 5G, wireless networks. After Adhikari (2008).

The tri-orthogonal arrangement potentially offers the ability to beam steer radiated energy towards a receiver over a wide range of angles, through relative phasing techniques which may be enhanced by applied variations in relative wave magnitude. The arrangement offers the potential of dual polarisation over all link directions in an extended field-of-view (FoV), such as may be required in a mobile terrestrial context, or in that of a non-geosynchronous satellite communicating to a ground receiver. Due to a reduced antenna size at mmWave operating frequencies, and a narrower beamwidth, it is possible to provide an array of sixteen antennas at 70 GHz in the effective aperture area of one antenna operating at 18 GHz (Adhikari 2008). A more compact design at mmWave frequencies offers the potential of beam steering through phased array techniques.

The concept of tri-orthogonal polarisation diversity is most prominently highlighted in Andrews *et al.* (2001). In this paper, the concept of tripling capacity using a colocated orthogonal arrangement of antennas is demonstrated under laboratory conditions at an operating frequency of 880 MHz. The use of a mirror provides a method of generating mutiple reflections, simulating the conditions of a rich scattering environment, as found in urban environments for example. The paper makes the claim that a tripling of capacity, in comparison to a DP radio signal, is observed in such an environment, as three electric and three magnetic polarised states are present. The concept delivers

a channel of rank six, suggesting that all states are contributing to system capacity as all eigenvalues are non-zero and distinct. This rank suggests a three fold increase over a DP electric signal with no scattering. Figure 2.3 illustrates the experimental arrangement. The orthogonality of the MIMO system provides a low mutual coupling value of -25 dB between polarised states. Each antenna associated with a polarised state provides an omnidirectional radiation pattern with nulls of -25 dB parallel to the antenna axis at the operating frequency used.

The proximity of experiment and theory is seen in the capacities of Figure 2.3. Theoretical studies on this arrangement have also highlighted the use of three electric and three magnetic polarised states, and the implications for enhanced channel capacity (Marzetta 2002, Svantesson *et al.* 2004). In Svantesson *et al.* (2004), electric current and magnetic current profiles generate six polarisation states and are analysed by ideal point sensors, providing a theoretical six-fold increase in capacity. Practical antennas are of finite size, however, and transmit and receive topologies of electric half-wave dipoles and magnetic full-wave loops are also analysed. In a rich scattering multipath environment, all six polarisation states are found to be uncorrelated and of equal strength. The magnetic states are not found to contain any additional information than that of the electric states, and as such are redundant. In addition, the radiation patterns are found to interfere, and become non-orthogonal. As such, no more than three orthogonal electric polarisation states are suggested as useful for a tri-orthogonal arrangement.

The coauthors of this research have suggested an interesting feature of diversity in relation to mutual coupling. In Wallace and Jensen (2004), the effect of mutual coupling on capacity is explored. The effect is considered for the case of two radiating elements that are sufficiently separated so as to not interfere with each other, but that are systematically brought closer together. The research is of interest as it is observed that capacity is observed to increase in the case of close spacing, which is counter to the understanding of mutual coupling impinging on capacity. As the radiating elements combine to form one element, capacity drops commensurately. The research is interesting for a tri-orthogonal arrangement in as much as such an arrangement consists of antennas that are already in close proximity, and that mutual coupling is being mitigated by the orthogonal nature of the arrangement. Indeed, a certain amount of confusion surrounds the effect of mutual coupling on capacity as suggested by the contradictory stances of

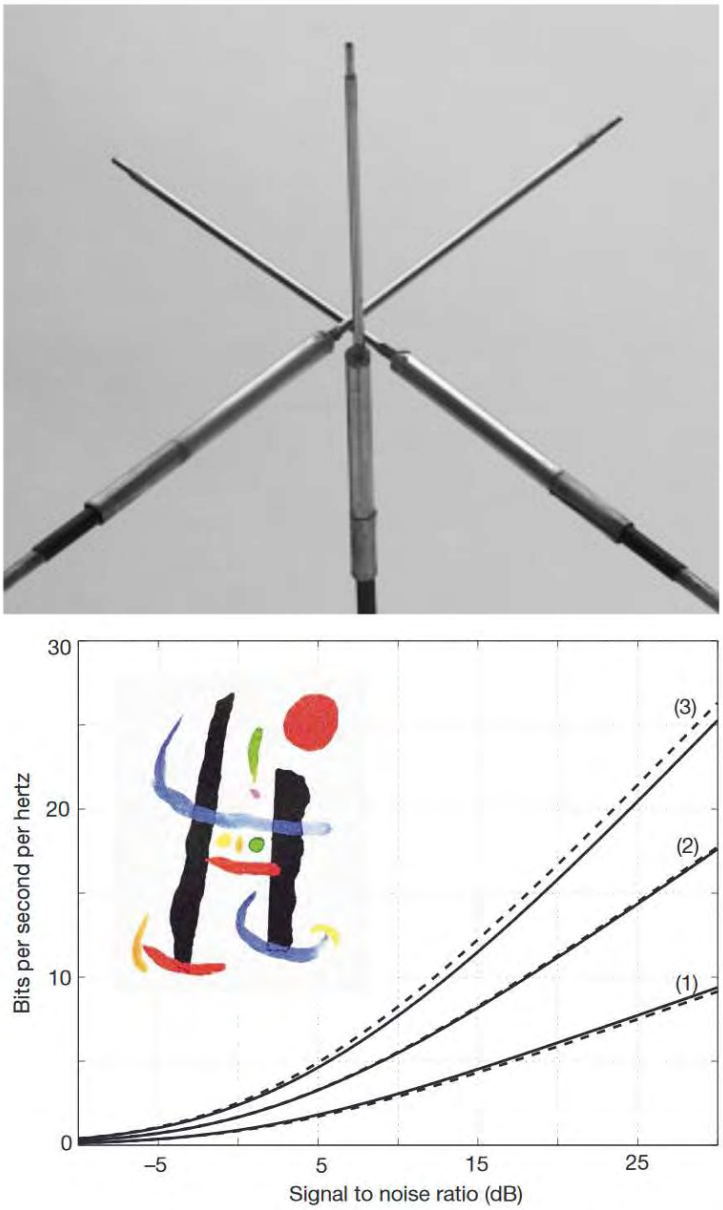

Figure 2.3. Colocated tri-orthogonal antenna arrangement. Capacity measurements made for one (1), two (2) and three (3) orthogonal antennas are shown by solid lines. Random matrix channel theory solutions are shown for the same arrangements by the dotted lines. A tripling of capacity over the rich scattering channel is observed for the case of the tri-orthogonal arrangement. The colour image, *A toute épreuve* by Joan Miro, is reconstructed from transmission of three distinct red, green, and blue monochrome subfields on each of the three orthogonally oriented antennas observed in the upper portion of the image. After Andrews *et al.* (2001).

Chiu *et al.* (2007a) and of Gao *et al.* (2010b). Whereas the former suggests the negative consequences of mutual coupling, the latter suggests that some amount of mutual coupling is useful. From a classical standpoint, capacity may be construed as received power. As such, a certain amount of mutual coupling is beneficial in the sense that received signal power is coupled to antennas that are in close proximity to each other; the point that is made in Wallace and Jensen (2004). However, mutual coupling affects pattern diversity, resulting in static asymmetric patterns that are unusable for providing an option to beam steer, or an option to differentiate link directions. Whereas a poorly defined radiation pattern is common in mobile phone, or planar inverted-F, antennas (PIFAs) (Diallo *et al.* 2006, Yang *et al.* 2008, Chebihi *et al.* 2008), this is mitigated by high power transmission from base stations. For higher operating frequencies, and LoS applications, this form of mitigation does not exist.

In Marzetta (2002), a four fold limit on capacity enhancement is placed on an array of planar antennas compared to a LP array. In effect, only four of the tri-orthogonal polarisation states are used, two electric and two magnetic states. A volume array, or arrangement of tri-orthogonal antennas, gives an additional logarithmic increase in capacity. This may be understood by the redundancy of two polarisation states in a direction of propagation along an antenna axis. However, it is the ability of the tri-orthogonal arrangement to compensate a loss of capacity on a pair of electric and magnetic polarisation states with an increase in capacity for the orthogonal polarisation states, in effect providing a quasi-isotropic solution and mitigating antenna misalignment, that is of interest.

In Mtumbuka and Edwards (2005), a colocated tri-orthogonal arrangement at both transmitter and receiver is demonstrated in an indoor environment at 2.44 GHz. Experimental results suggest that the arrangement is suitable for high capacity mobile systems. The authors suggest that there is degradation of capacity as a function of elevation, but not as a function of azimuth. Whereas there may be an issue regarding non-orthogonality of radiation patterns due to an effect of mutual coupling between radiation patterns in one direction and not the other, the difference in capacity performance as a function of angle is small. In Mtumbuka *et al.* (2005), a tri-orthogonal arrangement of UWB antennas is investigated. However, the experiment does not use a colocated arrangement, as it is conducted according to the method of Lukama *et al.* (2001). As such, the beneficial effects of spatial diversity and reduced mutual coupling

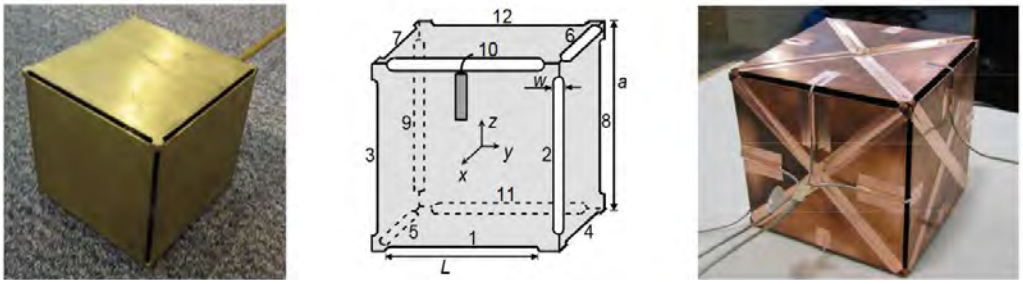

(a) (b) (c)

Figure 2.4. Slot radiator version of the MIMO cube. The images shown are: (a) original version, (b) hollow cube schematic, (c) second version where by internal polygon structures are included to reduce mutual coupling effects. After Yun and Vaughan (2010).

are included, and so the experiment does provide an exaggerated account of the performance of the tri-orthogonal arrangement.

The MIMO cube of Getu and Andersen (2005) is an interesting concept, highlighting the orthogonal and symmetric nature of tri-orthogonality through a cubic arrangement with the possibility of 12 distinct radiating elements, providing 12 subchannel paths or eigenmodes. In the work of Getu and Andersen (2005), for a half-wave dipole length of side and in a Rayleigh rich scattering channel, a theoretical capacity increase commensurate with the number of active eigenmodes is seen compared to LP polarisation state transmission. However, this capacity enhancement is observed to decrease as the side of cube is decreased, rendering the design impractical for mobile applications. In addition, the effects or mutual coupling and reduction of pattern diversity are not considered. Mutual coupling reduces capacity performance of close proximity radiating elements (Chiu *et al.* 2007a). In Getu and Janaswamy (2005), the effect on the MIMO cube is theoretically scrutinised, and it is suggested that mutual coupling reduces capacity only for cubes of length of side less than 1/3 of a wavelength. In effect, mutual coupling acts to limit antenna compactness.

A physical version of the MIMO cube, presented as a slot radiator rather than a dipole radiator, is provided in Yun and Vaughan (2010). This is shown in Figure 2.4. The design is observed to suffer from the effects of mutual coupling, and this in turn effects polarisation diversity through polarisation impurity which in turn affects pattern diversity. The design is elaborated through a series of internal polygon stuctures designed to reduce internal mutual coupling effects, and this in turn reduces mutual coupling by 20 dB, and improves the radiated patterns of the slots.

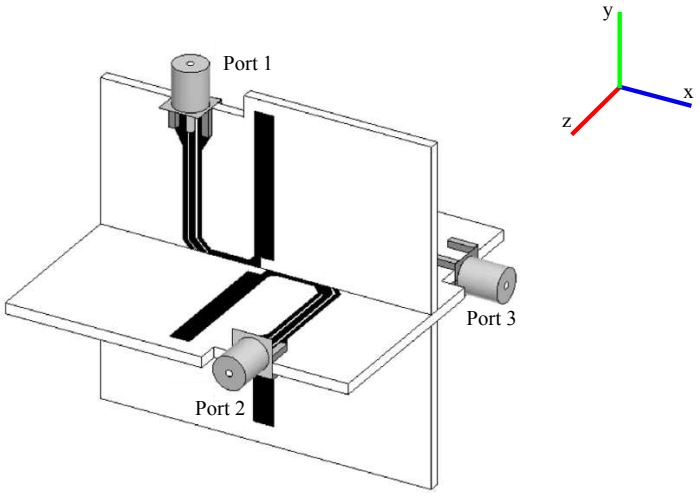

Figure 2.5. A tri-orthogonal antenna constructed using FR4 material. The tri-orthogonal design is slotted together to provide a third polarisation orthogonal to the planar xz surface, which is excited by port 1. After Chiu *et al.* (2007b).

A tri-orthogonal antenna design using FR4 dielectric material is demonstrated in Chiu *et al.* (2007b), operating at 2.55 GHz. Figure 2.5 presents the design. The design provides 18 dB of polarisation isolation between antennas. Radiation patterns are somewhat affected by this small degree of polarisation impurity, and the material and structure of the design itself, which is slotted together to provide a polarisation orthogonal to a typical planar surface. The design is tested and shown to provide a tripling of capacity, compared to that of a single LP mode design, in a rich scattering Rayleigh fading channel. At the transmitter, spatial diversity exists as the orthogonal radiating elements are not colocated. In addition, the transmitter is descibed as a linear arrangement of antennas, and it is not clear if these are all polarised in the same direction, or orthogonally, as is desired. At the receiver, orthogonally polarised antenna elements are colocated and so spatial diversity is minimised thereby demonstrating the benefits of polarisation diversity at the receiver. The effect of mutual coupling on radiation patterns is mitigated through matched termination of untested ports. An ideal capacity measurement is hence generated, as it is likely that pattern diversity would be affected if all three ports were excited simultaneously, as mutual coupling is -18 dB.

In essence, the designs and analysis given above provide the background to more recent research. A design based on a tri-orthogonal arrangement may be found in Zou and Fumeaux (2011). The publication demonstrates a compact tri-orthogonal arrangement using a cross-shaped dielectric resonator antenna (DRA), and operating at

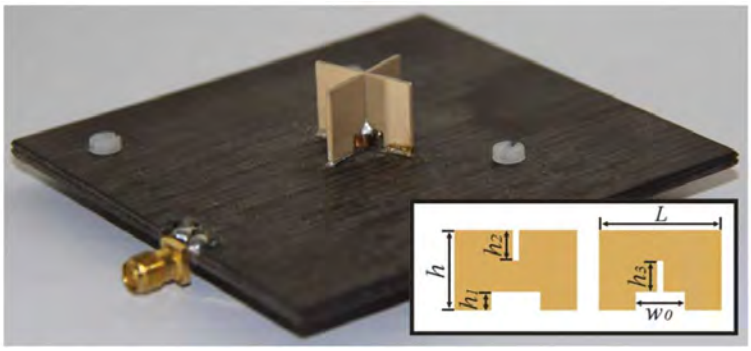

Figure 2.6. A cross-shaped dielectric resonator antenna (DRA) structure, operating at 4.7 GHz with a 6.8% overlapping bandwidth. Low mutual coupling of -30 dB due to the orthogonality and symmetry of the design is recorded for this design. After Zou and Fumeaux (2011).

4.7 GHz with a 6.8% overlapping bandwidth. The design is shown in Figure 2.6. Mutual coupling is kept below -30 dB by a symmetrical and orthogonal design. As a consequence, pattern diversity is maintained.

To summarise, research prior to this thesis has conceptually presented tri-orthogonal polarisation diversity through theoretical analysis. The following points are noted:

- a tripling of capacity is provided over a LP polarisation state in a rich scattering environment, such as a random Rayleigh fading channel. This supports anticipated capacity improvement
- antenna designs using a tri-orthogonally diverse approach operate at RF and microwave frequencies, conducive to beneficial multipath fading
- although three magnetic polarisation states are also available for channel propagation, there is no additional information that is conveyed by these magnetic states that may not be found in the three electric polarisation states. As such, their inclusion is suggested as unwarranted
- whereas an ideal sensing analysis is presented at the receiver, in practice the implementation of half-wave electric dipoles and full wave magnetic loops is impractical
- analysis over all antenna directions is not given, and as such results are somewhat limited, as are any drawn conclusions.

In terms of physical design and experimentation, the following points are noted from the results of research prior to this thesis:

- experimental results of capacity under rich scattering conditions largely match those calculated theoretically
- a tripling of capacity is provided over a LP polarisation state in a rich scattering environment, such as a random Rayleigh fading channel. This bolsters claims of capacity improvement as this tripling may not necessarily be observed for all antenna orientations, and will not be the case for LoS conditions
- spatial diversity is inadvertently included, and as a consequence mutual coupling effects are largely mitigated
- mutual coupling effects are reduced through load termination of untested ports. When included, these effects affect pattern diversity
- mutual coupling effects increase as antenna size is reduced
- the inclusion of a third orthogonal polarisation turns a planar antenna design into a volume antenna design, which compromises the design for mobile devices
- diversity performance is often erroneously presented, as performance should take radiation pattern weighting into account over an entire radiating FoV.

From this summary, two points are identified to which the research in this thesis attempts to contribute:

- what is the enhancement in performance offered by a tri-orthogonal arrangement over all antenna orientations, and over a range of wireless channels? The range includes channel extremes for a wireless terrestrial mobile system and a non-geosynchronous satellite orbit system. Both of these systems incorporate the aspect of a time-varying link geometry resulting from relative transmitter-receiver movement. Moreover, satellite systems are proposed to be integrated into the next generation of wireless terrestrial mobile systems (Mak *et al.* 2014, Evans *et al.* 2015).
- tri-orthogonal arrangements provide a polarisation orthogonal to the antenna surface at the expense of a planar design, which consequently becomes a volume design (Getu and Andersen 2005, Chiu *et al.* 2007b). Can three orthogonal polarisations be provided in a planar design?

Both of these points are important if the next generation of wireless design is to provide higher capacity and mobility while not ignoring fundamental constraints imposed on current technologies.

2.2 Critique of Applicable Modelling Techniques

Throughout this thesis, we highlight the enhancement of wireless communication through tri-orthogonal polarisation diversity. This is shown through parameter extremes over a range of channels. The channels have been chosen due to their interest with regard to the next generation of wireless mobile communications, which aims to seamlessly integrate wireless terrestrial and satellite systems (Mak *et al.* 2014, Evans *et al.* 2015). As systems become more mobile, the effect of misalignment becomes more pertinent to performance through polarisation misalignment issues, and mitigation is suggested through a tri-orthogonal arrangement.

The decision is made in this thesis to present system capacity data according to movement of a receive antenna over a sphere, as a means of analysing misalignment between transmitter and receiver. Studies of capacity performance, including that of MIMO transmission schemes, are typically presented in two dimensional line graph format (Gesbert *et al.* 2003, Tulino *et al.* 2005). Where inference is made to a particular angular orientation of an antenna, the line graph format is maintained (Turkmani *et al.* 1995). As tri-orthogonal polarisation diversity considers three dimensions, so a format encompassing all antenna orientations is required. In this thesis, capacity performance is displayed for all receive antenna orientations using a convenient circular two dimensional format, or FoV approach. Furthermore, and by extension, movement of a receive antenna over a sphere naturally lends itself to a satellite system analysis. Combined with a vectorised approach for both wireless terrestrial and satellite channels, three dimensional data is thus able to be presented in a convenient circular two dimensional, or FoV, format for both systems.

From a terrestrial wireless channel perspective, we acknowledge that channel models are accessible in the literature. However, we suggest that shortcomings are evident in these models:

- models for dual polarisation diverse links implicitly assume perfect antenna alignment or apply cross-polar correlations independent of link geometry

(Nabar *et al.* 2002, Erceg *et al.* 2006, Coldrey 2008, Arapoglou *et al.* 2011b, Arapoglou *et al.* 2012)

- where performance according to angular orientation is assessed, a two dimensional line graph format considering selected angular orientations is chosen (Turkmani *et al.* 1995)

- where three dimensional approaches to modelling are observed, research may not consider a tri-orthogonal system (Shafi *et al.* 2006, Kwon and Stuber 2011, Dao *et al.* 2011)

- a full appreciation of system performance over all antenna orientations in a FoV is typically not presented (Compton 1981)

- systems are shown that typically operate at frequencies where the effects of rich scattering environments may enhance performance considerably (Gupta *et al.* 2008, Quitin *et al.* 2009, Piao *et al.* 2015).

The terrestrial model demonstrated in this thesis presents a useful step in the implementation of a proposed mmWave tri-orthogonal system permitting short range, high capacity communication, independent of position and over all antenna orientations. The simulated results suggest that capacity improvement due to a tri-orthogonal approach is available, both in the presence and absence of a scattering environment. We suggest that our model provides a useful contribution in addition to previous research cited above.

With regard to a non-geosynchronous satellite orbit, we make the following points with regard to our model format in comparison to existing research:

- whereas satellite channel models examine link performance using conventional dual polarisation, including CP mode, techniques (Meyer and Nicoll 2008, Burgin and Moghaddam 2014), we apply a tri-orthogonal approach at the receiver in an effort to establish the possibility of enhanced link performance using such an approach

- a tri-orthogonal approach is applied to a satellite channel in Horváth and Frigyes (2006) and Horváth *et al.* (2007) using polarization-time coding, or PTC (Frigyes and Horváth 2005). Simulated results are in a two-dimensional line graph format,

and are presented over a small number of angular orientations. Any depolarising effect is represented through adoption of a statistical approach for local scatterers (King *et al.* 2005) at the ground receiver, within a small indoor environment. Reference to ionospheric effects is not found, nor is a vectorial approach applied to the analysis. In our analysis, we examine the effect of a third orthogonal polarisation at the receiver over an entire orbit for three diverse satellite systems. We analyse capacity performance over the entire orbit. We adopt a vectorial approach calculating realtime ionospheric effects on signal propagation, as a function of global positioning, geodetic height, and time. Where possible, we apply local scattering effects according to a statistical analysis (Fontan *et al.* 2001)

- to model the ionosphere, a vectorised approach to ionospheric effects is applied which deviates from a conventional trigonometrical approach (Jehle *et al.* 2005). Furthermore, whereas ionospheric interrogation is conventionally performed over satellite channels at a mid-point along a propagation path (Jehle *et al.* 2005, Le Vine and Utku Accessed: 2013, Le Vine *et al.* 2010), we vectorially interrogate the ionosphere at multiple points along the path. A comparison is made of the two approaches

- our model uses realtime ionospheric data (National Oceanic and Atmospheric Administration Accessed: 2014, Maus *et al.* 2010) that is included as a result of establishing the major ionospheric effects on signal propagation (Jehle *et al.* 2005, International Telecommunications Union (ITU-R) Accessed: 2013). Combined with our vectorial approach, this permits ionospheric effects to be calculated as an integration of effects along a propagation path. This approach is adopted for all propagation paths in a FoV, as observed from the perspective of a satellite transmitter

- our model employs antenna polarisation branches at the ground receiver as a function of global position within the FoV. These polarisation branches are subsequently aligned in accordance with manufacturer guidelines on conventional CP mode patch antennas (Cobham Plc Accessed: 2015, Taoglas Ltd 2015). As such, any bias regarding antenna orientation is removed, and a like-for-like comparison with conventional CP mode patch antennas is made possible. All antenna orientations of the receiver in the FoV are considered

- our analysis compares a tri-orthogonal approach at the receiver with conventional CP mode patch antennas, using carrier wave parameters (Johannsen 1995, Coverdale 1995, Maine *et al.* 1995, Braasch and van Dierendonck 1999, Orbcomm LLC Accessed: 2014, Chang and de Weck 2005, Leveson 2006, Iridium Communications Inc. Accessed: 2014, Orbcomm Inc. Accessed: 2014, United States Government Accessed: 2015).

The model we apply to satellite channel analysis provides a realtime vectorial approach to capacity performance, interrogating the ionosphere at multiple points along all propagation paths in a FoV seen from the perspective of a satellite transmitter. This model is applied to three diverse satellite systems. The simulated results suggest that capacity improvement due to a tri-orthogonal approach is available over an entire orbit. We suggest that our satellite model provides a useful contribution in addition to previous research cited above, and for the possible integration of terrestrial and satellite systems in the next generation of wireless communications.

2.3 Chapter Summary

In this chapter, a review of tri-orthogonal polarisation diversity is undertaken. For terrestrial systems, the review considers prior research on the topic, both from a system capacity perspective and a hardware design perspective.

A critique of modelling techniques is subsequently presented that considers prior modelling for both terrestrial and satellite systems.

In both the review and the critique, areas of research interest are suggested. These areas are then expanded to form the chapters of this thesis

In Chapter 3, the effect of a third orthogonal polarisation mode, in the form of a half-wavelength dipole, is considered at both transmitter and receiver for extreme cases of a terrestrial channel. More information on the modelling approaches in this thesis, and the use of prior research in establishing our models, is made available in Chapter 3 that considers a terrestrial channel, and in Chapters 4 and 5 that together consider tri-orthogonal polarisation diversity applied to non-geosynchronous satellite channels.

Chapter 3

Tri-Orthogonal Approach Applied to Terrestrial Channel

THIS chapter provides an introduction to the concept of tri-orthogonal transmission and reception and presents the specifications that make it an attractive implementation choice for new or improved transmission networks in the microwave region and beyond. It also explains the objectives and motivations behind the presented research.

Over a terrestrial link, this chapter suggests the benefits of a tri-orthogonal approach at the transmitter and receiver. Increased performance is illustrated through simulation resulting in a capacity comparison with conventional CP mode techniques. The model used to simulate performance acts as a precursor for further investigation later in the thesis into the benefits of tri-orthogonal receive diversity over non-geosynchronous satellite orbit channels.

3.1 Introduction

Consumer wireless applications are driving demand for increased user capacity, reliability and throughput. One has only to consider the Internet of Things (Coetzee and Eksteen 2011), dedicated short-range communications (DSRC) (Kenney 2011) including vehicle-to vehicle technology (v2v) (Biswas *et al.* 2006), and fifth generation (5G) wireless connectivity (Andrews *et al.* 2001, Rappaport *et al.* 2013b) to understand that telecommunications are indeed undergoing a marked transformation. In this new era, performance should ideally be consistent regardless of end user position and orientation. Multiple-input multiple-output (MIMO) signalling techniques exploiting spatial diversity through channel scattering have been widely adopted in wireless terrestrial applications to increase performance (Jakes 1974, Rappaport 1996, Paulraj *et al.* 2004, Goldsmith 2005). Signal processing theory has primarily considered spatial MIMO applied to LP mode networks (Foschini and Gans 1998, Telatar 1999, Shiu *et al.* 2000, Kermoal *et al.* 2002, Chuah *et al.* 2002), as this has been driven by commercial interests where one polarisation is typically transmitted.

At first, polarisation diversity did not receive as much attention as spatial diversity. A marked mean signal level difference between co-polarised and cross-polarised branches where one polarisation is transmitted is often cited as a reason for this lack of interest (Kozono *et al.* 1984), driven once again by commercial reasoning. There seemed no reason in providing an additional polarisation for little commercial benefit. A measure of this difference, known as cross polarisation discrimination or XPD, is shown at historic terrestrial network operating frequencies to be typically between 6–20 dB for a given system (Lee and Yeh 1972, Cox 1983), rising to higher values in suburban than in urban environments, due to a reduced scattering mechanism. The XPD is shown to be correspondingly higher in outdoor than in indoor environments (Cox *et al.* 1986), essentially for the same reason.

One advantage of a polarisation diverse method over a spatially diverse method is that antenna design may shrink, while providing a comparable, if not superior, performance (Dietrich *et al.* 2001, Nabar *et al.* 2002, Erceg *et al.* 2006, Coldrey 2008). Many CP mode patch antennas designed for operation using CP mode wave propagation demonstrate the case, as these antennas provide superior performance to their LP mode counterparts. Propagation involving a CP mode wave may be decomposed into two orthogonal LP propagation modes with a 90° phase shift between them. For a CP mode receive antenna, loss of reception on one antenna branch or element is mitigated

by an increase in reception on the orthogonal branch, providing depolarisation mitigation. The use of a propagating CP mode wave as opposed to a LP mode wave is typically at the expense of a reduced range. For a terrestrial telecommunications operator, range is often the most critical design criteria and, as a consequence, LP mode systems are typically used. A system using CP mode wave propagation and CP mode patch antennas is intended to mitigate depolarisation issues (Balanis 2005), and maintains optimum performance as long as antenna alignment exists. The introduction of misalignment reduces performance. In Chapter 5, performance of NGSO satellite systems using typical RHCP mode wave propagation and CP mode patch antennas to mitigate the depolarising nature of the ionosphere, introduced in Chapter 4, is considered. Measurement studies of terrestrial DP diversity involving translation and rotation of a second antenna polarisation or branch suggest low correlation and mutual coupling, with MIMO performance superior to that of a spatially diverse system due to the orthogonal nature of the design (Lee and Yeh 1972, Turkmani *et al.* 1995).

In an ideal antenna design, the effects of mutual coupling of antenna polarisations (Ramirez and De Flaviis 2003) and correlation of antenna polarisations (Turkmani *et al.* 1995) must be mitigated to fully capture the benefit of polarisation and pattern diversity (Gesbert *et al.* 2003, Wallace and Jensen 2004). In effect, antenna polarisations or branches act in an independent yet complementary manner. Additional studies of systems complementing what may be deemed to be spatially polarised diversity measurement, making use of the DP mode technique but not in a unique colocated position, suggest that superior system performance is indeed possible due to low mutual antenna interaction and low correlation (Kozono *et al.* 1984, Kyritsi *et al.* 2002, Erceg *et al.* 2004, Oestges *et al.* 2008, Degli-Esposti *et al.* 2011). Currently employed terrestrial systems utilise LP mode or DP mode signal propagation due to their ease of implementation. A comparison of spatial, pattern, and polarisation diversity (Dietrich *et al.* 2001) over a range of channel environments suggests that polarisation diversity provides 12 dB or more of improvement in SNR; intuitively, a drop in signal on one polarisation is compensated for by an increase on another polarisation orthogonally colocated. Antenna interaction and asymmetric antenna patterns in the case of closely located spatially diverse systems provide an additional argument for the use of polarisation diversity, where these two issues may be mitigated through design. Pattern diversity is also feasible for a polarisation diverse system, where low gain near-omnidirectional patterns are employed (Zou and Fumeaux 2011).

3.1 Introduction

From a simple geometrical analysis, performance of LP mode, DP mode, and CP mode methods is seen to be reliant on relative antenna positions as these types of polarisation do not account for a three dimensional environment, relying on optimal antenna alignment. Orientation robustness becomes an important limiting factor as design frequency increases to cope with higher data rates, as constant linear transmit power becomes typically harder to maintain and the benefits of multipath effects at the receiver are reduced; the consequence of which is suboptimal performance, or an exponential rise in system cost to correct this. Every possible design advantage needs to be sought.

Implementation at the widely adopted mobile communication frequencies in the RF and low microwave region typically benefits from a rich scattering environment but finds itself restricted to progressively complex processing techniques if it is to keep up with consumer demand for higher capacity. In the infrared region, propagation limitations are well documented (Federici and Moeller 2010). As a result, much interest has been given to the terahertz region where high data rate, together with an unallocated portion of spectrum, open the door to many possibilities (Kleine-Ostmann and Nagatsuma 2011). Implementation at terahertz frequencies, in contrast to that at RF and microwave frequencies, has been limited by available transmit power leading to a line-of-sight (LoS) system design, devoid of scattering mechanisms for increasing received energy at the receiver. In order to avoid link failure when LoS propagation is interrupted, steerable dielectric mirrors have been introduced (Turchinovich *et al.* 2002). For optical uplink systems to satellites, the effect of beam wander is significantly detrimental to the BER (Guo *et al.* 2010).

Innovative design at mmWave frequencies offers many of the advantages of both microwave and terahertz frequencies while minimising the disadvantages (Turchinovich *et al.* 2002). Firstly, a large 7 GHz frequency band at 60 GHz, within the mmWave spectrum, has been allocated to wireless design over short distances (Rappaport Accessed: 2014). This supports high data rate using low order modulation techniques, such as binary phase shift keying (BPSK). Secondly, any design and implementation may be influenced by well documented RF and microwave techniques. Thirdly, available power at this frequency does not necessarily restrict the system to LoS propagation. As a result, simple omnidirectional antenna configurations may be employed at the transmitter to improve performance through diversity

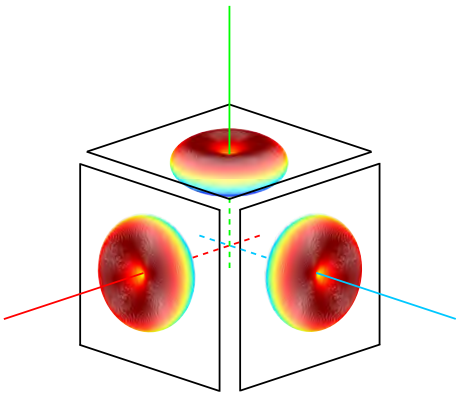

Figure 3.1. Tri-orthogonal arrangement of half-wavelength dipole modes. The familiar 'doughnut' radiation pattern of a half-wavelength dipole is associated with each of three orthogonal polarisations, or modes, represented by the red, green and blue coloured lines. Each polarisation mode is orthogonal to an associated exploded cube face. In the case of half-wavelength dipole modes, each radiation pattern provides maximum gain in a direction in the plane of an associated cube face. Reduction of the cube to an infinitesimal volume enables the three orthogonal polarisation mode radiation patterns to overlap. Together with high isolation between these modes, this overlap enables a desirable phase-centred system, minimising pattern asymmetry and providing the possibility of more than one polarisation mode in any link direction.

(Jacob and Schoebel 2008). Signal propagation may be further enhanced by the propagation environment itself, although this enhancement may be less beneficial at certain mmWave frequencies than at lower RF and microwave frequencies, due to path absorption and, more generally, path loss (Smulders 2002, Daniels and Heath 2007). However, in an atmospheric window such as that found at 28 GHz, the channel environment may provide propagation characteristics similar to those found at lower frequencies (Rappaport *et al.* 2013b). In addition to this, 5G wireless networks, operating at mmWave frequencies, may implement joint satellite and terrestrial connectivity through conventional CP mode techniques in order to provide the throughput promised by telecommunications providers (Mak *et al.* 2014).

Wave propagation using DP mode methods has been observed to enhance capacity in a LoS communication environment where relative transmitter-receiver antenna alignment varies slightly with relative position, (Vaughan 1990, Nabar *et al.* 2002, Erceg *et al.* 2006), and in more challenging longer range satellite conditions (Liolis *et al.* 2010, Arapoglou *et al.* 2011b). Spherical geometry required in satellite communication design is useful for demonstrating the benefit of polarisation diversity in three dimensions.

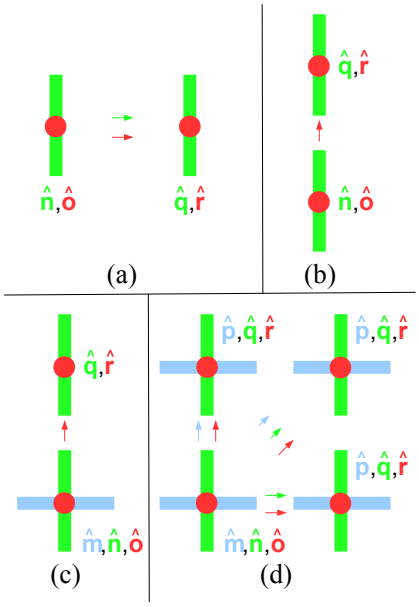

Figure 3.2. The benefit of a tri-orthogonal arrangement of polarisation modes. Mitigation of antenna misalignment is offered by the principle of tri-orthogonal polarisation diversity: (a) full capacity is observed between the receiver consisting of orthogonal polarisation modes $\hat{\mathbf{q}}$, $\hat{\mathbf{r}}$, and the transmitter consisting of orthogonal polarisation modes $\hat{\mathbf{n}}$, $\hat{\mathbf{o}}$, as a result of perfect antenna alignment. Polarisation modes $\hat{\mathbf{o}}$ and $\hat{\mathbf{r}}$ are vertical so point upwards out of the paper; (b) half capacity is observed at the receiver as only polarisation mode $\hat{\mathbf{r}}$ is broadside to the transmitter; (c) polarisation mode $\hat{\mathbf{m}}$ is introduced at the transmitter. Half capacity is once again observed as only polarisation mode $\hat{\mathbf{r}}$ is broadside to the transmitter; (d) full capacity is restored through inclusion of polarisation mode $\hat{\mathbf{p}}$ at the receiver. At least two orthogonal polarisation modes are offered in any link direction.

Inclusion of a third orthogonal dipole mode at the antenna, leading to a tri-orthogonal configuration, enhances performance beyond that of a DP mode system by mitigating antenna misalignment (Andrews *et al.* 2001, Chiu *et al.* 2007b). Figure 3.1 introduces radiation patterns associated with half-wavelength dipoles in a tri-orthogonal arrangement. Each of the three polarisations, or modes, represented by the red, green and blue coloured lines, is orthogonal to an exploded cube face. In the case of half-wavelength dipole modes, each radiation pattern provides maximum gain in a direction in the plane of an associated cube face. For a desirable phase-centred system, in an attempt to reduce asymmetry of radiation pattern to a minimum, the exploded cube is reduced to an infinitesimal volume. As such, the radiation patterns associated with each of the three orthogonal polarisation modes overlap. Together with high isolation between

these modes, this provides the possibility of more than one polarisation mode in any given link direction.

As this thesis considers polarisation diversity in three orthogonal directions, so the concept is demonstrated in Figure 3.2 through representation of orthogonal polarisations, or modes, solely. Nine links, or subchannels, are provided in Figure 3.2(d) by three orthogonal polarisations, denoted as $\hat{\mathbf{m}}$, $\hat{\mathbf{n}}$, and $\hat{\mathbf{o}}$ at the transmitter and at the receiver, denoted as $\hat{\mathbf{p}}$, $\hat{\mathbf{q}}$, and $\hat{\mathbf{r}}$. Three transmitted signals, each polarised orthogonally to the other two, may be received by each of three orthogonally polarised receive branches at the receiver. Theoretically, capacity is maintained in any given direction as, due to symmetry in six principal directions as a tri-orthogonal approach is assumed, DP mode signalling is offered over all unit vector directions. In the instance of LoS propagation, polarisation diversity offers the benefit of MIMO signalling techniques that is not always the case for a spatially diverse system.

The benefit of a rich scattering environment may further enhance this performance (Goldsmith 2005), and is often cited in reference papers pertaining to MIMO systems (Andrews *et al.* 2001, Shafi *et al.* 2006, Chiu *et al.* 2007b). Such an environment may not be available at mmWave frequencies. An arrangement of three orthogonal receive branch polarisations at the antenna may provide yet greater capacity if the orthogonality criteria between them is relaxed (Valenzuela-Valdes *et al.* 2009, Farkasvolgyi *et al.* 2009), or if polarisation diversity is used in tandem with spatial diversity (Valenzuela-Valdes and Sanchez-Hernandez 2009). However, these arrangements do not optimise capacity for all propagation directions in a FoV in which all antenna orientations are considered.

A wireless channel is a time-varying combination of a LoS signal together with a non-line-of-sight (NLoS) component arising from the channel environment, in which scatterers may provide multipath signal components. For high SNR, the multipath effect may provide beneficial diversity at the receiver, enhancing signal reception. For low SNR, the multipath effect may render reception impossible, since scattering of the signal over the channel may weaken received components to the extent that they are unusable as components required to build up an intelligible signal at the receiver. Relative transmitter-receiver motion may also be introduced. Due to orthogonality, the electric field orientations of the propagating electromagnetic signals are affected independently, reducing correlation which, together with any variation in the channel environment, presents many ways for a signal to arrive at the receiver. As a result,

throughput may be enhanced through no additional transmit power and little additional processing.

Terrestrial networks often employ single linear vertically polarised (VP mode) antennas (e.g. cellular mobile, AM and digital radio) or horizontally polarised (HP mode) antennas (e.g. some FM radio and television broadcast systems). To increase throughput, DP mode terrestrial networks may use two orthogonally polarised, or orthogonal LP mode, in-phase signals. The work of Shafi *et al* uses this arrangement, providing analysis and measurement which consider the impact of elevation angle at the receiver at low gigahertz frequencies (Shafi *et al.* 2006). Two common antenna configurations are VP/HP mode and 45° offset oriented polarisations. Terrestrial waveforms are not subject to ionospheric depolarisation effects such as Faraday rotation (Fowles 1989, Jehle *et al.* 2005) and so may typically be received by an aligned dipole arrangement at the receiver.

Wave propagation using a CP operation mode may be employed in challenging environments to ensure signal reception. However, this technique typically reduces transmitter range, as power is split equally over two orthogonal polarisation branches. At higher frequencies, this is not desirable as linear transmit power is harder to maintain, principally as a result of thermal dissipation issues resulting from smaller surface areas of active devices. In addition, a power transfer maximum is observed in the instance of perfect alignment, or the centre of a FoV, as seen from the perspective of the transmitter. With perfect alignment not typically the case for a mobile receiver, this has negative implications for link capacity, particularly in view of a world providing increasing receiver mobility. An additional degree of freedom at the receiver could mitigate this issue to an extent, in the form of an additional polarisation branch orthogonal to those seen in conventional CP mode patch antenna receivers (Balanis 2005, Mak *et al.* 2014).

Strong local scattering environments may require DCP mode wave propagation to circumvent channel effects, including depolarisation. State-of-the-art satellite research introduces DCP mode wave propagation in the form of 2×2 MIMO systems using simultaneous LHCP mode and RHCP mode wave transmission (Arapoglou *et al.* 2011b). As antenna alignment is critical in maintaining performance in a DCP mode system with evolving link geometry, tracking antennas are required. As well as being onerous to install and maintain, mechanical tracking is subject to physical failure.

Deriving full benefit from any of these systems is reliant on a precise alignment of transmit and receive antennas for a LoS channel that typically provides little in the

way of scattering. For a channel that provides a depolarising mechanism, the receive antenna should provide a polarisation state that is aligned with the electric field vector or electric field distribution of an impingent signal. Performance, including achievable capacity, is greatly affected by misalignment. In Figure 1.4, losses due to polarisation mismatch of aligned antennas are shown. The arrangements do not take into account misalignment of the antennas themselves, that may be encountered in a mobile environment and that further reduces link performance.

Performance of links employing tri-orthogonal antenna configurations has been shown to be less sensitive to orientation and antenna misalignment, providing diversity gain and increased capacity in rich scattering environments (Andrews *et al.* 2001, Horváth and Frigyes 2006, Chiu *et al.* 2007b, Sirianunpiboon *et al.* 2009). In effect, the arrangement offers the prospect of orientation robustness over a FoV, on condition that transmitter signalling and receiver processing account for radio wave polarisation according to link geometry at the receiver location. The additional degree of freedom offered by a third orthogonal polarisation may provide link enhancement in a channel devoid of scattering effects, where misalignment may occur, as well as in a rich scattering channel environment where extreme depolarisation may occur. At the transmitter, the antenna configuration permits signalling to align with the two dimensions of polarisation in the plane perpendicular to the direction of propagation. Any signal component in the direction of propagation is negligible in the far-field. At the receiver, MIMO detection and interference cancellation are feasible due to the tri-orthogonal arrangement. Polarisation-time code signalling is practicable (Proakis 2001, Paulraj *et al.* 2003).

In this chapter, a three dimensional channel model is proposed incorporating wireless link geometry between tri-orthogonal transmit and receive antennas. Simulations are initialised in accordance with references at the FoV centre (Chiu *et al.* 2007b, Wang *et al.* 2012). These references have been respectively chosen due to tri-orthogonal simulation and measurement at the receiver and an analytical approach taken in capacity simulation of linearly polarised antennas at mmWave frequencies. Both illustrate results in two dimensional line graph format. The model demonstrated in this chapter introduces tri-orthogonality at both ends of a link and a three dimensional approach to analysis. Simulation suggests that tri-orthogonality improves capacity performance in the absence of scattering mechanisms, providing orientation robustness in environments typically encountered at mmWave frequencies. The model is flexible in delivering both Rician fading simulations at any operating frequency and link decomposition; a useful

technique for evaluating system performance. In addition, the model offers the possibility of introducing near-field and correlation effects while allowing for signalling techniques to take advantage of the geometry of the FoV.

Signal-to-noise (SNR) ratios are calculated, according to which capacity is demonstrated over the FoV. Performance of our tri-orthogonal system is compared and contrasted with both reference papers and with simulated uni- and dual-polarised systems.

Many abstract two dimensional polarisation models for DP mode links implicitly assume perfect antenna alignment or apply cross-polar correlations independent of link geometry (Nabar *et al.* 2002, Erceg *et al.* 2006, Coldrey 2008, Arapoglou *et al.* 2011b, Arapoglou *et al.* 2012). Capacity improvement through a tri-orthogonal approach in environments both with and without scattering mechanisms is presented through consideration of three dimensional link geometry. While the consideration of a three dimensional approach to modelling is observed at this point, prior research may not consider a tri-orthogonal system (Shafi *et al.* 2006, Kwon and Stuber 2011, Dao *et al.* 2011), nor give a full appreciation of system performance over all antenna orientations in a FoV (Compton 1981), and in addition may operate at frequencies where the effects of rich scattering environments may enhance performance considerably (Gupta *et al.* 2008, Quitin *et al.* 2009, Piao *et al.* 2015). The model demonstrated in this thesis presents a useful step in the implementation of a proposed mmWave tri-orthogonal system permitting short range, high capacity communication, independent of position and over all antenna orientations. The simulated results suggest that capacity improvement due to a tri-orthogonal approach is available, both in the presence and absence of a scattering environment.

An allowance built into a system to cater for signal deterioration is known as link margin. A system built solely around an optimal power transfer scenario, typically at the FoV centre, may not propagate a signal, from transmitter to receiver, once power transfer loss in a particular direction exceeds that of the optimal case. A one-size-fits-all approach to link margin results in a system with greater link margin in certain directions than in others. Systems with greater link margin are typically more sensitive to signal variation and may suffer the effects of amplifier saturation. A trade-off exists, predominantly at higher frequencies, where linear transmit power becomes more difficult to maintain. Such systems tend to be more expensive as a result. Cost minimisation is of considerable benefit.

Implicitly assuming aligned antennas, as is often the case with design, means the effect of polarisation mismatch may be inadvertently ignored. In the instance of relative transmitter-receiver movement, this alignment may only occur for a small percentage of the time. Power transfer becomes dependent on the polarisation mismatch between transmitter and receiver, itself being a function of relative FoV position. At certain positions in the FoV, this may cause a theoretical infinite loss in power transfer, severely reducing capacity. For RFID systems, which may be considered as a proxy for the Internet of Things (Ashton 2009, Atzori *et al.* 2010), the effect of polarisation mismatch is considerable (Keskilammi *et al.* 2003).

The model aims to demonstrate the effect on capacity over the FoV of power transfer; itself being a function of polarisation mismatch, antenna gain and free space path loss in a channel environment.

3.2 Methods

The concept of link geometry is presented, together with its effect on power transfer for a mmWave, tri-orthogonal system. Channels employing MIMO signal propagation have shown improved performance in rich scattering environments (Goldsmith 2005). In the absence of a scattering mechanism, diversity gain is greatly reduced. MIMO polarisation diversity has demonstrated improved performance in both terrestrial and satellite channel environments (Lee and Yeh 1972, Turkmani *et al.* 1995, Chiu *et al.* 2007b, Sirianunpiboon *et al.* 2009, Arapoglou *et al.* 2010a, Arapoglou *et al.* 2010b).

To reduce the effects of antenna orientation on the signal, a tri-orthogonal dipole antenna arrangement may be used. Unlike spatially diverse MIMO systems using three orthogonal polarisations, and systems using DP mode arrangements, tri-orthogonal polarisation diverse MIMO permits a compact tri-orthogonal antenna design centred on a single point. Reconfigurable phase-centred radiation patterns are possible, enhancing gain in a given direction, and appropriate for mobile applications as in the IEEE (802.11ad) initiative at 60 GHz. As an example, the concept of massive MIMO looks to apply this technique in two dimensions, although it is largely confined to sub-5 GHz frequencies for the time being due to antenna array design complexity (Larsson *et al.* 2014).

In the NLoS case, providing a rich scattering environment, a marked capacity improvement has been observed using three dimensional polarisation diversity over that of DP

mode diversity (Andrews *et al.* 2001, Chiu *et al.* 2007b). Tri-orthogonal arrangements introduce a third degree of polarisation freedom, the benefit of which may be extended over a FoV. Where deep fading may occur with uni- or DP mode systems, it is unlikely that a signal sent from a third orthogonal polarisation branch will suffer the same fading.

Current techniques at RF and low microwave frequencies often demonstrate a perfomance improvement, enhanced by multipath effects in rich scattering environments, but fail to take channel geometry or physical channel effects into consideration (Getu and Andersen 2005). The channel may change rapidly due to relative transmitter-receiver movement. Accurate modelling of such a channel requires inclusion of additional effects such as Doppler phase shift, near-field effects and multipath (Goldsmith 2005). Such effects may indeed negate any capacity improvement seen through introduction of a third orthogonal polarisation. An estimated channel model requires a deterministic LoS channel component and a stochastic NLoS channel component. The latter component dominates in the case of a Rayleigh fading channel. A normalised NLoS channel component may be modelled as a correlated complex Gaussian matrix consisting of elements with zero mean and unity standard deviation (Erceg *et al.* 2002). Such a model may provide an at-a-glance determination of link performance over the entire FoV. Deep fade areas in the FoV may be determined with subsequent system design taking this into consideration. Power consumption may be used more efficiently so extending battery life, coverage and range. Overall link performance may benefit through enhanced capacity and improved consistency over the FoV.

We assume three mutually orthogonal unit vectors representing half-wavelength ($\lambda/2$) dipoles at both transmitter ($\hat{\mathbf{m}}$, $\hat{\mathbf{n}}$, $\hat{\mathbf{o}}$) and receiver ($\hat{\mathbf{p}}$, $\hat{\mathbf{q}}$, $\hat{\mathbf{r}}$). These dipoles possess orthogonally polarised radiation patterns at the antennas, at either end of the channel. A phase-centred approach at each antenna is required to avoid pattern distortion in the far-field as a result of superposition, and avoid any spatial diversity in the system. Without loss of generality, we assume no phase difference between transmitted signals. To understand the benefits of polarisation in three dimensions, we look to spherical geometry, which is used in satellite communications design, and is given according to textbook definitions (Ryan 2003, Roddy 2006) in Figures 3.3 and 3.4. The FoV and relevant nomenclature are now introduced. The receiver R is observed to move upon a spherical surface. This surface introduces both variable path length and orientation.

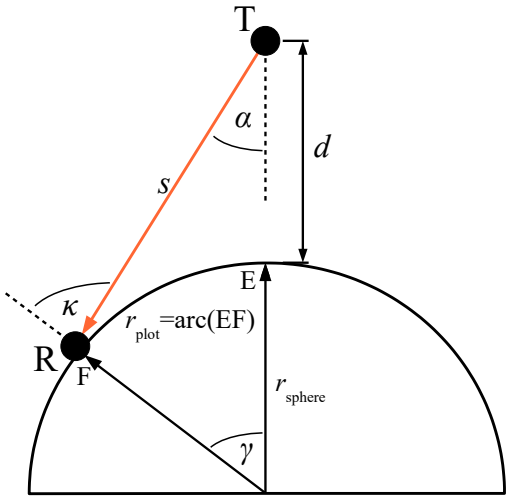

Figure 3.3. Terrestrial channel link geometry. The receiver R is positioned on a semi-circle determined by geometry. The proximal distance between T and R is d, s is path length while angles α, κ and γ are used to determine relative position. The entire system is rotated about the FoV centre by 360° to develop a spherical surface, forming the FoV. The number of concentric paths on the sphere together with the azimuthal step increment about the FoV centre is set by the user. The algorithm begins at the FoV centre and works out to the circular path where $\kappa = 90°$.

The outer radius of the FoV is the point at which unit dipole $\hat{\mathbf{r}}$ is broadside to power transfer from transmitter T. As the FoV is circular, all orientations of the proposed antenna system configuration are included in the FoV. Indeed, the tri-orthogonal system repeats its configuration, and hence the FoV, in six orthogonal directions when the FoV centre is aligned with each of the $\pm$ (a, b, c)-axes in Figure 3.4.

Referring to Figure 3.4, at T, unit vector $\hat{\mathbf{m}}$ is aligned with the positive b-axis, coinciding with an azimuthal angle θ_{T}, as observed from T, of 0°. Unit vector $\hat{\mathbf{n}}$ is aligned with the positive c-axis, coinciding with an azimuthal angle θ_{T} of 90°. Unit vector $\hat{\mathbf{o}}$ is aligned with the positive a-axis.

At R, and at the FoV centre, unit vector $\hat{\mathbf{p}}$ is aligned with the positive b-axis, coinciding with an azimuthal angle θ_{T} of 0°. Unit vector $\hat{\mathbf{q}}$ is aligned with the positive c-axis, coinciding with an azimuthal angle θ_{T} of 90°. Unit vector $\hat{\mathbf{r}}$ is a radial unit vector aligned with the positive a-axis, when R is at the FoV centre.

To effectively explain movement of R within the FoV, easterly and northerly compass directions are invoked, corresponding to azimuthal angles of θ_T of 0° and 90° respectively. In Figure 3.4, unit vector $\hat{\mathbf{p}}$ is deemed to point in an easterly direction while unit vector $\hat{\mathbf{q}}$ is deemed to point in a northerly direction, for any position of R in the FoV.

Link geometry is determined according to Figure 3.3 and to the following equations,

$$\gamma = \frac{r_{\text{plot}}}{r_{\text{sphere}}} \tag{3.1}$$

$$s = \sqrt{u^2 + {r_{\text{sphere}}}^2 - 2u r_{\text{sphere}} \cos\gamma} \tag{3.2}$$

$$\kappa = \arcsin\left(\frac{u}{s}\sin\gamma\right) \tag{3.3}$$

$$\alpha = \arcsin\left(\frac{u}{s}\sin\gamma\right) - \gamma \tag{3.4}$$

$$\gamma_{\max} = \arccos\left(\frac{r_{\text{sphere}}}{u}\right) \tag{3.5}$$

$$s_{\max} = u\cos\alpha \tag{3.6}$$

$$\alpha_{\max} = \arcsin\left(\frac{r_{\text{sphere}}}{u}\right) \tag{3.7}$$

where u is $r_{\text{sphere}} + d$.

Observing from T, counter clockwise rotation about the positive a-axis looking toward the FoV is deemed positive, as in Figure 3.4. Elevation at T is given by α with 0° in the negative a-axis direction, otherwise positive. Elevation at the receiver is given by κ, with 0° in the positive a-axis direction at the FoV centre, otherwise positive. The azimuthal angle θ_R, at R, in the FoV at a position given by the unit propagation vector $\hat{\mathbf{k}}$, differs from the corresponding angle θ_T, at T, by 180°. The receiver R is assumed to be at a distance s, from T, that varies according to FoV location. Ideally, power transfer over the FoV is high and constant. The possibility of high capacity communication in

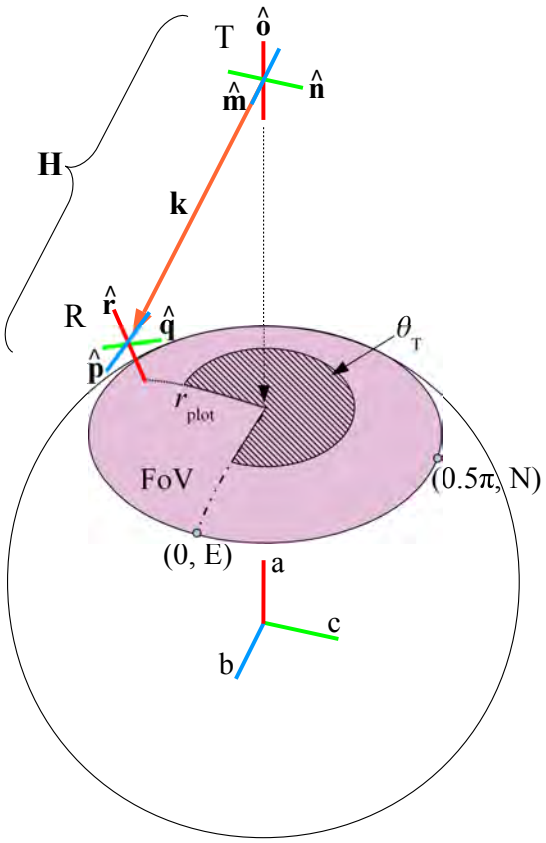

Figure 3.4. System according to specific location in the terrestrial FoV. The unit propagation vector $\hat{\mathbf{k}}$ is unique to any position in the FoV, and is given according to the azimuthal angle θ_T and the radial distance from the FoV centre, r_{plot}. Easterly and northerly directions simplify description of the movement of R in the FoV. Unit dipole orientations at R are calculated according to Equations (3.14), (3.15), and (3.16) in three dimensional space. These, along with the static unit dipole orientations, at T, of $\hat{\mathbf{m}}$, $\hat{\mathbf{n}}$ and $\hat{\mathbf{o}}$, then permit the determination of the parameters required to analyse the channel, $\mathbf{H}$, as a function of FoV location.

any unit vector direction can be evaluated. Where deep fading is encountered, diversity, through redundancy, may be introduced (Paulraj *et al.* 2003, Adve Accessed: 2013). An ideal channel is one where recourse to this is kept to a minimum.

Power transfer over a subchannel between a polarisation at T and at R is borne out through the Friis formula (Friis 1946). For a mutually tri-orthogonal antenna transmitter and receiver, nine subchannel paths are generated. The Friis formula is given as,

$$\frac{P_R}{P_T} = G_T(\phi_T, \theta_T) G_R(\phi_R, \theta_R) \left(\frac{\lambda}{4\pi s}\right)^2 e_{pol} L_{atmos} \tag{3.8}$$

where R refers to the receiver, T refers to the transmitter, P is power, G is dipole gain, λ is transmitted wavelength, s is separation of transmitter and receiver, e_{pol} is the polarisation mismatch between two polarisations and L_{atmos} is atmospheric attenuation due to the interaction with oxygen molecules at 60 GHz and is given here as 15 dBkm^{-1} (Wang *et al.* 2012).

The power gain G of a half-wavelength dipole is given by Equation (3.9) (Orfanidis 2002, Balanis 2005, Pozar 2011). This assumes 100 % dipole efficiency and is given as,

$$G(\theta, \phi) = \frac{1.64}{\sin^2\theta} \cos^2\left(\frac{\pi}{2}\cos\theta\right). \tag{3.9}$$

In the case of unit vector $\hat{\mathbf{o}}$ at T, angle θ is represented by α, as shown in Figure 3.3. At T, minimum gain is when α is 0°. Maximum gain is when α is 90°, which is not in the FoV. We note that the gain of unit dipole $\hat{\mathbf{o}}$ is independent of the azimuthal angle θ_{T}. For unit vectors $\hat{\mathbf{m}}$ and $\hat{\mathbf{n}}$ representing orthogonal polarisations, angle θ can be determined by considering the inner product of a unit polarisation vector and the unit propagation vector $\hat{\mathbf{k}}$ where,

$$\hat{\mathbf{k}} = \begin{bmatrix} -\cos\alpha \\ \cos\theta_{\text{T}}\sin\alpha \\ \sin\theta_{\text{T}}\sin\alpha \end{bmatrix}. \tag{3.10}$$

In the case of polarisation $\hat{\mathbf{r}}$ at R, angle θ is represented by κ, the sum of α and γ, as in Figure 3.3. For polarisations $\hat{\mathbf{p}}$ and $\hat{\mathbf{q}}$, angle θ is determined in the same manner as that for polarisations $\hat{\mathbf{m}}$ and $\hat{\mathbf{n}}$, with κ replacing α.

Figure 3.5 shows gain profiles of the six half-wavelength dipoles associated with each of the six individual polarisations.

A signal may incur polarisation mismatch loss over a link when two antennas do not have their polarisations perfectly aligned (Orfanidis 2002, Balanis 2005). In accordance with the geometry given in Figure 3.5, polarisation mismatch e_{pol} may be determined for any unit dipole pair. For the unit dipole pair $\hat{\mathbf{r}}\hat{\mathbf{o}}$, the polarisation mismatch may be given by the inner product in Equation (3.11),

$$e_{\text{pol}(\hat{\mathbf{r}}\hat{\mathbf{o}})} = |\hat{\mathbf{r}}_{\perp\mathbf{k}} \cdot \hat{\mathbf{o}}_{\perp\mathbf{k}}|^2 \tag{3.11}$$

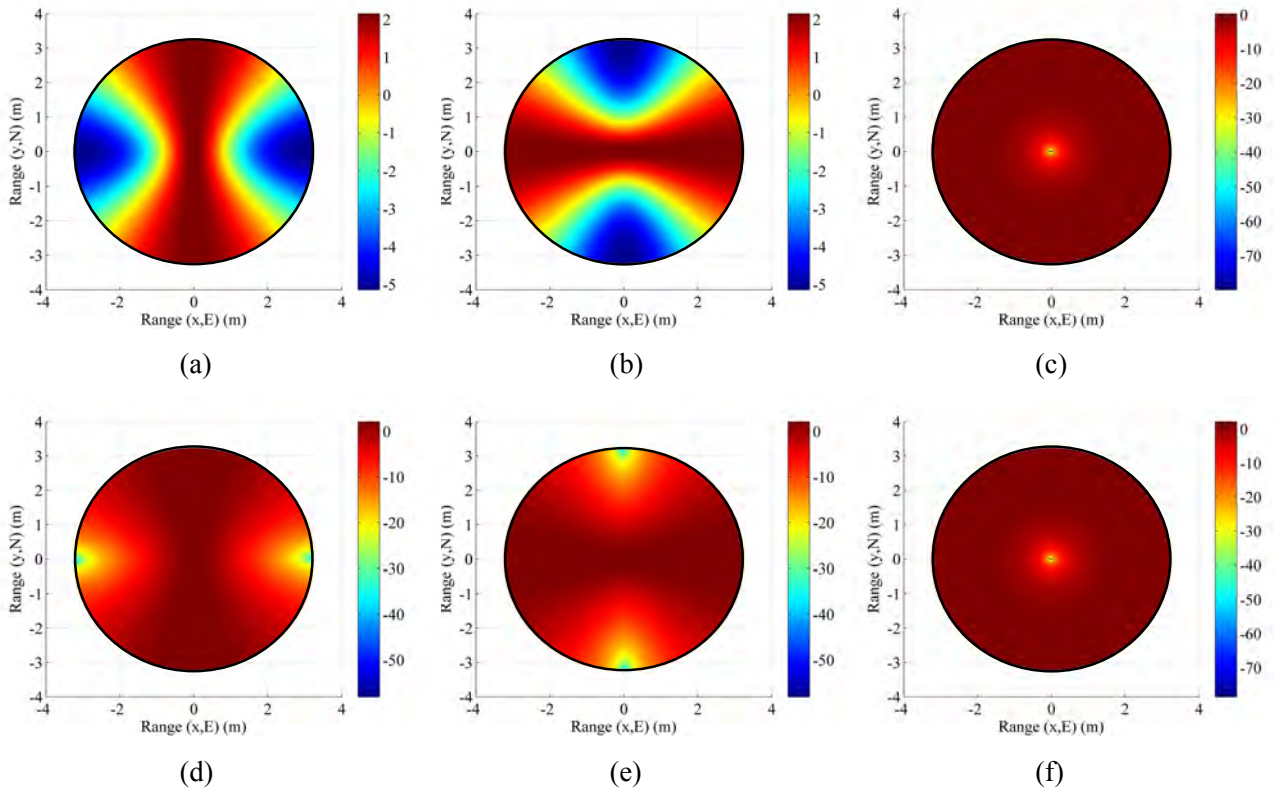

Figure 3.5. Gain (G) (dB) profiles of the six half-wavelength dipole modes over the terrestrial channel FoV. The polarised mode gains shown are: (a) $\hat{\mathbf{m}}$, (b) $\hat{\mathbf{n}}$, (c) $\hat{\mathbf{o}}$, (d) $\hat{\mathbf{p}}$, (e) $\hat{\mathbf{q}}$, (f) $\hat{\mathbf{r}}$.

where $\hat{\mathbf{r}}_{\perp\mathbf{k}}$ and $\hat{\mathbf{o}}_{\perp\mathbf{k}}$ are projections onto the plane perpendicular to the unit propagation vector $\hat{\mathbf{k}}$. As $\hat{\mathbf{r}}$ is a radial dipole, while $\hat{\mathbf{o}}$ is a static dipole in the zenith direction, no polarisation mismatch occurs for this unit dipole pair.

The projection of an arbitrary vector $\mathbf{v}$ onto the plane perpendicular to $\hat{\mathbf{k}}$ may be given by,

$$\mathbf{v}_{\perp\mathbf{k}} = \left(\mathbf{I_3} - \hat{\mathbf{k}}\hat{\mathbf{k}}^{\mathrm{T}}\right)\hat{\mathbf{v}}, \tag{3.12}$$

which can then normalised to give,

$$\hat{\mathbf{v}}_{\perp\mathbf{k}} = \frac{\mathbf{v}_{\perp\mathbf{k}}}{|\mathbf{v}_{\perp\mathbf{k}}|}. \tag{3.13}$$

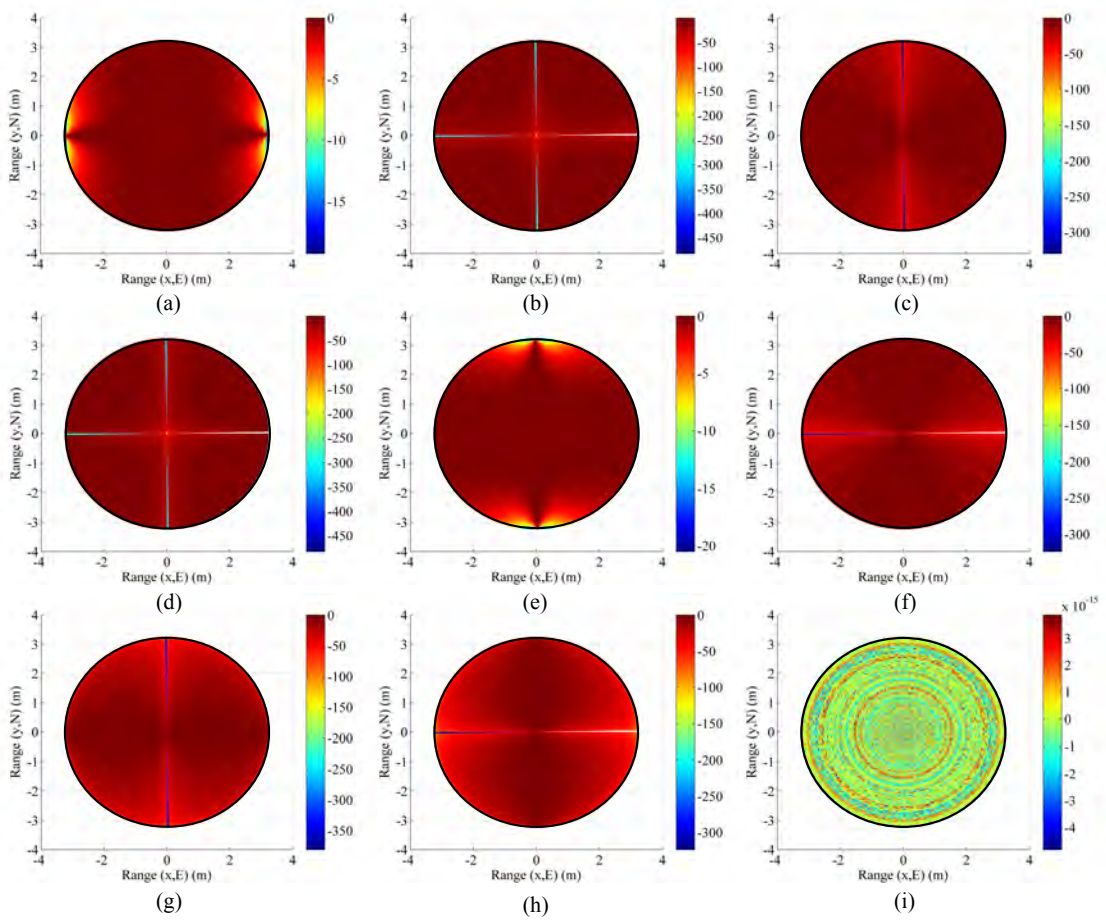

Figure 3.6. Polarisation mismatch (e_{pol}) (dB) profiles for each unit dipole mode pair. The following polarised mode pair mismatches are shown: (a) $\hat{\mathbf{p}}\hat{\mathbf{m}}$, (b) $\hat{\mathbf{p}}\hat{\mathbf{n}}$, (c) $\hat{\mathbf{p}}\hat{\mathbf{o}}$, (d) $\hat{\mathbf{q}}\hat{\mathbf{m}}$, (e) $\hat{\mathbf{q}}\hat{\mathbf{n}}$, (f) $\hat{\mathbf{q}}\hat{\mathbf{o}}$, (g) $\hat{\mathbf{r}}\hat{\mathbf{m}}$, (h) $\hat{\mathbf{r}}\hat{\mathbf{n}}$, (i) $\hat{\mathbf{r}}\hat{\mathbf{o}}$.

Polarisation mismatch profiles are given in Figure 3.6 for all unit dipole pair combinations.

To describe orientation of the six half-wavelength dipoles represented by the six signal polarisation unit vectors, the set of right-handed Cartesian axes in Figure 3.4 is considered. Axes a, b, c are used to describe the position of R on the sphere surface. Lengths a_1, b_1, c_1 are along these axes respectively, and are normalised by r_{sphere}. Unit vectors representing orthogonal polarisations are respectively $\hat{\mathbf{m}} = [010]^{\text{T}}$, $\hat{\mathbf{n}} = [001]^{\text{T}}$, $\hat{\mathbf{o}} = [100]^{\text{T}}$ and,

$$\hat{\mathbf{r}} = \begin{bmatrix} \cos\gamma \\ \cos\theta_{\mathrm{T}} \sin\gamma \\ \sin\theta_{\mathrm{T}} \sin\gamma \end{bmatrix} \tag{3.14}$$

where the superscript T denotes transpose.

The position on the spherical surface, relative to the FoV centre position, must be known to describe the orientation of polarisations $\hat{\mathbf{p}}$ and $\hat{\mathbf{q}}$,

$$\hat{\mathbf{p}} = \begin{bmatrix} -\sin(\mathrm{atan}_2(b_1, a_1)) \\ \cos(\mathrm{atan}_2(b_1, a_1)) \\ 0 \end{bmatrix} \tag{3.15}$$

$$\hat{\mathbf{q}} = \begin{bmatrix} -\sin(\arcsin(c_1))\cos(\mathrm{atan}_2(b_1, a_1)) \\ -\sin(\arcsin(c_1))\sin(\mathrm{atan}_2(b_1, a_1)) \\ \cos(\arcsin(c_1)) \end{bmatrix} \tag{3.16}$$

where $\mathrm{atan}_2(b_1, a_1)$ is described as,

$$\mathrm{atan}_2(b_1, a_1) = \begin{cases} \arctan(\frac{b_1}{a_1}) & (a_1 \succ 0) \\ \arctan(\frac{b_1}{a_1}) + \pi & (b_1 \succeq 0, a_1 \prec 0) \\ \arctan(\frac{b_1}{a_1}) - \pi & (b_1 \prec 0, a_1 \prec 0) \\ +\pi/2 & (b_1 \succ 0, a_1 = 0) \\ -\pi/2 & (b_1 \prec 0, a_1 = 0) \\ \text{undefined} & (b_1 = 0, a_1 = 0) \end{cases} \tag{3.17}$$

At the FoV centre in Figure 3.4, a_1=1, b_1=0, and c_1=0.

Received symbols at R over a channel may be given as (Goldsmith 2005),

$$\mathbf{Y} = \mathbf{H}\mathbf{X} + \mathbf{N}. \tag{3.18}$$

In Equation (3.18), $\mathbf{Y}$ is the set of received signals at the receiver, $\mathbf{H}$ represents a 3×3 complex fading channel matrix, $\mathbf{X}$ is a block of symbols sent and $\mathbf{N}$ is complex additive white Gaussian noise (AWGN) at the receiver R.

The complex fading channel matrix may be decomposed into the sum of a deterministic average LoS component ($\bar{\mathbf{H}}$), determined by application of Equation (3.8) for each subchannel, and a stochastic scattered NLoS component ($\tilde{\mathbf{H}}$), and is given as,

$$\mathbf{H} = \sqrt{\frac{K}{1+K}}\bar{\mathbf{H}} + \sqrt{\frac{1}{1+K}}\tilde{\mathbf{H}} \tag{3.19}$$

where K is the Ricean K-factor (Goldsmith 2005). Note that $K = 0$ corresponds to a pure stochastic Rayleigh, or complex Gaussian, fading channel with no LoS component, while $K = \infty$ corresponds to a pure AWGN fading channel or LoS system, with no signal scattering in the channel. A complex Gaussian distribution is circularly symmetric, and refers to a random complex variable, x+iy, where the x and iy components are independent with zero mean and unit variance, $\aleph(0,1)$. We may add a complex Gaussian component over each subchannel through a complex Gaussian random matrix, $\tilde{\mathbf{H}}$. Each element of this matrix is normalised by the square root of received power, $\sqrt{P_{\mathrm{R}}}$, over each individual subchannel. This introduces a stochastic component to multipath fading, that may provide enhanced capacity performance in the channel through scattering and reflection, provided that signalling from T and reception at R take account of the radio wave polarisation specific to the link geometry for the location of R during processing.

For this model we simulate channel capacity at an instant in time for Ricean K-factors of 0 and ∞. Without loss of generality, we assume the phase arguments of the deterministic LoS coefficients in $\bar{\mathbf{H}}$ to be zero. Thus any signal voltage sent over the channel is only subjected to a magnitude change. We also assume all half-wavelength dipoles, and hence polarisations, at T to be colocated, and the same assumption is made for half-wavelength dipoles, and hence polarisations, at R.

The LoS power transfer for each unit dipole pair, given by Equation (3.8), forms a basis to determine nine channel coefficients that describe power transfer over the channel, and that are unique to a FoV location.

These coefficients are obtained from $\sqrt{P_{\mathrm{R}}/P_{\mathrm{T}}}$ (Lawrence *et al.* 2013), and may be considered as being proportional to signal voltage amplitude changes as a result of channel propagation.

The polarisation mismatch factor, e_{pol}, includes projections via Equation (3.12), with the 3×3 matrix $\mathbf{H}$ being at most rank 2 in the LoS case. Channel rank, and therefore capacity, may be increased via multipath, or scattering, as the system approaches the

case of Rayleigh fading. In effect, a typical channel may provide localised uncorrelated fading through reflections of the propagating signal within zones close to the transmitter and the receiver. As a result, channel rank is not degraded to the same extent as propagation in between these zones where propagation distance is far larger than the radius of such a zone (Gesbert *et al.* 2003). The addition of a third orthogonal radiating dipole provides both antenna and polarisation diversity over the channel. As a consequence, channel rank is not impacted in the same way as for conventional CP mode techniques.

Applications of the channel model, in the AWGN fading or LoS case, are currently restricted and may include an improved determination of the LoS component used for channel state information (CSI) to optimise transmission. Use of omnidirectional antennas enhances the probability of multipath in the case of a scattering channel, increasing capacity over the FoV.

Doppler frequency shift, caused by relative transmitter-receiver motion, is omitted, as are near-field and correlation effects. For a polarisation diverse antenna design, in a terrestrial Rayleigh fading environment, correlation is near negligible (Turkmani *et al.* 1995, Gesbert *et al.* 2003). In Chapters 6 and 7, designs providing a measured maximum mutual port coupling between polarisations of -35 dB are demonstrated.

A channel matrix $\mathbf{H}$ for each receive antenna location, and subsequent orientation, in the FoV may be determined according to the calculation of the nine subchannels using Equation (3.8). For M receiver elements, or orthogonal branch polarisations in this instance, and N transmitter elements, or orthogonal branch polarisations in this instance, the channel matrix is of the form given below,

$$\mathbf{H} = \begin{bmatrix} h_{\hat{\mathbf{p}}\hat{\mathbf{m}}} & h_{\hat{\mathbf{p}}\hat{\mathbf{n}}} & h_{\hat{\mathbf{p}}\hat{\mathbf{o}}} \\ h_{\hat{\mathbf{q}}\hat{\mathbf{m}}} & h_{\hat{\mathbf{q}}\hat{\mathbf{n}}} & h_{\hat{\mathbf{q}}\hat{\mathbf{o}}} \\ h_{\hat{\mathbf{r}}\hat{\mathbf{m}}} & h_{\hat{\mathbf{r}}\hat{\mathbf{n}}} & h_{\hat{\mathbf{r}}\hat{\mathbf{o}}} \end{bmatrix} \tag{3.20}$$

where the matrix coefficients in Equation (3.20) represent signal transfer between a unit dipole receive-transmit pair.

Capacity for M receivers and N transmitters is given according to Equation (3.21) (Proakis 2001, Paulraj *et al.* 2003, Gesbert *et al.* 2003, Bohagen *et al.* 2005) as,

$$C = \log_2 \left| \left(\mathbf{I}_M + \frac{P_\mathrm{T}}{P_\mathrm{N} N} \mathbf{H}\mathbf{H}^\dagger \right) \right| \tag{3.21}$$

where P_T is the total transmit power at T, P_N is the noise power at R, $\mathbf{I}$ represents an identity matrix, and † denotes the Hermitian transpose. Division of transmit power by the number of transmitter elements N ensures that a like-to-like comparison is made for all systems. With identical transmit power assumed in all cases, a 3×3 tri-orthogonal system spreads transmit power over the FoV while providing additional diversity at the receiver over conventional CP mode and DP mode receive antenna designs. The tri-orthogonal arrangement provides orientation robustness, rather than concentrating power at the FoV centre, where typically the system operates optimally.

3.3 Results

In order to simulate, comparison with prior work in the field is invoked (Chiu *et al.* 2007b, Wang *et al.* 2012). Figure 3.7 shows data taken at the FoV centre, at 2.55 GHz in a channel with Rayleigh fading characteristics (Anreddy and Ingram 2006), with T and R aligned along the positive a-axis as per Figure 3.4, for a range of average SNR per receiver branch values (Chiu *et al.* 2007b). As expected, both the uni-polarised system developed in the model, as well as that of Chiu *et al.* (2007b), approach the Shannon capacity limit, shown for a 1 Hz bandwidth in Figure 3.7, due to perfect alignment, thus optimal signal transfer, along this axis. The same analysis applies to the DP mode case. A discrepancy exists between that of the simulated tri-orthogonal NLoS, or 3×3, case presented in this model and that of prior work (Chiu *et al.* 2007b). This is due to only the receiver being a tri-orthogonal arrangement, the transmitter being a three fold, linearly polarised system. As a consequence, the arrangement demonstrates a three fold increase in capacity over that of a uni-polarised arrangement. In the presented channel model, this is not the case due to the tri-orthogonal arrangement at T and link geometry. In Figure 3.7, this difference in 3×3 tri-orthogonal system capacity is clearly observed.

Figure 3.8 illustrates a uni-polarised LoS capacity comparison at 60 GHz, and again for a 1 Hz bandwidth, of the channel model with that of previous work in this area (Wang *et al.* 2012). This is extended to both DP mode and tri-orthogonal systems, since all considered arrangements base their channel coefficients on an average SNR at a point in the FoV, discerned through link geometry. The average SNR per receiver branch is calculated over a proximal distance, d, ranging from 1–20 m. The uni-polarised LoS capacity presented in this channel model shows good agreement

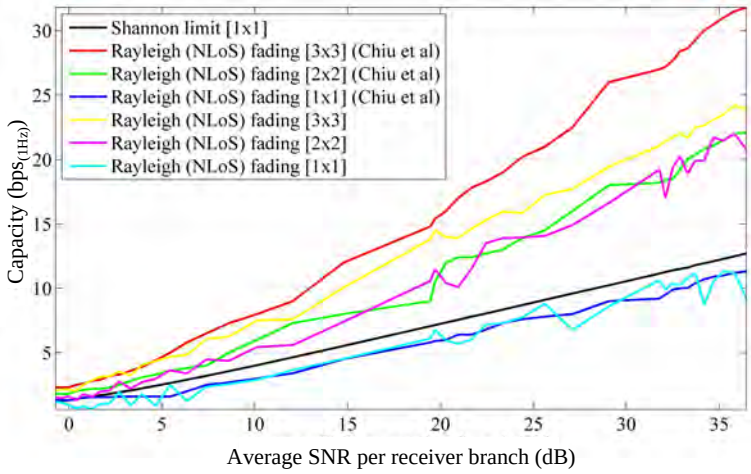

Figure 3.7. Simulated capacity ($bps_{(1\ Hz)}$), or spectral efficiency, at the FoV centre of uni-polarised, dual-polarised, and tri-orthogonal arrangements at 2.55 GHz. The simulations are provided in a Rayleigh (NLoS) fading channel, and as a function of average SNR per receiver branch at the FoV centre, according to prior work (Chiu *et al.* 2007b). A Ricean factor K of 10^{-2} is used. The transmitter is perfectly aligned with the receiver along the positive a-axis, as in Figure 3.4. The difference in capacity between the tri-orthogonal, or 3×3, arrangement of the presented model and the simulated and measured 3×3 arrangement in the work of Chiu *et al.* (2007b), is due to a non-orthogonal arrangement at the transmitter being previously employed.

with the line corresponding to the channel exponent of $n = 1.55$ in Figure 3 of the work by Wang *et al.* (2012).

The channel model is inherently based on SNR, as is any determination of link performance. Comparison with prior work (Chiu *et al.* 2007b, Wang *et al.* 2012) allows for the channel model to be compared over a full range of variables. These include frequency, power, NLoS and LoS configuration, and degrees of polarisation.

We present simulated three dimensional results over a FoV using an operating frequency of 60 GHz, a transmit power of 40 dBm, a bandwidth of 7 GHz, and a system noise temperature (Wang *et al.* 2012) of 290 K. The propagation distance at the FoV centre is 1 m, corresponding to a close proximity wireless personal area network (WPAN), while a spherical radius of 6 m is employed. A channel exponent of 1.55 (Wang *et al.* 2012) is used. These parameters correspond to a maximum average SNR per receiver branch at the FoV centre of 65 dB, as shown in Figure 3.9 (c). Ricean K-factors of $K = 0$ and $K = \infty$, corresponding to pure Rayleigh

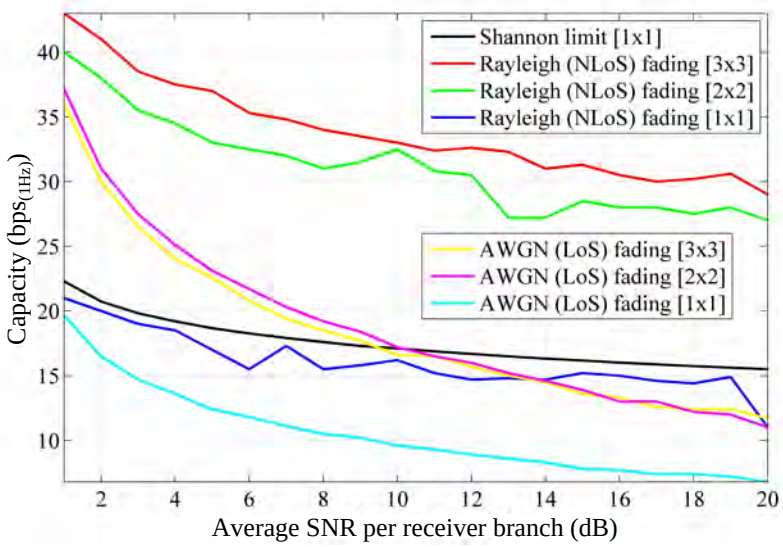

Figure 3.8. Simulated capacity ($bps_{(1\ Hz)}$), or spectral efficiency, at the FoV centre of uni-polarised, dual-polarised, and tri-orthogonal arrangements at 60 GHz. The simulations are provided in both AWGN (LoS) and Rayleigh (NLoS) fading channels, and as a function of proximal distance, or d as shown in Figure 3.3. Ricean factors of 10^{-2} and 10^{3} are used to simulate Rayleigh and AWGN fading channels respectively. The transmitter is perfectly aligned with the receiver along the positive a-axis, as in Figure 3.4. The dual-polarised and tri-orthogonal arrangements are extensions, through analysis of link geometry, to the uni-polarised system previously presented in Wang *et al.* (2012).

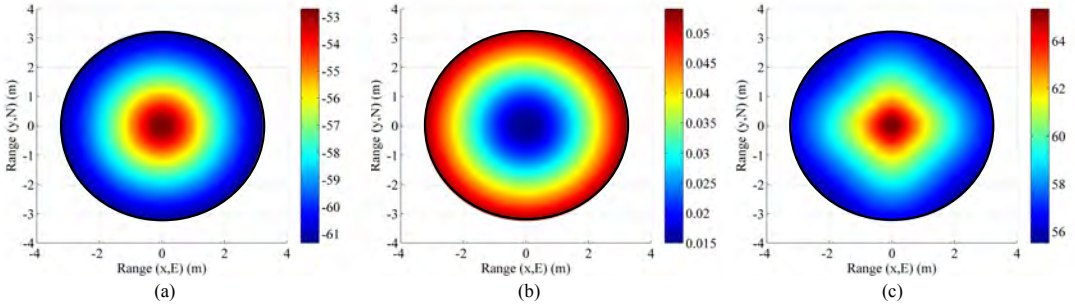

Figure 3.9. Channel parameters over the FoV. The images shown are: (a) free space path loss (dB), (b) atmospheric loss L_{atmos} (dB), and (c) average SNR per receiver branch for a tri-orthogonal system (dB) profiles over the FoV.

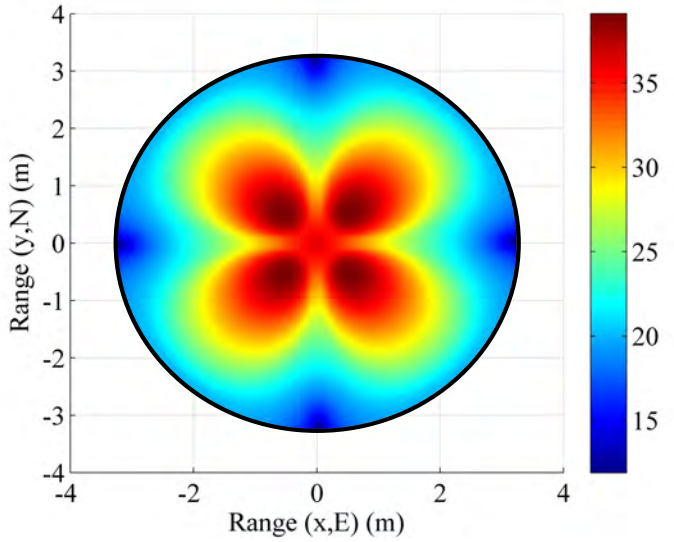

Figure 3.10. Tri-orthogonal, or 3 × 3, AWGN fading channel capacity ($bps_{(1\ Hz)}$), or spectral efficiency. Simulated results are presented in a FoV format for all receive antenna orientations and, by extension, all system orientations. The system operates with an operating frequency of 60 GHz, a transmit power of 40 dBm, a bandwidth of 7 GHz, and a system noise temperature of 290 K. The propagation distance at the FoV centre is 1 m, corresponding to a close proximity wireless personal area network (WPAN), while a spherical radius of 6 m is employed for receive antenna displacement over a sphere. The results show a maximum capacity that is offset in four positions from the FoV centre. Polarisation modes $\hat{\mathbf{r}}$ and $\hat{\mathbf{o}}$ are redundant at the FoV centre, and this is mitigated at the four offset positions while providing near optimal alignment of dipole pairs, or polarisation modes, $\hat{\mathbf{p}}$ and $\hat{\mathbf{m}}$, and $\hat{\mathbf{q}}$ and $\hat{\mathbf{n}}$.

(Choi *et al.* 2005, Wang *et al.* 2012) and AWGN fading channels, are used in these simulations. System specific values of free space path loss, atmospheric loss, and SNR are illustrated in Figure 3.9.

Figure 3.10 shows the AWGN fading channel capacity over the FoV, as produced by the tri-orthogonal 3 × 3 system. Figure 3.11 shows the AWGN fading channel capacity advantage over the FoV, as produced by a tri-orthogonal 3 × 3 system over an orthogonal DP mode 2 × 2 system. Figure 3.12 shows the Rayleigh fading channel capacity over the FoV, as produced by the tri-orthogonal 3 × 3 system. Figure 3.13 shows the Rayleigh fading channel capacity advantage over the FoV, as produced by a tri-orthogonal 3 × 3 system over an orthogonal DP mode 2 × 2 system.

We note from these figures that:

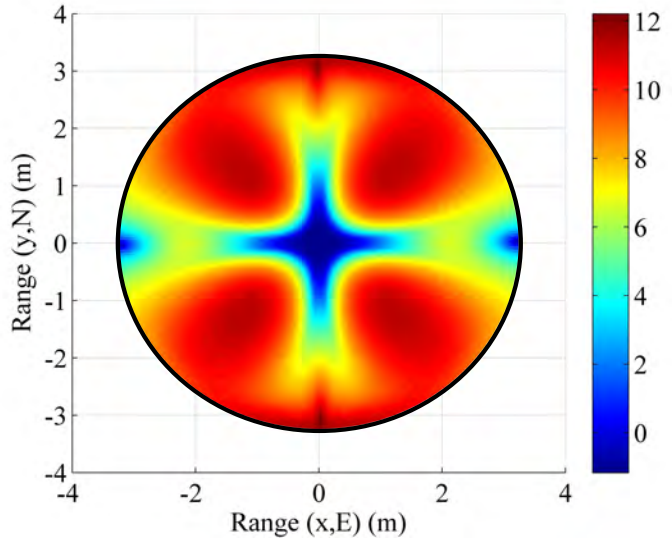

Figure 3.11. Capacity advantage ($bps_{(1\ Hz)}$), or spectral efficiency advantage, of a tri-orthogonal, or 3 $\times$ 3, system over that of a dual-polarised, or 2 $\times$ 2, system in an AWGN fading channel. Simulated results are presented in a FoV format for all receive antenna orientations and, by extension, all system orientations. The system operates with an operating frequency of 60 GHz, a transmit power of 40 dBm, a bandwidth of 7 GHz, and a system noise temperature of 290 K. The propagation distance at the FoV centre is 1 m, corresponding to a close proximity wireless personal area network (WPAN), while a spherical radius of 6 m is employed for receive antenna displacement over a sphere. At the FoV centre, redundancy of polarisation modes $\hat{\mathbf{r}}$ and $\hat{\mathbf{o}}$ provides a slight dip in capacity performance of the tri-orthogonal system when compared with the dual-polarised system. The tri-orthogonal arrangement is observed to provide enhanced capacity over the majority of the FoV, when compared with the dual-polarised system.

- the 3 $\times$ 3 system in both AWGN and Rayleigh fading regimes exhibits a channel capacity higher than that of the 2 $\times$ 2 and uni-polarised 1 $\times$ 1 systems over the majority of the FoV. This is most clearly seen in Figures 3.10 and 3.11. An absence of a scattering mechanism at mmWave frequencies does not stop the inclusion of a third orthogonal polarisation branch from improving performance over the majority of the FoV. The capacity is more consistent over the FoV and is observed to approach the Shannon capacity limit in the instance of a Rayleigh fading channel. This is seen in Figures 3.12 and 3.13.

- at the FoV centre, the 3 $\times$ 3 system experiences a small capacity disadvantage when compared to the 2 $\times$ 2 system, as seen in Figures 3.10 and 3.11. This is due

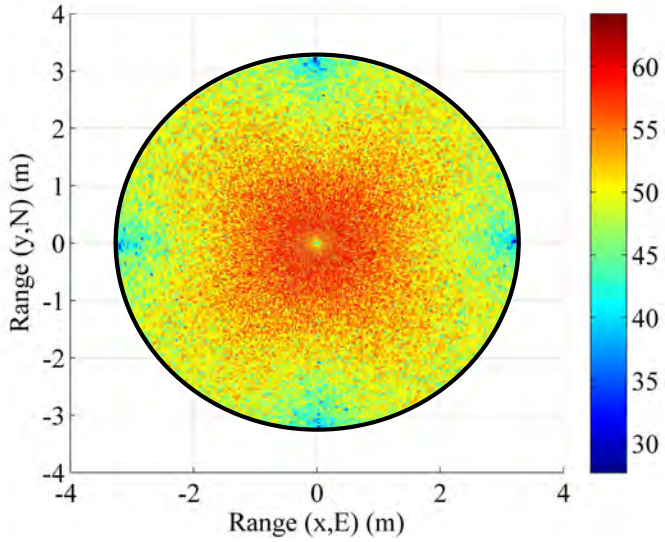

Figure 3.12. Tri-orthogonal, or 3 × 3, Rayleigh fading channel capacity ($bps_{(1\ Hz)}$), or spectral efficiency. Simulated results are presented in a FoV format for all receive antenna orientations and, by extension, all system orientations. The system operates with an operating frequency of 60 GHz, a transmit power of 40 dBm, a bandwidth of 7 GHz, and a system noise temperature of 290 K. The propagation distance at the FoV centre is 1 m, corresponding to a close proximity wireless personal area network (WPAN), while a spherical radius of 6 m is employed for receive antenna displacement over a sphere. Polarisation modes $\hat{\mathbf{r}}$ and $\hat{\boldsymbol{\theta}}$ are redundant at the FoV centre, although this redundancy is mitigated by the nature of the Rayleigh fading channel.

to redundancy of the third orthogonal unit dipole pair, or $\hat{\mathbf{r}}\hat{\boldsymbol{\theta}}$, at this point and is most prominent in the AWGN channel. In an absence of a scattering mechanism, any propagating signal from unit dipole $\hat{\boldsymbol{\theta}}$ cannot be reflected into this region, nor can unit dipole $\hat{\mathbf{r}}$ receive signals that are incumbent upon it end on. As the 2 × 2 system exhibits an approximate doubling of capacity over that of the 1 × 1 system and the FoV centre is where the 2 × 2 capacity is at a maximum, this small capacity disadvantage is seen as a reasonable trade-off to make for increased throughput and consistency over the majority of the FoV, known as orientation robustness. In the Rayleigh fading channel, this disadvantage is mitigated by the increased probability of propagation between two perfectly misaligned signal polarisation unit vectors in a rich scattering environment. It is of note that in Figure 3.8, the capacity disadvantage is not seen for the 3 × 3 system. This is attributable to an average of capacity being obtained from orthogonal azimuthal

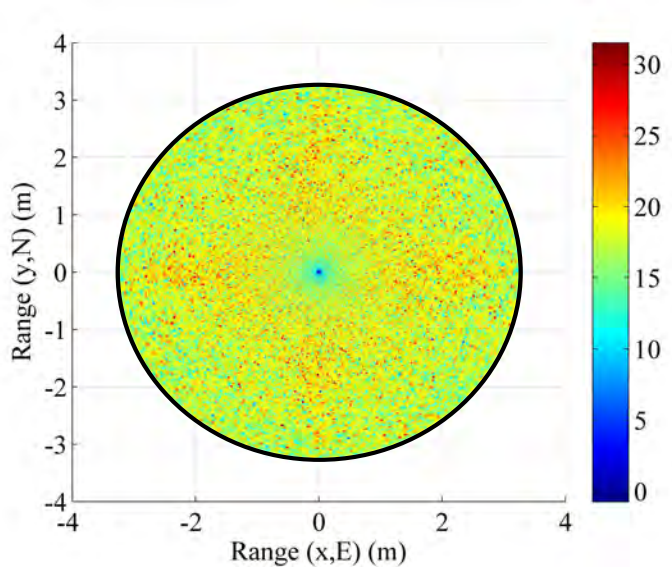

Figure 3.13. Capacity advantage ($bps_{(1\ Hz)}$), or spectral efficiency advantage, of a tri-orthogonal, or 3 $\times$ 3, system over that of a dual-polarised, or 2 $\times$ 2, system in a Rayleigh fading channel. Simulated results are presented in a FoV format for all receive antenna orientations and, by extension, all system orientations. The system operates with an operating frequency of 60 GHz, a transmit power of 40 dBm, a bandwidth of 7 GHz, and a system noise temperature of 290 K. The propagation distance at the FoV centre is 1 m, corresponding to a close proximity wireless personal area network (WPAN), while a spherical radius of 6 m is employed for receive antenna displacement over a sphere. At the FoV centre, redundancy of polarisation modes $\hat{\mathbf{r}}$ and $\hat{\mathbf{o}}$ provides a slight decrease in capacity performance of the tri-orthogonal system when compared with the dual-polarised system. The area of inferior performance is smaller than that observed in the AWGN channel, due to the nature of the Rayleigh fading channel. The tri-orthogonal arrangement is observed to provide enhanced capacity over the majority of the FoV, when compared with the dual-polarised system.

angle positions incrementally close to the exact FoV centre. Considering the orthogonal azimuthmal angle positions in Figures 3.14 and 3.15, we observe that, although the dip in capacity for the 3 $\times$ 3 system is prevalent in both instances, capacity does not fall below that of the 2 $\times$ 2 system.

- capacity for the 3 $\times$ 3 system in an AWGN channel is seen to be highest at four offset positions approximately 10° off-centre and at 45°, 135°, 215° and 305° azimuth. This is most clearly observed in Figure 3.10. At these points, a tripling of capacity compared to the 1 $\times$ 1 system, with capacity approaching the 3 $\times$ 3 Shannon capacity limit, is observed. This is suggestive of orientation robustness

even in the absence of a scattering mechanism, this environment being typically prevalent at mmWave frequencies.

- in a Rayleigh fading channel, capacity is observed to increase through inclusion of a third orthogonal unit dipole over the majority of the FoV. This is observed in Figure 3.13. An approximate tripling of capacity, with reference to the 1×1 case, is observed for all positions around the FoV centre, with capacity approaching the 3×3 Shannon capacity limit in Figure 3.12. This high capacity zone is more pronounced than for the AWGN channel, this being due to the increased probability of propagation between two perfectly misaligned signal polarisation unit vectors in a rich scattering environment. The capacity disdavantage at the FoV centre, observed in Figures 3.12 and 3.13, is once again observed in Figures 3.14 and 3.15, at azimuthal angles of θ_T of 0° and 90° respectively.

- the channel capacity advantage at the FoV centre, as observed in a Rayleigh fading channel, when compared to an AWGN fading channel, increases with increasing path distance, or decreasing average SNR per receiver branch, before levelling out. This is shown in Figure 3.16. The rich scattering environment is observed to be more beneficial for lower average SNR per receiver branch values.

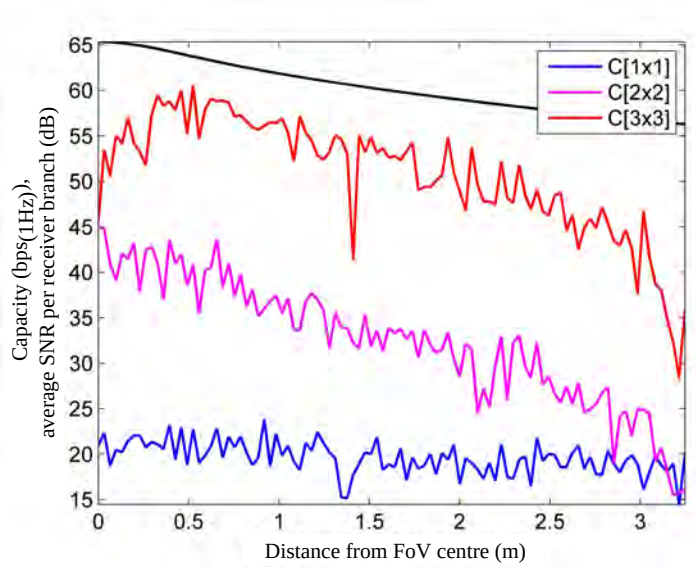

Figure 3.14. Rayleigh fading channel capacity ($\text{bps}_{(1\text{ Hz})}$), or spectral efficiency, profile at $\theta_T = 0^\circ$ for uni-polarised, dual-polarised and tri-orthogonal systems. This diagram represents system capacity observed as the arrangement of orthogonal half-wavelength dipoles at the receiver are displaced on the sphere of radius 6 m from the FoV centre, or alignment with the positive a-axis, in the positive c-axis direction in Figure 3.4 to the FoV edge. The 1×1, or uni-polarised system considers propagation between the dipole pair, or polarisation modes, $\hat{\mathbf{p}}$ and $\hat{\mathbf{m}}$. The 2×2, or dual-polarised system, considers propagation using dipoles, or polarisation modes, $\hat{\mathbf{p}}$, $\hat{\mathbf{q}}$ at R and $\hat{\mathbf{m}}$, $\hat{\mathbf{n}}$ at T. The 3×3, or tri-orthogonal system considers propagation using dipoles, or polarisation modes, $\hat{\mathbf{p}}$, $\hat{\mathbf{q}}$, and $\hat{\mathbf{r}}$ at R and $\hat{\mathbf{m}}$, $\hat{\mathbf{n}}$, and $\hat{\mathbf{o}}$ at T. The average SNR per receiver branch as a function of distance from the FoV centre is also shown.

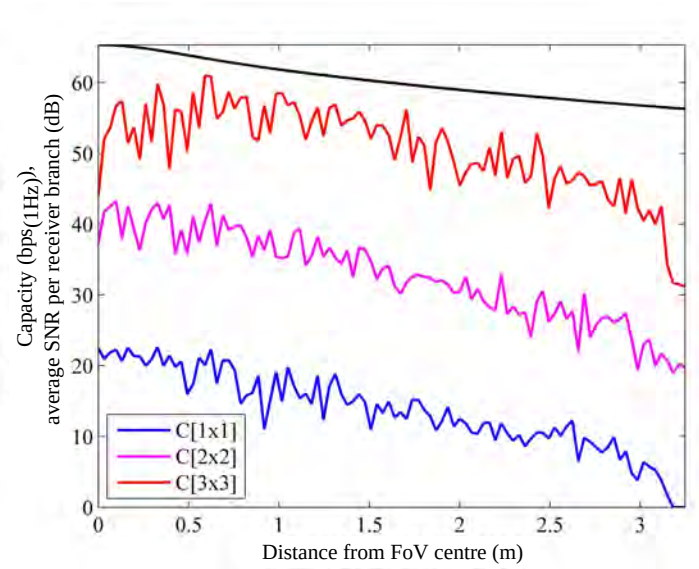

Figure 3.15. Rayleigh fading channel capacity ($bps_{(1\ Hz)}$), or spectral efficiency, profile at θ_T = 90° for uni-polarised, dual-polarised and tri-orthogonal systems. This diagram represents system capacity observed as the arrangement of orthogonal half-wavelength dipoles at the receiver is displaced on the sphere of radius 6 m from the FoV centre, or alignment with the positive a-axis, in the positive c-axis direction in Figure 3.4 to the FoV edge. The 1 × 1, or uni-polarised system, considers propagation between the dipole pair, or polarisation modes, $\hat{\mathbf{p}}$ and $\hat{\mathbf{m}}$. The 2 × 2, or dual-polarised system, considers propagation using dipoles, or polarisation modes, $\hat{\mathbf{p}}$, $\hat{\mathbf{q}}$ at R and $\hat{\mathbf{m}}$, $\hat{\mathbf{n}}$ at T. The 3 × 3, or tri-orthogonal system, considers propagation using dipoles, or polarisation modes, $\hat{\mathbf{p}}$, $\hat{\mathbf{q}}$, and $\hat{\mathbf{r}}$ at R and $\hat{\mathbf{m}}$, $\hat{\mathbf{n}}$, and $\hat{\mathbf{o}}$ at T. The average SNR per receiver branch as a function of distance from the FoV centre is also shown.

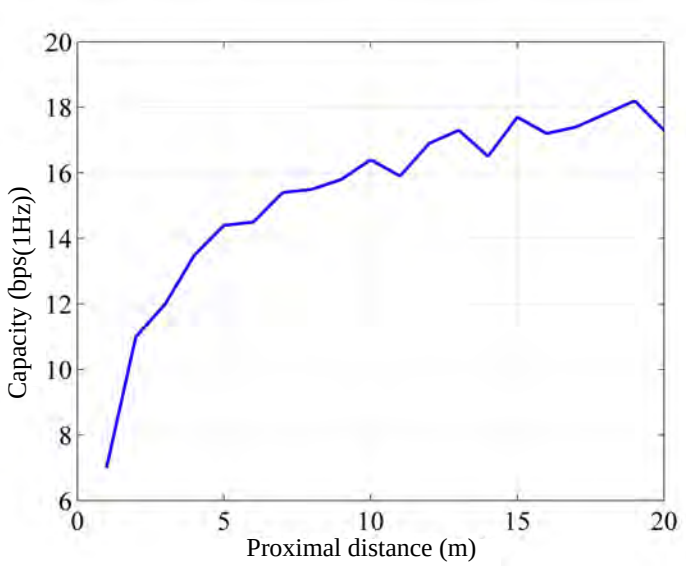

Figure 3.16. Capacity advantage ($bps_{(1\ Hz)}$), or spectral efficiency advantage, of a rich scattering environment such as a Rayleigh fading channel over that of a AWGN fading channel. The tri-orthogonal antenna arrangement at R is in perfect alignment with the tri-orthogonal antenna arrangement at T. As such, polarisation mode $\hat{\mathbf{p}}$ is aligned with the positive b-axis, polarisation mode $\hat{\mathbf{q}}$ is aligned with the positive c-axis, and polarisation mode $\hat{\mathbf{r}}$ is aligned with the positive a-axis in Figure 3.4. The capacity observed in a rich scattering Rayleigh fading channel compared to the capacity observed in a AWGN channel, devoid of scatterers, is shown for propagation at the FoV centre, or along the negative a-axis, as a function of proximal distance. The proximal distance is shown in Figure 3.3 as d.

3.4 Chapter Summary

The analysis provided in this chapter suggests that orientation robustness and overall increased capacity performance for communication at 60 GHz (Rappaport *et al.* 2011, University of South Wales Accessed: 2015) is provided over a majority of a FoV by inclusion of a third orthogonal dipole at both transmitter and receiver. For a wireless terrestrial system operating at mmWave frequencies, where free space path loss and transmit power capability may restrict operating range compared to operation at more conventional lower frequencies, and in the extreme case of an absence of channel scattering mechanism, multipath effects do not assist propagation. At lower RF and microwave frequencies, the advantage of a rich scattering environment is often included in references that consider the benefits of MIMO operation. Analysis is often limited to perfect alignment, or a few specific orientations. The presented simulations suggest that a third orthogonal dipole provides orientation robustness and improved capacity performance, even in the absence of a channel scattering mechanism. A small capacity disadvantage is noted at the FoV centre, where the 2×2 system provides optimal signal transfer, but is seen as a permissible trade-off for improved orientation robustness and overall capacity performance.

The simulated results presented here are based on an analysis of link geometry in three dimensions, together with comparative modelling at a FoV centre, using uni-polarised, dual-polarised and tri-orthogonal arrangements, and two sets of operational parameters. Good agreement is found, through this comparison, with both simulated and measured results from previous references.

With a phase-centred design avoiding pattern distortion in the far-field, and through the application of phased feeding techniques, beam steering of antenna radiation patterns becomes possible. The capacity over the FoV may in effect be adjusted through superposition of individual dipole radiation patterns, resulting in a maximum at a specific FoV location where the receiver exists. In addition, matrices may be added to the existing channel matrix that describe near-field antenna effects, such as correlation and mutual coupling effects. Correlation reduces MIMO performance, as diversity is reduced (Turkmani *et al.* 1995, Gesbert *et al.* 2003, Goldsmith 2005, Sirianunpiboon *et al.* 2009). Mutual coupling distorts radiation patterns and reduces both polarisation and pattern diversity, and so MIMO performance (Svantesson and Ranheim 2001, Janaswamy 2002, Fletcher *et al.* 2003, Wallace and Jensen 2004). In this

chapter, a fundamental approach highlighting the importance of polarisation diversity is assumed. Phased feeding techniques are not applied, no correlation effects are assumed (Turkmani *et al.* 1995, Gesbert *et al.* 2003), nor mutual coupling between polarisations, due to a tri-orthogonal arrangement (Zou and Fumeaux 2011). The model does not take relative transmitter-receiver velocity into account, but rather demonstrates the effect of antenna misalignment on system performance, and a method of mitigating against it.

In a typical environment at mmWave frequencies, applications of orientation robustness through tri-orthogonality range from very short-range personal communications, such as WPAN devices, to implementation of the IEEE (802.11ad) initiative at 60 GHz (Institute of Electrical and Electronics Engineers Accessed: 2015), an integral part of a tri-band wireless communications solution.

In Chapter 4, attention is turned towards satellite systems. Ionospheric effects on electromagnetic signal propagation are introduced through modelling, and these effects are used in Chapter 5 to model signal reception enhancement due to inclusion of a third orthogonal polarisation mode at the receiver.

Chapter 4

Faraday Rotation and Path Delay in the Ionosphere

AN electromagnetic wave propagating through the ionosphere is subject to path delay and the depolarising effect of Faraday rotation, both of which are dependent on global position and link geometry. These effects introduce error and consequently reduce the range resolution of remote sensing polarimetric measurements. Satellite-to-ground communications may be adversely altered by these effects so as to inhibit signal reception. The work presented here introduces a simple vectorised model for a large-field-of-view, low-Earth-orbit satellite system that yields Faraday rotation and path delay according to global position and geometric parameters.

Comparison is made with current models, through simulation of Faraday rotation and path delay. The presented work may extend the range over which Faraday rotation and path delay estimation is reliable. The work presented forms part of a large-field-of-view, low-Earth-orbit satellite model exploiting MIMO polarimetry in three dimensions.

4.1 Introduction

Faraday rotation and path delay are the two principle effects that reduce the effectiveness of remote sensing methods and systems performance of satellite communications (International Telecommunications Union (ITU-R) 1998). Range resolution of synthetic aperture radar (SAR) systems has been shown to adversely affect data obtained via remote sensing (Freeman and Saatchi 1998, Wright *et al.* 2003). Data and voice signals may be distorted by these effects so as to render the propagation channel inoperative. Polarimetric systems may make use of compensation techniques to offset these effects. Noise induced bias on Faraday rotation measurements may be estimated and compensated if the system noise and averaging scattering signature of an observed surface is known. Estimates and fittings may be applied as an enveloping technique according to the signal to noise ratio (SNR) and as such may not take account of the subtleties of the components that produce these detrimental effects (Meyer and Nicoll 2008).

In this thesis, path delay is used to refer to the less common term of dispersion delay, a first order ionospheric effect due to propagation through a dispersive medium. Typically, its effect may restrict accuracy of a GPS satellite position solution to an order of 10 m, and by so doing is two orders of magnitude greater than a second order term, and three orders of magnitude greater than a third order term for a signal propagating along a zenith path (Klobuchar 1996, Kaplan and Hegarty 2005, Misra and Enge 2006, Morton *et al.* 2009).

The dispersion is a result of the magneto-ionic effect (Shkarofsky 1961, Budden 1965) whereby a plane polarised LP signal or characteristic wave may be considered as propagating as an ordinary (O) wave mode and extraordinary (X) wave mode according to the localised ionospheric parameters in which it finds itself (Booker 1949, Ratcliffe 1972, Budden 1985). Typically, these wave modes are elliptically polarised, with the same axial ratio and orientation in space. These modes may be treated as approximately orthogonal in nature, with electric vectors rotating in opposite directions (Ratcliffe 1972, Budden 1985). The polarisation ellipses are less elongated as signal operating frequency increases. With their resultant being the signal or characteristic wave, their individual interactions with the ionosphere may cause the characteristic wave to rotate about the propagation vector as a function of propagation direction through the local ionosphere, and as a function of local ionospheric parameters such as terrestrial magnetic field and ionspheric electron density. This is Faraday rotation, and for a 850 MHz signal may cause a loss of 10 dB in received signal power in the instance

of LP signal transmission and aligned transmit and receive antennas (Mazda 2014). It is intuitive to consider that the more a signal propagating along a path is investigated at distinct points along its trajectory, the more the impact of ionospheric effects on it is likely to be accurate.

The terrestrial magnetic field vector, $\mathbf{b}$, and plasma density, n_e, are both functions of height as well as latitude and longitude. At a particular (latitude, longitude, height), or (L, l, h) position, they are time-varying. Their values may be determined through simulation and measurement (Maus *et al.* 2010, National Oceanic and Atmospheric Administration Accessed: 2014). Indeed, Faraday rotation may be determined through measurement, this being dependent on the satellite operating frequency and orbit (Le Vine *et al.* 2010, Le Vine and Utku Accessed: 2013). A simple vector-based estimation of Faraday rotation and path delay, taking into account the principle components causing these effects, potentially acts as a useful basis for constructing a model that determines these effects for a unique global position and geometry.

The ionosphere is typically given as a region of atmosphere beginning at a height of 50 km and extending into the magnetosphere. Yet, even this fundamental definition remains quantitatively undefined (Smith *et al.* 2008). Electromagnetic signals propagating through this region are subject to unwanted interaction with ionised particles (Kelley 2009). These ionised particles depolarise a propagating signal as well as introduce a propagation or path delay on it. These effects are dependent on signal frequency, atmospheric electron content and terrestrial magnetic field, themselves being dependent on time and global position, and link geometry within the satellite FoV (Freeman 2004, Afraimovich *et al.* 2013). In the instance of a low-Earth-orbit (LEO) satellite operating with a large-FoV, link geometry is additionally time-varying due to LEO relative movement. Coupled with low elevational angles, this means that any interaction with a ground receiver may be subject to periods of link failure. A large-FoV, in this instance, is defined relative to the spatial scale on which the ionospheric phase is approximately linear. This scale structure is subject to temporal and spatial variation (Spencer *et al.* 2004).

Faraday rotation (Fowles 1989), ψ_{FR}, and path delay (Roddy 2006), ζ, affect line-of-sight (LoS) transmission and are more pronounced as transmission frequency decreases. Their effects may be given in many forms (International Telecommunications Union (ITU-R) 1998, Yueh 2000, Hecht 2001, Freeman 2004, Le Vine and Utku Accessed: 2013). Propagation through the ionosphere may introduce multipath, typically

in the form of scintillations, instrument delays, and noise; the latter being a particular problem for detection of weak signals in radioastronomy (Kooi *et al.* 2014). For a more comprehensive understanding of effects that may affect ionospheric signal propagation, the reader is encouraged to review the work in Ratcliffe (1972), Basu and Kelley (2008), Budden (1985), and Kelley (2009). For the model presented here, the interpretations of Jehle *et al.* (2005) are used,

$$\psi_{\mathrm{FR}} = \frac{e^3\lambda^2 \sec\alpha}{8\pi^2\epsilon_0 m^2 c^3} \int_0^h n_{\mathrm{e}}(h) b_{||}(h) dh \tag{4.1}$$

$$\zeta = \frac{e^2\lambda^2 \sec\alpha}{8\pi^2\epsilon_0 m c^2} \int_0^h n_{\mathrm{e}}(h) dh \tag{4.2}$$

where h is the perpendicular height above the Earth's surface, $b_{||}$ is the terrestrial magnetic field component parallel to the propagation unit vector, e is electronic charge, λ is propagating signal wavelength, ϵ_0 is the permittivity of free space, m is electronic mass, c is the speed of light *in vacuo*, n_{e} is the electron density at a specific location in the ionosphere, and α is an off-nadir angle that is used to account for the additional path length of a slanted path. Path delay in Equation (4.2), being a first order dispersive effect, typically affects the signal more than Faraday rotation, which is a second order dispersive effect.

Satellite channels exhibiting a large time-varying FoV of the Earth's surface, such as those encountered in global positioning systems (GPS), remote sensing, satellite broadcast and telephony in remote areas, are often compromised due to the requirement of obtaining adequate orbital height to obtain the required coverage. In the absence of highly directive methods, free space path loss is the overriding factor determining practicality of the system. Highly directive methods at the receiver require steerable antennas and adaptive processing, both of which are prone to failure. A large-FoV, such as is encountered with a LEO satellite system providing coverage to ground receivers using omnidirectional low gain antenna arrangements, engenders a large variation of components that interact over the FoV to produce inhomogeneous Faraday rotations and path delays (Kintner and Ledvina 2005, Hernàndez-Pajares *et al.* 2009, National Oceanic and Atmospheric Administration Accessed: 2014, Royal Observatory of Belgium GNSS Research Group Accessed: 2014, International GNSS Service Accessed: 2014, MIT Haystack Observatory Accessed: 2014). Generally, at frequencies below 2 GHz, these effects on transmitted signals result in significant issues which are proportional to the inverse square of the frequency, as per Equations (4.1) & (4.2).

At frequencies approaching 2 GHz, the depolarising effect of Faraday rotation is strongest during times of solar maxima, and at midday when peak solar radiation effect is observed (Freeman 2004). In addition, these effects are time-varying. In the instance of a LEO system with a large-FoV, a varying link geometry exacerbates determination of Faraday rotation and path delay.

Path length delays add phase to a received signal, and so place an unwanted offset on measured backscatter. For low frequency repeat-pass interferometry, this can cause significant problems in phase measurement comparison from successive observations, compromising spatial resolution. To compensate this offset caused by ionospheric delay, one approach is to combine measurements at two widely separated frequencies (Thompson *et al.* 2008).

In polarimetric measurements, where typically a horizontal and vertical polarisation is used, relative phase error is measured between simultaneously transmitted polarisations. One assumption made is that the differences between path lengths at horizontal and vertical polarisations can be ignored for quasi-simultaneous measurements. In Rignot (2000), for L-band measurements, Faraday rotation of up to 90° is suggested during times of high solar activity. In Wright *et al.* (2003), it is concluded that a rotation of more than 5° is enough to significantly affect recovery of geophysical parameters from SAR backscatter measurements, including polarimetric measurements.

The polarimetric estimation of Faraday rotation and path delay is complex, since the ionosphere is constantly evolving in three spatial dimensions and a temporal dimension, largely as a function of solar radiation. The effect of Faraday rotation and path delay is particularly relevant to a large-FoV, LEO satellite system, exploiting MIMO methods through a tri-orthogonal antenna arrangement. A truly three dimensional system requires a three dimensional analysis of ionospheric effects. The aim of such a system, in both a communication and polarimetric sense, is not only to provide performance comparable to current systems, where CP or DP wave propagation is used and when perfect alignment exists between transmitter and receiver, but also to provide improved performance in the instance of imperfect alignment. An increase in system performance beyond that of conventional systems is desirable at the edges of the FoV where, at low elevation angles at the ground receiver, ionospheric effects are at their strongest.

4.1 Introduction

To model ionospheric effects, an ionospheric shell is typically adopted. Generally speaking, employment of the ionospheric shell model (Mannucci *et al.* 1998) is limited to higher elevation angles and on-axis signal transfer. The shell model is based on the ionosphere being able to modelled as a thin shell around the Earth. This presents its own set of issues, and associated errors (Smith *et al.* 2008). A vectorised approach is required for low elevation angles covering off-axis propagation. In order for this to be feasible and to achieve maximum benefit, channel effects on signal transfer in any given link direction need to be modelled.

To avoid the effects of Faraday rotation, engineers traditionally employ CP wave propagation techniques, equivalent to two orthogonally polarised signals being transmitted with a phase shift of 90° separating them and their electric fields orthogonal to the direction of propagation. As a result, any depolarising effects are mitigated (Meyer and Nicoll 2008, Burgin and Moghaddam 2014). To avoid the effects of path delay, two signal frequencies may be employed to measure a time delay on each signal that provides an approximate total electron content (TEC) value to correct for ionospheric aberrations along a signal path (Jehle *et al.* 2005). Over a particular region, TEC values may then be mapped using GPS data (Komjathy 1997, Hernàndez-Pajares *et al.* 1999). However, all TEC mesurements are subject to some associated error, as no absolute TEC measurement is possible (Ciraolo *et al.* 2006, Minter *et al.* 2007). By combining TEC measurements, such as those from lightning detectors (FORTE) and ocean surface monitors (TOPEX), improved accuracy of TEC measurements using a differential analysis may be obtained (Araujo-Pradere *et al.* 2007), primarily as a result of using non-identical propagation frequencies. Phase delay may provide information on TEC variations in time and satellite positions (Erickson *et al.* 2001) but is not typically used to calculate absolute TEC values, as it is subject to phase unwrapping ambiguities. An interesting exception of study does however exist (Smith 2004). A path of interest is often taken in isolation and the geometry of the satellite position is not fully taken into account. This approach is problematic for a large-FoV LEO system, as the three dimensional nature of the ionosphere should be considered (Minter *et al.* 2007).

A downside of CP wave transmission is that a proportion of transmit power is effectively wasted to guarantee reception. In the case of a LP receiver, the loss would be 3 dB in the perfectly aligned case. For RHCP transmission, and LHCP reception, the loss is theoretically infinite. Taking the case of an antenna in isolation providing CP transmission in the nadir direction, a power transmission maximum is centred at the

nadir position, where the shortest path length and thus least amount of ionosphere to traverse in the FoV also exist. As the ground receiver deviates from the satellite nadir position, so polarisation of signal reception is no longer of CP form, and polarisation loss becomes an issue. Wave propagation in the unit vector direction to the ground receiver is now of EP form, and finally of LP form when the ground receiver is at the satellite horizon. At the FoV edge, a power reduction of 3 dB, or 50% of the signal, may become critical in providing an intelligible signal at the ground receiver, particularly as the effects of shadowing are more pronounced at lower elevation angles (Lutz 1998). The problem of adequate reception is further exacerbated in the instance of a non-geosynchronous orbit such as a LEO where relative movement of ground receiver and satellite, and hence a rapidly evolving link geometry, are introduced. Although greater coverage is provided by an array of antennas aligned to provide CP transmission in slightly different link directions, since each antenna possesses a narrow beamwidth to provide optimised coverage over a small terrestrial zone, so the problem persists. For a satellite in a LEO orbit, communication with the ground receiver must be handed over rapidly between antennas, adding complexity and cost to the satellite system.

Models currently exist for the estimation of TEC, such as National Oceanic and Atmospheric Administration (Accessed: 2014) which uses solar emission data to predict terrestrial fluctuations, as well as empirical models derived from Global Navigation Satellite System (GNSS) observations (Bidaine and Warnant 2010). These may be used in conjunction with models that simulate terrestrial magnetic field strength and orientation to determine ionospheric effects (Sabaka *et al.* 2004). These may be specified by the (L, l) position with data given for a nadir path. The TEC data may be provided in slant path format. The additional propagation length encountered in a slant path is typically accounted for by the inclusion of a trigonometric secant function. Current models apply this function to a singular value of TEC and the Earth's magnetic field, at the ionospheric piercing point, for calculation of Faraday rotation along a propagation path. Measurement is often the only means to take ionospheric variation into account along a propagation path, but is unique to the operating parameters of the measurement system itself. A vectorised approach, taking into consideration the changing value of TEC and the Earth's magnetic field along the propagation path may provide improved simulated results closer to observable measurement, and not be constrained to the measuring system's operational parameters. A propagation vector varies considerably over a large-FoV and the interaction of signal with ionospheric particles varies accordingly, in addition to the fluctuations introduced through global position and

time. Over a large LEO FoV, this can lead to large variations of Faraday rotation and path delay from one ground receiver position to another. Furthermore, low elevation angles hamper measurement of Faraday rotation due to a severely reduced SNR at the ground receiver.

In the case of a satellite-to-ground system, where fast fading including multipath effects may be included as a function of elevation (Fontan *et al.* 2001) and estimated using a Ricean distribution for multiple fading channels all arriving at once, individual LoS analysis is required. A vector-based approach is seen as a viable means of estimating Faraday rotation and path delay over a large-FoV.

The model presented here forms part of a (L, l) specific, large-FoV, LEO satellite channel model incorporating MIMO polarimetry in three dimensions. Such a system offers the perspective of improved capacity performance over the FoV in its entirety, as compared to currently employed techniques. Faraday rotation and path delay are two effects requiring effective estimation if such a model is to demonstrate this benefit.

4.2 Methods

4.2.1 Link Geometry

Link geometry is given according to Ryan (2003) and Roddy (2006) and is illustrated in Figure 4.1. Relevant nomenclature is now introduced. The transmitter at the satellite shall be referred to as T with the ground receiver as R.

Link geometry is determined according to the following equations,

$$\gamma = \frac{r_{\text{plot}}}{r_{\text{e}}} \tag{4.3}$$

$$s = \sqrt{u^2 + {r_{\text{e}}}^2 - 2ur_{\text{e}}\cos\gamma} \tag{4.4}$$

$$\kappa = \arcsin\left(\frac{u}{s}\sin\gamma\right) \tag{4.5}$$

$$\alpha = \arcsin\left(\frac{u}{s}\sin\gamma\right) - \gamma \tag{4.6}$$

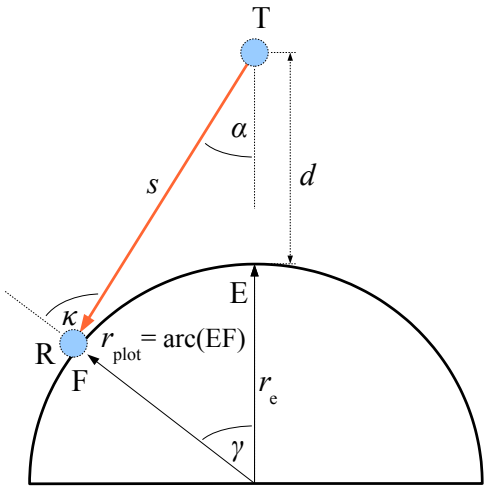

Figure 4.1. Ionospheric channel link geometry. Transmitter T is in an orbit of height d. The receiver R is positioned on a semi-circle determined by simple trigonometry. Propagation from T to R is along the path of length, s. At any FoV position, the radial distance from the FoV centre is a function of angle α or angle γ together with the radius of the Earth. The entire system is rotated about the FoV centre by 360° to develop a spherical surface. The number of concentric paths on the sphere together with the azimuthal step increment about the FoV centre is set by the user. The simulation begins at the FoV centre and works outward to the concentric circle where κ = 90°.

$$\gamma_{\max} = \arccos\left(\frac{r_e}{u}\right) \tag{4.7}$$

$$s_{\max} = \sqrt{u^2 - {r_e}^2} \tag{4.8}$$

$$\alpha_{\max} = \arcsin\left(\frac{r_e}{u}\right) \tag{4.9}$$

where r_e is the 6378 km radius of the Earth and u is $r_e + d$, d being orbit height.

Elevation at T is given by α with 0° in the nadir direction, otherwise positive. Elevation at R is given by κ with 0° in the zenith direction, otherwise positive. The azimuthal angle θ_R at R of the vector representing signal propagation $\mathbf{k}$ differs to that of the corresponding angle θ_T at T by 180°.

The receiver R is assumed to be at a distance s from T which changes according to FoV location. The FoV may subsequently be positioned, according to its centre, at any

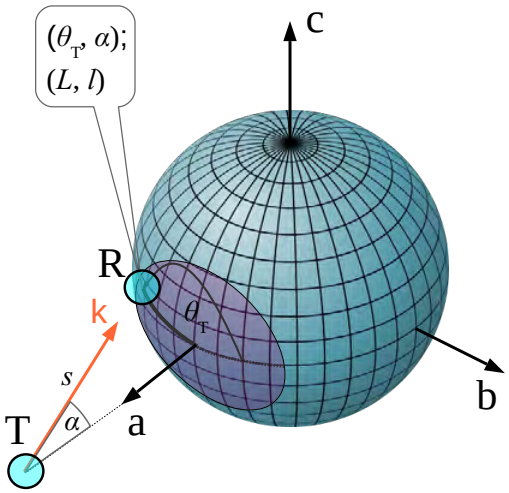

Figure 4.2. System according to specific location in NGSO ionospheric FoV. Earth-Centred Earth-Fixed (ECEF) coordinates identify the system in three dimensional space. Propagation is from satellite transmitter T to ground receiver R, along the propagation path of length, s, with the direction given by the propagation vector, **k**. Propagation to a point in the FoV is determined by α and θ_T. These angles correspond to a (latitude, longitude), or (L, l), global position. This permits the estimation of Faraday rotation and path delay as a function of global location and FoV geometry.

user specified (L_u, l_u) global position. An Earth-Centred Earth-Fixed (ECEF) coordinate system is invoked for this analysis. The a-axis is nominally aligned in a radial direction from the centre of the Earth, piercing the Earth's surface at (0°,0°). A FoV may subsequently be generated about this axis. At the FoV centre, an easterly direction $[0\ 1\ 0]^T$, where T refers to transpose, coincides with an azimuthal angle θ_T of 0°. Within the FoV, anti-clockwise rotation is deemed as positive. Figure 4.2 demonstrates the concept.

4.2.2 Latitude, Longitude and Height Determination for Faraday Rotation and Path Delay Simulation

To calculate the Faraday rotation and path delay from T to R, at a (L, l) position in the FoV, two analgous FoVs are determined. The first FoV, for vector calculation, is centred at (L_o, l_o), which is nominally set to (0°,0°) where the positive a-axis pierces

the terrestrial sphere in Figure 4.2. The second FoV, for determination of terrestrial magnetic field vector **b** and TEC at a (L, l) position in the FoV, is centred at (L_c, l_c).

The number of positions within the FoV are user defined through increments of the azimuthal and off-nadir angles, θ_T and α, respectively. Global positioning through (L, l) doublets for these positions may be given by Equations (4.10) & (4.11) (Movable Type Ltd. Accessed: 2014). These equations are based on the Haversine formula giving great-circle distances between two points on a sphere from their longitudes and latitudes (Smart 1960). Each (L, l) point may be determined within both FoVs through their corresponding (θ_T,α) parameters as,

$$\begin{aligned} L &= \arcsin\{\sin(L_u)\cos(r_{plot}/r_e) \\ &\quad + \cos(L_u)\sin(r_{plot}/r_e)\cos(\theta_b)\} \end{aligned} \tag{4.10}$$

$$\begin{aligned} l &= l_u + \text{atan}_2\{\sin\theta_b \sin(r_{plot}/r_e)\cos(L_u), \\ &\quad \cos(r_{plot}/r_e) - \sin(L_u)\sin(L)\} \end{aligned} \tag{4.11}$$

where (L_u, l_u) is a user-defined FoV centre, which may be replaced by (L_o, l_o) and (L_c, l_c) in each of the two FoVs being considered, and θ_b is a bearing angle from a FoV centre and is related to θ_T by,

$$\theta_b = \left|2.5\pi - \theta_T, 2\pi\right|. \tag{4.12}$$

The function $\text{atan}_2(\Delta_1, \Delta_2)$ in this instance is given as,

$$\text{atan}_2(\Delta_1,\Delta_2)=\begin{cases}\arctan(\frac{\Delta_1}{\Delta_2}) & (\Delta_2\succ 0)\\ \arctan(\frac{\Delta_1}{\Delta_2})+\pi & (\Delta_1\succeq 0,\Delta_2\prec 0)\\ \arctan(\frac{\Delta_1}{\Delta_2})-\pi & (\Delta_1\prec 0,\Delta_2\prec 0)\\ +\pi/2 & (\Delta_1\succ 0,\Delta_2=0)\\ -\pi/2 & (\Delta_1\prec 0,\Delta_2=0)\\ \text{undefined} & (\Delta_1=0,\Delta_2=0)\end{cases}. \tag{4.13}$$

Height h along the propagation path is determined as,

$$\begin{aligned} h &= (r_e+d)\\ &\quad -\left\{\left\{r_e\{1-\cos\gamma_{i_{FR}}\}+d\right\}\times\frac{(k_{FR}-1)}{(i_{FR}-0.999)}\right\}\\ &\quad -r_e\cos\gamma_{k_{FR}}. \end{aligned} \tag{4.14}$$

In Equation (4.14), i_{FR} is the i^{th} incremental position in terms of α from the nadir and k_{FR} is a variable running from the nadir position along a constant azimuthal path, θ_T, to the i^{th} incremental position of α. The curvature of the Earth, important in the instance of a large-FoV, is included in the model. Figure 4.4 illustrates the concept. Current models, such as those in Jehle *et al.* (2005) and Le Vine and Utku (Accessed: 2013), opt for a flat Earth approximation where the curvature of the Earth is not considered. Propagation to an FoV (L,l) doublet position is along a path with a constant azimuthal angle, θ_T. A propagation unit vector $\hat{\mathbf{k}}$ from T to R is determined for all positions in the FoV centred at (L_o,l_o) by,

$$\hat{\mathbf{k}}=\begin{bmatrix}-\cos\alpha\\ \cos\theta_T\sin\alpha\\ \sin\theta_T\sin\alpha\end{bmatrix}. \tag{4.15}$$

The simulation computes the set of $\hat{\mathbf{k}}$ and all investigated effects starting at the FoV centre, (L_o,l_o), or nadir position at θ_T=0°. The simulation refers to each FoV position

in turn through positive increments of θ_T which, after completion of one circle, moves radially outward by an increment of the off-nadir angle, α.

Consider transmission to a receiver position, R1. The introduction of h creates (L, l, h) triplets where h is calculated at each (L, l) doublet position along the unique path, given by $\hat{\mathbf{k}}_{R1}$, to the receiver position, (L_{R1}, l_{R1}). Once the accompanying effects of Faraday rotation and path delay have been computed for propagation from T to R1, the simulation moves to position R2. New values of h must be assigned to each (L, l) position along a propagation path each time a new receiver position is considered. Receiver positions on the same concentric circle utilise the same values of h along the path.

The values of h are used in the determination of the Earth's magnetic field vector and TEC and this is considered shortly.

Along a propagation path from T to R, globally referenced positions are passed through at progressively reducing heights with each set of encountered (L, l, h) triplets subsequently introducing an accompanying set of magnetic field vector and TEC data determined by values obtained according to the (L, l) positions in the FoV centred at (L_c, l_c). This data is then used to generate the estimates of Faraday rotation and path delay from T to (L, l) positions of R in the FoV centred at (L_o, l_o).

4.2.3 Magnetic Field Vector and Total Electron Content

Models of terrestrial magnetic fields include the International Geomagnetic Reference Field (IGRF) model, the World Magnetic Model (WMM), the British Geological Survey Global Magnetic Model (BGSGMM), and the Model of the Earth's Magnetic Environment (MEME), and the International Reference Ionosphere model (IRI). The two most referenced of these are the IGRF model and the WMM. The WMM is a predictive-only model and is valid for a quinquennial epoch, or five year period, at the time of simulation being 2010–2015. The IGRF is retrospectively updated and the update during simulation, IGRF-11, is valid for the years 1900–2015. The WMM is used extensively for navigation and in attitude and heading referencing systems by the UK Ministry of Defence, the US Department of Defense, the North Atlantic Treaty Organization and the International Hydrographic Organization. It is available in the Matlab programming environment, and so may be readily interfaced with proprietary coding. Determination of the Earth's magnetic field vector at a triplet position in this research is according

to the WMM (Maus *et al.* 2010). Each magnetic field unit vector may be orientated into the ECEF coordinate system beginning with an ECEF northerly pointing unit vector, $\hat{\mathbf{n}}_{0,0}$, or $[0\ 0\ 1]^{\mathrm{T}}$ representing the Earth's magnetic field at (0°,0°), in the FoV centred at $(L_{\mathrm{o}}, l_{\mathrm{o}})$. This is rotated by the declination, δ, and inclination, ι, of the magnetic field vector at a specific (L, l, h) triplet position for a given height. This triplet position is determined according to (L, l) positions, found through Equations (4.10) & (4.11), in the FoV centred at $(L_{\mathrm{c}}, l_{\mathrm{c}})$, and application of Equation (4.14), allowing rotation of $\hat{\mathbf{n}}_{0,0}$ in the FoV centred at $(L_{\mathrm{o}}, l_{\mathrm{o}})$ according to,

$$\mathbf{R}_{\delta} = \begin{bmatrix} 1 & 0 & 0 \\ 0 & \cos\delta & \sin\delta \\ 0 & -\sin\delta & \cos\delta \end{bmatrix} \tag{4.16}$$

$$\mathbf{R}_{\iota} = \begin{bmatrix} \cos\iota & 0 & -\sin\iota \\ 0 & 1 & 0 \\ \sin\iota & 0 & \cos\iota \end{bmatrix}. \tag{4.17}$$

Convention gives δ as positive in an easterly direction and ι as positive in a downward direction. For simplicity, vector rotations take place in the FoV centred at $(L_{\mathrm{o}}, l_{\mathrm{o}})$. Each vector may then be rotated to its (L, l) position in this FoV through Equations (4.18) & (4.19),

$$\mathbf{R}_{\mathrm{L}} = \begin{bmatrix} \cos(L) & 0 & -\sin(L) \\ 0 & 1 & 0 \\ \sin(L) & 0 & \cos(L) \end{bmatrix} \tag{4.18}$$

and

$$\mathbf{R}_{\mathrm{l}} = \begin{bmatrix} \cos(l) & -\sin(l) & 0 \\ \sin(l) & \cos(l) & 0 \\ 0 & 0 & 1 \end{bmatrix}. \tag{4.19}$$

The terrestrial magnetic field unit vector at a (L, l, h) triplet position in the FoV centred at $(L_{\mathrm{c}}, l_{\mathrm{c}})$ may thus be aligned in the analgous FoV centred at $(L_{\mathrm{o}}, l_{\mathrm{o}})$ as,

$$\hat{\mathbf{b}}_{\mathrm{L,l,h}} = \mathbf{R}_{\mathrm{l}}\mathbf{R}_{\mathrm{L}}\mathbf{R}_{\delta}\mathbf{R}_{\iota}\hat{\mathbf{n}}_{0,0}. \tag{4.20}$$

Magnetic magntitudes given by Maus *et al.* (2010) are then attributed to each triplet position.

Determination of the TEC value at a (L, l) position in the FoV centred at $(L_{\mathrm{o}}, l_{\mathrm{o}})$, used for vector analysis, is performed according to data obtained from the analgous (L, l) position in the FoV centred at $(L_{\mathrm{c}}, l_{\mathrm{c}})$. Maps of TEC provide valuable information regarding space weather events, user navigation improvement, and provide predictive possibilities for ionospheric parameters based on empirical modelling (Coster and Komjathy 2008). For the proposed model in this chapter, TEC data is given by the Coupled Thermosphere Ionosphere Plasmasphere Electrodynamics (CTIPe) model (National Oceanic and Atmospheric Administration Accessed: 2014). The assimiliation of TEC data may be made using ground-based or space-based GPS measurement (Wang *et al.* 2004). Filtering techniques may then provide quantitative estimation of ionospheric parameters (Pi *et al.* 2003, Hajj *et al.* 2004). Although the data is coarse with resolution of (2°,18°) and is renewed every 10 minutes, the CTIPe model is a physics-based model that aims to compete with empirical models during quiescent periods while providing more reliable global TEC value forecasts during periods of geomagnetic disturbance. In addition, it is a truly global model, and is not limited to certain geographical zones, as are many of its contemporaries, such as the IGS VTEC maps provided by the GNSS service (Hernàndez-Pajares *et al.* 2009). Each simulation run is generally ahead of realtime by 10–20 minutes, as it uses Advanced Composition Explorer (ACE) data for inputs, and so offers advantages over realtime empirical data offered by GPS. In order to produce a smooth interpretation of TEC for each (L, l) doublet in the FoV, bilinear interpolation is invoked. This is pertinent as most (L, l) positions do not align with the global positions used in the data collection performed in National Oceanic and Atmospheric Administration (Accessed: 2014).

The total electron content for a (L, l) nadir path is determined by the multiplication of a TEC value given by National Oceanic and Atmospheric Administration (Accessed: 2014) with a TECU or TEC unit defined globally as 10^{16} electrons per m^2 (Jehle *et al.* 2005). The resultant path value, VTEC, refers to the number of free electrons in a vertical column of cross section 1 m^2 along the nadir path at a specified (L, l) position and may be given as,

$$\text{VTEC} = \int_{s_{(\text{nadir})}} n_e ds_{(\text{nadir})} \tag{4.21}$$

where n_e refers to the electron density along the nadir path (Jehle *et al.* 2009).

Variability of interaction between ionised particles and an electromagnetic signal propagating along a path between transmitter and receiver is accounted for by the introduction of an interaction length over which the magnetic field vector and TEC, respectively (L, l, h) and (L, l) specific, interact with the signal. In Figure 4.4, s is assumed to be 1500 km. The FoV position is at the end of a constant azimuthal or θ_T trajectory path, at a position specified by α. For simplicity, this off-nadir angle shall be known as α_3.

Three interaction lengths, shown as purple, blue and green zones, are delineated in Figure 4.4. Each length is 500 km and attributed to each of the three (L, l) doublet positions along the path. Over an interaction length, the TEC is given according to the accompanying (L, l) position. The TEC for an interaction length requires attribution of the height, given by Equation (4.14), in order to determine the electron content at a (L, l, h) triplet position.

An ionospheric scaling factor is calculated by introducing an ionospheric layer profile covering 50 km to 1000 km in altitude above the Earth (Montenbruck and Gill 2012). The proposed model differs from the thick-shell model, which assumes a simplified Chapman profile of ionospheric electron distribution as a function of altitude (Mitch *et al.* 2013). This in turn contrasts with the computationally easier thin-shell model, as used in the comparison models of Jehle *et al.* (2005) and Le Vine and Utku (Accessed: 2013). Both thick- and thin-models consider on-axis, or LoS, propagation only. There has been work in this area to improve the modelling of the Chapman profile and render it more three dimensional, and so more realistic than conventional shell structures (Feltens 2007).

In this chapter and in Lawrence *et al.* (2015a), a non-simplified layered profile of electronic distribution is assumed, based on a daily solar maximum profile (Kelley 2009, University College London Accessed: 2016, University of Sheffield Accessed: 2016, Loudet Accessed: 2014), as shown in Figure 4.3. This is extended to a two state ionospheric layer profile in Chapter 5.

The profile is divided into 10 km altitude segments and an electron density is attributed to each segment. An average electronic density is calculated using these values. Certain altitudes have an electron density higher than this average, while others have

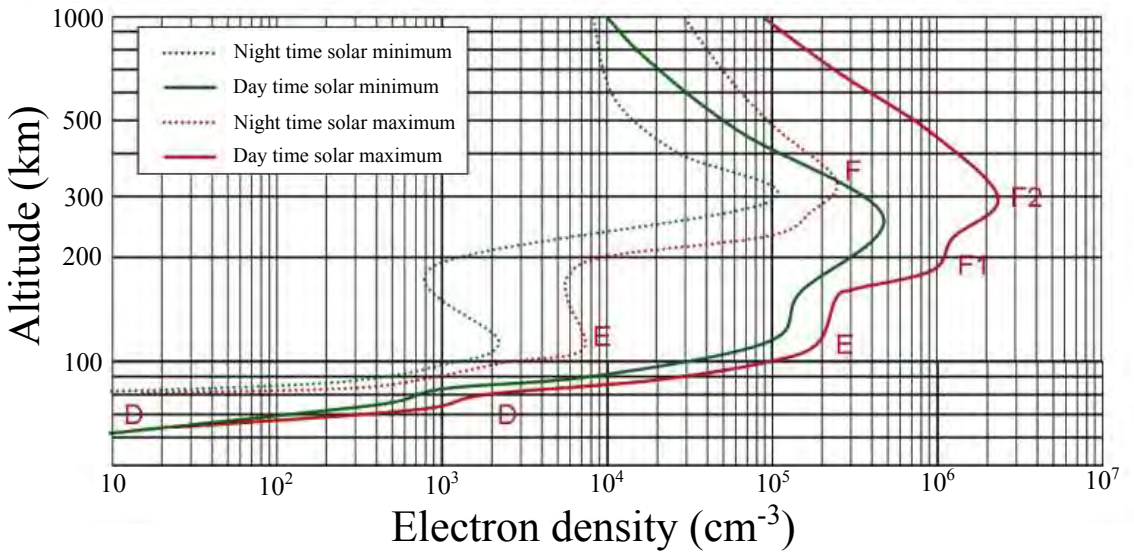

Figure 4.3. Typical ionospheric layer profile at low latitudes according to sun activity and diurnal effect. Ionospheric electrons are excited by the heating effect of the Sun, resulting in electron densities, commonly given as layers, that vary in accordance with this process. After Loudet (Accessed: 2014).

lower densities. A weighting may then be applied to each segment. The weighting is calculated by dividing the electron density in a segment by the average electron density. By treating the ionosphere in this manner, and by using multiple (L,l) dependent values of TEC and magnetic field strength, the model provides on-axis and off-axis estimates of path delay and Faraday rotation using a non-simplified approach to ionospheric distribution. Each estimate of Faraday rotation and ionospheric path delay is hence (L,l,h) specific, and so takes three dimensions into account.

As the factor is based on the electronic layer distribution and reflects how height, in addition to (L,l) position, affects the amount of Faraday rotation on a propagating signal at that point (Kelley 2009), so it may be considered as a three dimensional representation of the ionosphere. As a result, TEC becomes (L,l,h) specific for path effect calculations.

Over each interaction length along the propagation path, values of terrestrial magnetic field and TEC associated with a (L,l,h) triplet are then used in Equations (4.1) and (4.2). The resulting values from all interaction lengths are then integrated to provide an estimation of Faraday rotation and path delay for propagation from T to R at each (L,l) FoV position. Movement radially outward to the next concentric circle through

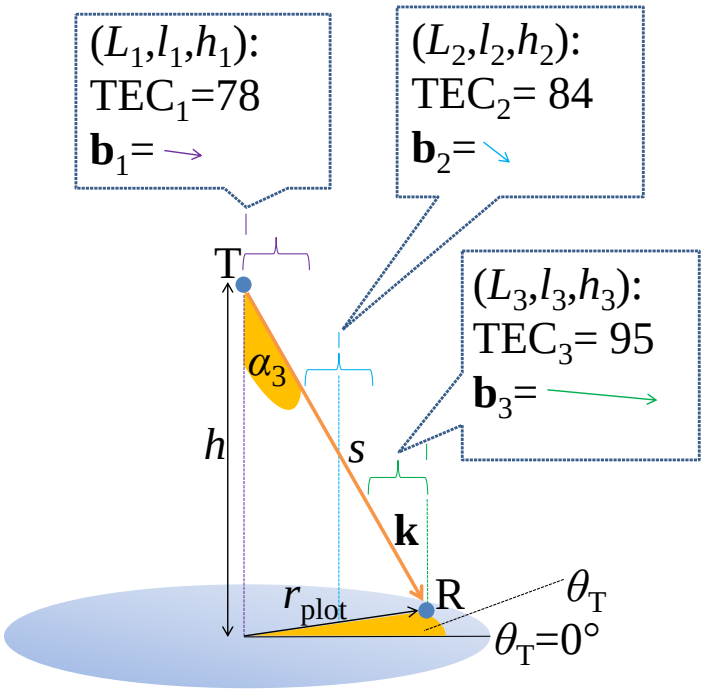

Figure 4.4. Height parameter within the ionospheric channel model. Heights h_1, h_2, and h_3 are calculated at respective FoV positions along the propagation path. Each of these FoV positions has an accompanying (L,l) reference so forming a unique (L,l,h) triplet along a propagation path of length, s, and of direction given by the unit propagation vector, $\hat{\mathbf{k}}$. Associated magnetic field and TEC data are respectively attached to each triplet along the path. Interactions between the ionosphere and the propagation vector $\mathbf{k}$ along the path at each encountered FoV position are then integrated to provide an estimate of Faraday rotation and path delay, both specific to a (L,l) FoV position where R is positioned. This is repeated for all (L,l) FoV positions.

increment of α redefines the parameters. In the case of Figure 4.4, the path is now split into four interaction lengths.

It is evident that the user is, in effect, able to control the resolution of the simulated Faraday rotation and path delay. Improved resolution would require improved TEC data resolution. Estimated errors of TEC values associated with the CTIPe model range between 1 and 12 TEC units, as compared with other estimation methods (Bilitza 2001, Jones 2008, National Oceanic and Atmospheric Administration Accessed: 2014).

Finally, the system may be seen from the perspective of the ground receiver at R or propagation from R to T. In this instance, the azimuthal angle θ_R is invoked with a propagation path determined by unit vector -$\hat{\mathbf{k}}$. A doubling of Faraday rotation occurs

for T to R followed by R to T propagation, as experienced in SAR systems (Titheridge 1972, Freeman and Saatchi 1998, Wright *et al.* 2003).

4.3 Results

Estimates are generated of path delay over the FoV, using recent TEC data acquired on 28th May 2014. The estimates generated are contrasted with those generated according to Jehle *et al.* (2005), and are shown in Figure 4.5. The date corresponds to a period of relatively high solar activity.

Estimates are generated of Faraday rotation over the FoV, using magnetic field and TEC data acquired on 15th January 2010. This date was chosen, in the absence of any specific reference date, as the positions of the north pole, south pole, and magnetic equator were readily available to the author. The date corresponds to a period of relative solar inactivity.

Northern latitudes and eastern longitudes are deemed positive, conforming to an ECEF reference system. On this date, positions of magnetic north and south pole, and magnetic equator are identified as (85°,-133°), (-64°,137°), and (-10°,-71°) respectively (Maus *et al.* 2010). The estimates generated are contrasted with those according to Le Vine and Utku (Accessed: 2013), based on published work in Le Vine and Abraham (2002), and Jehle *et al.* (2005), and are shown in Figure 4.6. The estimate of Faraday rotation in Le Vine and Utku (Accessed: 2013) is given as,

$$\psi_{\mathrm{FR}} = 6950 \cdot \mathrm{VTEC} \cdot \hat{\mathbf{b}}_{400\mathrm{km}} \cdot \hat{\mathbf{k}} \cdot \sec\ \alpha. \tag{4.22}$$

As the vectorised model presented is contrasted with references based on trigonometry, and using the same data in all model simulations, the choice of these dates is not seen as affecting the results.

Both path delay and Faraday rotation estimates of Jehle *et al.* (2005), and the Faraday rotation estimate of Le Vine and Utku (Accessed: 2013), use magnetic field and TEC data obtained at a single (L, l) position corresponding to the mid-point position of the propagation path. This type of model is described as a thin-shell ionospheric model. The shell is defined as infinitessimally thin, and is often given as being at the altitude of maximum electron density of 300–400 km. The ionospheric electron density is given as concentrated into this shell. An ionospheric piercing point is defined as

the point at which the LoS signal propagating between satellite and ground receiver pierces this shell. This point defines the (L, l) position at which TEC information is obtained, so defining first and second order effects such as path delay and Faraday rotation. A secant function may then be applied to derive an approximate value of TEC along a slanted propagation path. This model is valid for small FoVs, where neither the surrounding TEC values, magnetic field nor propagation path length vary considerably. However, the model may not operate correctly for large-FoVs, where towards the edges of the FoV these parameters may change considerably from those at the FoV centre. The angle of signal reception seen from R, shallower at the outer edges of the FoV, affects the interaction with the magnetic field, and hence the amount of Faraday rotation to be expected. A vectorised integration of these parameters, from the point of transmission from T to the point of reception at R, offers a credible approach to resolving this issue.

The magnetic field data is confined to a height of 400 km as a reference in the case of Le Vine and Utku (Accessed: 2013). No height is given in Jehle *et al.* (2005), although a single mean value lying at 400 km is suggested in the relevant reference, Wright *et al.* (2003). This height corresponds to the mid-height of the propagation path and is approaching the dense F2 electron layer. Both examples of Faraday rotation reference formulas in these models are hence based on a thin-shell representation of the ionosphere. The presented model deviates from this representation, as it takes the three dimensional structure of the ionosphere and off-axis propagation into consideration, and does not limit ionospheric parameters to a singular point at which the signal is deemed to pierce the ionosphere at 400 km. The estimates of the presented model deviate from the thin-shell model as they are calculated via integration of the varying strength of Faraday rotation and path delay to which a signal is subjected along the entire path.

An operating frequency of 1.616 GHz and orbit height of 780 km, in a region of the electromagnetic spectrum occupied by remote satellite telephony systems (Iridium Communications Inc. Accessed: 2014, Thuraya Telecommunications Company Accessed: 2016), is employed. All figures presented in this chapter make use of bilinear interpolated TEC data. The edge of the FoV is the point at which elevation at R is 0° and is orbit specific.

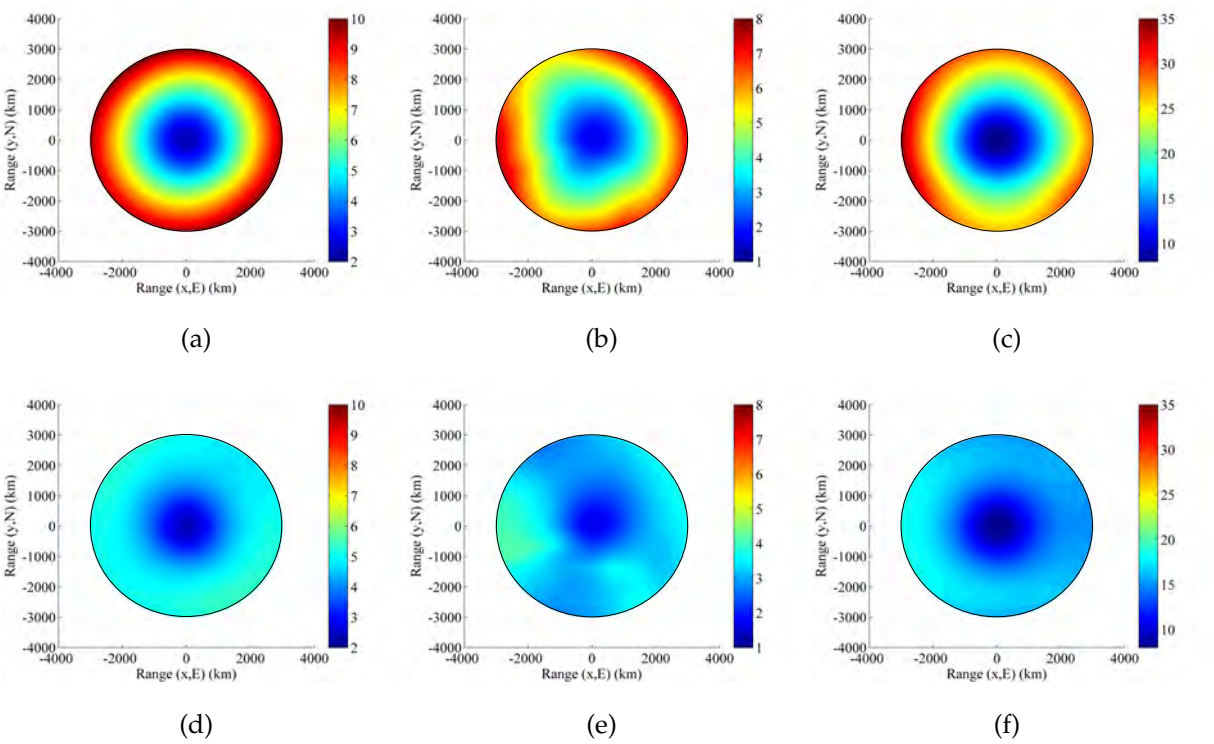

Figure 4.5. Path delay (m) estimates over the FoV (28th May 2014, frequency: 1.616 GHz, orbit height: 780 km). Rows: (1) presented model; (2) according to Jehle *et al.* (2005). Columns: (1) Magnetic North (85°,-133°); (2) Magnetic South (-64°,137°); (3) Magnetic Equator (-10°,-71°).

The vector nature of Faraday rotation is evident in Figure 4.6, as both positive and negative rotations are observed over a large extent of the FoV. This highlights the need to avoid an enveloping offset approach to this effect.

Near the nadir, all models provide similar estimates of Faraday rotation and path delay. This is as both TEC and the Earth's magnetic dipole do not change considerably for small values of α, the off-nadir angle. In effect, the additional path distance encountered as propagation moves away from the nadir is well approximated by a secant function.

However, moving out towards the FoV edge, the presented model estimates of both Faraday rotation and path delay diverge from those of Jehle *et al.* (2005) and Le Vine and Utku (Accessed: 2013). The full use of geometry in the presented model, including consideration of the Earth's curvature and replacement of trigonometrical approximation by three dimensional vector analysis, extends the FoV analysis. The assignment of (L, l, h) triplets along the path leads to estimates of both Faraday rotation and path

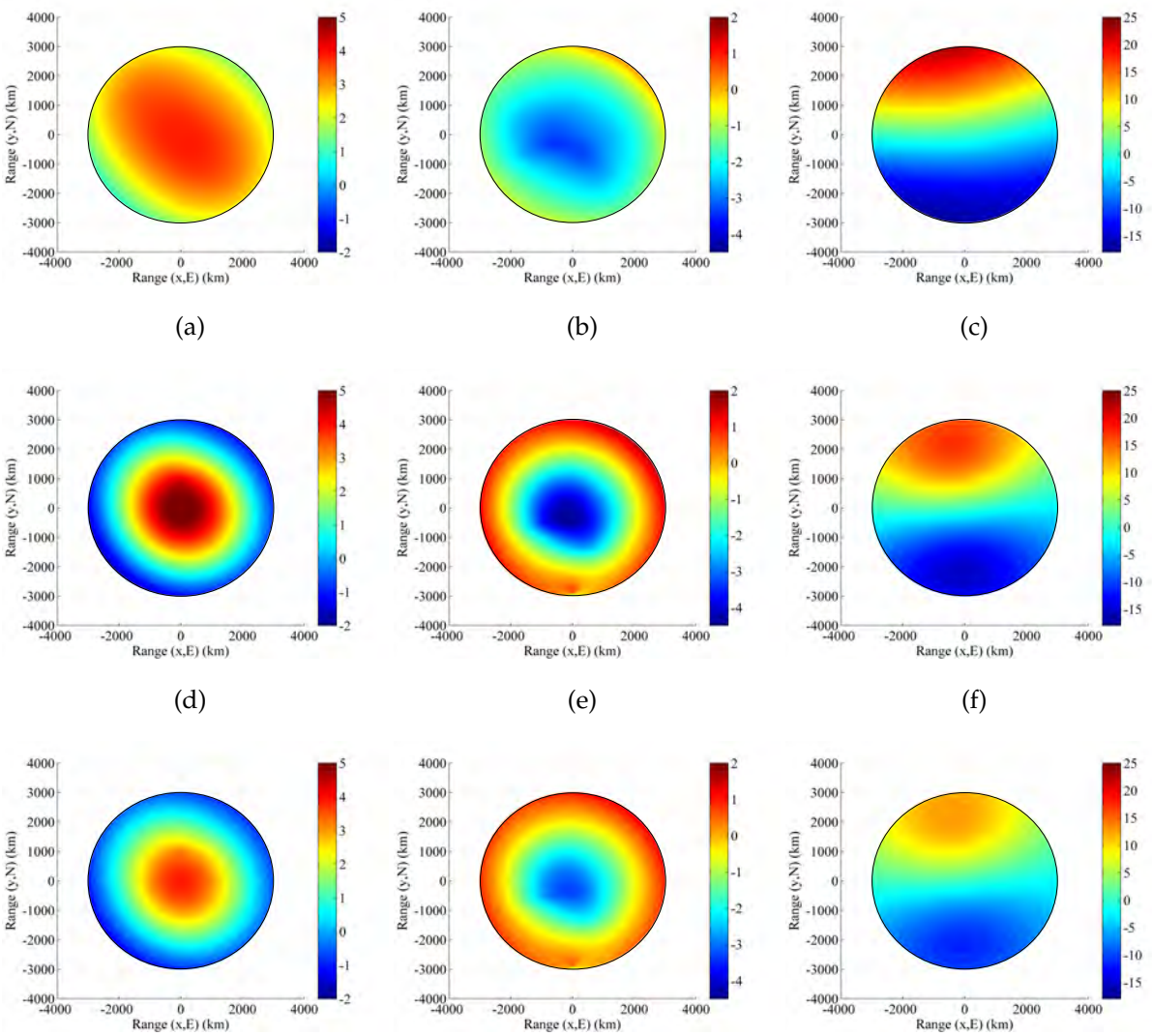

Figure 4.6. Faraday rotation (°) estimates over the FoV (15th January 2010, frequency: 1.616 GHz, orbit height: 780 km). Rows: (1) presented model; (2) according to Le Vine and Utku (Accessed: 2013) ; (3) according to Jehle *et al.* (2005). Columns: (1) Magnetic North (85°,-133°); (2) Magnetic South (-64°,137°); (3) Magnetic Equator (-10°,-71°).

delay that take into account the variable nature of the ionosphere, allowing for a more realistic approximation of these effects to be obtained in any propagation direction.

As the FoV edge is approached, more ionosphere is traversed than at the nadir. The effect of both Faraday rotation and path delay is dependent on the variability of TEC and the Earth's magnetic field along the path. Dense regions of electrons may be traversed but may not adversely affect the signal if the propagation vector is near orthogonal to the Earth's magnetic field at the (L, l, h) triplet position being considered. However, at an incremental distance further along the path, this may no longer be the case as the propagation vector may align closer with the terrestrial magnetic field vector. As such, it is suggested that, for the outer edges of the FoV, a vectorised treatment of the ionosphere, through integration along the path, is required.

The presented model demonstrates favourable magnitudinal and angular trend correlation of both Faraday rotation and path delay with those of Le Vine and Utku (Accessed: 2013) and Jehle *et al.* (2005). However, there is divergence in the overall FoV patterns, as a result of a vectorised approach, and not a geometric calculation, of propagation path.

It is noteworthy to recall that LEO systems may use lower frequencies, around 160 MHz, than that employed in this chapter, which would typically increase both path delay and Faraday rotation seen in Figures 4.5 and 4.6 by a factor of one hundred. At these lower frequencies, ionospheric disturbances are more prevalent and third order effects such as scintillations, decoherence, variable refraction and phase instability become more significant. Around 10 MHz, these effects become comparable to second order Faraday rotation effects.

The point is made in Le Vine and Utku (Accessed: 2013) that Faraday rotation measurements obtained for values of κ greater than 60° are unreliable due to low SNRs. This angle corresponds to a radial distance, from the FoV centre, of 1000 km. The vectorised approach, through integration along the path, may offer the possibility to model the FoV radially outward beyond values of κ greater than 60°. This is useful for simulating and improving measurement through the method of tri-orthogonal polarimetric MIMO signalling. Such a method may extend the range of measurement as SNR, towards the outer edge of a large-FoV, is typically higher for such a method than for conventional CP wave propagation.

In the instance of a constant TEC and terrestrial magnetic field vector along the propagation path, and no measurement errors in any of the required parameters, the estimates in Faraday rotation and path delay can differ between the thin-shell models of Jehle *et al.* (2005) and Le Vine and Utku (Accessed: 2013) and the presented vectorised model. This difference results from the interpretation of the ionospheric layers and is found to be of the order of 6%. As a result, at the FoV centre, the vectorised model estimates are 6% higher and 5.3% higher respectively while at the FoV edge, the vectorised model estimates are 13.7% higher and 12.1% higher respectively. This can be factored out at the nadir to mitigate this effect. The ionospheric interpretation in the proposed vectorised model provides a layered distribution as a function of height that is not a function of (L, l) and so is assumed to extend in all directions. If we introduce a 10% decrease in a TEC value at a particular (L, l) position that coincides with the 400 km altitude point of the thin-shell model of Jehle *et al.* (2005) and Le Vine and Utku (Accessed: 2013), the difference in Faraday rotation and path delay estimates at the outer edge increases commensurately to the order of 22%. The singular value dependency of the thin-shell model has a large effect on the estimate. The vectorised model takes the direction of magnetic field into account at multiple positions along the propagation path, whereas the thin-shell model uses a singular value. This would further alter the estimate difference between models, as the alignment of propagation and magnetic field determines the amount of coupling that exists betwen them.

At the outer edge of a large-FoV, the Earth's curvature needs to be taken into account, that the vectorised model does.

We assume that any measurement error in TEC and magnetic field is constant over the FoV. This is reasonable as the measuring system is likely to be calibrated to the same degree over the entire FoV. This alters both estimates of thin-shell model and vectorised model by the same amount, or percentage change in TEC and magnetic field measurement, due to the measurement error. Variations in measurement error are typically a function of the distribution of TEC itself. For a slant TEC GNSS system, the error in ionospheric path delay is typically 0.162 m per TECU (Ciraolo *et al.* 2006). For the error in Faraday rotation due to a constant measurement error across the FoV in TEC and magnetic field component aligned with the direction of propagation, we have,

$$\Delta_{\mathrm{rms},\psi_{\mathrm{FR(thin\text{-}shell)}}} = \left\{ \left(b_{||(400\mathrm{km})} \times \delta\mathrm{TEC}_{(400\mathrm{km})} \right)^2 + \left(\mathrm{TEC}_{(400\mathrm{km})} \times \delta b_{||(400\mathrm{km})} \right)^2 \right\}^{\frac{1}{2}} \tag{4.23}$$

$$\Delta_{\mathrm{rms},\psi_{\mathrm{FR(vectorised)}}} = \frac{1}{i_{\mathrm{FR}}} \int_0^{i_{\mathrm{FR}}} \left\{ \left(b_{||(\mathrm{k_{FR}})} \times \delta\mathrm{TEC}_{(\mathrm{k_{FR}})} \right)^2 + \left(\mathrm{TEC}_{(\mathrm{k_{FR}})} \times \delta b_{||(\mathrm{k_{FR}})} \right)^2 \right\}^{\frac{1}{2}}. \tag{4.24}$$

An identical analysis supports the RMS error in path delay due to a constant measurement error in TEC across the FoV.

4.4 Chapter Summary

This research takes the well documented effects of Faraday rotation and path delay and presents them over a large-FoV, using vectorisation of time-varying parameter values and link geometry.

Estimates of Faraday rotation and path delay for a large-FoV LEO system are presented using parameter vectorisation in three dimensions. Results are demonstrated for a suggested system operation of remote satellite telephony. A comparison is made with existing theoretical modelling of Faraday rotation and path delay over FoVs centred at the magnetic north and south poles, and at the magnetic equator. This comparison demonstrates favourable magnitudinal and angular trend correlation of both Faraday rotation and path delay. However, there is divergence in the overall FoV patterns, as a result of a vectorised approach and a geometric interpretation of propagation path.

Whereas previous models employ a single value of the Earth's magnetic field dipole and TEC for analysis of ionospheric effects on an electromagnetic signal as it propagates through the ionosphere, the presented model extends the estimates of Faraday

rotation and path delay into three dimensions. These ionospheric effects may then be calculated for receiver positions toward the edge of the FoV, according to the integration of variables along a propagation path. The non-uniform nature of the ionosphere is taken into account, according to height as well as global (L, l) position.

This chapter forms part of research on a large-FoV NGSO satellite channel model employing MIMO polarimetry in three dimensions. This is to model capacity over the entire FoV, in an effort to develop performance that is less dependent of signal propagation direction. This is particularly relevant at the FoV edge, where received signal power is typically much lower than that received by a receiver at the FoV centre. To ensure signal reception through diversity, the traditional use of CP wave propagation techniques may lead to reduced signal power at the receiver, when compared to aligned linear techniques, as diversity of two orthogonal signals transmitted from the satellite comes at the expense of reduced transmit power in association with each transmitted polarisation mode. In addition, CP wave propagation is only feasible for a perfectly aligned system, typically when the satellite is at the receiver zenith, and where the least ionospheric disturbance is encountered. Signal propagation becomes elliptically polarised away from the zenith position, and linearly polarised at the horizon (Balanis 2005), with signal reception suffering as a result of diversity being reduced. The use of MIMO polarimetric techniques, in three dimensions, may provide the power transfer characteristics of LP propagation techniques, while providing diversity performance and reception characteristics typical of those provided through the use of CP wave mode propagation.

An all encompassing approach to the mitigation of Faraday rotation and path delay, often in the form of CP propagation techniques may not always be the best solution. This is pertinent at the FoV edge where the propagation path is longest, and *a priori* subject to the most variability along its length. Any propagating signal along this path is most likely to suffer the greatest depolarising effect.

The tri-orthogonal arrangement may allow improved measurement of Faraday rotation at greater off-nadir angles, or towards the FoV edge, since the arrangement promises additional diversity and performance in this region through orthogonality being used in a three dimensional environment (Andrews *et al.* 2001).

Whereas the model is presented according to demonstrable geometry, and compares favourably with both Jehle *et al.* (2005) and Le Vine and Utku (Accessed: 2013), further revisions are now listed that can improve the model in any future iteration.

- Data for total electron content remains coarse and, despite the use of bilinear interpolation, may require resourcing in any future revision to the model.
- The ionospheric scaling factor is currently based on a daytime maximum profile of the ionosphere. As the ionosphere is time-varying, this requires consideration in any future iteration. Differentiation between daytime and nighttime profiles, and local and seasonal variances, would be required; thus greatly expanding the model. In Chapter 5, a two state ionosphere is introduced.
- Magnetic field vector data has been obtained at any height along the path, including very low levels. Although this has been demonstrated in Maus *et al.* (2010), further investigation into the validity of these low level techniques is required.
- Measured data is required to fully validate the model at these outer lying regions of the FoV.

With the ionospheric model in this chapter providing information regarding the ionospheric effects of Faraday rotation and path delay typically found over a LEO satellite FoV, the impact of these effects on an electromagnetic signal propagating through the ionosphere is now examined.

In Chapter 5, the ionospheric modelling provided in this chapter is used in a model that considers three distinct NGSO satellite systems, and the improvement in link performance that is possible through the introduction of a third orthogonal polarisation mode at the receiver.

Chapter 5

Tri-Orthogonal Approach Applied to Non-Geosynchronous Satellite Orbit Ionospheric Channel

In this chapter, the unwanted ionospheric effects of path delay and Faraday rotation are applied to a conventional CP mode transmitted satellite signal propagating towards a ground receiver. Three distinct NGSO satellite systems are considered as the performance of a tri-orthogonal ground receiver, with a third polarisation orthogonal to the antenna surface, is compared to that of a conventional CP mode ground receiver in an ionospheric channel. System performance over the link is dependent on global position and link geometry within a FoV, and so performance is considered over a set of FoVs simulated over random orbits for each of the NGSO satellite systems. Antenna orientation over the FoV acts as a proxy for antenna misalignment resulting from meteorological or topological effects at link positions where reception would be expected to be optimal. The work presented forms part of a large-FoV NGSO satellite system model exploiting tri-orthogonal receive polarimetry in three dimensions.

5.1 Introduction

Many ground receive antennas relying on communication with non-geosynchronous satellites, including those used for voice and data communications, global telemetry, tracking and command applications, and global positioning systems (GPS), offer optimum performance through a maximised radiation gain pattern in a zenith direction. This performance degrades as the communication link between satellite and receiver moves away from this alignment. In addition, and as a means of avoiding communication degradation resulting from reduced power reception due to the depolarising effect of Faraday rotation, satellite systems typically provide link reliability using circular polarisation (CP) wave propagation. This form of polarisation provides diversity, and may be fundamentally resolved into two orthogonal linear polarised (LP) waves, with a $\pm 90^{\circ}$ phase offset between them (Pozar 2011). This phase offset determines whether right-handed CP (RHCP), or left-handed CP (LHCP) wave propagation occurs. For an aligned system, CP propagation provides a higher probability of reception than its LP counterpart. The penalty for link reliability using CP propagation is that range may be reduced, as 3 dB of transmitted signal power is effectively given to an orthogonal transmit polarisation, or branch. In addition, polarisation diversity offered by CP wave propagation may degenerate to LP performance at low satellite elevation angles, where typically Faraday rotation is strong. This is as the radiating surface of a CP mode receiver is typically aligned with this surface orthogonal to the zenith, with optimal performance in the zenith direction (Mittra *et al.* 1993, Cobham Plc Accessed: 2015, Taoglas Ltd 2015). Wave propagation using CP and LP waveforms represents two extremes of the more general form of elliptical polarisation (EP).

With a ground receive antenna aligned for optimal zenith performance, a satellite passing overhead and transmitting a CP waveform in a sub-satellite, or nadir, direction transmits along the shortest possible channel link. At equatorial latitudes, ionospheric effects such as Faraday rotation and path delay on a propagating signal are typically weak in the nadir direction, due to both a short ionospheric path length and low interaction between the transmitted signal and the terrestrial magnetic field. As link geometry diverges from this aligned case, from the perspective of a ground receiver for example, receive performance is typically more difficult to maintain as antenna misalignment increases. At higher latitudes, within the polar regions for example, an increased strength and inclination of the terrestrial magnetic field component

(Kelley 2009, Maus *et al.* 2010), coupled with reduced satellite coverage, increases the possibility of degraded receiver performance (Ilčev 2005).

A satellite spot beam may transmit a CP waveform, and thus provide polarisation diversity, in a unique direction of propagation. At the receiver, angular departure from this direction causes reception to become EP, as an axial ratio of 0 dB is no longer demonstrated by the propagating waveform (Toh *et al.* 2003). For a CP mode ground receiver aligned with its radiating surface orthogonal to the zenith, this may result in a loss of polarisation diversity as the received signal degenerates towards a horizontally polarised (HP) waveform near the ground receiver's horizon, due to fundamental radiation pattern constraints of a CP mode antenna (Pozar *et al.* 1995). Ionospheric effects on a propagating signal are typically strong at such elevations, due to a maximised path length and strong interaction between the signal and a parallel component of the terrestrial magnetic field (Tirró 1993). Link reliabilty can no longer be guaranteed over an extended field-of-view (FoV). In this chapter, we consider the FoV to be a circular area on the Earth seen from the perspective of the satellite in which a ground receive antenna may be positioned. The size of the FoV is determined by satellite orbit height, with the ground range at which the radiating surface of the receive antenna is orthogonal to an incoming satellite signal providing the circular FoV perimeter.

The problem of link reliability is prevalent for LEO satellite systems, where relative link geometry varies rapidly as a function of time (Farserotu and Prasad 2000, Roddy 2006). To counter detrimental effects on a transmitted signal, a ground receiver may be perfectly aligned with a transmitting satellite, using manual or mechanical means, provided the location of the satellite is known. This may not always be possible, and may be subject to mechanical failure.

Polarisation diverse receive antennas, such as geodetic radomes and patch antennas, may receive signals from satellites in NGSOs and exhibit a low gain, and so low noise, and optimal zenith performance with a gain roll-off as departure is made from the zenith direction (Antcom Corporation Accessed: 2016). Cross polarisation rejection is degraded as the elevation of received signal decreases. In environments where the surfaces of such antennas may no longer be parallel to the Earth's surface, such as in rough seas, suboptimal perfomance may occur at the worst possible time as zenith alignment is no longer maintained. In an ideal world, we would like to avoid this constraint.

In the case of global navigation satellite systems (GNSS), receiving simultaneous signals from satellites provides a more accurate global position (Levine 2009, Panther Accessed: 2015). Increasing diversity over a greater coverage area would increase the probability of simultaneous satellite signal reception at the receiver.

Synthetic aperture radar (SAR) systems typically, but not exclusively, operating at L-band (1–2 GHz) use horizontal and vertical polarisation as a means of mitigating Faraday rotation depolarisation. Operational examples of satellites using this diversity technique for applications such as Earth observation include ALOS (Advanced Land Observing Satellite) and ALOS-2 (Earth Observation Research Center Accessed: 2016), Radarsat-2 (Canadian Space Agency Accessed: 2016a), TerraSAR-X (Earth Observation Portal Accessed: 2016c), Envisat-ASAR (Advanced Synthetic Aperture Radar) (European Space Agency Accessed: 2016a), Sentinel-1a/b (European Space Agency Accessed: 2016c). The technique is also earmarked for future satellite missions including RCM (RADARSAT Constellation Mission) (Canadian Space Agency Accessed: 2016b), SAOCOM (Satellites for Observation and Communications) (European Space Agency Accessed: 2016b) and SAOCOM-CS (Satellites for Observation and Communications-Companion Satellite) (Davidson Accessed: 2016), Cosmo-Skymed (Constellation of Small Satellites for Mediterranean basin Observation) 2nd generation (Earth Observation Portal Accessed: 2016a) and PAZ (Earth Observation Portal Accessed: 2016b). In Wright *et al.* (2003), a Faraday rotation of just 5° is suggested as reducing the dynamic range of wanted co-polarised channels while driving cross-polarised channels to resemble co-polarised channels. As a consequence, sensitivity is reduced to the point that differentation of received ground backscatter is severely degraded. In effect, when cross polarisation rejection is degraded, a dual-polarised system reverts to a singularly polarised one.

Detrimental effects on LEO satellite communication receivers, such as Iridium, typically operating at L-band (1–2 GHz) frequencies and lower, may also increase due to suboptimal cross polarisation rejection at low elevation angles, as gain is optimised at the zenith and rolls off with decreasing elevation (Padros *et al.* 1997). Specular reflections on a propagating signal, where 180° phase changes occur, may render RHCP transmission as LHCP transmission, with a theoretical received power of zero at a RHCP configured receive antenna. Multipath fading may resolve a LoS signal into diverse signal components that are effectively too weak to be superimposed at the receiver, as the result of scattering effects in the channel. Both specular reflections and

multipath effects typically reduce signal reception at the receiver, as inelastic interactions and division of wave energy take their toll. The use of simultaneous RHCP and LHCP signal propagation is suggested in Arapoglou *et al.* (2011b) as a solution for mitigating local scattering effects near the antenna. Once again, RHCP and LHCP mode signal transmissions are only available in one direction of propagation, typically in the satellite nadir or ground receive antenna zenith direction, with degradation of system performance typically being observed at lower elevation angles at the receiver. Both Iridium and GPS receive antennas often share a common housing, since operating frequencies are in close proximity (Antcom Corporation Accessed: 2016). These designs are optimised for zenith communication, since a gain roll-off exists away from this point. Figure 5.1 highlights such an antenna. For system operation over channels with satellites already in orbit, the receiver configuration becomes important in offering the possibility of enhanced system performance through diversity at lower elevation angles.

Coupled with zenith-optimised CP wave propagation, the introduction of a vertical polarisation at the receiver would add additional diversity at lower elevations where often a worst case perfomance is encountered due to increased Faraday rotation and ionospheric path delay, and a higher probability of signal blockage due to structures on the horizon (Lutz *et al.* 1991, Fontan *et al.* 2001). Polarisation purity in three orthogonal directions may improve reception at lower elevation angles, and so extend the range of useful reception.

The advantages of polarisation diversity through a tri-orthogonally polarised antenna configuration have been presented in previous work, typically in consideration of terrestrial applications (Andrews *et al.* 2001, Mtumbuka *et al.* 2005, Mtumbuka and Edwards 2005) where increased data rate, or capacity, is the aim. Such environments typically do not suffer synchronisation issues between received signals as the propagation distances are relatively small, compared to a satellite channel path length. In addition, terrestrial channels may make use of multipath effects to increase capacity at the receiver, as the SNR is more readily maintained at a high level (Goldsmith 2005).

To increase capacity over a satellite link, MIMO satellite diversity is one option (Yamashita *et al.* 2005, King *et al.* 2005, King 2007, Liolis *et al.* 2007, Arapoglou *et al.* 2011b) but this suffers from synchronisation effects, especially in the instance of LEO satellites where path lengths vary greatly according to a satellite position relative to a ground receiver. In Horváth and Frigyes (2006) and Horváth *et al.* (2007), the concept

	IN PORT								GPS PORT	
	Rx Inmarsat (RHCP)		L1 GPS, E1, E2 Galileo, L1 IRNSS (RHCP)		IRIDIUM L1 GLONASS (RHCP) OR Tx-GLOBALSTAR (LHCP)		Tx-Inmarsat (RHCP)		L1 GPS	
FREQUENCY:	(1542.5 ± 24.5) MHz		(1575 ± 17) MHz		(1609 -1626) MHz		(1642.5 ± 32.5) MHz		(1575.42 ±12) MHz	
RADIATION PATTERN:	HEMISPHERICAL									
VSWR:	< 1.5:1		< 1.5:1		< 1.5:1		< 1.5:1		< 2.1:1	
IMPEDANCE:	50 ohms		50 ohms		50 ohms		50 ohms		50 ohms	
ANTENNA GAIN (dBic):	Free Space	4 ft G.P.	Free Space	4 ft G.P.	Free Space	4 ft G.P.	Free Space	4 ft G.P.	Free Space	4 ft G.P.
@ 90 ° Above Elevation (Top):	+ 3.8	+ 2.9	+ 3.6	+ 3.6	+ 3.7	+ 3.3	+ 3.8	+ 2.9	- 0.8	+ 3.8
@ 10 ° Above Elevation:	- 6.2	- 5.5	- 6.6	- 5.2	- 6.6	- 6.1	- 6.6	- 6.9	- 9.3	- 4.3
@ 15 ° Above Elevation:	- 5.1	- 3.8	- 5.5	- 3.6	- 5.5	- 4.4	- 5.4	- 5.2	- 8.1	- 3.3
@ 20 ° Above Elevation:	- 3.9	- 2.1	- 4.1	- 1.9	- 4.1	- 2.7	- 4.1	- 3.5	- 6.8	- 2.2
@ 25 ° Above Elevation:	- 2.9	- 1.3	- 3.1	- 1.2	- 3.2	- 1.9	- 3.2	- 2.6	- 6.0	- 1.5
@ 30 ° Above Elevation:	- 1.8	- 0.5	- 2.1	- 0.5	- 2.2	- 1.1	- 2.2	- 1.7	- 5.2	- 0.7
@ 70 ° Above Elevation:	+ 3.1	+ 2.5	+ 3.0	+ 2.5	+ 3.1	+ 2.4	+ 3.1	+ 2.3	- 2.1	+ 2.5
BEAM WIDTH (3dB):	90 Deg.	110 Deg.	90 Deg.	95 Deg.	90 Deg.	95 Deg.	90 Deg.	95 Deg.	100 Deg.	120 Deg.
AXIAL RATIO:	1 dB	3 dB	1 dB	3 dB	1 dB	3 dB	1 dB	3 dB	2.5 dB	
LIGHTNING PROTECTION:	DC GROUNDING									
LNA GAIN (GPS ONLY):	33 dB Gain									
LNA NOISE FIGURE:	3.0 dB									
LNA P1dB Out:	+13 dBm									
LNA DC POWER:	2.5V/20mA, 3V/29mA, 3.3V/35mA, (2.5-24)V/<50mA									
REJECTION @ (-50/+50) MHz	-40 dB / -40 dB									
@ (-100/+100) MHz	< -65 dB									
POWER HANDLING:	50 Watts CW (WITHOUT LNA) , 1 Watt CW (WITH LNA)									

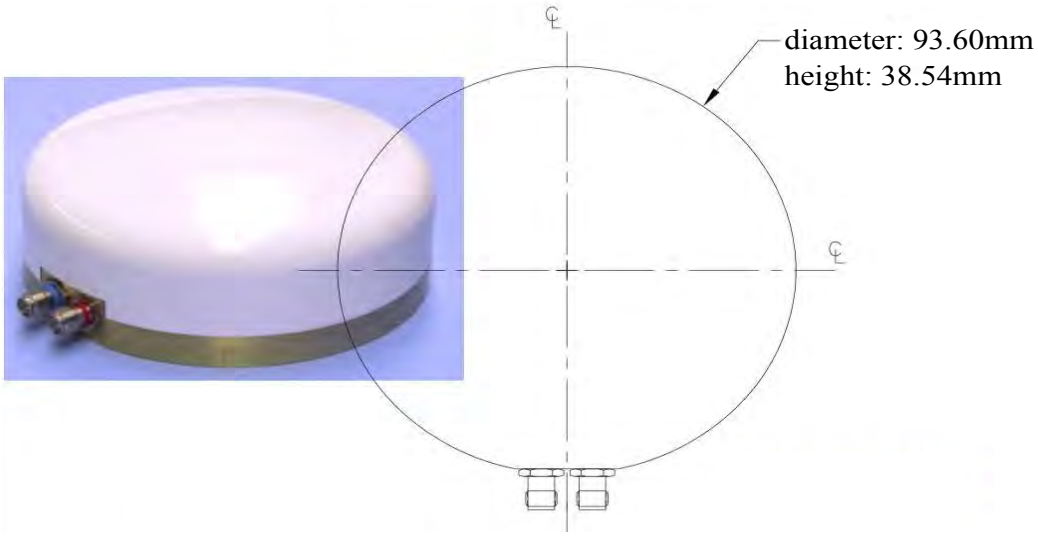

Figure 5.1. Commercial patch antenna providing L1 GPS and Iridium satellite signal reception. After Antcom Corporation (Accessed: 2016). This design is typical of GPS and Iridium receivers, being optimised for CP propagation in the zenith direction.

of 3D polarisation diversity through the use of polarisation time coding (Frigyes and Horváth 2005) to increase capacity over a satellite link is invoked, after consideration of the theoretical vector element antenna (Svantesson *et al.* 2004), and its physical counterpart, the MIMO cube (Getu and Andersen 2005). For a rich scattering environment, which is not typically the case of a satellite channel, a six fold increase is suggested in Horváth *et al.* (2007) over a SISO antenna arrangement, due to the employment of three orthogonal infinitesimal electric dipoles and three orthogonal infinitesimal magnetic dipoles colocated at both the transmitter and receiver. In Marzetta (2002), a more conservative four fold limit on capacity is suggested for a tri-orthogonally polarised

arrangement at both transmitter and receiver in a rich scattering environment. It is intuitive to recognise that the configuration does offer additional degrees of freedom beyond conventional CP techniques that may improve performance in the instance of severe fading due to polarisation mismatch, for example, as a result of channel depolarising effects. Over a satellite channel, polarisation mismatch is both time and location dependent, and so to mitigate its effect over an entire FoV requires a generic solution. In this chapter, a tri-orthogonal receiver is only considered at the receiver, as a means to improving link performance, as we assume alteration of an *in situ* satellite system to be financially unviable at the time of writing. As a consequence, we maintain calculation of power transfer over nine subchannels within a channel matrix, while providing analysis using conventional CP wave propagation, through two transmitted orthogonal signal polarisations with a 90° phase difference between them. As such, we consider six of the nine subchannels in this analysis.

5.2 Method

Three diverse NGSO satellite systems are analysed, all transmitting a RHCP signal in an ionospheric channel; the LEO Iridium satellite system (Johannsen 1995, Maine *et al.* 1995, Chang and de Weck 2005, Iridium Communications Inc. Accessed: 2014), the LEO Orbcomm TT&C system (Coverdale 1995, Orbcomm LLC Accessed: 2014, Orbcomm Inc. Accessed: 2014) and the Global Positioning System (GPS) system (Braasch and van Dierendonck 1999, Leveson 2006, United States Government Accessed: 2015), operating in a mid-Earth-orbit (MEO).

A novel vectorised model is described using a fundamental physical approach, which subsequently uses realtime ionospheric data inputs, in order to calculate system capacity performance at the receiver for system operation with and without a third orthogonal polarisation branch at the receiver, orthogonal to the antenna surface. Constant transmit power is assumed in these calculations. This power is divided equally between orthogonal transmit polarisations.

The following assumptions are made in the model.

- Interest is aimed at power transfer, since this forms a basis for determining electric field transfer across the channel. As such, we consider the channel to begin at the point at which the transmitter radiates energy into free space and end at

the point where transferred energy originating from the transmitter is impingent on the receiver. We calculate the noise power according to an antenna noise temperature at the receiver of 290 K. The NGSO satellite systems being considered use low gain at the receiver in order to improve reception coverage (Levine 2009). Noise power at the receiver is dependent on the direction of propagation of the received wave, and is typically higher for lower elevations, since the temperature of the Earth is higher than that of the sky. At lower elevations, receiver gain of conventional receive antennas rolls off (Antcom Corporation Accessed: 2016). Although we introduce a third orthogonal polarisation at the receiver to specifically receive signals at low elevations, the radiation pattern of this polarisation is of low gain, and so is not considered to adversely affect received noise at the receiver. As a consequence, our noise temperature assumption provides a noise power value that is high in comparison to many systems (Langley 1997). As a result, our assumption provides a reduced SNR at the receiver. The SNR is applied to all channel coefficients, or signal transfer elements, in the channel matrix. Since a conventional CP antenna has subchannels within the channel matrix of a tri-orthogonal arrangement, we consider this assumption to not skew the results in favour of one antenna arrangement over another.

- A system initially based on LoS signal transfer is considered, with no effects of blockages, reflections or scatterings of propagated electromagnetic wave energy. Such effects are incorporated into the model through (i) a total fade margin and (ii) a statistical approach which considers these effects as slow and fast fading effects, resulting in shadowing and multipath effects witnessed over the FoV as a function of elevation at the receiver, and channel environment. For strongly received signals at one spatial position at a given time, resulting from useful scattering of a strong LoS signal incoming from one direction, multipath fading may prove detrimental to reception by effectively assisting received signal component cancellation through superposition at the receiver as the channel changes over time. This signal cancellation process is equally applicable to the effects of polarisation mismatch which may also change over time as a function of the channel. A variable link geometry adds an additional dimension of uncertainty to signal reception, requiring a diversity approach to provide additional mechanisms for the received signal to remain strong. Signal cancellation as a function of wave superposition may be mitigated through techniques such as frequency channel

hopping (Watteyne *et al.* 2010), for instance, where a region of deep fade at the receiver is alleviated through a switching of carrier frequency, and hence carrier wavelength, resulting in a different interference metric at the receiver. For a weak LoS signal, the effect of multipath is extremely debilitating, as resultant signal components at the receiver are rendered too weak to be received. In the proposed model, and from a physical standpoint, it is reasonable to assume that increased diversity in the form of an additional polarisation at the receiver shall reduce the effect of any signal cancellation through superposition (Goldsmith 2005).

The commercially available characteristics of the three satellite systems, in terms of a single transmitted carrier wave, are given in Table 5.1. The transmitter at the satellite shall be referred to as T, with the receiver on the ground referred to as R. The gain at T is denoted as G_{T}, and for the Iridium and GPS systems is modelled assuming an ideal conical beam (Schuss *et al.* 1993, Parkinson and Spilker 1996, Marquis Accessed: 2014, Marquis and Reigh Accessed: 2015, Betz 2015). Such a radiation pattern attempts to mitigate free space path loss by providing power gain that increases as a function of off-nadir angle.

An Iridium satellite transmit system comprises three panels of phased array patch antennas, with each panel providing sixteen spot beams. Beams providing coverage at the FoV edge, or EoE, are shaped to increase gain at the FoV edge.

A GPS satellite transmit system consists of four inner and eight outer phased patch antennas, arranged in two concentric circles. Radiation profiles once again provide increased gain at the FoV edge. It is noted that the term 'Legacy' is used in Marquis (Accessed: 2014) with regard to an older gain profile that is considered in this thesis. The 'Legacy' and 'Improved' gain profiles are shown in Figure 5.2. The improvement in gain profile is small, but useful in providing a more uniform gain profile over the entire FoV. Indeed, performance uniformity over the FoV is a system aim, and it will be seen later in this chapter that the inclusion of a third orthogonal polarisation at R, orthogonal to the ground receive antenna surface, provides higher and more uniform capacity across the FoV. The use of the 'Legacy' gain profile in this thesis does not detract from the GPS system simulations, as the gain profile of the CP wave transmission is the same for consideration of both a conventional CP mode or tri-orthogonal antenna arrangement at R.

For the Orbcomm system, the gain at T is modelled according to the profile in Figure 5.3.

The gain associated with a polarised mode of the ground receive antenna at R is denoted as G_R.

For the Iridium and GPS systems, the gain associated with each orthogonal polarisation mode at R is modelled on that of a half-wavelength dipole, since when the orthogonal polarisation modes are combined the resulting profile is similar to the gain profile associated with a typical commercial receive antenna (Levine 2009, Antcom Corporation Accessed: 2016).

For the Orbcomm system, we apply the same approach at R while noting that both patch-style and vertical whip antennas are commercially available (Antenna Research Associates Accessed: 2016, Inevitable Technologies Accessed: 2016). By opting for the former, the instance of optimal reception at R can be examined using full RHCP mode wave propagation methods, in the same manner as that employed by the Iridium and GPS receive antenna arrangements.

In addition, the following points are made in regard to our opting for a half-wavelength dipole gain associated with polarisation modes $\hat{\mathbf{p}}$ and $\hat{\mathbf{q}}$ at R, which together represent a typical CP mode ground receive antenna prior to the addition of the third orthogonal polarisation mode, $\hat{\mathbf{r}}$:

- the gain of a half-wavelength dipole, of which the maximum is at the broadside position, and is of 2.15 dBi in magnitude, is similar in form to that provided by commercially available receiver antennas. The boresight, or zenith, direction provides a maximum gain which drops off with increasing off-boresight angle.
- the choice of orthogonal half-wavelength dipole gain patterns at R provides uniformity, as a result of an identical radiation pattern associated with each orthogonal polarisation mode at R, namely on $\hat{\mathbf{p}}$, $\hat{\mathbf{q}}$, and $\hat{\mathbf{r}}$. Bias is removed.
- a typical CP mode gain of a commercial receive antenna for the Iridium and GPS systems at R is of the order of 3.7 dBiC at boresight, as shown in Table 5.1 (Levine 2009, Antcom Corporation Accessed: 2016). A commercial CP mode gain of 4.5 dB at R is observed in the case of the Orbcomm system in Table 5.1, as a hemispherical low gain is once again sought. A half-wavelength dipole gain profile with a maximum power gain of 2.15 dBi at boresight is used in the model as the associated radiation pattern is broader than the radiation pattern of a commercial receive antenna. As such, it reduces any bias from introducing the third orthogonal polarisation, $\hat{\mathbf{r}}$, at the FoV edges.

Table 5.1. Commercial system information on three distinct NGSO satellite systems considered in this thesis.

Type	Orbit (km)	Inclination (°)	Power (dBm)	Frequency (MHz)	Bandwidth (kHz)	Polarisation	$\text{Gain}_{(\text{Transmitter,boresight})}$ (dBiC)	$\text{Gain}_{(\text{Receiver,max})}$ (dBiC)	Fading Margin (dB)
Iridium	780	86.4	27.7	1616	41.7	RHCP	23.1	3.7	16
Orbcomm	775	48.6	39	138	25	RHCP	0.8	4.5	16
GPS	20200	55	25.4	1575 (L1)	2000	RHCP	13.1	3.7	22

- commercially available receive antennas are optimised for performance at the FoV centre, or zenith position. To analyse the satellite systems with their CP mode receiver gain highly focused at the centre of the FoV, when the CP mode receiver forms part of the tri-orthogonal arrangement, would not provide an unbiased metric for the improvement in performance due to the inclusion of the third orthogonal polarisation mode, $\hat{\mathbf{r}}$.

- the linear power scaling of 2.15 dBi is 1.64, while that of 3.7 dBi is 2.34. This is not a great difference of scaling, and it is dwarfed by the scaling of polarisation mismatch, which may be of the order of -30 dB, or 0.001 (Golio and Golio 2007). Indeed, the effect of polarisation is that of which this thesis is primarily concerned. A uniform approach, gainwise, at R provides the most justifiable approach for analysing improvement at the receiver through the introduction of a third orthogonal polarisation at R, as no bias is introduced into receiver performance.

5.2.1 Link Geometry

Link geometry is given according to Subsection 4.2.1 in Chapter 4. In this chapter, the modelling of Chapter 4 is introduced into a NGSO satellite performance model. Table 5.2 provides orbital parameter data for the three NGSO satellites considered in this thesis.

Table 5.2. Orbital parameters for the three distinct NGSO satellite systems considered in this thesis.

Variable	Iridium	Orbcomm	GPS
α_{max}	63°	63.1°	13.9°
γ_{max}	27°	26.9°	76.1°
$r_{plot(max)}$	3 005 km	2 996 km	8 472 km
s_{max}	3 249 km	3 238 km	25 801 km
$FSPL_{min}$	154.4 dB	133 dB	182.5 dB
$FSPL_{max}$	166.8 dB	145.4 dB	184.6 dB

An Earth-Centred Earth-Fixed (ECEF) coordinate system is invoked for this work. The a-axis is positioned at the latitude, longitude (L, l) position (0,0). In a first instance, we may generate the FoV about this axis. At the FoV centre, an easterly direction $[0\ 1\ 0]^{\mathrm{T}}$, where the superscript refers to transpose, coincides with an azimuthal angle θ_{T} of 0°. Within the FoV, anti-clockwise rotation is deemed as positive. Calculation of signal transfer according to a 3×3 channel matrix is performed, although analysis of the benefit of a third orthogonal polarisation at R is performed using six subchannels in the matrix, as conventional CP wave propagation from T is assumed. As such, we begin by omitting all signal transmission at T using the polarisation mode radial to the Earth's surface, or $\hat{\mathbf{o}}$ in Figure 1.6. Figure 5.4 demonstrates the resulting concept, with five system polarisation modes labelled as ($\hat{\mathbf{m}}$, $\hat{\mathbf{n}}$) at T, and ($\hat{\mathbf{p}}$, $\hat{\mathbf{q}}$, $\hat{\mathbf{r}}$) at R, providing six subchannels for signal transfer from T to R. These polarisation modes will be determined in vector form in Subsection 5.2.2.

A unit propagation vector $\hat{\mathbf{k}}$ from T to all (L, l) positions in the FoV where the ground receive antenna at R is positioned is determined by,

$$\hat{\mathbf{k}} = \begin{bmatrix} -\cos\alpha \\ \cos\theta_{\mathrm{T}} \sin\alpha \\ \sin\theta_{\mathrm{T}} \sin\alpha \end{bmatrix}. \tag{5.1}$$

The perimeter of the FoV is determined as the ground range at which $\kappa = 90°$. Elevation at T is given by α with 0° in the nadir direction, otherwise positive. Elevation at R is given by κ with 0° in the zenith direction, otherwise positive. The azimuthal angle

θ_R at R of the unit vector representing signal propagation $\hat{\mathbf{k}}$ differs to that of the corresponding angle θ_T at T by 180°. The receiver R is assumed to be at a distance s from T which changes according to FoV location. The FoV may subsequently be positioned, according to its centre, at any user specified (L_u,l_u) global position.

In this chapter, we specify dimensional metrics of terrestrial footprints for the distinct FoVs of each of the three NGSO satellite systems according to Figures 5.5, 5.6, and 5.7.

5.2.2 Transmitter and Receiver Arrangement

We introduce antenna configurations at T and at R, as shown in Figure 5.4. The FoV for vector calculations of Chapter 4, centred at (L_o,l_o), is reintroduced. At T, we position orthogonal polarisation modes $\hat{\mathbf{m}}$, $\hat{\mathbf{n}}$ that are respectively aligned in an easterly and northerly direction.

To increase diversity over a large-FoV through polarisation techniques, a tri-orthogonal half-wavelength dipole mode structure is employed at receiver R. Half-wavelength dipole modes $\hat{\mathbf{p}}$, $\hat{\mathbf{q}}$, and $\hat{\mathbf{r}}$ are respectively aligned in an easterly, northerly, and radial direction. In accordance with typical small ground receive antenna guidelines, the antenna surface is held orthogonal to the zenith direction. The third vertical polarisation, $\hat{\mathbf{r}}$, is maintained orthogonal to the antenna surface, and so is aligned with the zenith direction. The ground receiver is assumed to be stationary, that is to say, with no vector displacement. Any CP mode signal transmission in a direction may be fundamentally described using an arrangement of two colocated orthogonal polarisation modes with identical amplitude electric field displacement orthogonal to the link direction, a 90° phase difference between the orthogonal modes, and a superimposed gain pattern or directivity in the direction of transmission according to the electric field displacement (Balanis 2005, Pozar 2011). Including a third orthogonal half-wavelength dipole mode, $\hat{\mathbf{r}}$, at the receiver is anticipated to increase diversity, providing two orthogonal reception polarisation modes for any link direction. Ideally, the gain of such a receiver should be low, to avoid noise issues at the receiver, and to provide quasi-omnidirectional coverage (Levine 2009).

For conventional CP mode wave transmission, we may describe five polarisation orientations according to their latitude (L) and longitude (l) positions within the FoV centred at (L_o,l_o), or (0,0). In addition, and for completeness, we include a sixth polarisation mode orientation, $\hat{\mathbf{o}}$, orthogonal to polarisation modes $\hat{\mathbf{m}}$ and $\hat{\mathbf{n}}$ at T. For CP

mode wave transmission from T, we omit transmission using polarisation mode $\hat{\mathbf{o}}$. At T, we have,

$$\hat{\mathbf{m}} = \begin{bmatrix} -\sin l_{\mathrm{o}} \\ \cos l_{\mathrm{o}} \\ 0 \end{bmatrix} \tag{5.2}$$

$$\hat{\mathbf{n}} = \begin{bmatrix} -\sin L_{\mathrm{o}} \cos l_{\mathrm{o}} \\ -\sin L_{\mathrm{o}} \sin l_{\mathrm{o}} \\ \cos L_{\mathrm{o}} \end{bmatrix} \tag{5.3}$$

$$\hat{\mathbf{o}} = \begin{bmatrix} \cos L_{\mathrm{o}} \cos l_{\mathrm{o}} \\ \cos L_{\mathrm{o}} \sin l_{\mathrm{o}} \\ \sin L_{\mathrm{o}} \end{bmatrix}. \tag{5.4}$$

At R, we have,

$$\hat{\mathbf{p}} = \begin{bmatrix} -\sin l \\ \cos l \\ 0 \end{bmatrix} \tag{5.5}$$

$$\hat{\mathbf{q}} = \begin{bmatrix} -\sin L \cos l \\ -\sin L \sin l \\ \cos L \end{bmatrix} \tag{5.6}$$

$$\hat{\mathbf{r}} = \begin{bmatrix} \cos L \cos l \\ \cos L \sin l \\ \sin L \end{bmatrix}. \tag{5.7}$$

Latitude and longitude (L, l) determination is given in the next section.

5.2.3 Latitude and Longitude Determination for Non-Geosynchronous Satellite Orbit Track

We begin by determining a FoV centre (L_c,l_c), along an orbit track and according to orbit parameters, and the user specified FoV centre starting point, (L_o,l_o), that we set at (0°,0°) for ease of understanding. After a time t, and with the satellite orbit dictating a tangential velocity of $\mathbf{v}_T$, of magnitude given by Kepler orbital mechanics, and of direction given by an orbital inclination angle, θ_{inc}, where this angle is positive for counter clockwise rotation about the a-axis and is 0° for an easterly direction, we arrive at the new FoV centre, (L_c,l_c). A unique satellite bearing angle at (L_o,l_o), which is 0° in a northerly direction and positive for a clockwise rotation about the a-axis, is determined as,

$$\theta_{bFoV} = \left| 2.5\pi - \theta_{inc}, 2\pi \right| \tag{5.8}$$

where θ_{inc} values for all three satellites are given in Table 5.1.

As per Chapter 4, all (L,l) positions of R within a second FoV centred at (L_c,l_c), required for determination of ionospheric parameters of TEC and $\mathbf{b}$, are determined from a FoV centre latitude and longitude, (L_c,l_c), given respectively from (L_o,l_o) and θ_{bFoV} as,

$$\begin{aligned} L_c &= \arcsin\{\sin(L_o)\cos(\|\mathbf{v}_T\|t/u) \\ &\quad + \cos(L_o)\sin(\|\mathbf{v}_T\|t/u)\cos\theta_{bFoV}\} \end{aligned} \tag{5.9}$$

$$\begin{aligned} l_c &= l_o - \frac{2\pi t}{60.60.24} + \text{atan}_2\{\sin\theta_{bFoV}\sin(\|\mathbf{v}_T\|t/u)\cos(L_o), \\ &\quad \cos(\|\mathbf{v}_T\|t/u) - \sin(L_o)\sin(L_c)\} \end{aligned} \tag{5.10}$$

where the function $\text{atan}_2(\Delta_1, \Delta_2)$ is given as,

$$\text{atan}_2(\Delta_1, \Delta_2) = \begin{cases} \arctan(\frac{\Delta_1}{\Delta_2}) & (\Delta_2 \succ 0) \\ \arctan(\frac{\Delta_1}{\Delta_2}) + \pi & (\Delta_1 \succeq 0, \Delta_2 \prec 0) \\ \arctan(\frac{\Delta_1}{\Delta_2}) - \pi & (\Delta_1 \prec 0, \Delta_2 \prec 0) \\ +\pi/2 & (\Delta_1 \succ 0, \Delta_2 = 0) \\ -\pi/2 & (\Delta_1 \prec 0, \Delta_2 = 0) \\ \text{undefined} & (\Delta_1 = 0, \Delta_2 = 0) \end{cases} \tag{5.11}$$

and the effect on longitude of the Earth's rotation is accounted for in Equation (5.10) by the second term.

As given in Chapter 4, we proceed to calculate latitude and longitude, or (L,l), values for every position within the FoVs centred at (L_o,l_o) and at (L_c,l_c), according to Equations (4.10) and (4.11).

Equations (5.9) and (5.10), used to generate the (L_c,l_c) FoV centre position, are based on the Haversine formula giving great-circle distances between two points on a sphere from their latitudes and longitudes (Smart 1960). The versions presented, according to Movable Type Ltd. (Accessed: 2014), have been extensively evaluated and verified fit for purpose.

Figure 5.8 gives examples of latitude and longitude for three determined FoVs, their centres being given as: (0N,0E), (85N,133W), and (64S,137E).

We require the ability to perform vector calculations in the FoV centred at (L_o,l_o). Polarisations $\hat{\mathbf{m}}$, $\hat{\mathbf{n}}$, and $\hat{\mathbf{r}}$ remain constant in their alignment within a FoV regardless of the centre position of the FoV in which they are found. Polarisations $\hat{\mathbf{p}}$ and $\hat{\mathbf{q}}$ are (L, l) dependent however, and so calculations involving these two polarisations may be performed in the FoV centred at (L_o,l_o) through rotation back from their alignments at respective (L,l) positions in the FoV centred at (L_c,l_c). Their orientations within the FoV centred at (L_c,l_c) are given by Equations (5.5) and (5.6), where (L, l) values are determined through Equations (5.9), (5.10) to determine the FoV centre (L_c,l_c) to which the satellite has tracked, and (4.10), (4.11) to determine all (L,l) positions within this FoV. Their orientations within the FoV centred at (L_o,l_o) are given as,

$$\hat{\mathbf{p}}_{\text{FoV(Lo,lo)}} = \mathbf{R}_{\text{-l}}\mathbf{R}_{\text{-L}}\hat{\mathbf{p}}_{\text{FoV(Lc,lc)}} \tag{5.12}$$

and,

$$\hat{\mathbf{q}}_{\text{FoV(Lo,lo)}} = \mathbf{R}_{\text{-l}}\mathbf{R}_{\text{-L}}\hat{\mathbf{q}}_{\text{FoV(Lc,lc)}} \tag{5.13}$$

where,

$$\mathbf{R}_{\text{-L}} = \begin{bmatrix} \cos(-L) & 0 & -\sin(-L) \\ 0 & 1 & 0 \\ \sin(-L) & 0 & \cos(-L) \end{bmatrix} \tag{5.14}$$

and

$$\mathbf{R}_{\text{-l}} = \begin{bmatrix} \cos(-l) & -\sin(-l) & 0 \\ \sin(-l) & \cos(-l) & 0 \\ 0 & 0 & 1 \end{bmatrix}. \tag{5.15}$$

5.2.4 The Channel

Over a channel, received symbols may be given according to Goldsmith (2005) where,

$$\mathbf{Y} = \mathbf{H}\mathbf{X} + \mathbf{N}. \tag{5.16}$$

In Equation (5.16), $\mathbf{Y}$ is the set of received signals at the receiver, $\mathbf{H}$ represents a 3×3 complex fading channel matrix, $\mathbf{X}$ is a block of symbols sent and $\mathbf{N}$ is complex additive white Gaussian noise (AWGN) at the receiver R. Even though a 3×3 complex fading channel matrix is determined, only the first two columns of this matrix are required in a final determination of the tri-orthogonal arrangement at R, as the polarisation mode represented by unit vector $\hat{\mathbf{o}}$ is omitted from T.

A satellite channel typically does not provide a rich scattering environment that may benefit signal propagation in, for example, a densely populated urban environment employing wireless frequencies typically less than 6 GHz (Goldsmith 2005). In urban environments, a component of the signal may be reflected, or scattered, so as to arrive at the receiver. As propagation distances are relatively small, so received signal strength remains relatively high. Satellite channels are typically low rank and LoS in

nature (International Telecommunications Union (ITU-R) 1998, Lutz 1998, Fontan *et al.* 2001, Arapoglou *et al.* 2010b, Liolis *et al.* 2010). To provide additional capacity over satellite channels devoted to broadcasting and high capacity streaming, the introduction of dual polarisation per beam has been suggested as an option to more conventional linear polarisation techniques (Zorba *et al.* 2008, Arapoglou *et al.* 2011a); the advantage being that MIMO methods may provide additional diversity and hence performance over that of conventional SISO techniques, even in a channel devoid of scatterers and reflectors. While the adoption of a LHCP and RHCP system is suggested as a means of improving satellite link performance (Arapoglou *et al.* 2011b), the system would continue to be bound by antenna alignment, with CP mode propagation only possible in one alignment.

Here, consideration is made of a tri-orthogonal approach at the ground receiver at R which offers additional polarisation diversity over conventional CP mode antennas. The inclusion of a second tri-orthogonal arrangement in a satellite link would allow the possibility of simultaneous LHCP and RHCP transmission in more than one direction, through phasing techniques. For the system shown in Figure 5.4, the channel has six subchannels. Vector calculations are performed within the FoV centred at (L_o,l_o), while ionospheric parameters are obtained from the FoV centred at (L_c,l_c), which changes its position according to orbit parameters and time. The general form of the channel matrix, which is of rank 2, may be given as,

$$\mathbf{H} = \begin{bmatrix} h_{\hat{\mathbf{p}}\hat{\mathbf{m}}} & h_{\hat{\mathbf{p}}\hat{\mathbf{n}}} & h_{\hat{\mathbf{p}}\hat{\mathbf{o}}} \\ h_{\hat{\mathbf{q}}\hat{\mathbf{m}}} & h_{\hat{\mathbf{q}}\hat{\mathbf{n}}} & h_{\hat{\mathbf{q}}\hat{\mathbf{o}}} \\ h_{\hat{\mathbf{r}}\hat{\mathbf{m}}} & h_{\hat{\mathbf{r}}\hat{\mathbf{n}}} & h_{\hat{\mathbf{r}}\hat{\mathbf{o}}} \end{bmatrix} \tag{5.17}$$

where the matrix coefficients in Equation (5.17) represent signal transfer between polarisations. We include the polarisation denoted by unit vector $\hat{\mathbf{o}}$ at T for completeness.

For a LoS system, the magnitude of the electric field voltage transfer channel coefficients may be given by the square root of the power transfer coefficients from T to R (Lawrence *et al.* 2013), where power transfer is determined by the Friis power transfer equation (Friis 1946), which is readily found in Orfanidis (2002) and Pozar (2011), and is shown in this thesis in Equation (5.19). The channel matrix $\mathbf{H}$ is calculated for all positions within the FoV.

A channel matrix is typically complex in nature, consisting of a LoS component and a NLoS component. A complex Ricean fading channel matrix $\mathbf{H}$ may be decomposed into the sum of an average LoS component ($\bar{\mathbf{H}}$), as determined through Equation (5.19), and a variable scattered NLoS component ($\tilde{\mathbf{H}}$) determined by a Rayleigh, or complex Gaussian, distribution (Jakes 1974, Goldsmith 2005),

$$\mathbf{H} = \sqrt{\frac{K}{1+K}}\bar{\mathbf{H}} + \sqrt{\frac{1}{1+K}}\tilde{\mathbf{H}}. \tag{5.18}$$

The Ricean K-factor (Goldsmith 2005) determines the proportion of LoS component and NLoS component that propagate in the channel. The Ricean K-factor is determined as a function of environment.

In this chapter:

- a pure LoS channel is initially assumed for the NGSO satellite model, since this forms the backbone to which any statistical analysis may be applied. All three considered NGSO satellites are assumed to exhibit narrowband flat fading across their narrow bandwidths (Goldsmith 2005). As a result, it is possible to derive a pure LoS power transfer channel matrix, according to Equation (5.19), leading to a pure LoS electric voltage transfer channel matrix through square rooting of each channel element (Lawrence *et al.* 2013).

- the NLoS component, $\tilde{\mathbf{H}}$, is included according to a fast fading multipath component incorporated within a total fading margin. Total fading margins are given in Table 5.1 for the three presented NGSO satellites, and these are applied to the LoS power transfer channel matrix, to give a worst case reception at R. The effect of scintillation may be considered as adding to multipath power, which is included as a component of the total fading margin. It is not considered as one of the principle effects that impinge on satellite to terrestrial link propagation. The principle effects on such propagation are given as the Faraday effect and path delay (International Telecommunications Union (ITU-R) 1998). In Fontan *et al.* (2001), the effect of Doppler shift is included as a dispersion effect or spread on the signal.

- a general statistical analysis is performed for each of the three NGSO satellites, according to total fading margin.

- extension is made to the statistical analysis of the Iridium satellite system over the FoV according to empirical measurement (Fontan *et al.* 2001). This analysis includes the slow fading effect of shadowing, and the fast fading effect of multipath, that are both given as a function of elevation and channel environment.

Several factors affect signal transfer over the six subchannels, and the Friis power transfer equation is used to calculate their influence on power transfer between each receive-transmit polarisation pair for every (L,l) point within the FoV. The Friis power transfer formula for calculating deterministic LoS power transfer from T to R is given as,

$$\frac{P_{\mathrm{R}}}{P_{\mathrm{T}}} = G_{\mathrm{T}} G_{\mathrm{R}} \left(\frac{\lambda}{4\pi s} \right)^2 e_{\mathrm{pol}} L_{\mathrm{atmos}} \tag{5.19}$$

where R refers to the ground receiver, T refers to the satellite transmitter, P is power, G is antenna mode gain, λ is transmitted signal wavelength, s is separation of T and R, e_{pol} is the polarisation mismatch between a polarisation at T and a polarisation at R, and L_{atmos} is atmospheric attenuation. At L-band frequencies, both precipitation effects and atmospheric attenuation are negligible (Roddy 2006, Pozar 2011).

5.2.5 Polarisation

Propagation between a polarisation at T and at R may be represented as a channel coefficient in the power transfer form of the channel matrix, given in Equation 5.17.

For a polarisation pair such as $\hat{\mathbf{r}}\hat{\mathbf{m}}$, polarisation mismatch may be given by the inner product in Equation (5.20) (Orfanidis 2002),

$$e_{\mathrm{pol}(\hat{\mathbf{r}}\hat{\mathbf{m}})} = |\hat{\mathbf{r}}_{\perp\mathbf{k}} \cdot \hat{\mathbf{m}}_{\perp\mathbf{k}}|^2 \tag{5.20}$$

where $\hat{\mathbf{r}}_{\perp\mathbf{k}}$ and $\hat{\mathbf{m}}_{\perp\mathbf{k}}$ are projections onto the plane perpendicular to the unit propagation vector $\hat{\mathbf{k}}$.

The projection of an arbitrary vector $\mathbf{v}$ onto the plane perpendicular to $\hat{\mathbf{k}}$ may be given by,

$$\mathbf{v}_{\perp\mathbf{k}} = \left(\mathbf{I_3} - \hat{\mathbf{k}}\hat{\mathbf{k}}^{\mathrm{T}} \right) \hat{\mathbf{v}}, \tag{5.21}$$

which may be normalised to give,

$$\hat{\mathbf{v}}_{\perp\mathbf{k}} = \frac{\mathbf{v}_{\perp\mathbf{k}}}{|\mathbf{v}_{\perp\mathbf{k}}|}. \tag{5.22}$$

5.2.6 Gain

The boresight gains at T for each of the three satellite systems are given in Table 5.1, and in Figure 5.3.

At the receiver R, the power gain G of a half-wavelength dipole (Orfanidis 2002, Balanis 2005), such as that associated with polarisation mode $\hat{\mathbf{r}}$, is given by Equation (5.23). This assumes 100% dipole efficiency and is given as,

$$G(\theta,\phi) = \frac{1.64}{\sin^2\theta}\cos^2\left(\frac{\pi}{2}\cos\theta\right). \tag{5.23}$$

In the case of a vertical half-wavelength dipole mode, with polarisation orthogonal to the antenna surface, minimum gain occurs when θ is 0°, or at the endfire position. Maximum gain occurs when θ is 90°, or at the broadside position, and is independent of the azimuthal angle. As the antenna surface is held orthogonal to the zenith direction, so minimum gain is in the zenith direction. The gain profile of a half-wavelength dipole provides a wide hemispherical radiation pattern of low gain, which is typical of a receive antenna for the three NGSO satellite systems being considered.

In the case of the half-wavelength dipole gain associated with polarisation mode $\hat{\mathbf{r}}$ at R, angle θ is represented by κ, the sum of α and γ, as in Figure 4.1.

For an orthogonally polarised arrangement at R, it is important to recognise that the gain profile, as well as the polarisation mismatch profile, changes for polarisation modes $\hat{\mathbf{p}}$ and $\hat{\mathbf{q}}$ as a function of latitude and longitude, or global (L,l) position. For half-wavelength dipole gains associated with polarisation modes $\hat{\mathbf{p}}$ and $\hat{\mathbf{q}}$, and following rotation of these polarisation modes back into the FoV centred at (L_o,l_o) through Equations (5.12) and (5.13), we use Equation (5.24) to determine gain,

$$G(\theta,\phi) = 1.64|\hat{\mathbf{v}} \wedge \hat{\mathbf{k}}|^3 \tag{5.24}$$

where $\hat{\mathbf{v}}$ represents the unit polarisation mode vector in question, and $\hat{\mathbf{k}}$ is the unit propagation vector. As an example, for the Iridium system, gains are attributed to

polarisation modes $\hat{\mathbf{p}}$ and $\hat{\mathbf{q}}$ as a function of (L,l) global position, shown in Figure 5.9, along with the fixed gains attributed to polarisation modes $\hat{\mathbf{m}}$, $\hat{\mathbf{n}}$, $\hat{\mathbf{o}}$, and $\hat{\mathbf{r}}$.

5.2.7 Faraday Rotation and Path Delay

For the method of calculating Faraday rotation and path delay in this thesis, the reader is referred to Chapter 4.

Faraday rotation is implemented in the simulation by a rotation of the polarisation modes $\hat{\mathbf{m}}$ and $\hat{\mathbf{n}}$, at T, about the propagation vector $\hat{\mathbf{k}}$, by the Faraday rotation angle. This is subsequently used in the determination of polarisation mismatches between T and R, as per Equation (5.20). The effect of Faraday rotation is to improve subchannel propagation at some global (L, l) locations where R is positioned, while worsen it for others.

Figures 5.10 and 5.11 show the effect of Faraday rotation on system polarisation mismatch over each subchannel using realtime data, and according to orbital parameters of the Iridium system. It is noteworthy to recall that, according to Wright *et al.* (2003), a Faraday rotation of 5° is enough to greatly affect DP mode SAR signal recovery.

5.2.8 Doppler Frequency Shift

Fast fading considers the effect of multipath power on signal reception. The principle contributors to this phenomenon are a large number of scattered rays. Each ray is subjected to attenuation, time delay, phase and Doppler shift. Fast fading may be represented by a Rayleigh, or complex Gaussian, distribution (Goldsmith 2005, Bohagen *et al.* 2005), in the guise of multipath power or MP (Fontan *et al.* 2001). For a NGSO satellite system, fast fading is typically small, due to the absence of scatterers in the channel, with Doppler shift being small due to the relative velocities involved.

Doppler shift is time-varying as the satellite moves over the ground receiver. The Doppler shift in three dimensions of the NGSO satellite with respect to a stationary ground receiver is computed in the channel model. Due to the tangential velocity of LEO satellites, of the order of 7.5km/s, any velocity of a receiver on the ground may be neglected (Stavroulakis 2012). Doppler shift is most pronounced when a LEO satellite, at the horizon, begins a path over the ground receiver that passes through the receiver zenith point. As a LEO satellite approaches from the ground receiver horizon toward

the ground receiver, it is considered to be in a slow fading regime. As the satellite approaches the zenith position, a faster fading regime is encountered as the Doppler shift passes overhead (Stavroulakis 2012). At the zenith point, the Doppler shift has zero magnitude, after which its magnitude begins to increase again but with a reversal in polarity. The magnitude of the maximum shift is a function of elevation at the receiver. An example of three dimensional Doppler shift for an Iridium satellite tracking west to east while passing over a stationary ground receiver at any (L,l) position within the FoV is shown in Figure 5.12.

In Figure 5.12, agreement with the Doppler shift shown in Fontan *et al.* (2001) is observed for the Iridium LEO satellite in a 780 km orbit, and a stationary ground receiver. A maximum magnitude of Doppler shift of 35 kHz is observed at the FoV edges.

In the model, the ground receiver is assumed stationary. The Doppler shift due to a fast-evolving LEO satellite orbit may affect receiver synchronisation, although relative satellite motion may be compensated for at the receiver (Katayama *et al.* 1992, Ali *et al.* 2006). Anomalies occur as a result of changes in orbit and terrain contours (Davis *et al.* 1997).

The direction of tangential velocity associated with the NGSO satellite at T changes as a function of time, in order to maintain the orbit path, and is given by a shortest route bearing angle, θ_{sb} (Movable Type Ltd. Accessed: 2014),

$$\begin{aligned}\theta_{\text{sb}} \;=\; &\Big|\text{atan}_2\{\sin(L_{\text{o}}-L_{\text{c}})\cos(L_{\text{c}}),\\ &\cos(L_{\text{c}})\sin(L_{\text{o}})-\sin(L_{\text{c}})\cos(L_{\text{o}})\cos(l_{\text{o}}-l_{\text{c}})\},\\ &2\pi\Big|\end{aligned} \tag{5.25}$$

where the function $\text{atan}_2(\Delta_1, \Delta_2)$ is given in Equation (5.11).

Figure 5.13 illustrates the changing nature of the unit velocity vector, $\hat{\mathbf{v}}_{\text{T}}$, associated with T, as a function of global (L_{c},l_{c}) position. In effect, the velocity vector of T, $\mathbf{v}_{\text{T}}$, is seen to rotate about the FoV centre (L_{o},l_{o}) to $\mathbf{v}_{\text{T}'}$, as a function of global (L_{c},l_{c}) position.

To determine the Doppler frequency shift as a function of the position of T along the orbit path, we start with the initial bearing angle at the centre of the (L_{o},l_{o}) FoV, θ_{bFoV}, and determine the bearing angle at the centre of the (L_{c},l_{c}) FoV, $\theta_{\text{bFoV}'}$. This is given as,

$$\theta_{\text{bFoV}'} = \begin{cases} \theta_{\text{sb}}(t=0) \\ \theta_{\text{sb}} + \pi\left(\left|\|\mathbf{v}_{\text{T}}\|t/r_{\text{e}}, 1\right| \prec 0.5\right) \\ \theta_{\text{sb}}\left(\left|\|\mathbf{v}_{\text{T}}\|t/r_{\text{e}}, 1\right| \succeq 0.5\right). \end{cases} \tag{5.26}$$

We may align the (L_{c},l_{c}) FoV with the initial (L_{o},l_{o}) FoV on the ECEF a-axis, as illustrated in Figure 5.13. The bearing angle, $\theta_{\text{bFoV}'}$, may then rotate in the bc plane, or local xy FoV plane, about the a-axis, as a function of FoV centre position, (L_{c},l_{c}), along the orbit path.

In the (L_{c},l_{c}) FoV, the orbital inclination angle $\theta_{\text{inc}'}$ is analgous to that of the initial (L_{o},l_{o}) FoV, θ_{inc}. It is used in conjunction with $\theta_{\text{bFoV}'}$, for the determination of the Doppler frequency shift uniquely, as a function of (L_{c},l_{c}) FoV centre position,

$$\theta_{\text{inc}'} = \left|\theta_{\text{bFoV}'} - 2.5\pi, 2\pi\right|. \tag{5.27}$$

The tangential velocity unit vector for any FoV centre position, (L_{c},l_{c}), along the orbit path may be given in the FoV centred at (L_{o},l_{o}) as,

$$\hat{\mathbf{v}_{\text{T}}} = \begin{bmatrix} 0 \\ \cos\theta_{\text{inc}'} \\ \sin\theta_{\text{inc}'} \end{bmatrix}. \tag{5.28}$$

If required, receiver velocity, $\mathbf{v}_{\text{R}}$, may be given according to a user defined magnitude and a unit vector direction $\hat{\mathbf{v}_{\text{R}}}$, specified by rotating $\hat{\mathbf{p}}$ around $\hat{\mathbf{r}}$ by a user defined angle. In this thesis, $\mathbf{v}_{\text{R}}$ is set to zero. The Doppler frequency shift is given according to Ali *et al.* (1998) and Boiardt and Rodriguez (2010),

$$f_{\text{Doppler}} = \frac{v_{\text{closing}} f}{c} \tag{5.29}$$

where v_{closing} is the relative velocity of T and R, and is given as,

$$v_{\text{closing}} = \hat{\mathbf{v}_{\text{T}}} \cdot \hat{\mathbf{k}} + \hat{\mathbf{v}_{\text{R}}} \cdot \hat{\mathbf{k}}. \tag{5.30}$$

Examples of three dimensional Doppler shifts due to various Iridium LEO satellite orbit trajectories and ground receiver motions are shown in Figure 5.14.

5.2.9 Two State Ionosphere

In the satellite channel simulations demonstrated in this chapter, enhancement is made of the ionospheric modelling by providing a two state diurnal ionosphere as a function of (l) and Coordinated Universal Time, or UTC (Bureau International des Poids et Mesures Accessed: 2016). Coordinated Universal Time is not a time zone, but rather an atomc time scale that does not have daylight saving applied to it. It is often mistaken for Greenwich Mean Time, or GMT, as the two are aligned on the Greenwich Meridian in London, UK. The two states of the ionosphere in the simulations are given as either a day or night profile corresponding to an average of the day time solar minimum and maximum, or night time solar minimum and maximum respectively. The variation between day and night profiles stems from changes in ionospheric electron density at a specific altitude as a function of solar activity (Feltens 2007, Mitch *et al.* 2013). The two states, or scaled ionospheric profiles, are generated from those in Figure 4.3 of Chapter 4. The two profiles are calculated as the mean of solar maxima and minima ionospheric electron density profiles for both day and night (Kelley 2009). The two diurnal states scale the interaction between the ionosphere and a propagating signal as a function of ionospheric electron density at a (L, l, h) position along a propagation path normalised by an average of ionospheric electron density in a vertical column which passes through the ionosphere at this (L, l, h) position. We assume the ionosphere to lie between 50 km and 1000 km in geodetic altitude. Figure 5.15 shows the day and night scaling factors as a function of altitude. The scaling factors for both averaged day and night profiles provide a profile equivalent to a unity scale for propagation through the entire ionosphere. For off-nadir transmission, TEC may vary as a function of (L,l) position. By introducing the scaling factors, we provide the possibility of simulating ionospheric effects on a transmitted signal as a function of (L, l, h) position, at multiple points along the propagation path.

The Earth's rotation provides movement of longitudinal position at the angular rate of 15°/hr, regardless of latitudinal position. As well as affecting the celestial position of a satellite, this movement affects the position of a ground receiver relative to the Sun. Coordinated Universal Time provides a reference that we may use in order to provide either of the two ionospheric profiles. Figure 5.16 illustrates the concept according to

a plane AB that effectively separates terrestrial night and day as a function of (l) and temporal positioning according to UTC. The global position (0,0), where all simulations are begun, is positioned in the middle of the night, or midnight, at 0000 UTC. At this time, all longitudes lying between 90° and 270° are assumed to possess a daytime ionospheric profile. Six hours later, at 0600 UTC, the Earth has rotated eastward by 90°, and all longitudes lying between 0° and 180° are now assumed to possess a daytime ionospheric profile.

5.2.10 Satellite Channel Matrix

The aim of a tri-orthogonal approach at R is to increase diversity, and hence captured signal for processing into intelligible information at the receiver. Interest centres around the electric voltage transfer of each of the two transmitted waveforms from T to R, that are the components of CP mode wave transmission.

To derive the final form of a matrix describing complex electric voltage transfer from T to R, with both LoS and NLoS components represented, a general procedure may be applied at all (L,l) positions in the FoV, as detailed below.

- (a) Determine LoS power transfer over each subchannel according to the Friis power transfer formula, given by Equation 5.19.
- (b) Determine the magnitude of LoS electric voltage transfer through the square root of the LoS power transfer over each subchannel.
- (c) Determine a relative phase offset matrix at T, and multiply this elementwise with the matrix of magnitudes of LoS electric voltage transfer in (b).
- (d) Determine a matrix for the complex exponential phase change of the LoS electric voltage transfer across the channel, and a relative phase offset matrix at R. Multiply these matrices elementwise with the resultant matrix in (c). This provides a complex phasor voltage form matrix which may be readily converted to complex $x + iy$ form. This is the complex LoS electric voltage transfer channel matrix, $\bar{\mathbf{H}}$.
- (e) Determine a mutual coupling matrix at T, and multiply with the resultant matrix in (d). This results in a matrix describing complex LoS electric voltage

transfer from a polarisation at T to a polarisation at R, prior to mutual coupling effects at R.

- (f) Determine subchannel complex NLoS electric voltage transfers through a complex Gaussian random matrix with independent zero mean and unit variance. Scale this matrix elementwise according to the square root of received signal power over each subchannel at R. The resulting matrix is then multiplied with correlation matrices at T and at R. This provides the complex NLoS electric voltage transfer channel matrix, $\tilde{\mathbf{H}}$.
- (g) Through application of the Ricean K-factor, provide LoS and NLoS electric voltage transfer proportioned coefficients in complex matrix form, using final matrices established in (e) and (f). This determines a complex electric voltage transfer matrix across the channel, prior to mutual coupling effects at R.
- (h) Apply a mutual coupling matrix at R through multiplication with the LoS and NLoS Ricean K-factor proportioned components of (g). This provides the final complex channel matrix, $\mathbf{H}$, which describes all channel effects on emitted signals from T to the point of reception at R.
- (i) Determine the capacity at a given location in the FoV, using Equation 5.41.
- (j) Repeat for all positions in the FoV.

Magnitude of LoS Electric Voltage Transfer Magnitude

We introduce the magnitude of LoS electric voltage signal transfer, $\|h_{\mathrm{E}}\|$, as proportional to the square root of LoS power transfer through each subchannel (Lawrence *et al.* 2013).

The matrix form of the magnitude of LoS electric voltage signal transfer is given by,

$$\bar{\mathbf{H}}_{\mathrm{E}} = \begin{bmatrix} \sqrt{\frac{P_{\hat{\mathbf{p}}\hat{\mathbf{m}}}}{P_{\hat{\mathbf{m}}}}} & \sqrt{\frac{P_{\hat{\mathbf{p}}\hat{\mathbf{n}}}}{P_{\hat{\mathbf{n}}}}} & \sqrt{\frac{P_{\hat{\mathbf{p}}\hat{\mathbf{o}}}}{P_{\hat{\mathbf{o}}}}} \\ \sqrt{\frac{P_{\hat{\mathbf{q}}\hat{\mathbf{m}}}}{P_{\hat{\mathbf{m}}}}} & \sqrt{\frac{P_{\hat{\mathbf{q}}\hat{\mathbf{n}}}}{P_{\hat{\mathbf{n}}}}} & \sqrt{\frac{P_{\hat{\mathbf{q}}\hat{\mathbf{o}}}}{P_{\hat{\mathbf{o}}}}} \\ \sqrt{\frac{P_{\hat{\mathbf{r}}\hat{\mathbf{m}}}}{P_{\hat{\mathbf{m}}}}} & \sqrt{\frac{P_{\hat{\mathbf{r}}\hat{\mathbf{n}}}}{P_{\hat{\mathbf{n}}}}} & \sqrt{\frac{P_{\hat{\mathbf{r}}\hat{\mathbf{o}}}}{P_{\hat{\mathbf{o}}}}} \end{bmatrix}. \tag{5.31}$$

Complex Phase Offset of LoS Electric Voltage Transfer at T

A phase matrix is required that introduces a relative complex phase offset at T on the transmitted signals to undergo LoS electric voltage transfer.

$$\mathbf{Ph}_{\mathrm{T}} = \begin{bmatrix} \exp(-j\phi_{\mathrm{T}\hat{\mathbf{p}}\hat{\mathbf{m}}}) & \exp(-j\phi_{\mathrm{T}\hat{\mathbf{p}}\hat{\mathbf{n}}}) & \exp(-j\phi_{\mathrm{T}\hat{\mathbf{p}}\hat{\mathbf{o}}}) \\ \exp(-j\phi_{\mathrm{T}\hat{\mathbf{q}}\hat{\mathbf{m}}}) & \exp(-j\phi_{\mathrm{T}\hat{\mathbf{q}}\hat{\mathbf{n}}}) & \exp(-j\phi_{\mathrm{T}\hat{\mathbf{q}}\hat{\mathbf{o}}}) \\ \exp(-j\phi_{\mathrm{T}\hat{\mathbf{r}}\hat{\mathbf{m}}}) & \exp(-j\phi_{\mathrm{T}\hat{\mathbf{r}}\hat{\mathbf{n}}}) & \exp(-j\phi_{\mathrm{T}\hat{\mathbf{r}}\hat{\mathbf{o}}}) \end{bmatrix}. \tag{5.32}$$

The complex LoS phase matrix $\mathbf{Ph}_{\mathrm{T}}$ of Equation (5.32) is multiplied elementwise with the channel matrix of the magnitudes of LoS electric voltage transfer $\bar{\mathbf{H}}_{\mathrm{E}}$ in Equation (5.31).

Complex Phase of LoS Electric Voltage Transfer Through Channel

A phase matrix is required that introduces a complex phase change for LoS electric voltage transfer along a subchannel from T to R as a result of deterministic path delay, and Doppler shift. A phase argument, ϕ, for each subchannel is given by,

$$\phi_{\mathrm{Ch}} = 2\pi(f + f_{\mathrm{Doppler}})\left(\frac{s+\zeta}{c}\right). \tag{5.33}$$

In Equation (5.33), f is the transmitted signal frequency, f_{Doppler} is the Doppler frequency shift, and c is the speed of light. A complex LoS phase matrix for channel propagation $\mathbf{Ph}_{\mathrm{Ch}}$ is established of the form,

$$\mathbf{Ph}_{\mathrm{Ch}} = \begin{bmatrix} \exp(-j\phi_{\mathrm{Ch}\hat{\mathbf{p}}\hat{\mathbf{m}}}) & \exp(-j\phi_{\mathrm{Ch}\hat{\mathbf{p}}\hat{\mathbf{n}}}) & \exp(-j\phi_{\mathrm{Ch}\hat{\mathbf{p}}\hat{\mathbf{o}}}) \\ \exp(-j\phi_{\mathrm{Ch}\hat{\mathbf{q}}\hat{\mathbf{m}}}) & \exp(-j\phi_{\mathrm{Ch}\hat{\mathbf{q}}\hat{\mathbf{n}}}) & \exp(-j\phi_{\mathrm{Ch}\hat{\mathbf{q}}\hat{\mathbf{o}}}) \\ \exp(-j\phi_{\mathrm{Ch}\hat{\mathbf{r}}\hat{\mathbf{m}}}) & \exp(-j\phi_{\mathrm{Ch}\hat{\mathbf{r}}\hat{\mathbf{n}}}) & \exp(-j\phi_{\mathrm{Ch}\hat{\mathbf{r}}\hat{\mathbf{o}}}) \end{bmatrix}. \tag{5.34}$$

Finally, we may represent a complex relative LoS phase offset matrix at R as,

$$\mathbf{Ph}_{\mathrm{R}} = \begin{bmatrix} \exp(-j\phi_{\mathrm{R}\hat{\mathbf{p}}\hat{\mathbf{m}}}) & \exp(-j\phi_{\mathrm{R}\hat{\mathbf{p}}\hat{\mathbf{n}}}) & \exp(-j\phi_{\mathrm{R}\hat{\mathbf{p}}\hat{\mathbf{o}}}) \\ \exp(-j\phi_{\mathrm{R}\hat{\mathbf{q}}\hat{\mathbf{m}}}) & \exp(-j\phi_{\mathrm{R}\hat{\mathbf{q}}\hat{\mathbf{n}}}) & \exp(-j\phi_{\mathrm{R}\hat{\mathbf{q}}\hat{\mathbf{o}}}) \\ \exp(-j\phi_{\mathrm{R}\hat{\mathbf{r}}\hat{\mathbf{m}}}) & \exp(-j\phi_{\mathrm{R}\hat{\mathbf{r}}\hat{\mathbf{n}}}) & \exp(-j\phi_{\mathrm{R}\hat{\mathbf{r}}\hat{\mathbf{o}}}) \end{bmatrix}. \tag{5.35}$$

The matrices of Equations (5.34) and (5.35) are multiplied elementwise with the matrices of Equations (5.31) and (5.32). The resulting matrix is in complex exponential phasor form, but may be readily converted to a matrix of complex x+iy form. The complex LoS electric voltage transfer channel matrix over a set of subchannels may be given as,

$$\bar{\mathbf{H}} = \bar{\mathbf{H}}_{\mathrm{E}} \odot \mathbf{Ph}_{\mathrm{T}} \odot \mathbf{Ph}_{\mathrm{Ch}} \odot \mathbf{Ph}_{\mathrm{R}}. \tag{5.36}$$

Equation (5.36), where $\odot$ represents the elementwise or Hadamard product, provides the LoS electric voltage transfer channel matrix, $\bar{\mathbf{H}}$, which is then multiplied with a mutual coupling matrix, $\mathbf{X}_{\mathrm{T}}$, representing mutual polarisation coupling at T through matrix coefficients,

$$\mathbf{X}_{\mathrm{T}} = \frac{1}{\sqrt{W}} \begin{bmatrix} 1 & \rho_{\hat{\mathbf{m}}\hat{\mathbf{n}}} & \rho_{\hat{\mathbf{m}}\hat{\mathbf{o}}} \\ \rho_{\hat{\mathbf{n}}\hat{\mathbf{m}}} & 1 & \rho_{\hat{\mathbf{n}}\hat{\mathbf{o}}} \\ \rho_{\hat{\mathbf{o}}\hat{\mathbf{m}}} & \rho_{\hat{\mathbf{o}}\hat{\mathbf{n}}} & 1 \end{bmatrix}. \tag{5.37}$$

As mutual coupling reciprocity exists, in other words $\rho_{\hat{\mathbf{m}}\hat{\mathbf{n}}}$ equals $\rho_{\hat{\mathbf{n}}\hat{\mathbf{m}}}$, so the normalising term W in Equation (5.37) is given by Sirianunpiboon *et al.* (2009) as,

$$W = \max(1 + |\rho_{\hat{\mathbf{m}}\hat{\mathbf{n}}}|^2 + |\rho_{\hat{\mathbf{m}}\hat{\mathbf{o}}}|^2, 1 + |\rho_{\hat{\mathbf{m}}\hat{\mathbf{n}}}|^2 + |\rho_{\hat{\mathbf{n}}\hat{\mathbf{o}}}|^2, 1 + |\rho_{\hat{\mathbf{m}}\hat{\mathbf{o}}}|^2 + |\rho_{\hat{\mathbf{n}}\hat{\mathbf{o}}}|^2). \tag{5.38}$$

This resulting matrix is the complex LoS electric voltage transfer matrix, prior to mutual coupling effects at R.

5.2.11 Pure LoS Power Transfer

The final channel matrix form for a pure LoS signal transfer regime is given according to Sirianunpiboon *et al.* (2009) and Arapoglou *et al.* (2011b) as,

$$\mathbf{H} = \mathbf{X}_{\mathrm{R}}{}^{\dagger} \bar{\mathbf{H}} \mathbf{X}_{\mathrm{T}} \tag{5.39}$$

where the superscript denotes the Hermitian transpose, $\mathbf{X}_{\mathrm{T}}$ is given in Equation (5.37), and $\bar{\mathbf{H}}$ is given in Equation (5.36). Mutual coupling at R, where mutual coupling reciprocity once again exists, is given by $\mathbf{X}_{\mathrm{R}}$ as,

$$\mathbf{X}_{\mathrm{R}} = \frac{1}{\sqrt{W}} \begin{bmatrix} 1 & \rho_{\hat{\mathbf{p}}\hat{\mathbf{q}}} & \rho_{\hat{\mathbf{p}}\hat{\mathbf{r}}} \\ \rho_{\hat{\mathbf{q}}\hat{\mathbf{p}}} & 1 & \rho_{\hat{\mathbf{q}}\hat{\mathbf{r}}} \\ \rho_{\hat{\mathbf{r}}\hat{\mathbf{p}}} & \rho_{\hat{\mathbf{r}}\hat{\mathbf{q}}} & 1 \end{bmatrix}, \tag{5.40}$$

where the normalising term, W, is given in Equation (5.38).

A polarisation coupling factor, ρ, of 0.3 (Sirianunpiboon *et al.* 2009), is applied at both T and R, in Equations (5.37) and (5.40). This value corresponds to a mutual coupling coefficient of -10.45 dB, which sits at the upper bound of tolerated mutual coupling for antennas (Ding *et al.* 2007, Verdone and Zanella 2012). For mobile PIFA antennas, this figure is often not achieved. Examination of the inclusion of a third orthogonal polarisation mode at R is to be made, and so system parameters that err on the side of caution are used. As such, a lower bound on capacity improvement is provided through the inclusion of a third orthogonal polarisation at R. In King and Stavrou (2007), cross polarisation discrimination values of 15 dB at R and 20 dB at T are noted, and the limitation on dynamic range validity that this imposes. Providing increased polarisation decoupling, or isolation, at R would reduce mutual coupling, and improve performance of the system. Mutual coupling distorts radiation patterns and reduces both polarisation and pattern diversity, and so MIMO performance (Svantesson and Ranheim 2001, Janaswamy 2002, Fletcher *et al.* 2003, Wallace and Jensen 2004). The assumption is made of mutual coupling reciprocity between polarisation mode pairs in Equations (5.37) and (5.40). As a singular value of ρ of 0.3 is assumed, so this value is applied to the denominator of the scalar multiplier in Equations (5.37) and (5.40). The normalising term, W, equals 1.18 as a result of the choice of polarisation coupling factor.

Within the final form of the pure LoS channel matrix, $\mathbf{H}$, in Equation (5.39), for a tri-orthogonal arrangement at T and at R, nine signal transfer matrix elements exist. Each element represents subchannel propagation, with the channel matrix being of the form in Equation (5.17). For a measurement of system performance, through capacity, six subchannels are used, or the first two columns in this instance. This is because transmission from T using conventional CP mode wave propagation is employed. As previously stated, no transmission is assumed from polarisation mode $\hat{\mathbf{o}}$.

As a comparison is being made with conventional RHCP waveform transmission, so it is reasonable to invoke phase offsets on a polarised mode at T and a polarised mode at R that are aligned at the FoV centre.

In Equation (5.32), for RHCP mode transmission from T, ϕ_{T} is set to 90° for transmission using polarisation mode $\hat{\mathbf{m}}$. At R, for RHCP mode reception, we set ϕ_{R} to -90° in Equation (5.35) for reception using polarisation mode $\hat{\mathbf{p}}$. All remaining polarisation

mode phase offsets at T and at R are set to zero. In so doing, the system conforms with standard convention (Balanis 2005).

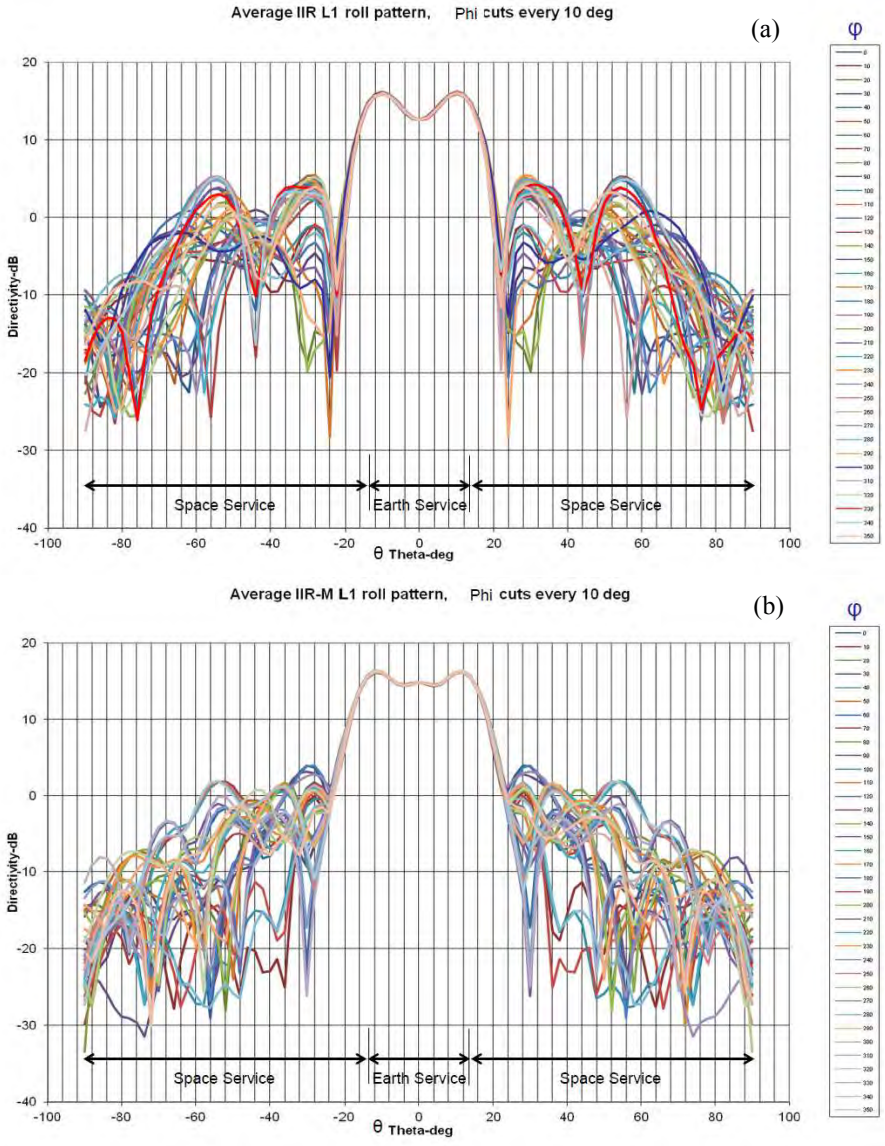

Figure 5.2. Transmit gain profile of L1 GPS system. Images shown are: (a) 'Legacy' profile, (b) 'Improved profile'. After Marquis (Accessed: 2014) and Marquis and Reigh (Accessed: 2015).

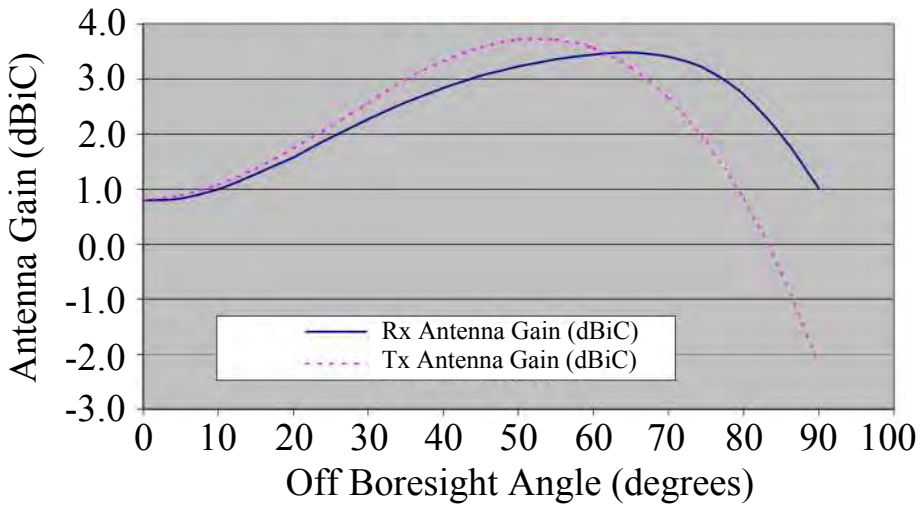

Figure 5.3. Orbcomm LEO satellite system Tx and Rx gains at the satellite, T. After Orbcomm LLC (Accessed: 2014).

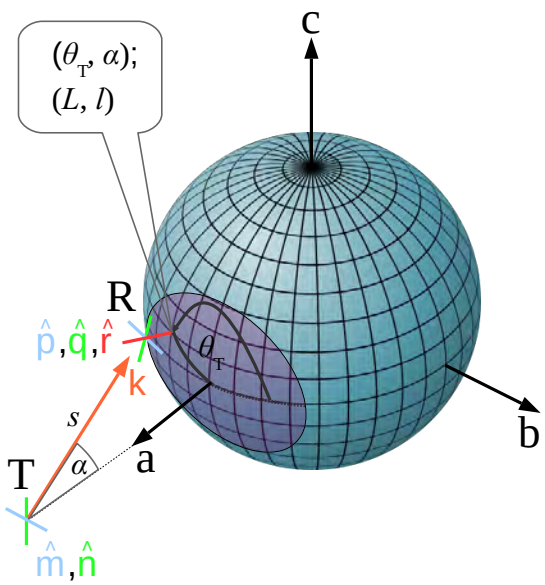

Figure 5.4. Satellite system providing conventional CP mode wave transmission to the nadir location in the NGSO ionospheric channel FoV. An Earth Centred Earth Fixed (ECEF) coordinate system locates position in three dimensional space. Propagation is from transmitter T, using two orthogonal polarisation modes to represent CP wave transmission, to receiver R, using a tri-orthogonal arrangement, along a path of length s. The five system polarisation modes are labelled $\hat{\mathbf{m}}$ to $\hat{\mathbf{r}}$. Link direction is given by a propagation vector, $\mathbf{k}$. Propagation to a point in the FoV is determined by α and θ_T. These angles correspond to a (latitude, longitude), or (L,l), global position, enabling link characteristics to be determined as a function of global location and NGSO FoV geometry.

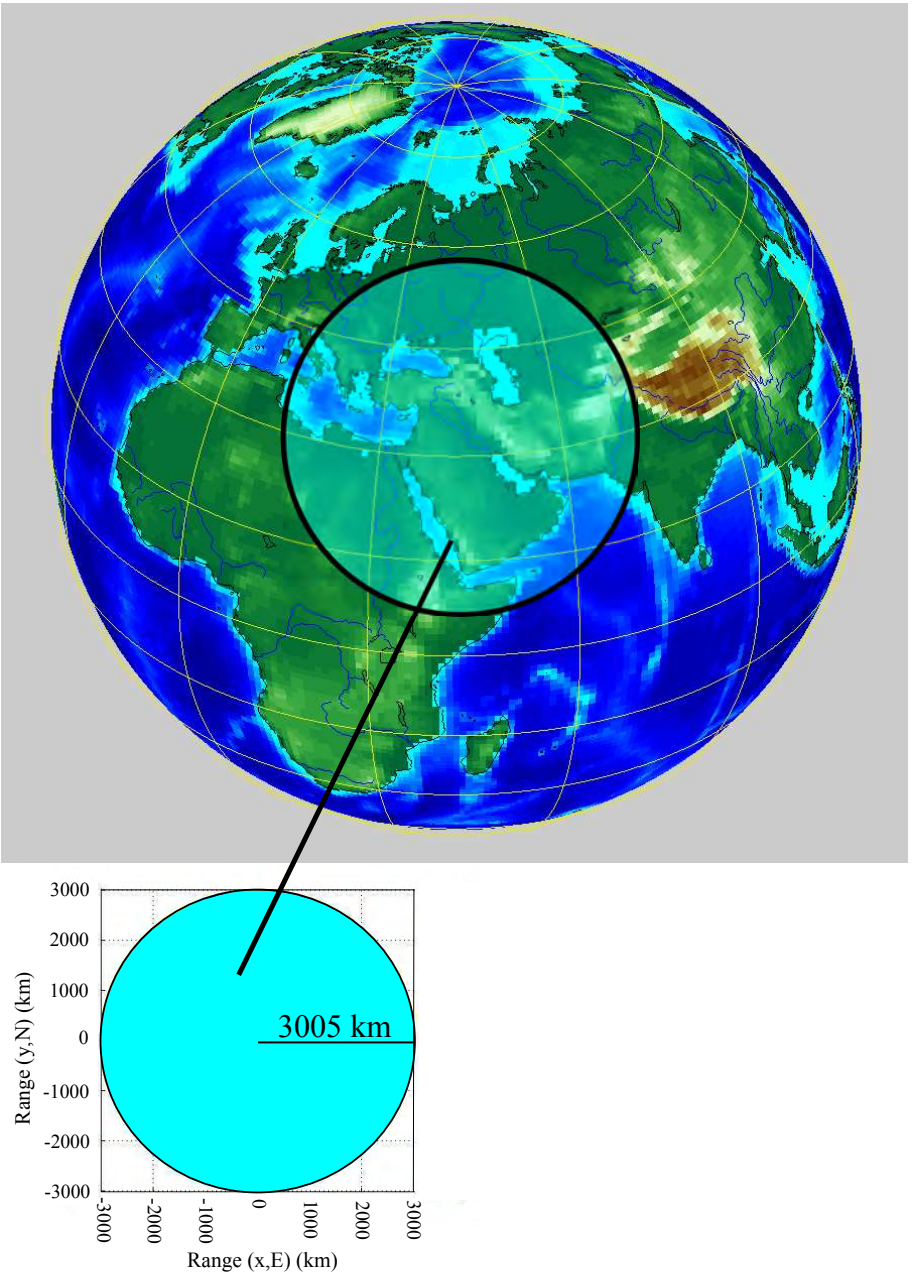

Figure 5.5. Iridium system FoV dimensional metrics, according to orbital parameters in Table 5.1. The FoV is given as a function of orbit height (780 km), with the FoV edge being a perimeter where the half-wavelength dipole, or polarisation mode, $\hat{\mathbf{r}}$ is broadside to the unit propagation vector, $\hat{\mathbf{k}}$. At this point, $\kappa = 90°$, as observed in Figure 4.1. The image of the Earth is generated in Matlab using a mapping toolbox function.

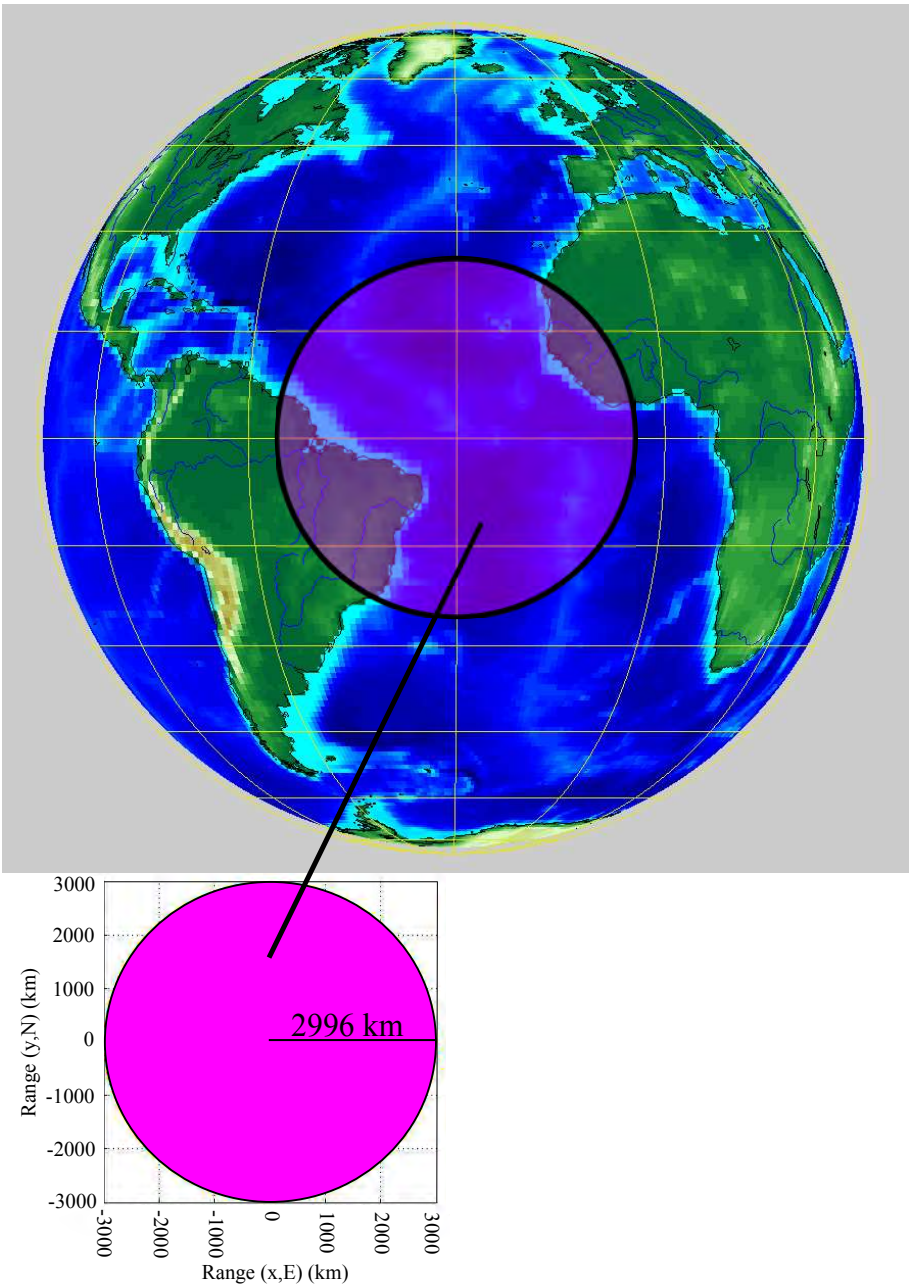

Figure 5.6. Orbcomm system FoV dimensional metrics, according to orbital parameters in Table 5.1. The FoV is given as a function of orbit height (775 km), with the FoV edge being a perimeter where the half-wavelength dipole, or polarisation mode, $\hat{\mathbf{r}}$ is broadside to the unit propagation vector, $\hat{\mathbf{k}}$. At this point, $\kappa = 90°$, as observed in Figure 4.1. The image of the Earth is generated in Matlab using a mapping toolbox function.

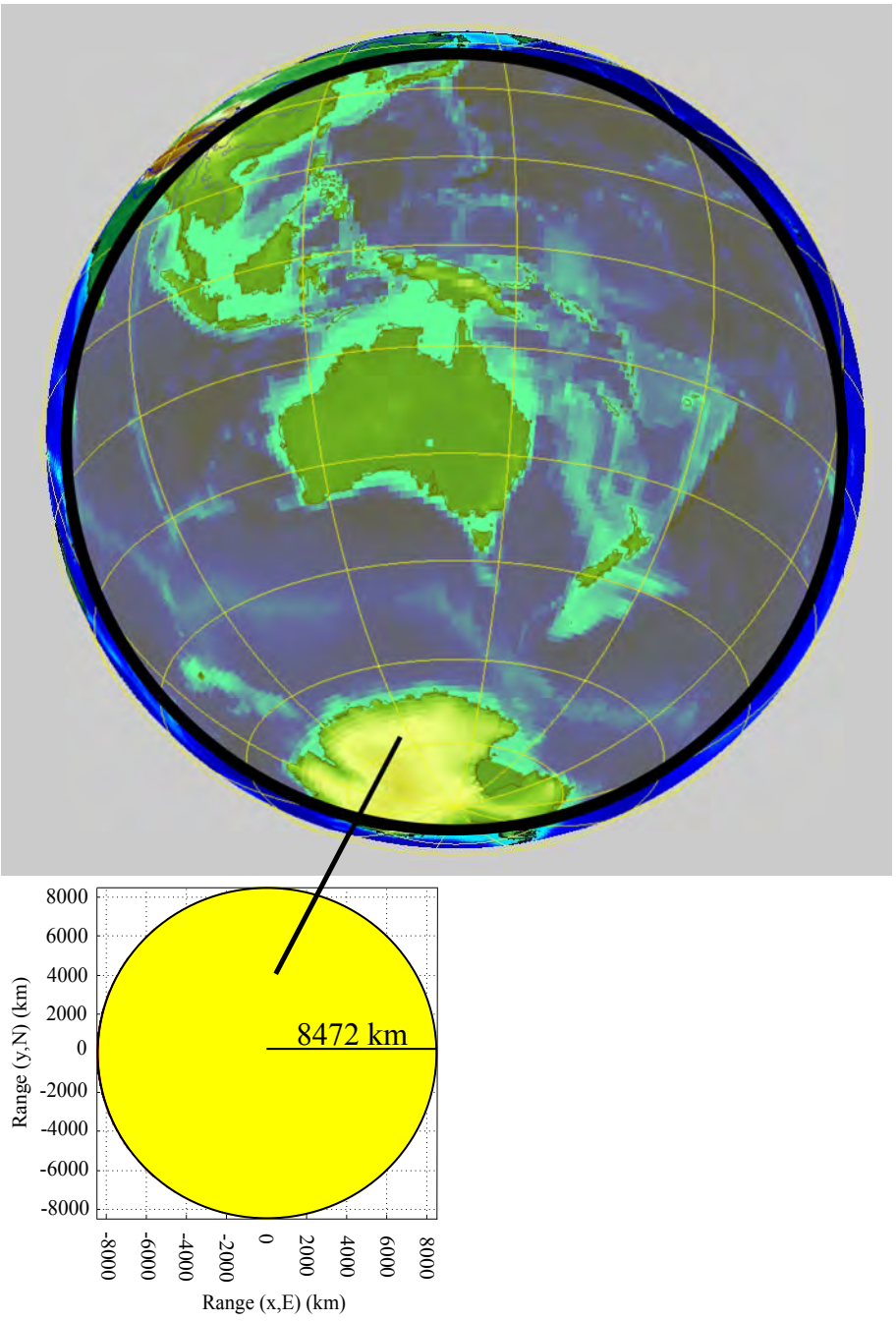

Figure 5.7. GPS system FoV dimensional metrics, according to orbital parameters in Table 5.1. The FoV is given as a function of orbit height (20200 km), with the FoV edge being a perimeter where the half-wavelength dipole, or polarisation mode, $\hat{\mathbf{r}}$ is broadside to the unit propagation vector, $\hat{\mathbf{k}}$. At this point, $\kappa = 90°$, as observed in Figure 4.1. The image of the Earth is generated in Matlab using a mapping toolbox function.

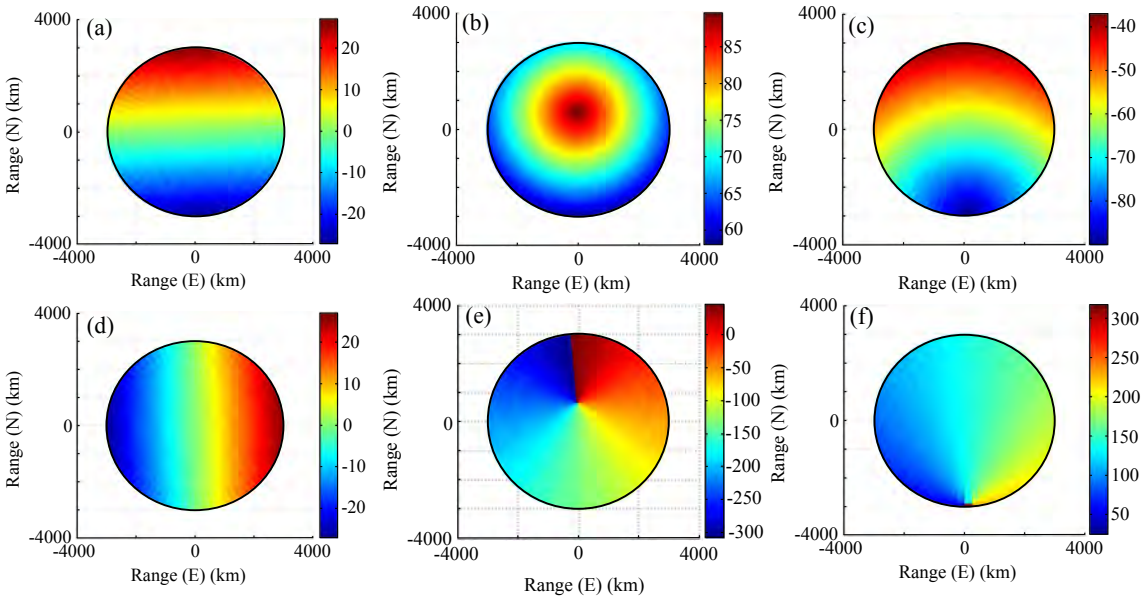

Figure 5.8. Determination of the NGSO FoV according to latitude (L) and longitude (l). Images shown represent latitudes and longitudes within NGSO FoVs: (a) L0N, (b)L85N, (c)L64S, (d)l0E (e)l133W, (f)l137E. The FoVs are subsequently grouped to give all (L,l) values within a determined NGSO FoV. In this instance: the FoV centred at (0N,0E) is given by ((a),(d)); the FoV centred at (85N,133W) is given by ((b),(e)); and the FoV centred at (64S,137E) is given by ((c),(f)).

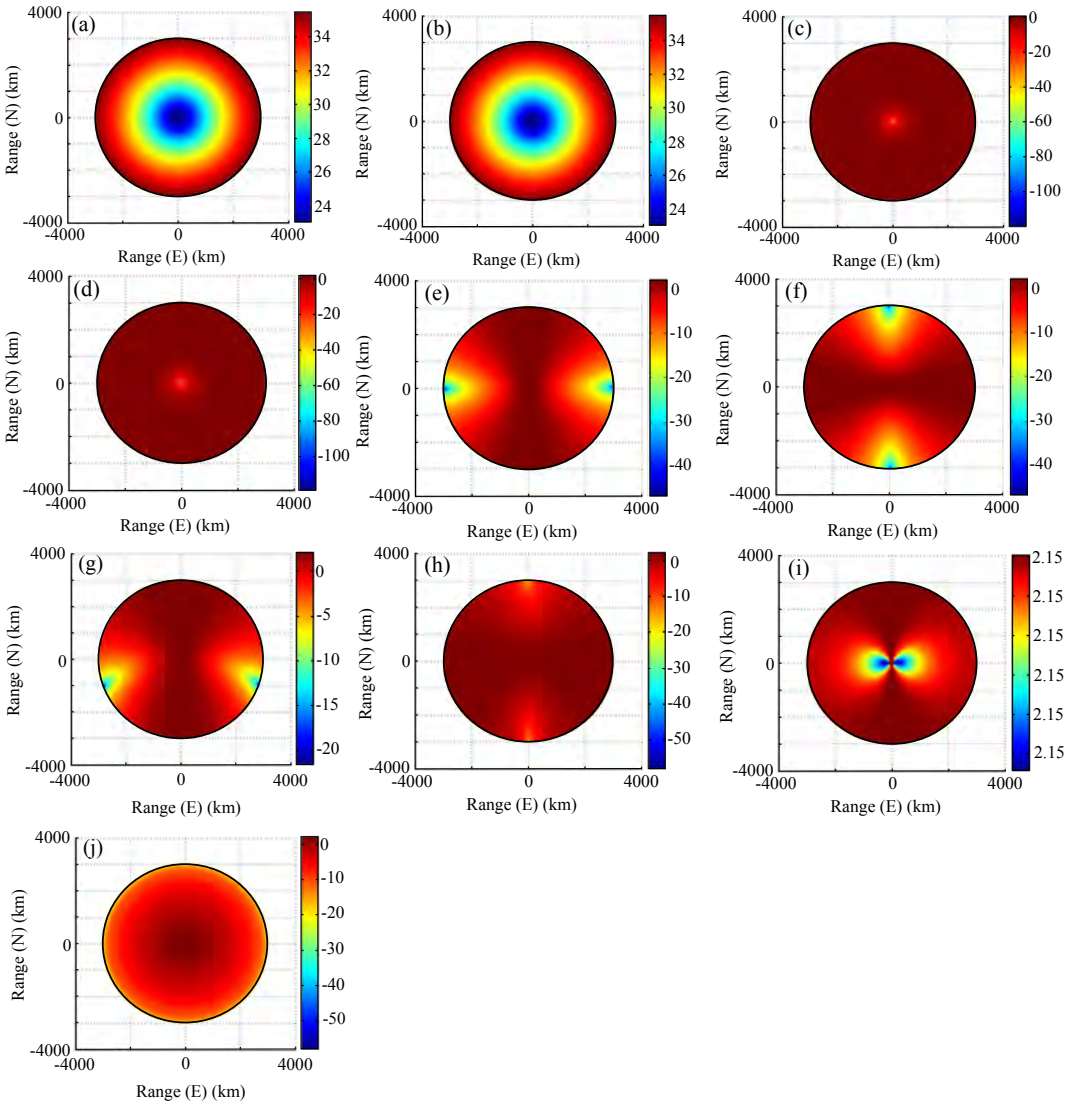

Figure 5.9. Iridium system gains (dB). Gains attributed to polarisation modes $\hat{\mathbf{p}}$ and $\hat{\mathbf{q}}$ are determined as a function of global (L,l) position, while gains attributed to the remaining polarisation modes are fixed within the NGSO FoV, regardless of FoV centre position. (a)G$\hat{\mathbf{m}}$, (b)G$\hat{\mathbf{n}}$, (c)G$\hat{\mathbf{o}}$, (d)G$\hat{\mathbf{r}}$, (e)G$\hat{\mathbf{p}}$(0°,0°), (f)G$\hat{\mathbf{q}}$(0°,0°), (g)G$\hat{\mathbf{p}}$(-34.9°,138.6°), (h)G$\hat{\mathbf{q}}$(-34.9°,138.6°), (i)G$\hat{\mathbf{p}}$(90°,0°), (j)G$\hat{\mathbf{q}}$(90°,0°).

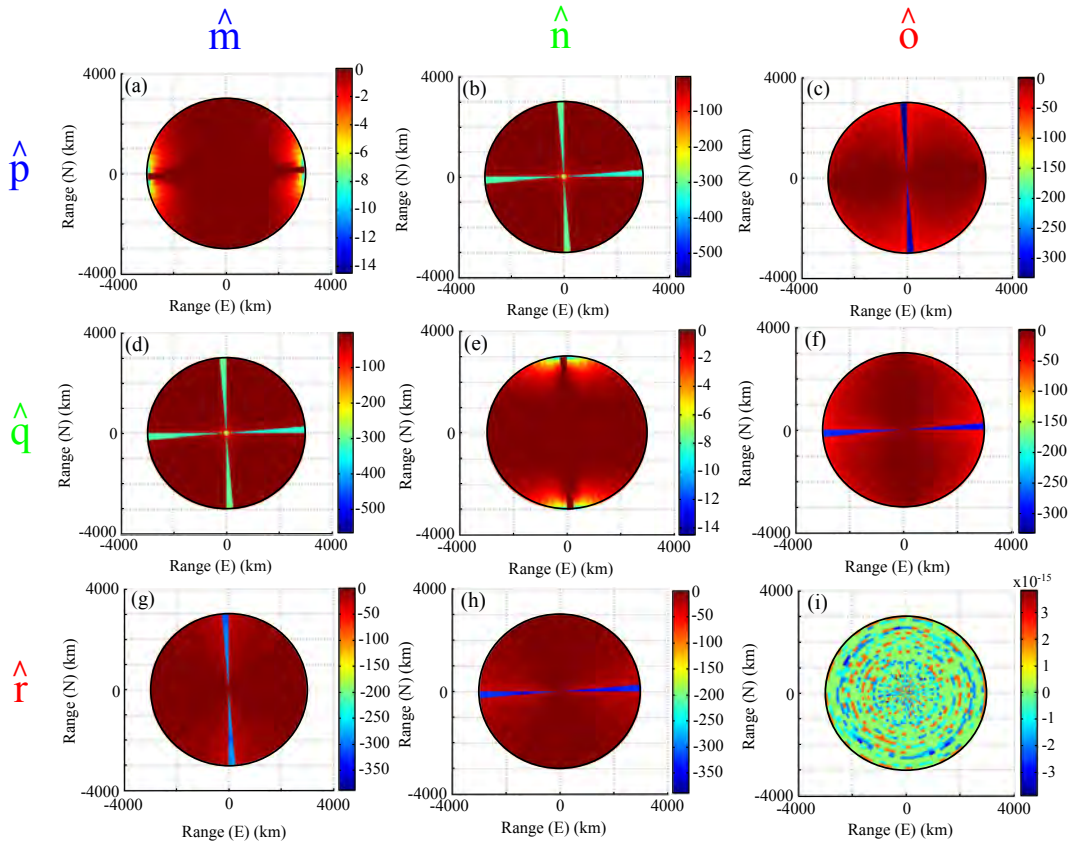

Figure 5.10. Iridium system polarisation mismatches (dB) without the effect of Faraday rotation, (operating frequency: 1616 MHz; (L,l): (0°,0°)). The images are representative of polarisation mismatch over a full transfer matrix of nine subchannels, resuting from a tri-orthogonal arrangement of polarisation modes at both T and R. The tri-orthogonal arrangement at R is displaced over the Earth's surface in a FoV determined by orbit height (780 km). The polarisation mismatch observed is solely a function of antenna arrangement, since the ionospheric effect of Faraday rotation is omitted. For the analysis in this Chapter, six subchannel links are used, as polarisation mode **ô** is omitted. In so doing, conventional CP mode wave transmission from the satellite at T is employed.

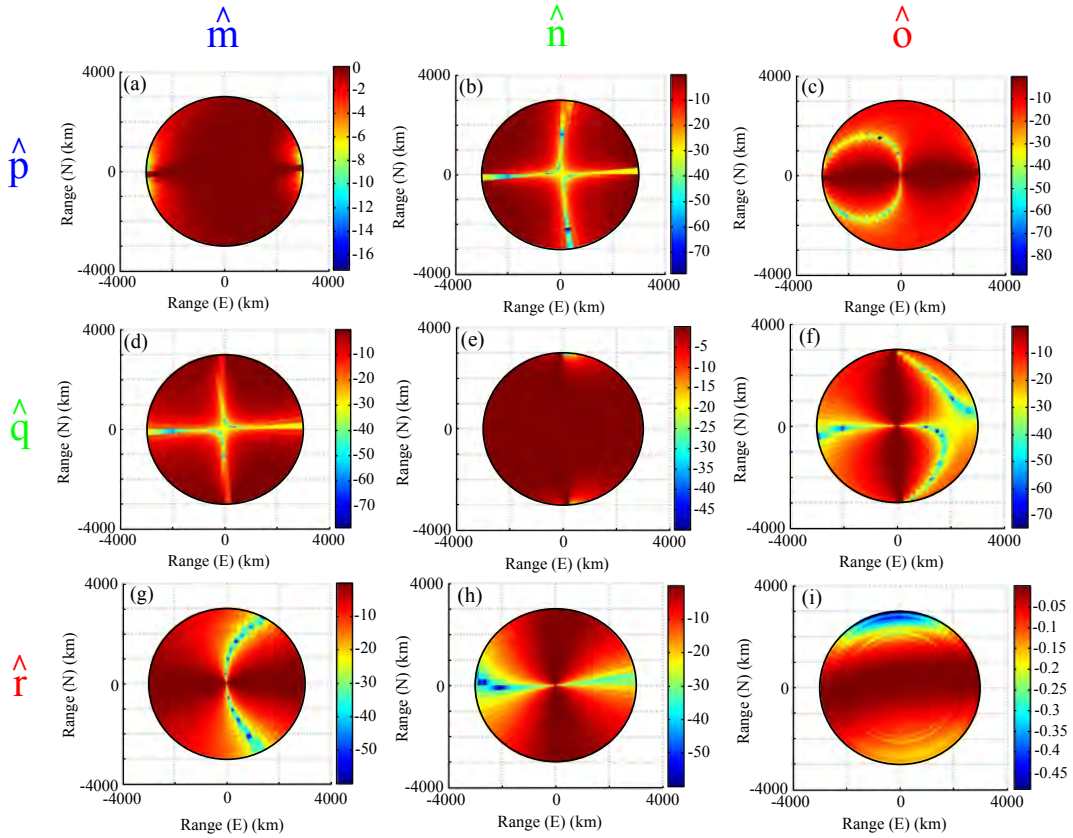

Figure 5.11. Iridium system polarisation mismatches (dB) with the effect of Faraday rotation, (operating frequency: 1616 MHz; (L,l): (0°,0°)). The images are representative of polarisation mismatch over a full transfer matrix of nine subchannels, resuting from a tri-orthogonal arrangement of polarisation modes at both T and R. The tri-orthogonal arrangement at R is displaced over the Earth's surface in a FoV determined by orbit height (780 km). The polarisation mismatch observed is a function of antenna arrangement coupled with the ionospheric effect of Faraday rotation. For the analysis in this Chapter, six subchannel links are used, as polarisation mode **ô** is omitted. In so doing, conventional CP mode wave transmission from the satellite at T is employed.

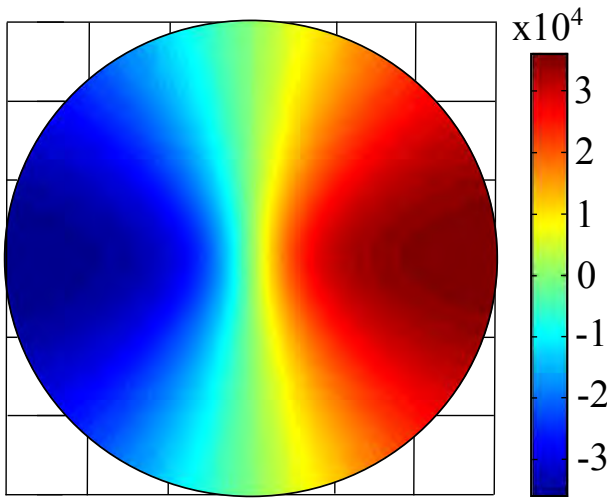

Figure 5.12. Doppler shift (Hz) for an Iridium satellite tracking west to east while passing over a stationary ground receiver at any (L,l) position within the NGSO FoV. To maintain a trajectory along an orbit path, a non-geosynchronous satellite velocity vector must change as a function of FoV centre, or (L_c,l_c) position of T. This allows calculation of the Doppler frequency shift. In the FoV shown, and according to the Frames of Reference in Figure 1.6, we have the Iridium LEO satellite velocity vector, $\mathbf{v}_T$=$\|7470\|$[1 0 0], with no motion at R.

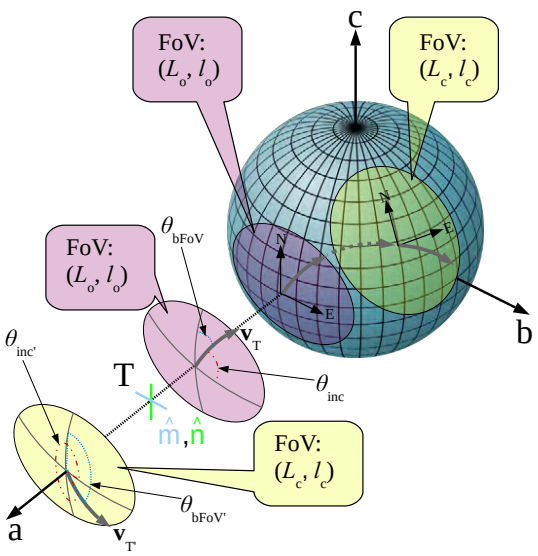

Figure 5.13. Doppler frequency shift of a NGSO satellite system. To maintain a trajectory along an orbit path, the NGSO satellite velocity vector must change as a function of FoV centre, or (L_c,l_c) position of T. This allows for calculation of the Doppler frequency shift.

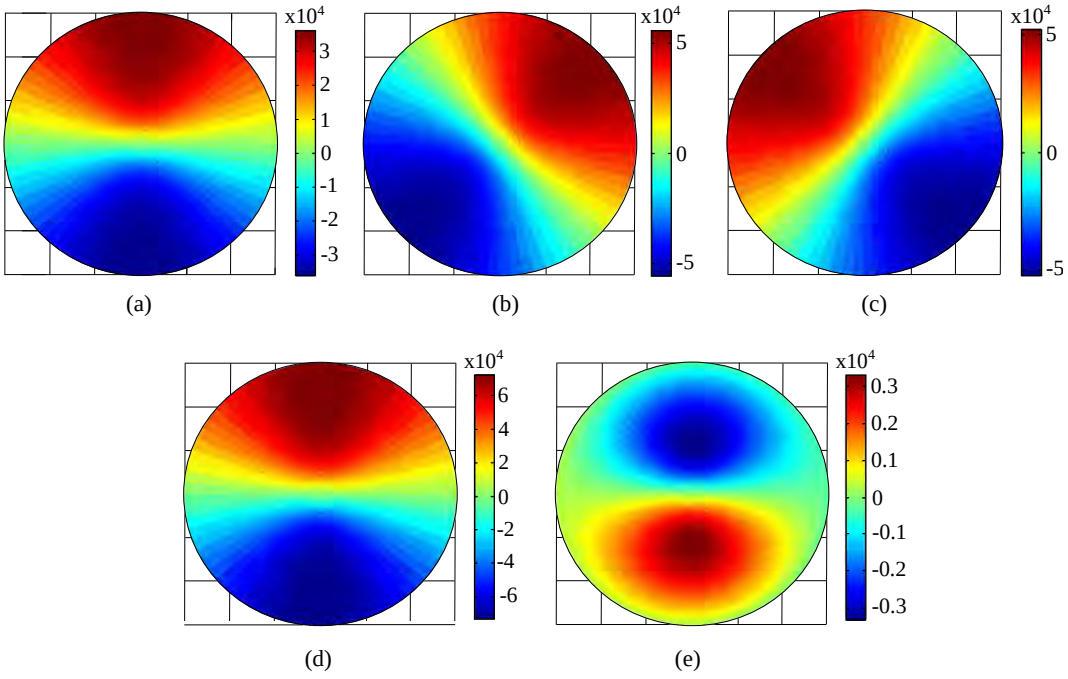

Figure 5.14. Three dimensional Doppler shifts (Hz) for the Iridium LEO satellite travelling in an orbit inclined at $\theta_{\text{inc}} = 86.4^\circ$ and five distinct ground receiver vectors. All vectors are given in the FoV centred at (L_o, l_o), and according to the Frames of Reference in Figure 1.6. In the FoV, we have $\mathbf{v}_T = \|7470\|$[0.063 0.998 0]: (a) $\mathbf{v}_R = \|0\|$[0 0 0], (b) $\mathbf{v}_R = \|7470\|$[-1 0 0], (c) $\mathbf{v}_R = \|7470\|$[1 0 0], (d) $\mathbf{v}_R = \|7470\|$[-0.063 -0.098 0], (e) $\mathbf{v}_R = \|7470\|$[0.063 0.098 0]

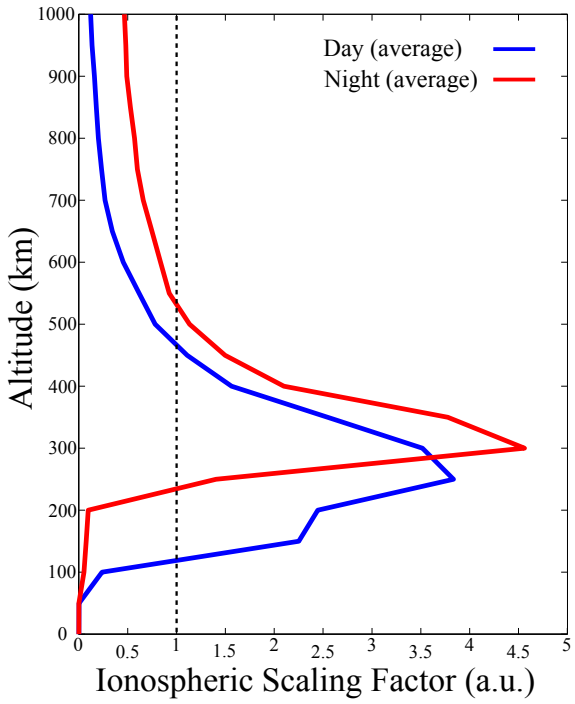

Figure 5.15. Diurnal ionospheric scaling factors. Two state or diurnal ionospheric scaling factors are averaged from solar maxima and minima profiles to make day and night averaged ionospheric profiles. Both of these profiles provide a profile equivalent to a unity scale for propagation through the entire ionosphere. For off-nadir transmission, TEC may vary as a function of (L,l) position. By introducing the scaling factors, we provide the possibility of simulating ionospheric effects on a transmitted signal as a function of (L,l,h) position.

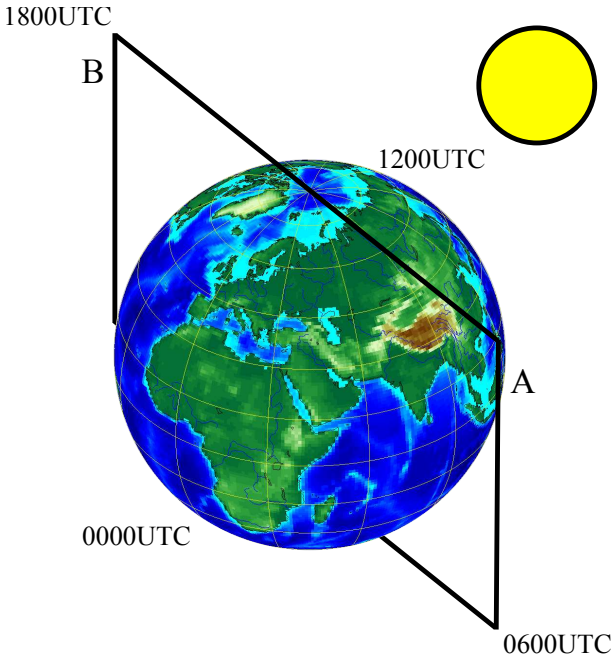

Figure 5.16. Ionospheric profiling as a function of longitudinal position, or (l) and Coordinated Universal Time, or UTC. The plane AB separates terrestrial night and day, and so day and night ionospheric profiles, according to the position of the Sun. Rotation of the Earth in an eastward direction occurs at the angular rate of 15°/hr. At 0000 UTC, global positions with values of (l) between 90° and 270° experience a day time ionospheric profile. At 0600 UTC, global positions with values of (l) between 0° and 180° experience a day time ionospheric profile.

5.3 Capacity

Capacity for M receive polarisation modes and N transmit polarisation modes is given according to Proakis (2001), Paulraj *et al.* (2003), and Bohagen *et al.* (2005) as,

$$C = \log_2 \left| \left(\mathbf{I}_M + \frac{P_\mathrm{T}}{P_\mathrm{N} N} \mathbf{H}\mathbf{H}^\dagger \right) \right| \tag{5.41}$$

where P_T is the total transmit power at T, P_N is the noise power at R, N is the number of transmitters, M is the number of receivers, $\mathbf{I}$ is an identity matrix, and $\mathbf{H}$ is the complex electric voltage transfer channel matrix, inclusive of mutual coupling effects at T and at R. The superscript † represents the Hermitian transpose. For a pure LoS channel, no NLoS component is present, and so $\mathbf{H}$ is represented by Equation (5.39). A full NLoS component is added in Section 5.4.4. Prior to Section 5.4.4, NLoS components are added where applicable as stochastic multipath fading components, and this is mentioned where employed. In this chapter, transmit powers shown in Table 5.1 are assumed to be split uniformally over transmit polarisation mode branches. The third orthogonal polarisation mode at the receiver, orthogonal to the antenna surface, provides a third degree of freedom, and so provides signal transfer over two additional subchannels to improve system performance.

Simulations are performed over the FoV, using magnetic field and TEC data acquired over random orbital periods extending from 0000 UTC, 17th November to 0140 UTC, 17th November 2014 for the case of the Iridium and Orbcomm systems, and from 0000 UTC, 17th November to 0000 UTC, 18th November 2014 for the case of the GPS system. Over these time frames, the values of TEC vary from from 1-100. Northern latitudes and eastern longitudes are deemed positive. The edge of the FoV is the point at which elevation at R is 0°, and is orbit specific.

In order to show the system improvement through implementation of a third orthogonal half-wavelength dipole mode at the receiver, the notion of a percentage improvement in capacity of a 3×2 system over a 2×2 system is introduced. A percentage capacity improvement due to the inclusion of the third orthogonal polarisation mode at the ground receiver is given as,

$$C_\mathrm{Imp} = \frac{C_{3\times2} - C_{2\times2}}{C_{2\times2}} \times 100. \tag{5.42}$$

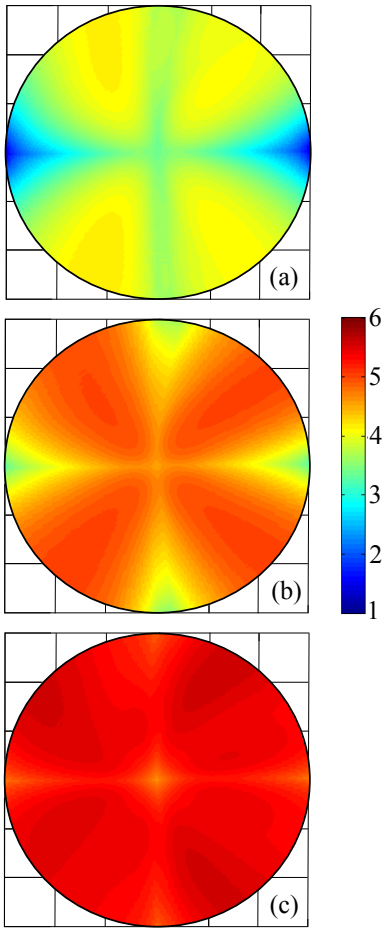

Figure 5.17. Simulated Iridium system style capacity ($\text{bps}_{(1\text{ Hz})}$), or spectral efficiency, over a FoV centred at (0,0) and according to orbital parameters. Capacities shown are: (a) 1 $\times$ 1 capacity between polarisation modes $\hat{\mathbf{m}}$ and $\hat{\mathbf{p}}$, (b) conventional CP mode wave propagation or 2 $\times$ 2 capacity between polarisation modes $\hat{\mathbf{m}}$, $\hat{\mathbf{n}}$ at T and $\hat{\mathbf{p}}$, $\hat{\mathbf{q}}$ at R, (c) conventional CP mode wave propagation but with the addition of a third orthogonal polarisation mode, $\hat{\mathbf{r}}$, at R.

From the perspective of capacity, it is informative to gauge model performance with cited values associated with an operational NGSO satellite system. Simulated capacity in a 1 Hz bandwidth, or spectral efficiency, results are displayed in Figure 5.17, and are given in Table 5.3. For the Iridium system, the capacity of a carrier may be determined from Johannsen (1995) and Chang and de Weck (2005), this being a preferred method for evaluating any improvement by the tri-orthogonal arrangement at R. For a carrier rate of 50 kbps, ten TDMA carriers per cell and 48 cells per satellite, the satellite capacity is given as,

$$C_{\text{Ir1}} = 50000 \times 10 \times 48 = 24 \text{ Mbps}. \tag{5.43}$$

Table 5.3. Iridium style channel capacity ($bps_{(1\ Hz)}$), or spectral efficiency, minima, maxima, and range over the NGSO ionospheric FoV centred at (0,0).

Polarisations	$C_{min}(bps_{(1\ Hz)})$	$C_{max}(bps_{(1\ Hz)})$	ΔC (%)
$(\hat{\mathbf{p}})(\hat{\mathbf{m}})$	1.2	4.2	220
$(\hat{\mathbf{p}}\hat{\mathbf{q}}(\hat{\mathbf{m}}\hat{\mathbf{n}})$	3.2	5	56
$(\hat{\mathbf{p}}\hat{\mathbf{q}}\hat{\mathbf{r}})(\hat{\mathbf{m}}\hat{\mathbf{n}})$	4.7	5.6	20

From the NGSO FoV plot in Figure 5.17(b), the spectral efficiency of the conventional Iridium style system using 2×2 CP mode wave propagation system is 5 $bpsHz^{-1}$, assuming a worst case total fading margin, including the effects of multipath fading, of 16 dB. According to conventional CP mode wave propagation, Iridium satellite capacity may be determined by the model according to a carrier channel bandwidth of 41.7 kHz and 120 frequency channels as,

$$C_{Ir2} = 5 \times 41700 \times 120 = 25 \text{ Mbps}. \tag{5.44}$$

Given that the spectral efficiency of 5 $bpsHz^{-1}$ is a value held over much of the FoV, this value suggests agreement with the value given in the literature for the Iridium satellite (Chang and de Weck 2005).

Figure 5.17 highlights the benefit of the tri-orthogonal arrangement at R. An increase is seen in capacity as a result of the third orthogonal polarisation mode. In addition the range of capacity over the FoV is reduced. The minimum capacity, C_{min}, over the FoV increases in approximate linear proportion to the number of receiver polarisation modes, as the effect of Faraday rotation is limited at 1.6 GHz. The maximum capacity, C_{max}, does not follow this rule. Research articles suggest a tripling of capacity as a result of using tri-orthogonal arrangements (Andrews *et al.* 2001, Chiu *et al.* 2007b), but Figure 5.17 clearly suggests that this is not the case over all antenna orientations.

5.3.1 Consideration of Array Panellisation

For the Iridium satellite, consideration is now made of the panellisation of antenna arrays, or phased arrays of antennas. Each panel provides sixteen beams, that are oriented to provide complete coverage over the FoV given in Figure 5.5. It is possible to

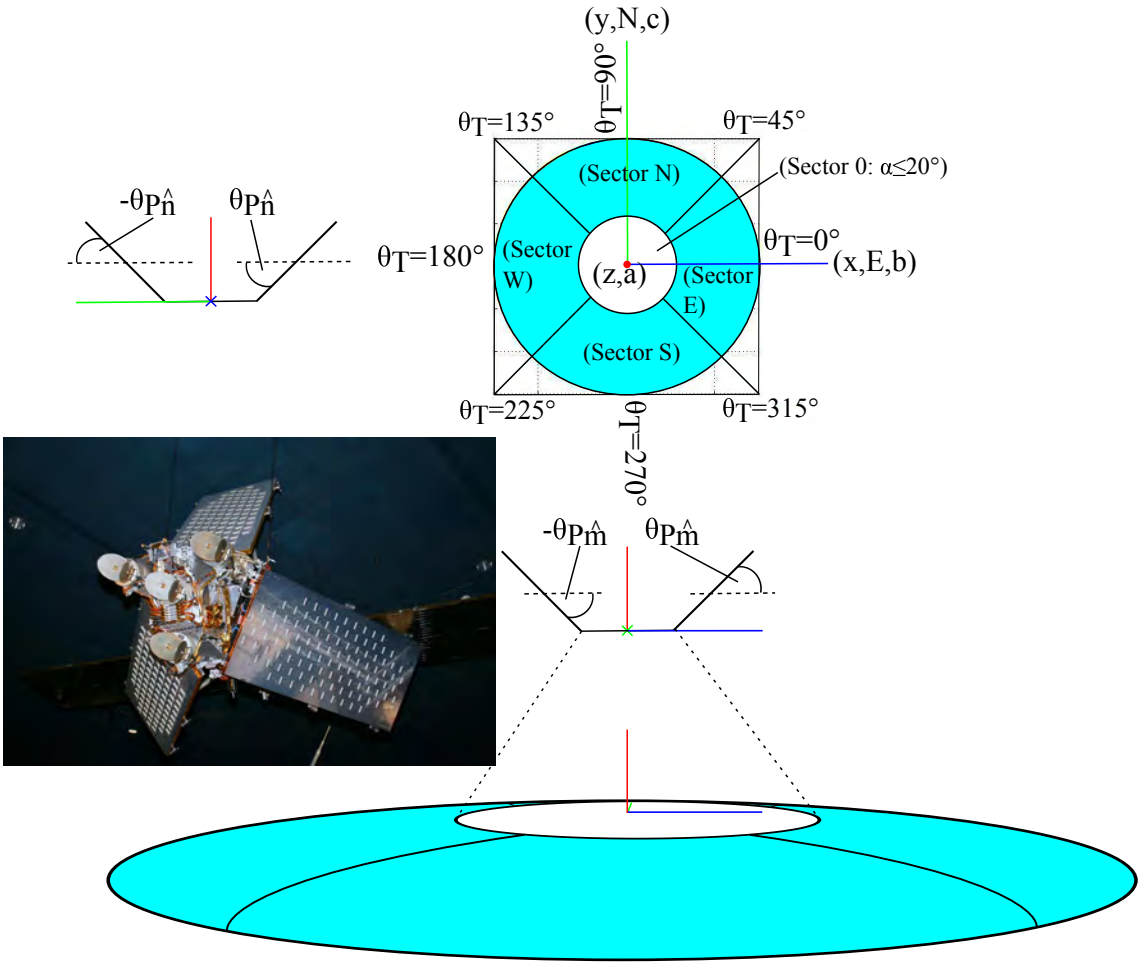

Figure 5.18. Phased Array Panellisation. In order to model RHCP mode waveforms transmitted normal to a phased antenna array (inset shows three such arrays on an Iridium satellite), we may rotate a transmitting polarisation, $\hat{\mathbf{m}}$ or $\hat{\mathbf{n}}$, according to the sector into which the propagation vector $\hat{\mathbf{k}}$ lies. We specify no rotation within a circle about the FoV centre, defined by α (Sector 0). Outside of this circle, polarisation $\hat{\mathbf{m}}$ is rotated by an angle $\theta_{P\hat{\mathbf{m}}}$ for propagation in an easterly direction (Sector E), and by $-\theta_{P\hat{\mathbf{m}}}$ for propagation in a westerly direction (Sector W). We may rotate polarisation $\hat{\mathbf{n}}$ by an angle $\theta_{P\hat{\mathbf{n}}}$ for propagation in a northerly direction (Sector N), and by $-\theta_{P\hat{\mathbf{n}}}$ for propagation in a southerly direction (Sector S).

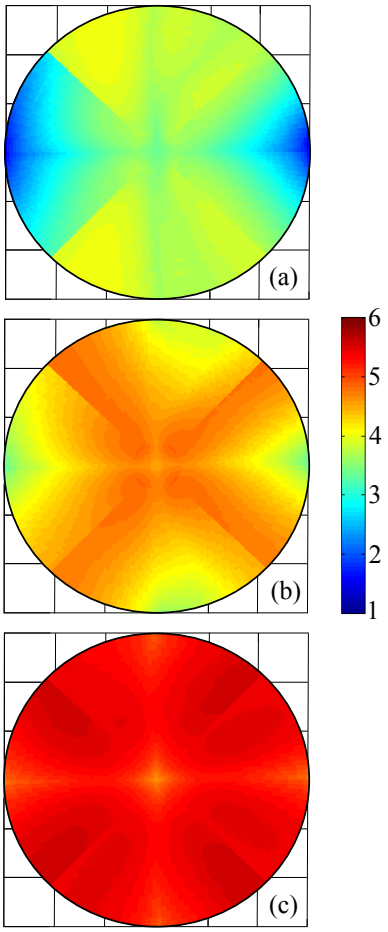

Figure 5.19. Simulated Iridium system style capacity ($bps_{(1\ Hz)}$), or spectral efficiency, using a method of array panellisation, over a NGSO ionospheric FoV centred at (0,0) and according to orbital parameters. Capacities shown are: (a) 1 $\times$ 1 capacity between polarisation modes $\hat{\mathbf{m}}$ and $\hat{\mathbf{p}}$, (b) conventional CP mode wave propagation or 2 $\times$ 2 capacity between polarisation modes $\hat{\mathbf{m}}$, $\hat{\mathbf{n}}$ at T and $\hat{\mathbf{p}}$, $\hat{\mathbf{q}}$ at R, (c) conventional CP mode wave propagation but with the addition of a third orthogonal polarisation mode, $\hat{\mathbf{r}}$, at R.

model a sectorised approach to RHCP mode transmission from T in five distinct directions, as observed in Figure 5.18. The resulting capacity in a 1 Hz bandwidth, or spectral efficiency, over such a sectorised FoV, with each sector defining a zone into which a transmitted RHCP mode waveform from T is emitted, with polarisations providing a RHCP mode waveform normal to a phased array, is shown in Figure 5.19. While the Iridium system provides three panels, five panels in nadir and compass directions are considered due to ease of implementation. By including an additional two panels, the argument is made that the model provides an enhanced performance above that of the physical system.

For the analysis, the nadir sector (Sector 0) is specified by values of $\alpha < 20°$. The eastern sector (Sector E) is specified by values of θ_T between $\pm 45°$, the northern sector (Sector N) by values of θ_T between 45° and 135°, the western sector (Sector W) by values of θ_T between 135° and 225°, and the southern sector (S) by values of θ_T between 225° and 315°. For the panels themselves, a rotation of magnitude 40° is specified in each of four directions. This places CP mode wave propagation at the halfway position between the edge of the nadir sector, Sector 0, and the edge of the FoV itself. Wave propagation in directions that are not normal to the phased array panels is elliptically polarised, but does not become linearly polarised, as a result of sectorising the orientation of the phased arrays, and so the two linear polarisations of the RHCP mode waveform.

The matrices of Equations (5.45) and (5.46) are used to rotate unit polarisation mode vectors $\hat{\mathbf{m}}$ and $\hat{\mathbf{n}}$ respectively:

$$\mathbf{R}_{\hat{\mathbf{m}}} = \begin{bmatrix} \cos\theta_{P\hat{\mathbf{m}}} & -\sin\theta_{P\hat{\mathbf{m}}} & 0 \\ \sin\theta_{P\hat{\mathbf{m}}} & \cos\theta_{P\hat{\mathbf{m}}} & 0 \\ 0 & 0 & 1 \end{bmatrix} \tag{5.45}$$

and

$$\mathbf{R}_{\hat{\mathbf{n}}} = \begin{bmatrix} \cos\theta_{P\hat{\mathbf{n}}} & 0 & -\sin\theta_{P\hat{\mathbf{n}}} \\ 0 & 1 & 0 \\ \sin\theta_{P\hat{\mathbf{n}}} & 0 & \cos\theta_{P\hat{\mathbf{n}}} \end{bmatrix}. \tag{5.46}$$

Thus, it is possible to construct polarisations for RHCP mode waveforms in each of the five distinct sectors shown in Figure 5.18 according to the following rotations in the ECEF system of Figure 5.4.

- In the nadir sector (Sector 0), there is no rotation of polarisations $\hat{\mathbf{m}}$ and $\hat{\mathbf{n}}$ at T.
- In the eastern sector (Sector E), there is rotation of polarisation $\hat{\mathbf{m}}$ [0 1 0] by $\theta_{P\hat{\mathbf{m}}}$=40° at T.
- In the northern sector (Sector N), there is rotation of polarisation $\hat{\mathbf{n}}$ [0 0 1] by $\theta_{P\hat{\mathbf{n}}}$=-40° at T.
- In the western sector (Sector W), there is rotation of polarisation $\hat{\mathbf{m}}$ [0 1 0] by $\theta_{P\hat{\mathbf{m}}}$=-40° at T.

- In the southern sector (Sector S), there is rotation of polarisation $\hat{\mathbf{n}}$ [0 0 1] by $\theta_{P\hat{\mathbf{n}}}$=40° at T.

From comparison of Figure 5.19 with Figure 5.17, we note that implementation of array panellisation in this instance is problematic due to:

- the exact nature of the phasing and beam positioning being unknown. This in turn results in the suboptimal capacity performance observed in Figure 5.19.

- the alignment of polarisations perpendicular to all propagation vectors being not possible.

- ground receiver polarisations at R being aligned in a northerly, easterly, and radial direction, and so alignment of polarisations at T would not offer any additional insight into the system. That polarisations considered over the channel for a traditional RHCP, or 2 × 2 system, are included within the 3 × 2 system, means that bias is not introduced into the analysis.

As a consequence of this consideration, a panellised approach is not implemented for the simulation. Indeed, misalignment is considered over the entire FoV which, in effect, allows system capacity performance to be considered for all cases of antenna orientation. This may be seen as a proxy pathway to a reduced number of spot beams at T, due to the enhanced performance over the FoV, and particularly at the FoV outer edges, of the tri-orthogonal arrangement at R over a conventional RHCP arrangement at R.

From a purely geometrical standpoint devoid of channel effects, the angle κ reaches 90° at the outer edge of the FoV, where the receiver polarisation branch $\hat{\mathbf{r}}$ is broadside to the transmitter T, as the radiating surface of R remains orthogonal to the zenith over the entire FoV. The maximum misalignment for each system observed in this instance between T and R is given by values of the angle γ_{max} in Table 5.2. As a consequence, it is suggested that the performance of the tri-orthogonal configuration is understated as the deviation from the perfectly aligned case at the FoV centre is less than might be first assumed.

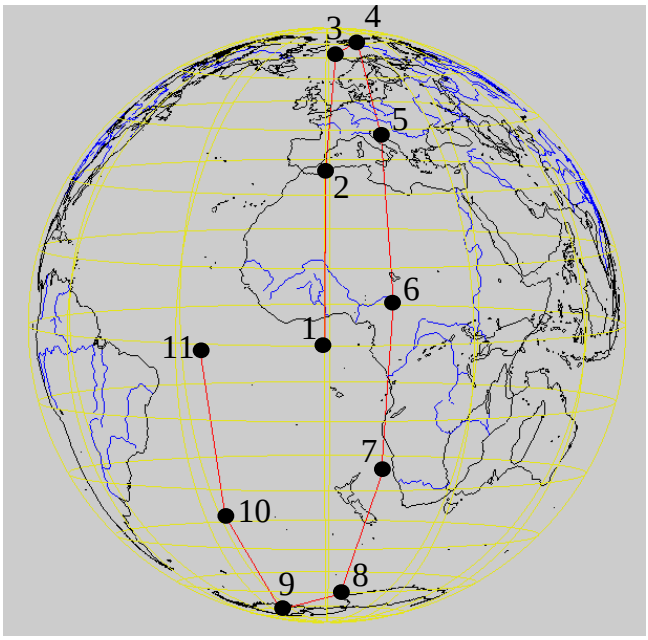

Figure 5.20. Iridium orbit track lasting 6027s over the globe, with FoV measurements made every 600s. The FoV centres are numbered in sequential order, with (L_c,l_c) positions given.

5.4 Results

The FoVs in all figures in this section represent terrestrial footprints according to the dimensional metrics of Figures 5.5, 5.6, and 5.7.

The orbits to be considered are shown in Figures 5.20, 5.21, and 5.22 for the Iridium, Orbcomm, and GPS NGSO satellite systems respectively. The FoVs, and their respective (L,l) positions are given in these figures. The Iridium and Orbcomm systems use magnetic data (Maus *et al.* 2010) provided on a daily basis and TEC data (National Oceanic and Atmospheric Administration Accessed: 2014) provided every 10 minutes for calculation of ionospheric effects, with the orbits to be considered being 6027s and 6021s in duration respectively, after taking into account the Earth's rotation. The GPS system uses magnetic data provided on a daily basis and TEC data provided on an hourly basis, with the orbit to be considered being 23h 57m 24s in duration, after taking into account the Earth's rotation.

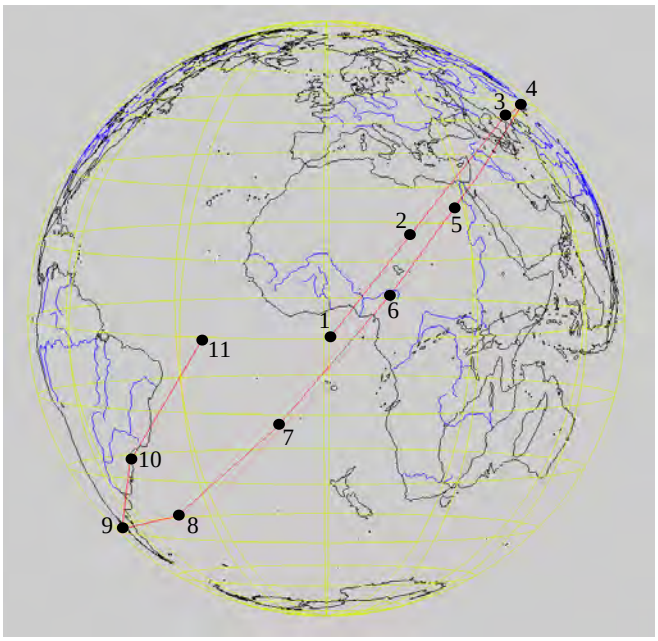

Figure 5.21. Orbcomm orbit track lasting 6021s over the globe, with FoV measurements made every 600s. The FoV centres are numbered in sequential order, with (L,l) positions given.

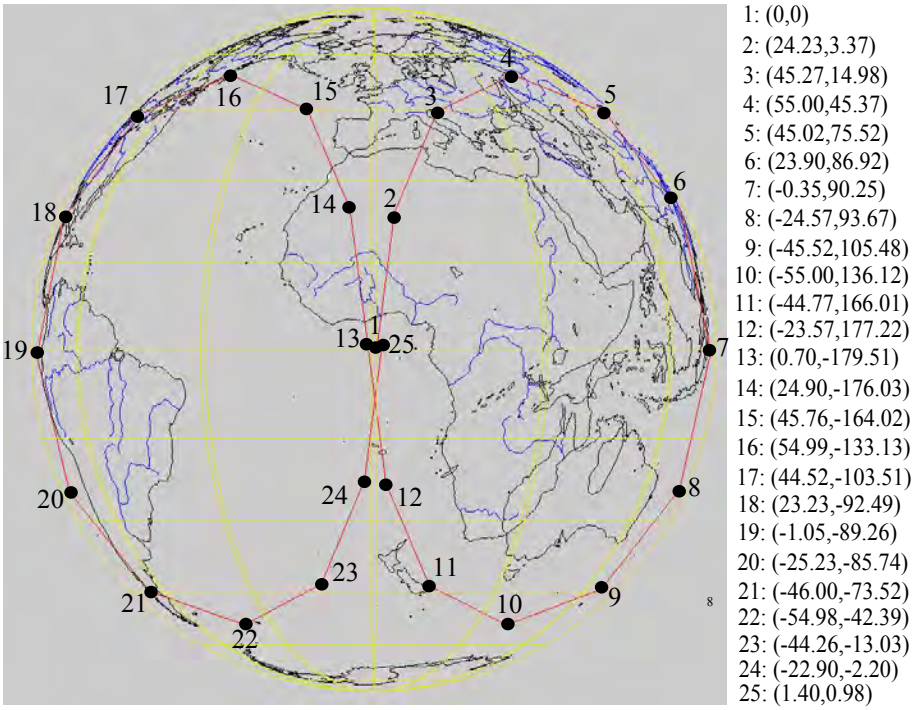

Figure 5.22. GPS track lasting 23h 57m 24s over the globe, with FoV measurements made every hour. The FoV centres are numbered in sequential order, with (L,l) positions given.

5.4.1 Application of Total Fading Margin Over the FoV Over a Random Orbital Period

Figures 5.23, 5.24, and 5.25 are individual sets of considered orbital period large-FoVs centred at global (L_c,l_c) positions given in Figures 5.20, 5.21, and 5.22, for the Iridium, Orbcomm and GPS satellite systems respectively. The orbit tracks of each of the three NGSO satellite arrangements are calculated from orbital parameters given in Table 5.1. For the Iridium and Orbcomm systems, the FoVs are generated every 10 minutes, while for the GPS system FoVs are generated every hour. Figures 5.23, 5.24, and 5.25 represent worst case reception scenarios at R for each of the three satellite arrangements, according to the application of total fading margins (Braasch and van Dierendonck 1999, Orbcomm LLC Accessed: 2014, Chang and de Weck 2005) given in Table 5.1. As such, they incorporate both slow and fast fading effects, such as shadowing and multipath effects respectively. Application of fast fading means that the FoVs in Figures 5.23, 5.24, and 5.25 provide percentage capacity improvements according to a complex electric voltage transfer channel matrix calculated for all (L,l) positions over each FoV. The total fading margin used in Orbcomm LLC (Accessed: 2014) is based on a worst case low elevation scenario although this case is not made clear in the literature for Iridium or GPS. In the absence of additional information, this approach is adopted for the Iridium and GPS systems.

The observed effect in Figure 5.24 results from Faraday rotation effects on signal propagation, as the Orbcomm satellite operates with a lower frequency than both the Iridium and GPS satellite systems, of 138 MHz. As a result, peaks and troughs of capacity performance are encountered for a ground receiver R, at a static (L,l) position in the FoV, over the 804 seconds that the Orbcomm satellite is in view.

5.4.2 No Fading Margin Application Over the FoV Over a Random Orbital Period

In Figures 5.26 and 5.27, best case reception is considered at R for the Orbcomm and GPS satellite systems where no slow or fast fading is assumed in the channel. As fast fading is not implemented, Figures 5.26 and 5.27 provide percentage LoS capacity improvements according to a complex LoS electric voltage transfer channel matrix calculated for all (L,l) positions over each FoV. A 100 minute analysis over the orbital period showing the percentage improvement in LoS capacity as a consequence of including a

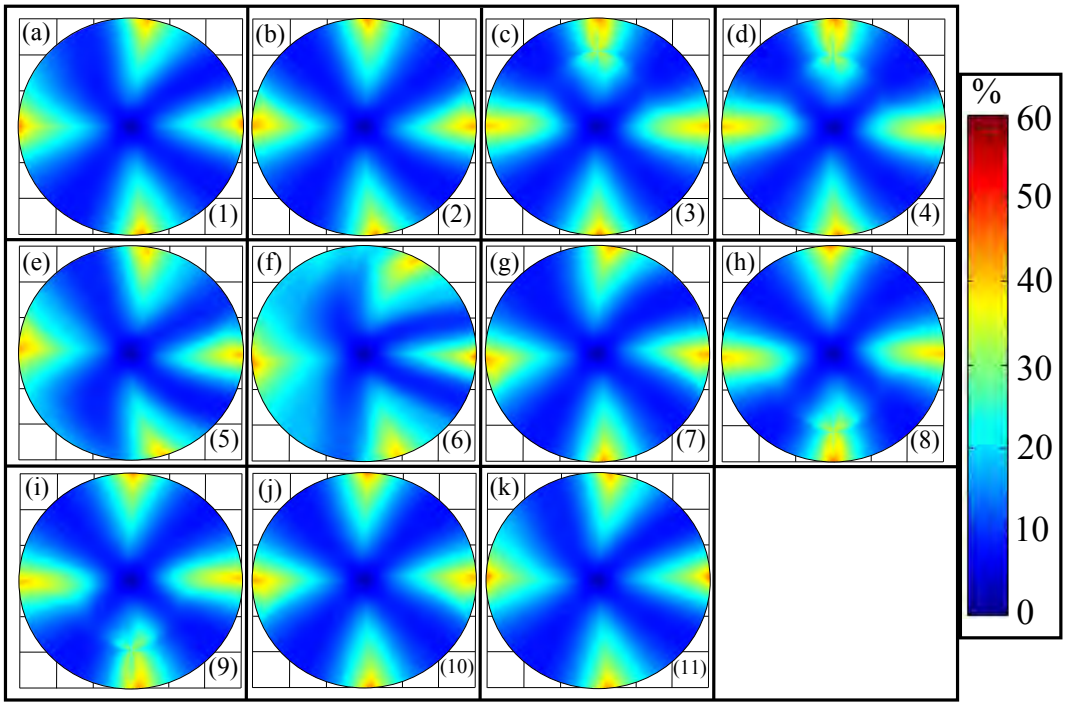

Figure 5.23. Simulated percentage improvement in Iridium system capacity, over a NGSO ionospheric FoV according to Iridium orbital parameters and a total fading margin of 16 dB, as a result of implementing a third orthogonal polarisation mode at the receiver. The FoVs are sequentially simulated in a 600s progression over a period of 100 minutes hours from 0000 UTC on 17th November 2014, to 0140 UTC on 17th November 2014 along a typical Iridium trajectory, using realtime TEC (National Oceanic and Atmospheric Administration Accessed: 2014) and magnetic field data (Maus *et al.* 2010). The number in the bottom right corner of each FoV corresponds to the FoV number given in 5.20.

third orthogonal polarisation at R, over eleven distinct FoVs measured every 10 minutes, is shown for the Orbcomm system in Figure 5.26. A 24 hour analysis over the orbital period showing the percentage improvement in LoS capacity as a consequence of including a third orthogonal polarisation at R, over 25 distinct FoVs measured every hour, is shown for the GPS system in Figure 5.27.

It is to be expected that at the FoV centre, or nadir path, there is minimal if any improvement to capacity performance as a result of introducing a third orthogonal polarisation mode at the receiver, orthogonal to the antenna surface. Due to the inclination of the terrestrial magnetic vector at the centre of the FoV, the NGSO satellite system capacity at the centre may drop, even though for a 2×2 conventional CP mode system, the antennas are perfectly aligned. Over the FoV, the improvement in performance,

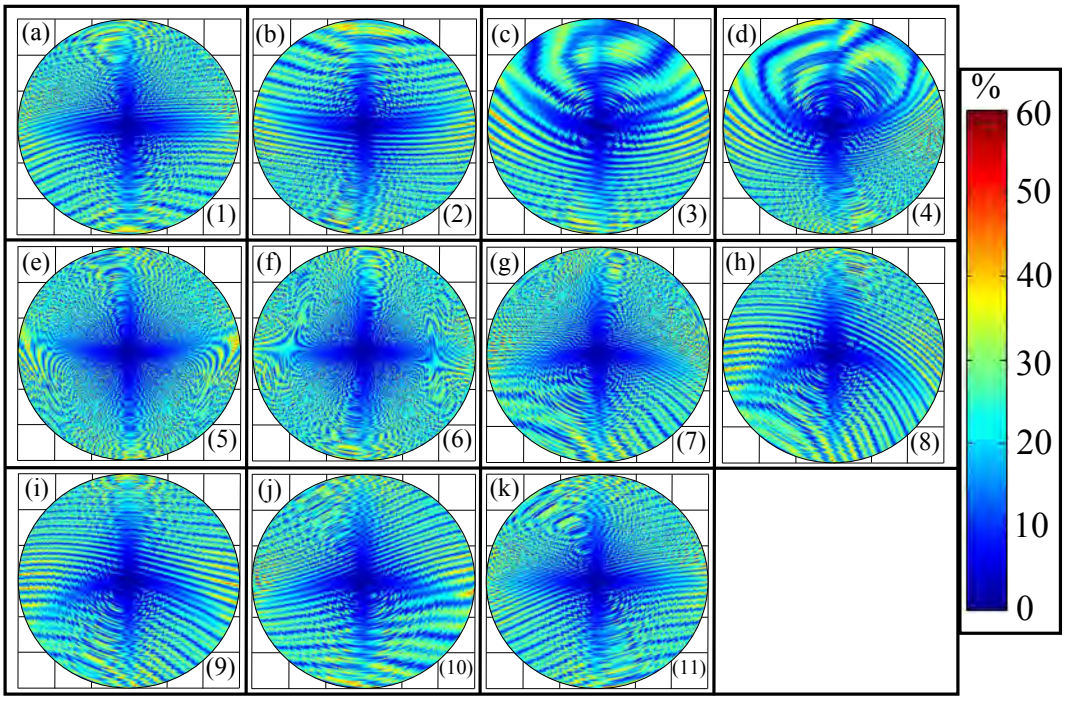

Figure 5.24. Simulated percentage improvement in Orbcomm system capacity, over a NGSO ionospheric FoV according to Orbcomm orbital parameters and a total fading margin of 16 dB, as a result of implementing a third orthogonal polarisation mode at the receiver. The FoVs are sequentially simulated in a 600s progression over a period of 100 minutes from 0000 UTC on 17th November 2014, to 0140 UTC on 17th November 2014 along a typical Orbcomm trajectory, using realtime TEC (National Oceanic and Atmospheric Administration Accessed: 2014) and magnetic field data (Maus *et al*. 2010). The number in the bottom right corner of each FoV corresponds to the FoV number given in 5.21.

as demonstrated by the 3×2 tri-orthogonal receiver system over that of the 2×2 conventional CP mode receiver system, is significant. A percentage improvement in capacity is observed for all three NGSO satellite systems in an ionospheric channel over all of the considered global NGSO FoVs during their trajectories in their respective orbits. There is no position where the tri-orthogonal arrangement at R offers worse performance than its conventional CP mode counterpart.

The observed effect in the FoVs of Figure 5.26, as in those of Figure 5.24, results from Faraday rotation effects on signal propagation, as the Orbcomm satellite operates with a lower frequency than the Iridium and GPS satellite systems. As a result, peaks and troughs of capacity performance are encountered for a ground receiver R, at a static

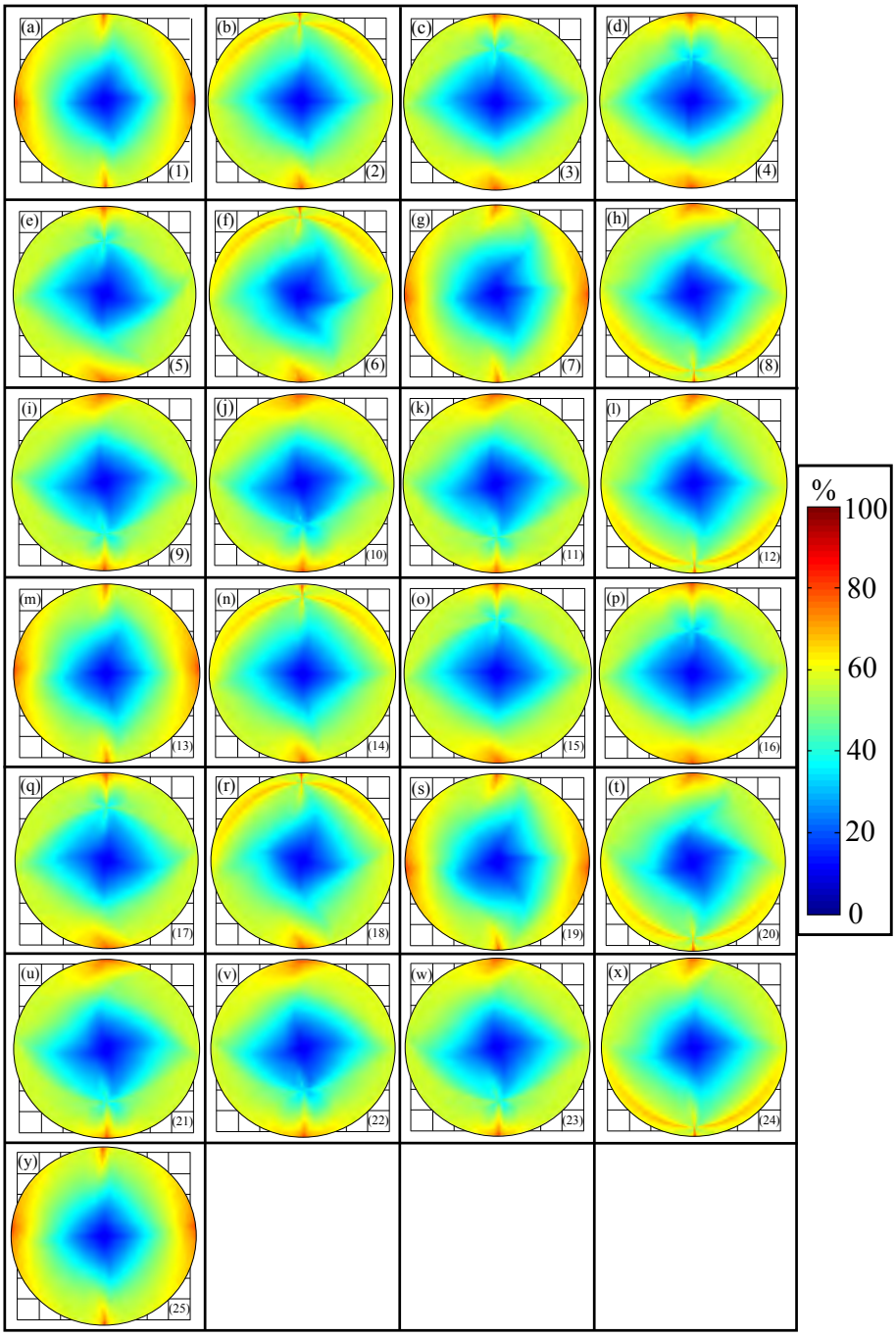

Figure 5.25. Simulated percentage improvement in GPS system capacity, over a NGSO ionospheric FoV according to GPS orbital parameters and a total fading margin of 22 dB, as a result of implementing a third orthogonal polarisation mode at the receiver. The FoVs are sequentially simulated in an hourly progression over a period of 24 hours from 0000 UTC on 17th November 2014, to 0000 UTC on 18th November 2014 along a typical GPS trajectory, using realtime TEC (National Oceanic and Atmospheric Administration Accessed: 2014) and magnetic field data (Maus *et al.* 2010). The number in the bottom right corner of each FoV corresponds to the FoV number given in 5.22.

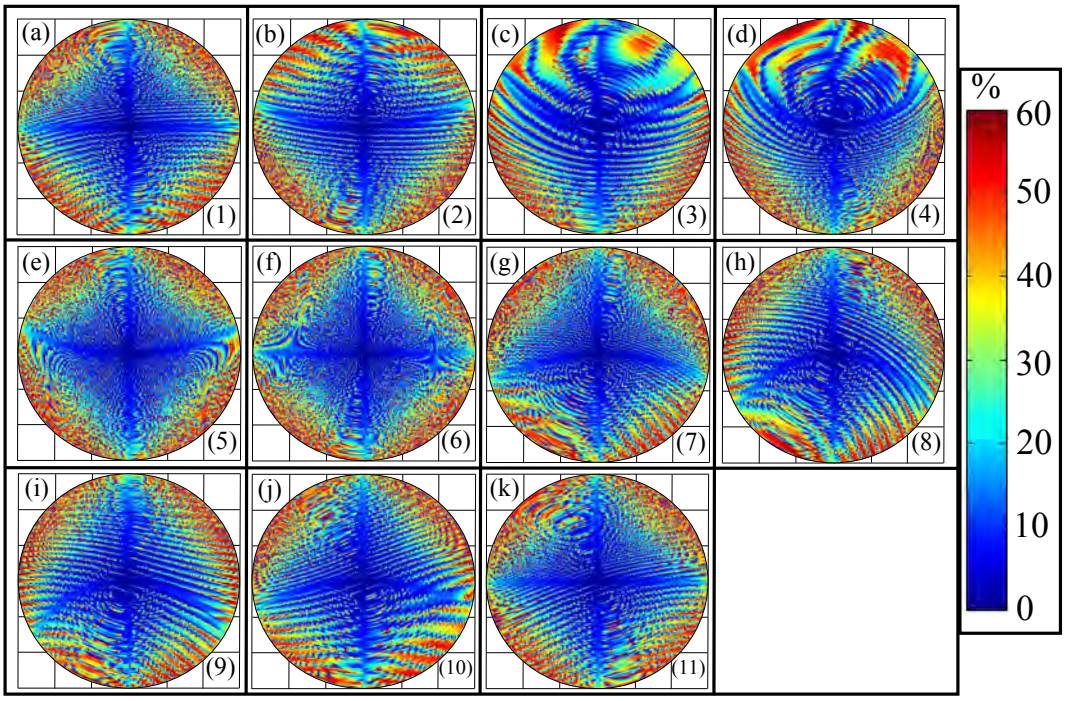

Figure 5.26. Simulated percentage improvement in Orbcomm system capacity, over a NGSO ionospheric FoV according to Orbcomm orbital parameters and a deterministic complex LoS voltage transfer with no fading, as a result of implementing a third orthogonal polarisation mode at the receiver. The FoVs are sequentially simulated in a 600s progression over a period of 100 minutes from 0000 UTC on 17th November 2014, to 0140 UTC on 17th November 2014 along a typical Orbcomm trajectory, using realtime TEC (National Oceanic and Atmospheric Administration Accessed: 2014) and magnetic field data (Maus *et al.* 2010). The number in the bottom right corner of each FoV corresponds to the FoV number given in 5.21.

(L,l) position in the FoV, over the 804 seconds that the Orbcomm satellite is in view of the ground receiver, R.

5.4.3 Statistical Analysis of Channel Capacity With No Application of Fading

A LoS statistical analysis is provided for the Orbcomm and GPS satellite systems, over the respective random orbital periods of 0000 UTC, 17th November 2014 to 0140 UTC, 17th November 2014, and 0000 UTC, 17th November 2014 to 0000 UTC, 18th November 2014. The null hypothesis is that the inclusion of a third orthogonal polarisation mode

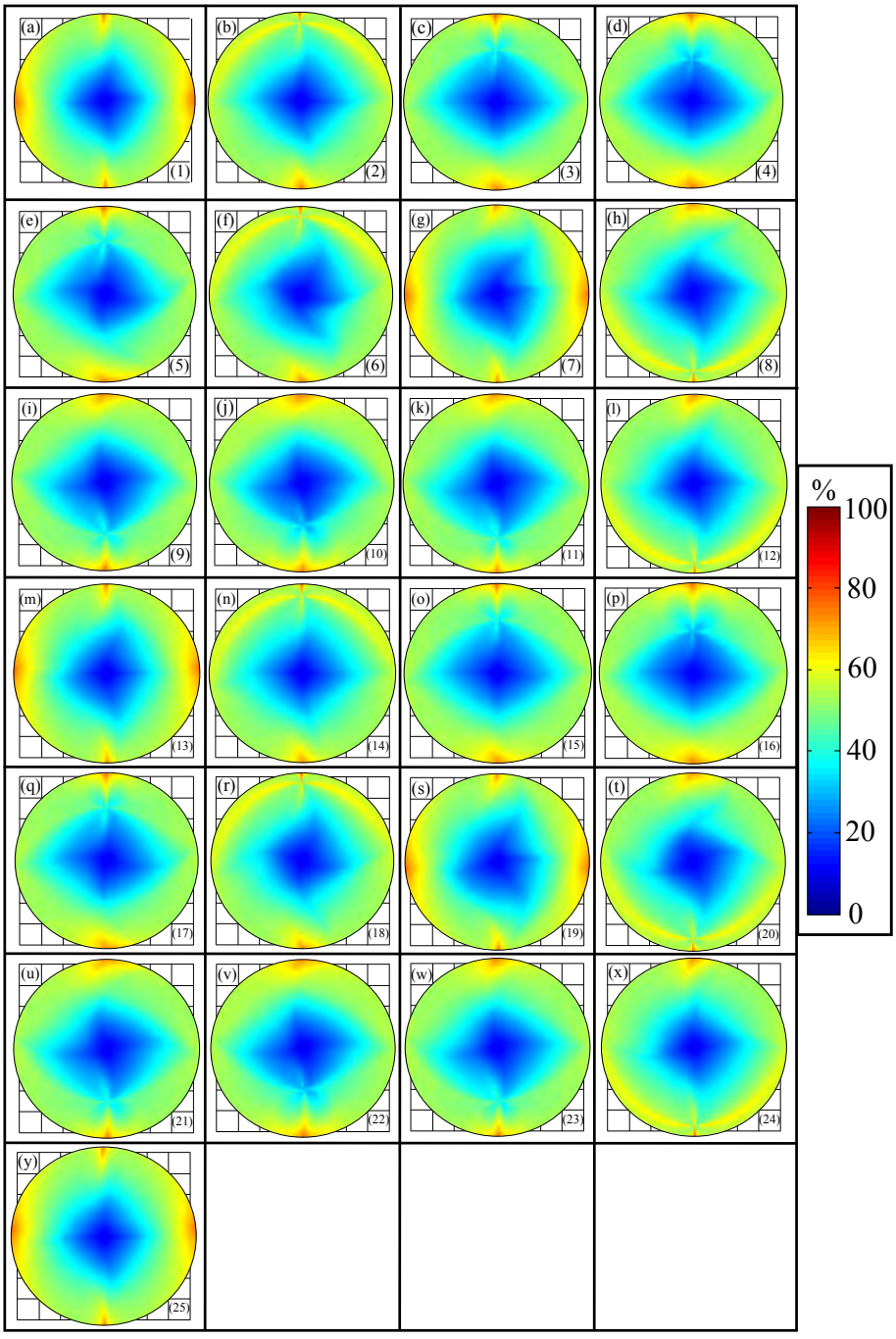

Figure 5.27. Simulated percentage improvement in GPS system capacity, over a NGSO ionospheric FoV according to GPS orbital parameters and a deterministic complex LoS voltage transfer with no fading, as a result of implementing a third orthogonal polarisation mode at the receiver. The FoVs are sequentially simulated in an hourly progression over a period of 24 hours from 0000 UTC on 17th November 2014, to 0000 UTC on 18th November 2014 along a typical GPS trajectory, using realtime TEC (National Oceanic and Atmospheric Administration Accessed: 2014) and magnetic field data (Maus *et al.* 2010). The number in the bottom right corner of each FoV corresponds to the FoV number given in 5.22.

at R, orthogonal to the receive antenna surface, has no effect on the capacity of the satellite system.

Independent sample Student t-tests on the average LoS capacity improvement of both the Orbcomm and GPS systems, expressed as a percentage, and as a result of the inclusion of a third orthogonal polarisation at R, are found to support the findings illustrated in Figures 5.26 and 5.27.

Two data sets of 11 FoVs each, which are used to provide the FoVs observed in Figure 5.26, are used for the Orbcomm satellite system statistical analysis. One data set uses a conventional CP mode, or dual orthogonal 90° phase-shifted DP mode, at the receiver R, while the other data set includes an additional mode at the receiver R, polarised orthogonally to the modes of the conventional CP mode, which produces a tri-orthogonal arrangement of polarised modes at the receiver, R.

For the GPS satellite system, two data sets of 25 FoVs each, which are used to generate the FoVs seen in Figure 5.27, are employed following the same procedure as that for the Orbcomm satellite system.

For the Orbcomm satellite system, $(t(11) = 1485,\ p \leq 0.001)$ is established, while $(t(25) = 238,\ p \leq 0.001)$ is established for the GPS satellite system.

For both the Orbcomm and GPS satellite systems, probabilities of a chance finding are well below 5%, as established by their calculated associated p-values, suggesting that the findings did not occur by chance and that they are repeatable. The calculated t-values for both satellite systems are well in excess of 2.96 meaning that the tri-orthogonal arrangement at the receiver R provides a highly significant improvement over a conventional CP mode, or dual orthogonal 90° phase-shifted DP mode, arrangement at R.

An identical statistical analysis of average LoS capacity improvement for the Iridium system, over an orbital period from 0000 UTC, 17th November, 2014 to 0140 UTC, 17th November, 2014, establishes a metric of $(t(11) = 77,\ p \leq 0.001)$ using two sets of 11 FoVs employed in an identical manner to that of the Orbcomm and GPS statistical analyses.

As a result of this statistical analysis, the null hypothesis is rejected suggesting that the third orthogonal polarisation mode at R does indeed improve the average LoS capacity of the Orbcomm, GPS and Iridium NGSO satellite systems.

Table 5.4. Narrowband fading statistics (suburban area, handheld antenna, 1.82 GHz). Three channel environments are considered as a function of elevation at R: LoS shadowing (columns 2-4), intermediate shadowing (columns 5-7), and deep shadowing (columns 8-10). Shadowing is given by an average value, α, and a standard deviation Φ, while multipath fading is given according to multipath power, or MP.

Elevation at R	α (dB)	Φ (dB)	MP (dB)	α (dB)	Φ (dB)	MP (dB)	α (dB)	Φ (dB)	MP (dB)
10°	-0.1	0.5	-19.0	-8.1	3.5	5.7	-19.0	-12.6	25.2
20°	-0.7	1.0	-25.2	-10.3	3.5	-12.0	-17.0	6.1	-21.5
30°	-0.5	1.0	-23.0	-10.3	4.5	-12.5	-18.0	6.1	-23.0
40°	-0.5	1.1	-24.0	-9.9	3.6	-12.0	-17.1	4.3	-21.0
50°	-0.1	1.0	-25.0	-10.2	2.0	-15.0	-18.0	4.6	-20.0
60°	-0.9	0.5	-20.0	-10.1	2.1	-14.0	-15.2	4.1	-20.0
70°	-0.2	0.5	-25.0	-8.0	2.1	-14.0	-17.6	4.0	-14.0

5.4.4 Analysis of Iridium System Channel According to Empirical Slow and Fast Fading Statistics

We now turn our consideration to the effect on the Iridium system channel capacity of slow and fast fading over the orbit track. A random orbital period from 0000 UTC, 17th November 2014 to 0140 UTC, 17th November 2014 is chosen. As a result, a set of FoV analyses, over the considered orbit period of 100 minutes, showing percentage improvement in capacity as a result of the inclusion of a third orthogonal polarisation mode at R, orthogonal to the receive antenna surface, is shown over eleven distinct FoVs, or every 10 minutes at global positions observed in Figure 5.20. The analyses are shown in Figures 5.28 to 5.33, according to the fading statistics of Tables 5.4 and 5.5.

A statistical analysis on the Iridium satellite system, according to prior research (Loo 1985, Lutz *et al.* 1991, Corazza and Vatalaro 1994, Fontan *et al.* 2001) in this area is now performed. The Loo parameters in Tables 5.4 and 5.5 are obtained from Fontan *et al.* (2001), and are taken over a narrowband channel operating at L-band (Jahn and Lutz 1995), for suburban and urban environments respectively. In this thesis, elevation at R is given by 90°-κ, where κ is given in Equation (4.5). The Loo parameters provide both slow fading statistics in the form of shadowing, and fast fading statistics in the form of multipath. These values are taken at 1.82 GHz over a LMS channel. The values are associated with a LoS shadowed, intermediately shadowed, and deeply

Table 5.5. Narrowband fading statistics (urban area, handheld antenna, 1.82 GHz). Three channel environments are considered as a function of elevation at R: LoS shadowing (columns 2-4), intermediate shadowing (columns 5-7), and deep shadowing (columns 8-10). Shadowing is given by an average value, α, and a standard deviation Φ, while multipath fading is given according to multipath power, or MP.

Elevation at R	α (dB)	Φ (dB)	MP (dB)	α (dB)	Φ (dB)	MP (dB)	α (dB)	Φ (dB)	MP (dB)
10°	-0.7	1.9	-38.3	-18.4	8.6	-14.7	-24.4	9.4	-23.9
20°	0.7	2.1	-25.5	-10.0	4.9	-23.3	-25.3	7.9	-26.5
30°	0.4	2.5	-34.0	-11.5	5.4	-16.0	-19.2	7.0	-22.0
40°	-0.2	1.0	-32.9	-8.6	3.8	-16.1	-15.1	2.6	-16.0
50°	0.0	0.5	-34.5	-6.1	2.7	-17.0	-13.0	4.3	-17.7
60°	0.1	1.9	-27.2	-6.9	2.2	-18.6	-13.1	4.2	-19.7
70°	-0.7	1.8	-25.1	-5.7	1.0	-23.8	-12.7	3.2	-20.2

shadowed link. Taking these criteria into account, the Loo parameters are considered as an effective proxy for statistical analysis of the Iridium system channel over the FoV.

As the statistics of Tables 5.4 and 5.5 are applied over all FoVs simulated over a random 100 minute orbital period generated using realistic orbital data, and that they are given as a function of elevation at the receiver, and that the conventional 2×2 CP mode system channel matrix forms part of the 3×2 channel matrix, the assumption is put forward that this model provides a comprehensive evaluation of the capacity benefit of a third orthogonal polarisation mode at the receiver, orthogonal to the receive antenna surface, for any (L,l) position within all simulated FoVs.

The LMS system slow and fast fading statistics may be implemented as Ricean fading over the FoV using a full general channel matrix form $\mathbf{H}$, in voltage form, given as (Gesbert *et al.* 2003, Bohagen *et al.* 2005, King and Stavrou 2006, Sirianunpiboon *et al.* 2009, Arapoglou *et al.* 2011b),

$$\mathbf{H} = \mathbf{X}_{\mathrm{R}}{}^{\dagger}\left(\sqrt{\frac{K}{1+K}}(\bar{\mathbf{H}} \odot \mathbf{S} \odot \mathbf{P})\mathbf{X}_{\mathrm{T}} + \sqrt{\frac{1}{1+K}}\tilde{\mathbf{H}}\right). \tag{5.47}$$

The channel matrix $\bar{\mathbf{H}}$ refers to the complex LoS electric voltage transfer channel matrix in Equation (5.36).

A shadowing matrix, **S**, applies shadowing according to Tables 5.4 for a suburban environment and 5.5 for an urban environment. A scaling matrix, **P**, may be applied if required, with the purpose of varying the amount of transmit power propagated from each polarisation branch at T. For the purposes of this thesis the scaling of transmit power is maintained at unity, as this provides a ready method for comparison at R of the tri-orthogonal arrangement with a conventional CP mode arrangement. The mutual coupling matrix at T, $\mathbf{X}_{\mathrm{T}}$, is given by Equation (5.37), while mutual coupling at R, $\mathbf{X}_{\mathrm{R}}$, is given by Equation (5.40).

It is important to understand that calculations remain in terms of power ratios (dB) where applicable, and that these may be readily converted to voltage ratios for the final form of the channel matrix. The transformation to voltages is required for work in phasor form, leading to a complex voltage form. Conversion from a power ratio (dB) to a voltage ratio is according to $10^{\mathrm{Power(dB)}/20}$.

The NLoS component, $\tilde{\mathbf{H}}$, is derived from a complex Gaussian random matrix. A complex Gaussian distribution is circularly symmetric, and refers to a random complex variable, $x + iy$, where the x and iy components are independent with zero mean and unit variance, $\aleph(0,1)$. Coefficients of the resulting matrix are then normalised elementwise by the square root of received signal power over each subchannel, $\sqrt{P_{\mathrm{R}}}$. The resulting matrix is then multiplied by a correlation matrix, **C**, at T and at R, to produce the NLoS component of the channel matrix. The form of the correlation matrices at R, $\mathbf{C}_{\mathrm{R}}$, and at T, $\mathbf{C}_{\mathrm{T}}$, are given in Equations (5.48) and (5.49) as,

$$\mathbf{C}_{\mathrm{R}} = \begin{bmatrix} 1 & r & r \\ r & 1 & r \\ r & r & 1 \end{bmatrix} \tag{5.48}$$

and

$$\mathbf{C}_{\mathrm{T}} = \begin{bmatrix} 1 & t & t \\ t & 1 & t \\ t & t & 1 \end{bmatrix} \tag{5.49}$$

where r and t are correlation coefficients at R and T respectively and $\mathbf{C}_{\mathrm{R}}=\mathbf{C}_{\mathrm{R}}^{\frac{1}{2}}\mathbf{C}_{\mathrm{R}}^{\frac{1}{2}\dagger}$ and $\mathbf{C}_{\mathrm{T}}=\mathbf{C}_{\mathrm{T}}^{\frac{1}{2}}\mathbf{C}_{\mathrm{T}}^{\frac{1}{2}\dagger}$, with † being the Hermitian transpose (Goldsmith 2005, Sirianunpiboon *et al.* 2009).

The NLoS component, or IID ZMCSCG component as it is often called, models scattering effects on the propagating signal through the channel, themselves dependent on environment. Some form of correlation typically exists at R, after propagation through the channel and the near-field environment at R. Any correlation at T is due to the near-field environment and the emitted waveforms themselves (Turkmani *et al.* 1995, Gesbert *et al.* 2003, King and Stavrou 2007). An orthogonal DP mode arrangement with a 90° phase shift between emitted waveforms provides diversity which, in the absence of scatterers at T, suffers negligible correlation. We assume no correlation at T, or $t = 0$ in Equation (5.49), as the orthogonal nature of the transmitted LP mode waveforms that form CP mode propagation, together with an absence of scatterers, provides negligible correlation at T (Gesbert *et al.* 2003, King and Stavrou 2006, King and Stavrou 2007). High correlation of signals is typically detrimental to MIMO capacity (Tulino *et al.* 2005). The form of the NLoS component may be given as (Goldsmith 2005, Sirianunpiboon *et al.* 2009),

$$\tilde{\mathbf{H}} = \mathbf{C}_{\mathrm{R}}{}^{\frac{1}{2}} \frac{\sqrt{\mathrm{P_R}}}{\sqrt{2}} (1+i) \mathbf{C}_{\mathrm{T}}{}^{\frac{1}{2}}. \tag{5.50}$$

Correlation of signals in MIMO wireless systems (Shiu *et al.* 2000, Chuah *et al.* 2002) typically reduces diversity performance of a polarisation diverse antenna (Lee and Yeh 1972, Kozono *et al.* 1984, Eggers *et al.* 1993, Turkmani *et al.* 1995, Gesbert *et al.* 2002, Tulino *et al.* 2005, Sirianunpiboon *et al.* 2009). Correlation is typically higher in channels with a large deterministic LoS component, since scattering effects are small and so diversity through individual fading paths is limited (Foschini and Gans 1998, Telatar 1999, Zheng and Tse 2003).

For a satellite channel, an absence of scatterers typically exists along much of the channel. For low elevations at R, scattering and shadowing effects may be greater due to ground topology and the near-field environment at R. This is seen by the multipath or multipower values which increase with lower elevation in Table 5.4, in a suburban environment for propagation in a LoS shadowing, intermediate shadowing and deep shadowing channel. In an urban environment, the effect of elevation at R on multipath is mitigated, as seen by the multipath or multipower values in Table 5.5 that show negligible correlation with elevation. In effect, an environment full of reflectors, refractors, and scatterers that may extend far above the receiver renders multipath independent of elevation at R. In King and Stavrou (2007), a maximum correlation coefficient for 90% of the time of 0.73 is measured for a LMS DCP (RHCP and LHCP) mode system

operating at low elevation angles at R. It is suggested in Lutz (1996) and King and Stavrou (2007) that correlation is largely time-dependent and dependent on scattering in the channel. Close proximity scatterers lead to higher correlation coefficients whereas separated scatterers lead to lower correlation coefficients.

In this analysis, we assume a correlation coefficient $r = 0.7$ at R (King and Stavrou 2007), in Equation (5.48). For a spatially diverse system, an empirical formula is presented in Jakes (1974), and is reproduced in King *et al.* (2005). A value of 0.7 is given in Brennan (1959) and Sakamoto *et al.* (1982) as an upper threshold value for effective diversity performance. As such, we provide analysis of a correlated system, that reduces MIMO performance (Gesbert *et al.* 2003), but which provides diversity nonetheless.

In similar research conducted in a terrestrial channel (Turkmani *et al.* 1995), in which spatial and orthogonally polarised diversity measurements are made using vertical and horizontal antenna arrays and orthogonal DP mode arrangements at 1800 MHz, a correlation coefficent of less than 0.7 for 95% of the time is measured using orthogonal polarisation diversity in scenarios ranging from rural to urban environments. The lowest correlation coefficient of 0.2 is found for an urban environment, which corresponds with the idea of an environment which scatters, reflects and refracts orthogonally polarised propagating waves on an individual basis. In effect, what happens to a received signal level on one orthogonally polarised antenna branch as an incoming signal suffers depolarisation through the channel, does not necessarily happen on another, and so an antenna has a compensatory aspect between orthogonally polarised branches which provides diversity gain.

For a DP mode antenna and use of MRC, diversity gain is highest when there is no difference in received polarised signal levels and no correlation. For EGC, performance deteriorates rapidly as a function of difference in signal levels on each polarisation, as additional unwanted noise is simply added by the antenna polarisation branch with lower received signal strength. In effect, a tri-orthogonally polarised antenna arrangement aims to exploit polarised signal reception over three dimensions, using polarisation compensation or diversity to provide possibilities of CSI-adaptive MRC, EGC or indeed selection of a maximum signal (Jakes 1974) on incoming signals from a greater range of directions than would be the case using DP mode reception techniques. In Sirianunpiboon *et al.* (2009), for cases of higher correlation both at T and at R, the inclusion of a third orthogonal polarisation renders the antenna robust over all orientations.

The performance of a DP mode antenna is seen to deteriorate severely in the same channel.

In King and Stavrou (2007), isolations between polarisations of 15 dB at the mobile ground receiver, and 20 dB at the satellite transmitter are given. In the analysis shown in this chapter, an examination is made of the performance of the tri-orthogonal arrangement using values that err on the side of caution, and so an isolation between polarisations of 10.45 dB is assumed (Ding *et al.* 2007, Verdone and Zanella 2012), at the lower end of acceptable isolation between polarisations for a wireless communications antenna. In Chapter 6, a planar tri-orthogonal antenna design with port isolation between polarisation modes of 35 dB is demonstrated.

In Equation (5.47), the proportion of a transmitted signal attributed to the NLoS component, as a result of fast fading in the channel, is determined by the Ricean K-factor, that may be determined from multipath power, or MP (Fontan *et al.* 2001, Goldsmith 2005) in Tables 5.4 and 5.5. The mutual coupling factor between polarisations influences system perfomance over the channel through $\mathbf{X}_{\mathrm{T}}$ and $\mathbf{X}_{\mathrm{R}}$, with the superscript denoting the Hermitian transpose once again in the case of $\mathbf{X}_{\mathrm{R}}$. For high mutual coupling, system performance approaches that of a singularly polarised system.

Figures 5.28, 5.29, and 5.30 show the cases of LoS shadow, intermediate shadow, and deep shadow suburban channel propagation over the FoV according to the fading statistics of Table 5.4 (Fontan *et al.* 2001), for the Iridium system downlink channel.

Figures 5.31, 5.32, and 5.33 show the cases of LoS shadow, intermediate shadow, and deep shadow urban channel propagation over the FoV according to the fading statistics of Table 5.5 (Fontan *et al.* 2001), for the Iridium system downlink channel.

Slow fading affects LoS signal propagation and is represented by shadowing, or signal blockage, which is given in Tables 5.4 and 5.5 by an average shadowing variable, α, and a standard deviation Φ. Shadowing follows a log-normal distribution, while fast fading is given by multipath power, MP, which follows an inverse relationship with the Ricean K-factor. For both suburban and urban environments, the LoS shadowing FoV plots provide the largest percentage capacity improvement through a tri-orthogonal arrangement at R. This is observed in Figures 5.28 and 5.31 respectively. A degradation of the benefit generated by a third orthogonal polarisation mode at R, orthogonal to the antenna surface, as the channel deteriorates to a deep shadowing regime may be observed in Figures 5.29, 5.30 and 5.32, 5.33. As the channel deteriorates, the benefit of the tri-orthogonal arrangement at the receiver remains everpresent, however.

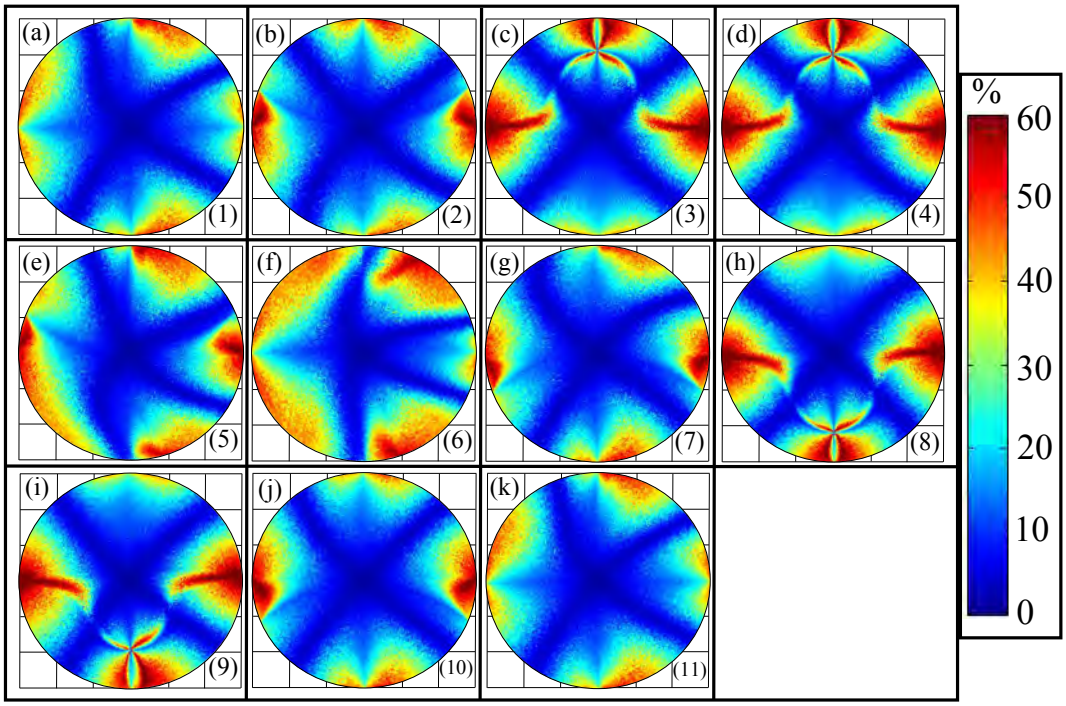

Figure 5.28. Simulated percentage improvement in Iridium system capacity, over a NGSO ionospheric FoV according to Iridium orbital parameters and suburban LoS shadowing statistical fading, as a result of implementing a third orthogonal polarisation mode at the receiver. The FoVs are sequentially simulated in a 10-minute progression over a random orbital period of 100 minutes from 0000 UTC on 17th November 2014, to 0140 UTC on 17th November 2014 along a typical Iridium trajectory, using realtime TEC (National Oceanic and Atmospheric Administration Accessed: 2014) and magnetic field data (Maus *et al.* 2010). The number in the bottom right corner of each FoV corresponds to the FoV number given in 5.20.

On average, and over all (L,l) positions analysed over the orbital path, an increase in capacity performance as a result of the implementation of a third orthogonal polarisation mode $\hat{\mathbf{r}}$, orthogonal to the ground receiver patch antenna radiating surface, is observed for each NGSO satellite system. The average improvement, as a percentage of capacity performance of a conventional CP mode patch antenna at R, is given as follows:

- Iridium: 14.6$\pm$2.5%
- Orbcomm: 16.7$\pm$1.8%
- GPS: 38.8$\pm$3.1%.

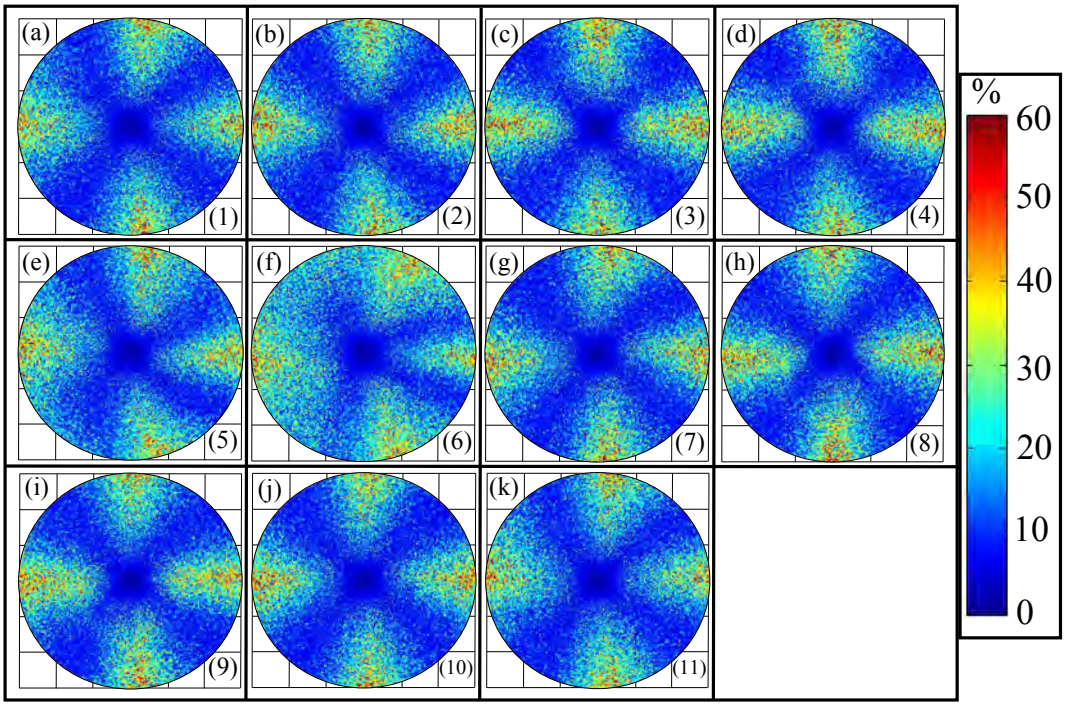

Figure 5.29. Simulated percentage improvement in Iridium system capacity, over a NGSO ionospheric FoV according to Iridium orbital parameters and suburban intermediate shadowing statistical fading, as a result of implementing a third orthogonal polarisation mode at the receiver. The FoVs are sequentially simulated in a 10-minute progression over a random orbital period of 100 minutes from 0000 UTC on 17th November 2014, to 0140 UTC on 17th November 2014 along a typical Iridium trajectory, using realtime TEC (National Oceanic and Atmospheric Administration Accessed: 2014) and magnetic field data (Maus *et al.* 2010). The number in the bottom right corner of each FoV corresponds to the FoV number given in 5.20.

At R, the patch antenna radiating surface is held orthogonal to the zenith position. As such, these values do not take into account misalignment of the receive antenna with the zenith. At the FoV centre, such misalignment would increase the capacity improvement due to the third orthogonal polarisation $\hat{\mathbf{r}}$, as this polarisation branch would mitigate any drop in performance on polarisation branches $\hat{\mathbf{p}}$ and $\hat{\mathbf{q}}$, associated with a conventional CP mode patch antenna.

As shown in Table 5.2, the inclination of the receiver, given by γ, is a function of orbit height. As a consequence, and using Equation (4.7), the antenna of the Orbcomm system ground receiver R has a maximum misalignment from the Orbcomm satellite of just 26.9°, with this value being 27° for the Iridium system, and 76.1° for the GPS

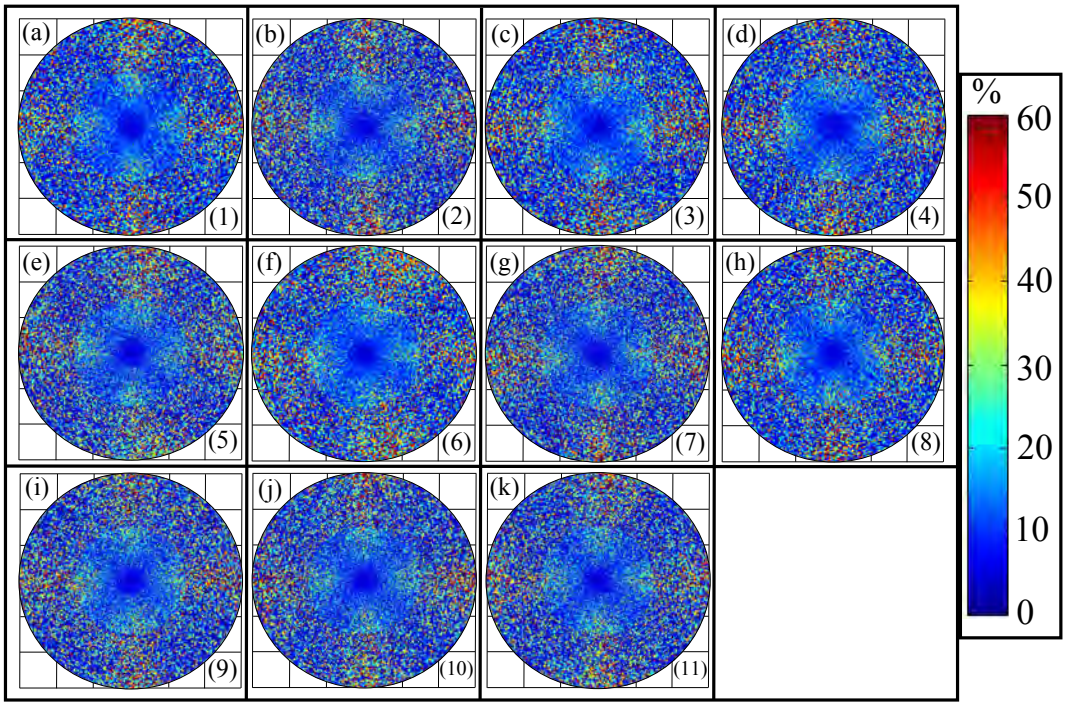

Figure 5.30. Simulated percentage improvement in Iridium system capacity, over a NGSO ionospheric FoV according to Iridium orbital parameters and suburban deep shadowing statistical fading, as a result of implementing a third orthogonal polarisation mode at the receiver. The FoVs are sequentially simulated in a 10-minute progression over a random orbital period of 100 minutes from 0000 UTC on 17th November 2014, to 0140 UTC on 17th November 2014 along a typical Iridium trajectory, using realtime TEC (National Oceanic and Atmospheric Administration Accessed: 2014) and magnetic field data (Maus *et al.* 2010). The number in the bottom right corner of each FoV corresponds to the FoV number given in 5.20.

system. Consequently, it may be observed that the percentage improvement in capacity through inclusion of the radial orthogonal polarisation mode at R, $\hat{\mathbf{r}}$, is generally higher for the GPS system than for the Iridium and Orbcomm systems. It should be noted that, as the ground receive antenna at R is assumed to be placed with its radiating surface orthogonal to the zenith, in accordance with manufacturer guidelines for such antennas (Cobham Plc Accessed: 2015, Taoglas Ltd 2015), so any additional misalignment caused by surface topology or weather events would only be mitigated by a tri-orthogonal design.

The depolarising effect of Faraday rotation and its mitigation by a tri-orthogonal arrangement is observed for all three NGSO satellite systems. For the Orbcomm system, operating at 138 MHz, the effect is far greater, resulting in troughs where, due to

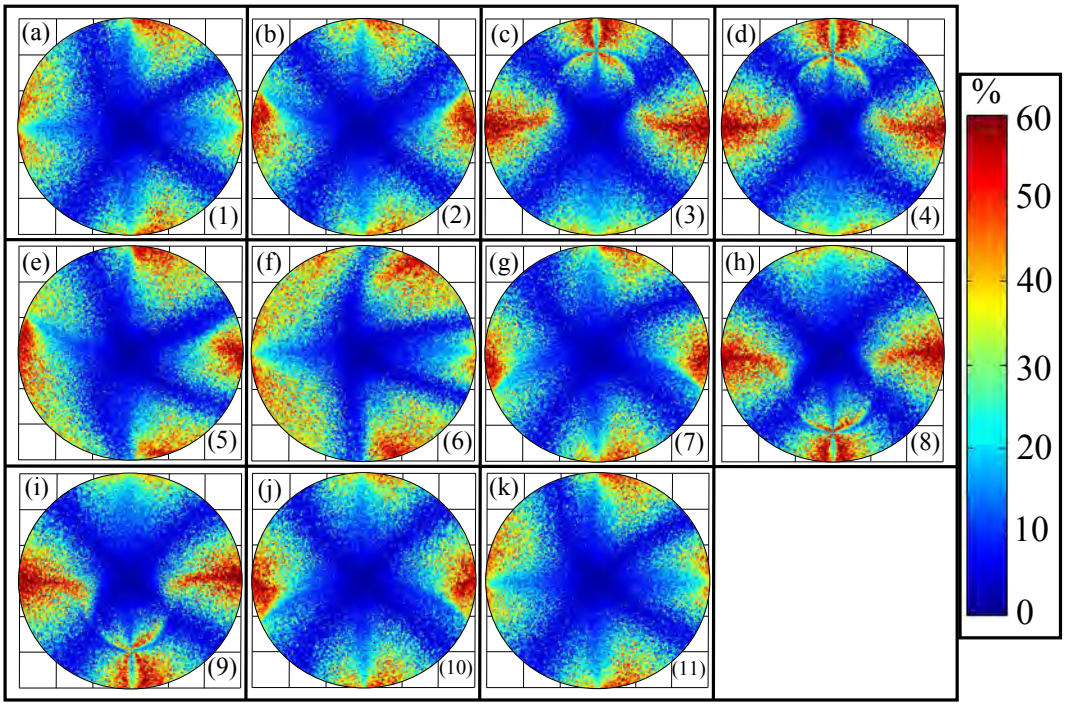

Figure 5.31. Simulated percentage improvement in Iridium system capacity, over a NGSO ionospheric FoV according to Iridium orbital parameters and urban LoS shadowing statistical fading, as a result of implementing a third orthogonal polarisation mode at the receiver. The FoVs are sequentially simulated in a 10-minute progression over a random orbital period of 100 minutes from 0000 UTC on 17th November 2014, to 0140 UTC on 17th November 2014 along a typical Iridium trajectory, using realtime TEC (National Oceanic and Atmospheric Administration Accessed: 2014) and magnetic field data (Maus *et al.* 2010). The number in the bottom right corner of each FoV corresponds to the FoV number given in 5.20.

ground receiver alignment, the capacity is seen to drop off for a 2×2 conventional CP mode system, resulting in a capacity improvement by the 3×2 system with the tri-orthogonal arrangement at R.

For the Iridium and GPS systems, both operating near 1.6 GHz, the depolarising effect of Faraday rotation is weaker, and so the perturbing effect on capacity performance seen in the FoVs of Figures 5.23, 5.28 to 5.33, and 5.25 and 5.27 is less.

5.4.5 Effect of Mutual Coupling on System Performance

The simulations over an orbit for each of the three NGSO satellite systems have been performed using a mutual or polarisation coupling factor of 0.3 applied at both T and

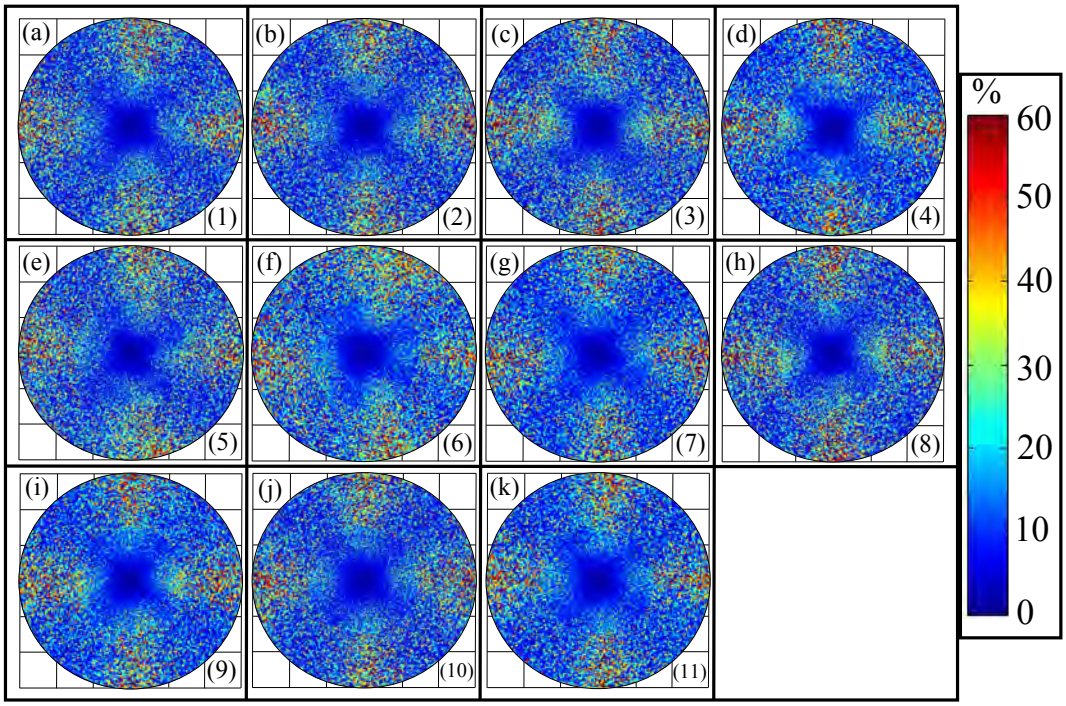

Figure 5.32. Simulated percentage improvement in Iridium system capacity, over a NGSO ionospheric FoV according to Iridium orbital parameters and urban intermediate shadowing statistical fading, as a result of implementing a third orthogonal polarisation mode at the receiver. The FoVs are sequentially simulated in a 10-minute progression over a random orbital period of 100 minutes from 0000 UTC on 17th November 2014, to 0140 UTC on 17th November 2014 along a typical Iridium trajectory, using realtime TEC (National Oceanic and Atmospheric Administration Accessed: 2014) and magnetic field data (Maus *et al.* 2010). The number in the bottom right corner of each FoV corresponds to the FoV number given in 5.20.

at R. This value is used in Equations (5.37) and (5.40). This provides a lower bound of performance, or worst case scenario.

Attention is now passed to examining the effect of mutual coupling at the receiver by varying the mutual coupling factor, ρ_{R}, between polarisations at R from no mutual coupling, or 0, to full mutual coupling, or 1. A mutual coupling factor, ρ_{T}, of 0.3 is maintained at T.

In Figure 5.34, an average capacity metric is observed over the entire considered orbit for the 3×2 system. The following points are noted.

- For both the Iridium and Orbcomm systems a small amount of mutual coupling at R, of the order of 0.1–0.2 appears to increase performance. In Wallace and

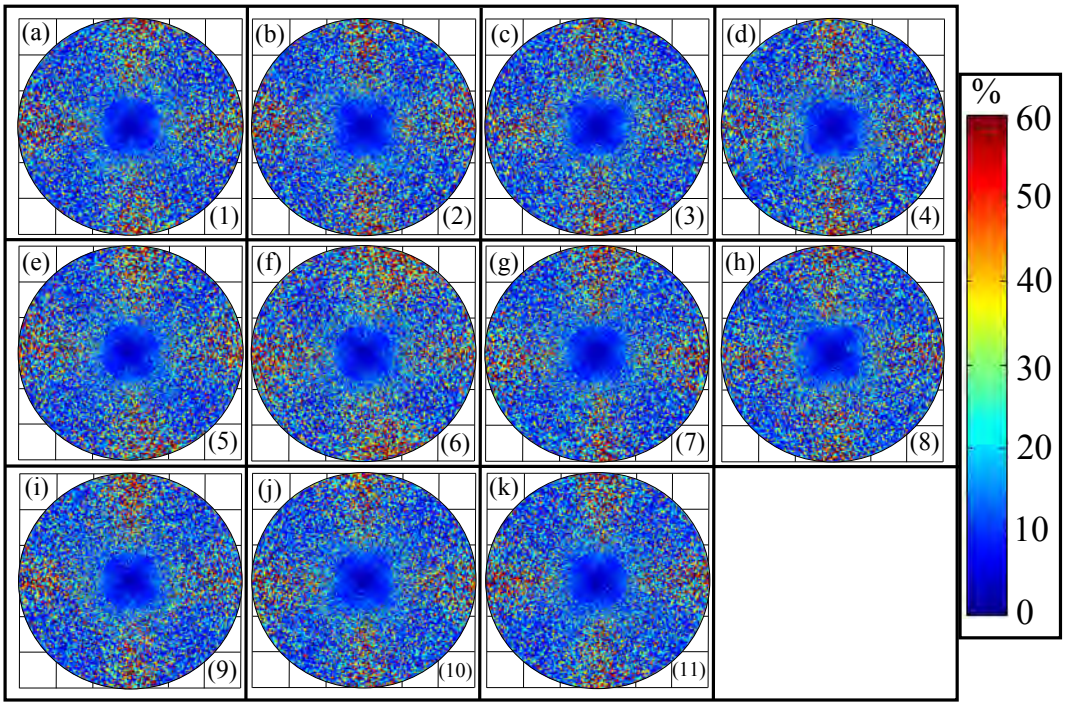

Figure 5.33. Simulated percentage improvement in Iridium system capacity, over a NGSO ionospheric FoV according to Iridium orbital parameters and urban deep shadowing statistical fading, as a result of implementing a third orthogonal polarisation mode at the receiver. The FoVs are sequentially simulated in a 10-minute progression over a random orbital period of 100 minutes from 0000 UTC on 17th November 2014, to 0140 UTC on 17th November 2014 along a typical Iridium trajectory, using realtime TEC (National Oceanic and Atmospheric Administration Accessed: 2014) and magnetic field data (Maus *et al.* 2010). The number in the bottom right corner of each FoV corresponds to the FoV number given in 5.20.

Jensen (2004), mutual coupling between two dipoles is shown to increase capacity performance due to an increased effective aperture of coupled dipoles. An adjacent dipole provides a recapturing mechanism for power scattered by a receiving dipole, particularly when the matching network is appropriately implemented. In all simulations in this chapter, a matched network is assumed. For the Iridium and Orbcomm systems, link geometry is similar due to orbit height, and so differences over an orbit in average capacity performance, essentially a function of SNR, become a function of transmit power and frequency of operation, or electromagnetic parameters. According to Table 5.2, maximum values of α and γ of 63° and 27° respectively are given for both systems. From a purely geometrical standpoint devoid of channel effects, the maximum misalignment

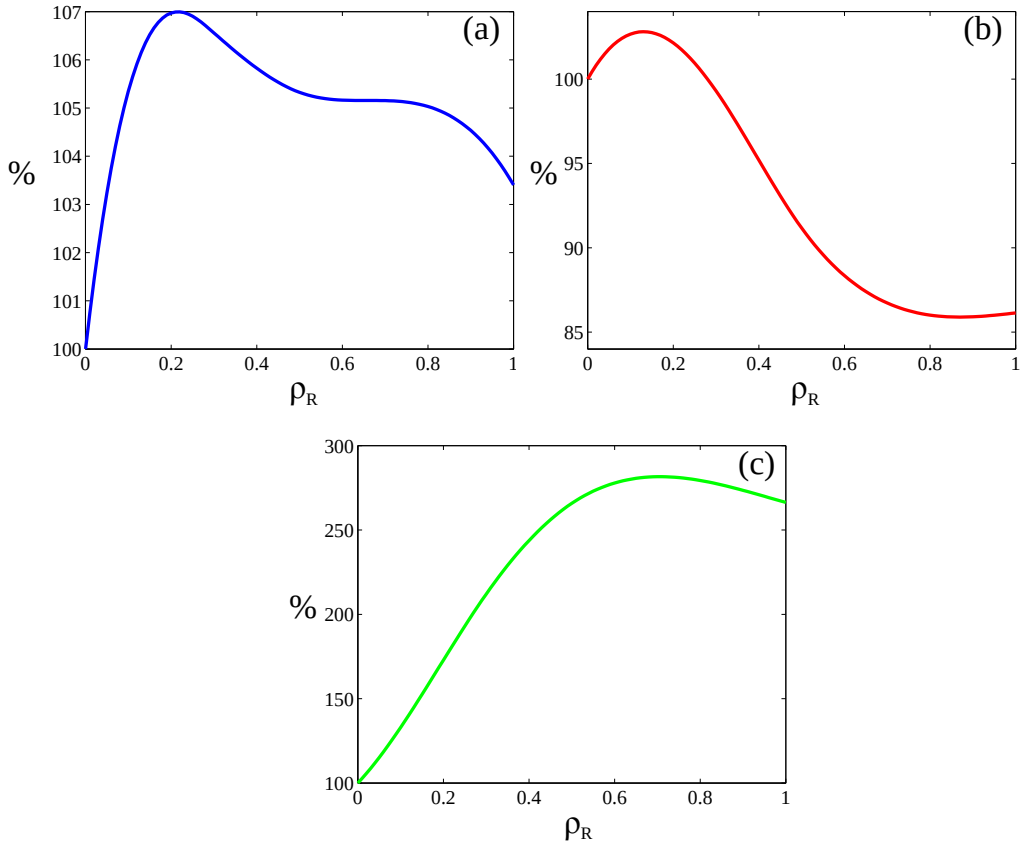

Figure 5.34. Average capacity performance of the 3 $\times$ 2 arrangement over an orbit. Results are given as a function of mutual coupling, ρ_R, between orthogonal polarisation modes at R. A mutual coupling factor, ρ_T, of 0.3 is maintained at T. The effect of mutual coupling on the average orbital capacity of the system consisting of a CP transmitter at T and tri-orthogonal receiver at R is shown as a percentage of average orbital capacity of a system where there is no mutual coupling at R, or $\rho = 0$: (a) Iridium system, (b) Orbcomm system, (c) GPS system.

experienced by R in relation to T is 27° for both systems, and this is small in a rotational sense, and so the impact of polarisation branch mode $\hat{\mathbf{r}}$, orthogonal to the receive antenna surface, is small on performance over the entire FoV. The effect of mutual coupling is not seen to affect average capacity performance over the orbit to a large extent.

- For the GPS system, according to Table 5.2, the maximum value of α and γ is 13.9° and 76.1° respectively. From a purely geometrical standpoint devoid of channel effects, the maximum misalignment experienced by R in relation to T is 76.1°, and this is large in a rotational sense, and so the impact of the additional orthogonal polarisation mode $\hat{\mathbf{r}}$, orthogonal to the receive antenna surface, on average

capacity performance over an orbit, is large. The outer edges of each FoV in Figures 5.25 and 5.27, covering the two extremes of GPS signal propagation in the channel, are seen to benefit from an additional degree of freedom at the receiver, in the guise of orthogonal polarisation branch mode $\hat{\mathbf{r}}$. The effect of mutual coupling at R, at least from an average capacity perspective over the orbit, provides additional received power at the outer edges of the FoV due to orthogonal polarisation branch mode $\hat{\mathbf{r}}$, which operates most effectively in this region. For the GPS system, this results in best average capacity performance when the mutual coupling factor is high, of the order of 0.7–0.8. Average capacity performance remains high as the mutual coupling factor at R approaches unity. In Dong *et al.* (2005), mutual coupling and casing effects in a polarisation diverse antenna structure are suggested as providing a large capacity increase with less constraint on the antenna configurations than an idealised tri-orthogonal arrangement. It is suggested that pattern diversity is far less a contributory factor to capacity performance than polarisation diversity. In effect, mutual coupling is suggested as being beneficial for MIMO schemes, as received power is augmented through mutual coupling.

- For the NGSO satellite systems considered in this chapter, the ground receiver at R is aligned with its radiating surface orthogonal to the zenith, in accordance with manufacturer guidelines for patch antennas (Cobham Plc Accessed: 2015, Taoglas Ltd 2015). Any additional misalignment caused by terrestrial surface topology or weather events would only be mitigated by a tri-orthogonal design. For a tri-orthogonal receiver at R experiencing severe misalignment with a CP mode transmitter at T, it is suggested that average capacity would benefit from increased mutual coupling effects at R, as the inclusion of orthogonal receive antenna polarisation branch mode $\hat{\mathbf{r}}$ would increase received power, providing enhancement similar to that observed for the GPS system in Figure 5.34 (c).

Expanding on the idea of mutual coupling effects on system performance, in Figure 5.35 we examine the performance of the 2×2 and 3×2 systems as a function of mutual coupling at the receiver at R, and as a function of mutual coupling extremes likely to be experienced at the transmitter at T. We recall that both 2×2 conventional and 3×2 systems consist of a CP mode transmitter at T, with the 2×2 conventional system employing a CP mode patch receive antenna at R, while the 3×2 system employs a tri-orthogonal receiver at R.

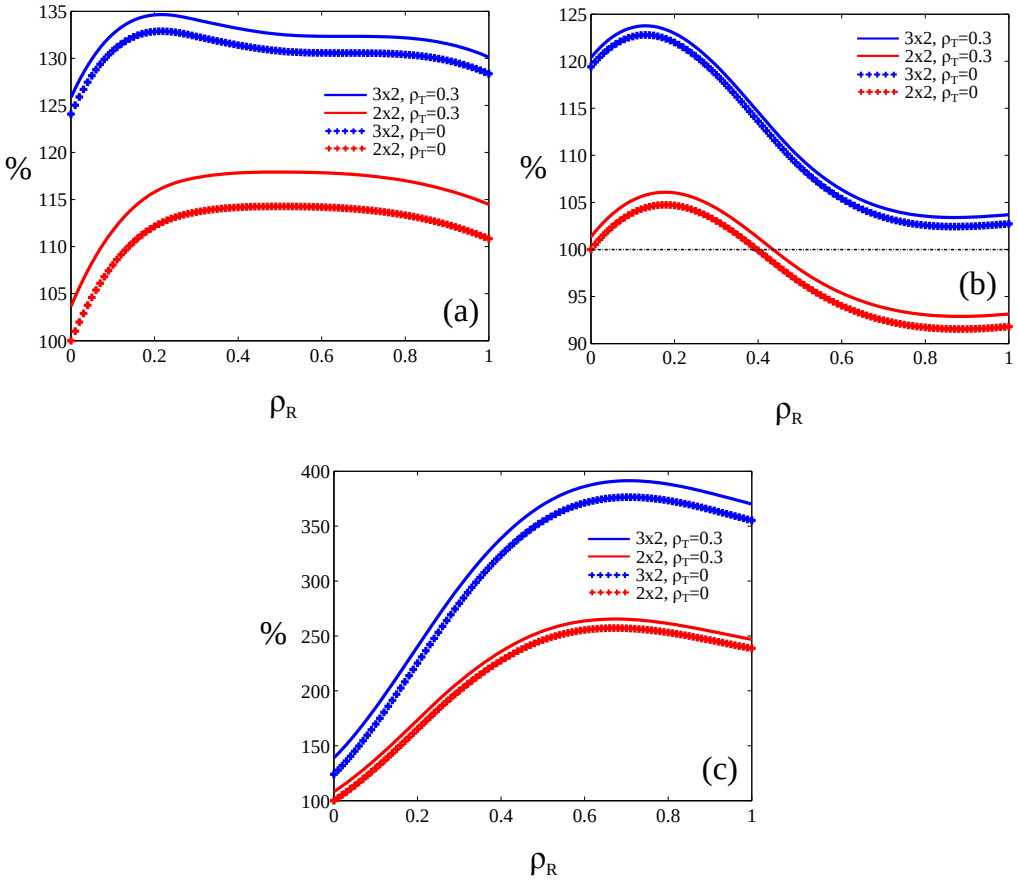

Figure 5.35. Average capacity performance of the 3 × 2 tri-orthogonal receiver and 2 × 2 conventional CP mode receiver system arrangement over an orbit. Results are given as a function of mutual coupling, ρ_R, between orthogonal polarisation modes at R, and two extremes of mutual coupling factor, ρ_T, between orthogonal polarisation modes at T. We use mutual coupling factors, ρ_T, of 0 and 0.3 to represent the extremes of a range of mutual coupling that would likely be experienced at T. Both 2 × 2 and 3 × 2 systems consist of a CP mode transmitter at T, with the 2 × 2 system employing a CP mode patch antenna at R, while the 3 × 2 system employs a tri-orthogonal receiver at R. The effect of mutual coupling, ρ_R, at R on the average orbital capacity of both systems is shown as a percentage of average orbital capacity of a 2 × 2 system with no mutual coupling, or $\rho_T = 0$ and $\rho_R = 0$: (a) Iridium system, (b) Orbcomm system, (c) GPS system.

The following points are noted.

- The third orthogonal polarisation branch, $\hat{\mathbf{r}}$, at R increases average orbital capacity regardless of the amount of mutual coupling between polarisation branches for all three NGSO satellite systems.
- The effect of mutual coupling at T on the system is smaller than that of mutual coupling at R. This suggests that the design of the receiver plays a pivotal role in system performance.
- High mutual coupling is detrimental to average capacity performance for the Orbcomm system. The Orbcomm system operates at 138 MHz, and is impacted by the ionosphere in the form of Faraday rotation moreso than the Iridium and GPS satellite systems.
- A system experiencing severe misalignment is impacted to a greater extent by the effect of mutual coupling at R than a system experiencing slight misalignment. This is highlighted by the case of the GPS system. We recall that the antenna at R is placed with its radiating surface orthogonal to the zenith, and that any deviation from this alignment may increase the unwanted effects attributed to misalignment. This would only be mitigated by the tri-orthogonal receiver design at R.

Beamforming, or steering a beam to enhance SNR in a link direction, is only possible through low mutual coupling. The effect of mutual coupling affects pattern diversity, or the overall radiation pattern resulting from individual patterns associated with each polarisation. Mutual coupling is considered an unwanted effect in antenna design providing deviation from expected performance, radiation nulls in certain link directions, and pattern asymmetry (Chiu *et al.* 2007a). It has been the focus of compensation techniques at the receiver in an attempt to enhance beamforming performance (Steyskal and Herd 1990, Dandekar *et al.* 2002). The effect of mutual coupling on system performance is often omitted in papers which focus solely on MIMO schemes (Telatar 1999, Nabar *et al.* 2002).

The contrast in the perceived utility of mutual coupling, observed between MIMO and beamforming applications, is stark. Indeed, in Gesbert *et al.* (2003), the note is made that a decision at system level should be made on whether to optimise channel

performance according to a MIMO scheme or a beamforming application. In Chapter 6, a scalable antenna design is proposed that provides a tri-orthogonal solution in planar form, with low mutual coupling between polarisations. By phasing individual ports appropriately, it is possible to beamform using all three orthogonal polarisations, providing an increased SNR response in a given propagation direction, akin to a beamforming application. Furthermore, the pattern diversity that provides a radiation pattern optimised in a propagation direction may be azimuthally cycled through the implementation of simple phasing techniques, providing a tri-orthogonal polarisation diverse operation, akin to a MIMO system operation. Such a design would be applicable as a ground receiver at R in a satellite channel. The orthogonality and symmetry of the design provides low mutual coupling, for what is suggested to be an extremely useful design for diversity applications. As such, it is suggested that the ability to provide beamforming through low mutual coupling and enhanced performance in the form of tri-orthogonal polarisation diverse MIMO operation may tentatively sit alongside each other according to such a design.

The increase in diversity gain (Adve Accessed: 2013) over the considered orbital path due to the inclusion of the third orthogonal polarisation mode at R, orthogonal to the antenna surface, is calculated for each NGSO satellite system and is shown in Figure 5.36. The receive patch antenna radiating surface is once again held orthogonal to the zenith position. Applying maximal ratio combining at R, the increase in diversity gain for 99% communication reliability is given as follows:

- Iridium: 2.43 dB
- Orbcomm: 2.23 dB
- GPS: 3.18 dB.

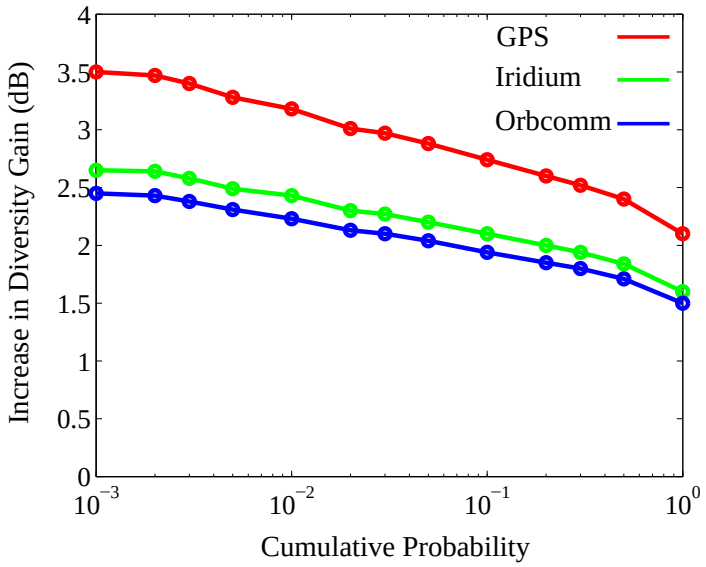

Figure 5.36. Simulated increase in diversity gain (dB). Over an orbital path for each satellite, and as a result of implementing a third orthogonal polarisation mode, or half-wavelength dipole, $\hat{\mathbf{r}}$ at R, an increase in diversity gain is observed for all three satellite systems. The larger increase observed for the GPS system results from the increased angular displacement of the receive antenna as observed from T due to the higher orbit and hence larger FoV. As the ground receive antenna surface is held orthogonal to the zenith direction for all three satellite systems within the FoV, the increased rollover of the GPS receive antenna may be viewed as a proxy for weather conditions or topography at the FoV centre that inhibit the antenna surface from being held orthogonal to the zenith direction. An aim of the tri-orthogonal antenna design at R is to mitigate against misalignment, which is suggested by the increased diversity gain of all three satellite systems, and in particular by the GPS system.

5.5 Chapter Summary

This chapter highlights a novel channel model that provides a vectorised analysis of three NGSO satellite systems that, using realistic simulated and measured values in accordance with a fundamental physical design approach, suggests that the inclusion of a third signal polarisation at the receiver R, orthogonal to signal polarisations of an existing CP mode patch or helical CP mode antenna structure, provides increased capacity over a large NGSO FoV. This is provided that signalling from transmitter T and reception at receiver R take account of the radio wave polarisation specific to the link geometry for the location of R during processing. This extends receiver range and is relevant to all NGSO satellites, and particularly so to LEO satellite systems, where

link geometry changes rapidly and low elevation link geometry occurs frequently. A typical satellite LoS channel offers little in the way of a rich scattering environment for propagation enhancement. A tri-orthogonal approach at the receiver renders a satellite link less dependent on alignment, as the possibility of at least two orthogonal polarisation modes is provided at the receiver in any link direction.

The model is first compared through a capacity metric to conventional CP mode performance of an Iridium system satellite, and calculation and comparison of FDMA and TDMA capacities is provided.

Simulations performed consider the full range of channel conditions, through inclusion of a total fading margin in a complex signal transfer channel matrix.

The Iridium system channel is modelled over the FoV in three diverse channel environments, using empirical LMS channel slow and fast fading data. The benefit of a third orthogonal polarisation at the receiver is made apparent in all cases considered.

For a conventional CP mode receive antenna, a CP mode signal is only able to be received where perfect receive-transmit antenna alignment exists, typically when a satellite is near the zenith position of the ground receive patch antenna. This constraint is due to design restrictions and manufacturer guidelines. Signal polarisation reverts to EP mode form as receive link geometry deviates from perfect receive-transmit antenna alignment, ultimately resulting in HP mode signal reception at the receiver horizon. Coupled with a reduced receive antenna gain at lower elevation angles, this impairs cross polarisation rejection and reduces system capacity. The ability to maintain gain at lower elevation angles, while maintaining polarisation diversity, would increase link range and extend the FoV.

The inclusion of a third orthogonal half-wavelength dipole mode at the receiver provides additional polarisation diversity. Through no increase in system transmit power, a capacity improvement is observed over severe fading channels, for all three distinct NGSO satellite systems considered. Analysis over a random orbital period for each satellite system, using realtime ionospheric data, suggests this improvement to be statistically significant. This is reinforced by the implementation of LMS empirical data used in a subsequent stochastic channel simulation for the Iridium system.

A third orthogonal polarisation mode, $\hat{\mathbf{o}}$, at the satellite would further extend this concept to allow at least two orthogonal polarisations to be transmitted to any position

within the FoV. An ability to vary transmit power and phase on three orthogonal polarisations would add even greater flexibility to a system with limited linear transmit power, providing beam steering of the transmitted wave to specific FoV locations, and the possibility of CP wave propagation to a specific receiver position within the FoV.

The model suggests that the inclusion of a third orthogonal polarisation mode at a ground receiver, orthogonal to an existing patch or helical structure antenna surface, provides, over a large NGSO satellite system FoV, the following advantages:

- increased capacity over a majority of a FoV, or antenna orientations
- provision of orientation robustness in instances of antenna misalignment
- increased FoV range extending the outer edge of the FoV
- increased diversity gain over the considered orbit path, providing communication reliability with a reduction in transmit power at the satellite
- possible reduction of transmit spot beams at the satellite
- implementable on ground receiver, requiring no intervention at the satellite.

This is particularly relevant to LEO satellite systems, where link geometry changes rapidly, and near horizontal link geometry occurs frequently. A tri-orthogonal approach at the ground receiver renders a satellite link less dependent on alignment, as at least two orthogonal receive polarisation modes are offered at the receiver for any receive link direction.

The case is considered whereby the ground receiver patch antenna radiating surface is orthogonal to the zenith position. This alignment is unlikely to be maintained for most applications, due to local topography, weather effects, and movement. At or near the FoV centre, this idea suggests that, where a low or negligible improvement in capacity due to a third orthogonal polarisation branch is observed in our simulations, the probabilty of a capacity improvement as observed in the outer FoV edges of our simulations is increased through a tri-orthogonal polarisation diverse approach. This would additionally increase the diversity gain of the NGSO satellite system.

The inclusion of a third orthogonal polarisation mode at the ground receiver, orthogonal to the radiating surface of the antenna and so orthogonal to conventional CP mode

patch antenna polarisations, provides additional polarisation diversity. Through no alteration to the satellite transmission mechanism, such an arrangement provides a capacity improvement and additional diversity gain over a FoV for three distinct NGSO satellites. Realtime global ionospheric data and physical satellite characteristics are used to provide these results. The capacity improvement and additional diversity gain are a consequence of increased gain at low elevation angles, coupled with enhanced polarisation diversity performance at low elevation angles. Analysis is performed over a random orbital period for each of three distinct NGSO satellite systems, with results suggesting that capacity improvement is statistically significant.

The effect of mutual coupling on link performance is considered and is in agreement with similar studies. The following points are made.

- In the instance of severe misalignment between a CP mode transmitter at T and a tri-orthogonal receiver at R, high mutual coupling at R provides enhanced MIMO scheme performance. In effect, received power is increased at R due to inclusion of a third orthogonal polarisation mode branch orthogonal to the radiating surface, providing a higher average capacity metric.
- Beamforming requires low mutual coupling, in juxtaposition to the point made above.
- In Chapter 6, an antenna design is presented that provides a tri-orthogonal polarisation diverse solution in planar form. As the design is planar, the antenna is not subject to an increase in volume that has dogged existing antenna design in the area of tri-orthogonal polarisation diversity. The orthogonality and symmetry of the design provides low mutual coupling, and so beamforming possibilities, and tri-orthogonal polarisation diverse MIMO operation as three orthogonal polarisations may be used to enhance average capacity through phase-cycled feeding techniques. As such, the two points made above may coexist in one planar design.

Chapter 6

Planar Tri-orthogonal Diversity Slot Antenna

THIS chapter proposes an easily manufacturable multifunction multiport planar slot antenna with tri-orthogonal pattern diversity. Distinct radiation patterns are emitted via a common square radiative slot by exploiting three orthogonal modes. These slot modes consist of a magnetic current loop mode with an omnidirectional linearly polarised (OLP) radiation pattern, and two degenerated linear slot modes radiating broadside with orthogonal linear polarisation modes (LP). The tri-orthogonal patterns are obtained in an overlapping frequency band, and the mutual coupling between the ports is minimised through a differential feeding arrangement. This new concept of multiport diversity slot antenna is validated experimentally at a frequency of 5.9 GHz, successfully demonstrating the operation modalities of OLP and LP radiation patterns. A minimum tri-orthogonal overlapping impedance bandwidth of 2.3% is measured with inter-port coupling below -35 dB. The proposed antenna could be used as a pattern and polarisation diversity antenna, where additionally, linear combination of the primary tri-orthogonal patterns can be exploited to further enhance flexibility in pattern generation.

6.1 Introduction

6.1.1 Tri-Orthogonality

An increasing number of wireless communications technologies in the microwave region, and indeed beyond, are focused on driving up transmission rate. An increase in rate is often at the expense of coverage. In a mobile world, the ability to send and receive signals in any direction without compromising link reliability would be highly desirable.

Using a single multiport antenna structure with pattern diversity and low mutual coupling between different ports is one possible solution towards higher link reliability for mobile and vehicular applications. The available literature mostly focuses on multiport printed diversity antennas or planar inverted-F antennas (PIFA) due to their compactness, low cost, and low profile (Diallo *et al.* 2006, Yang *et al.* 2008, Chebihi *et al.* 2008). However, these antennas often suffer from a combination of a complicated structure, large size, poor radiation pattern symmetry, relatively low gain, and little consideration of polarisation, or the polarisation mode, orthogonal to the antenna surface.

The benefit of transmitting a second orthogonally polarised signal is well known (Nabar *et al.* 2002, Kyritsi *et al.* 2002, Gesbert *et al.* 2003, Erceg *et al.* 2006). Polarisation diversity offers performance robustness in a small volume, provided mutual coupling between polarisation modes (Li *et al.* 2012) can be kept low, such as in an orthogonal system (Ramirez and De Flaviis 2003). The robustness of dual-polarised systems is however adversely affected by transmitter-receiver misalignment.

To mitigate this problem and introduce orientation robustness in a rich scattering environment, the increase in capacity performance offered by colocated antennas in a tri-orthogonal arrangement has previously been highlighted (Andrews *et al.* 2001, Mtumbuka *et al.* 2005, Mtumbuka and Edwards 2005, Getu and Janaswamy 2005, Getu and Andersen 2005, Yan *et al.* 2006, Chiu *et al.* 2007b, Gupta *et al.* 2008, Chiu *et al.* 2009, Yun and Vaughan 2010, Omote *et al.* 2015, Piao *et al.* 2015). Such systems demonstrate the benefit of a third orthogonal antenna, but realised configurations are typically large and impractical. To emit three isolated and orthogonal polarisation modes from a small volume would be highly desirable for mobile, and in particular vehicular, applications.

A colocated tri-orthogonal antenna employing a dielectric resonator antenna (DRA) as an integrated solution to generate three orthogonally polarised signals, including one

parallel to the direction of propagation, has been demonstrated in Zou and Fumeaux (2011), in a non-planar solution. Monopoles placed at the centre of a tri-orthogonal antenna add to design and implementation complexity requiring dual-substrate manufacture (Zhong *et al.* 2009, Gao *et al.* 2010a). A low profile tri-orthogonal design was presented in Tong *et al.* (2013), however, with an asymmetric configuration creating a pattern asymmetry in the far field.

This chapter proposes a multiport planar slot antenna capable of transmitting phase-centred polarised signals in three orthogonal directions, while providing high inter-port isolation due to a differential feeding technique. Two broadside patterns with orthogonal polarisation modes are generated by selective excitation of degenerated slot modes, whereas the third polarisation, in the z direction, is offered through inclusion of a low-profile magnetic current loop electric monopole (Kaufmann and Fumeaux 2015).

The chapter provides firstly a generic description of the proposed concept of a multiport slot antenna with differential feeding. It then describes as illustration a specific design at a frequency of 5.9 GHz, in the dedicated short-range communications (DSRC) allocated spectrum (Kenney 2011), which includes vehicle-to-vehicle (v2v) applications (Biswas *et al.* 2006). A purpose-built feeding network is then combined with the antenna to experimentally demonstrate the performance in tri-orthogonal modes. In summary, the experimental results validate the concept, in particular with measured inter-port coupling coefficients below -35 dB.

6.2 Antenna Design and Feed Network

6.2.1 Concept

The proposed design in Figure 6.1 may be considered as a square slot antenna allowing three orthogonal polarised modes to radiate from the antenna upper surface. Figure 6.2 illustrates the modes of operation in the antenna, namely a magnetic current loop mode, for omnidirectional linearly polarised (OLP) radiation, and a degenerated broadside mode, for linear polarisation (LP) radiation. The radiative mechanism of both modes through the common radiative slot on the antenna upper surface, enabling tri-orthogonal polarisation generation, is clearly shown.

The two orthogonal degenerated LP modes are obtained by differential feeding of port pairs numbered 1 and 3, and 2 and 4, on opposite corners of the square slot

(Paryani *et al.* 2010). This provides the first two degrees of polarisation freedom with broadside radiation.

The central part of the antenna is viewed as a design integration area into which a substrate-integrated cavity, with four radiating slots at its periphery, is inserted. When excited in its centre, at port 0, the substrate-integrated geometry forms a magnetic current loop consisting of a topside square patch, shorted to the intact metallised antenna backside ground plane at its corners by 8 vias, two at each corner, creating four radiating cavity walls. This can be understood from the equivalence of a small constant magnetic current loop and an electric dipole, which is the dual case of a small loop of constant electric current being equivalent to a magnetic dipole. This introduces a magnetic current loop mode of operation, with a monopole pattern and vertical polarisation orthogonal to the antenna surface (Kaufmann and Fumeaux 2015). The work of Chen *et al.* (2005) supports this concept and suggests that up to 40% of the antenna may be used in this way without compromising the performance of the original design. As a consequence, a low-profile electric monopole made of a magnetic current loop is established at the antenna centre. This provides a third degree of polarisation freedom.

The magnetic current loop mode radiates through the common radiative slot, through which the two orthogonal degenerated broadside modes also radiate (Garg *et al.* 2001). The distance between opposing sides of the radiative slot is of the order of a half-wavelength at the design frequency. Unlike uni- and dual-polarised designs that do not need to consider the implications of a slight break of symmetry about the centre of the design, the design presented in this chapter requires a high grade of mode symmetry to achieve high isolation between polarisation modes. The antenna, as a standalone device, is coaxially probe fed in five positions from the backside of the substrate, with selected combinations of probe excitations providing diversity operation. A feeding network, described later in Section 7.2.3, introduces differential feeding of opposite ports of the square slot, thus making the antenna effectively a three-port device. In summary, port 0 refers to the OLP port at the antenna centre, providing the magnetic current loop mode of operation, while ports 1 to 4 are labelled sequentially about the outer portion of the antenna, providing the two orthogonal degenerated broadside modes of operation. All ports are designed using a 50 Ω characteristic, and so the antenna may be integrated with a variety of feeding networks, or be used as a standalone device with high frequency digital inputs.

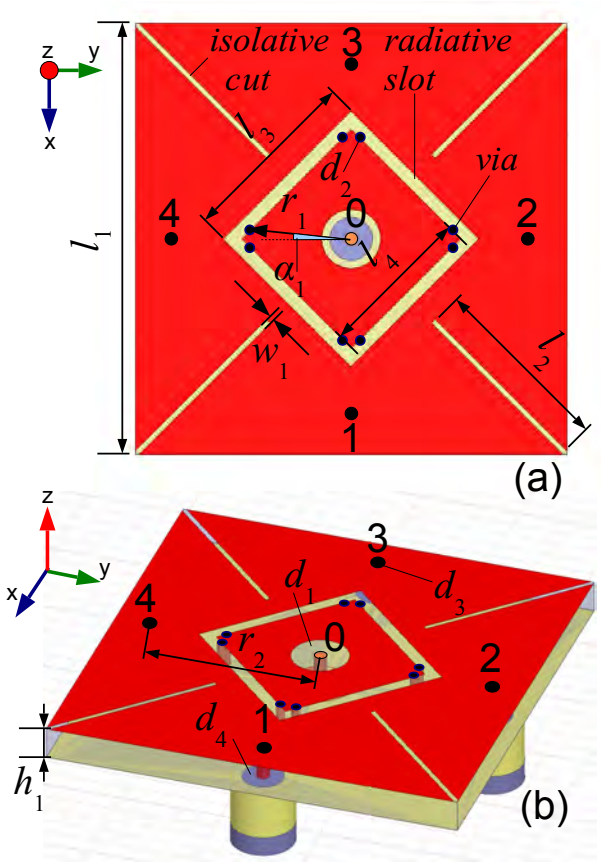

Figure 6.1. Antenna design with port referencing. The design is symmetrical about the z axis and includes a common radiative slot through which polarisation in three orthogonal directions is radiated. (a) antenna topside view showing the square slot and the position of the eight monopole cavity grounding via connections, and five coaxial probe feed connections, 0 to 4. Port 0 has topside clearance d_1 as a result of its mode of operation. In this chapter, the coaxial probe feeds are replaced with five via pin connections inserted and soldered between the three-port feed backside and the antenna topside, (b) additional dimension detailing of the antenna. The antenna backside is completely metallised, except for the five coaxial port ground clearances. Dielectric material is removed from Figure 6.1(b) for convenience. Dimensions are explicitly described in Table 6.1.

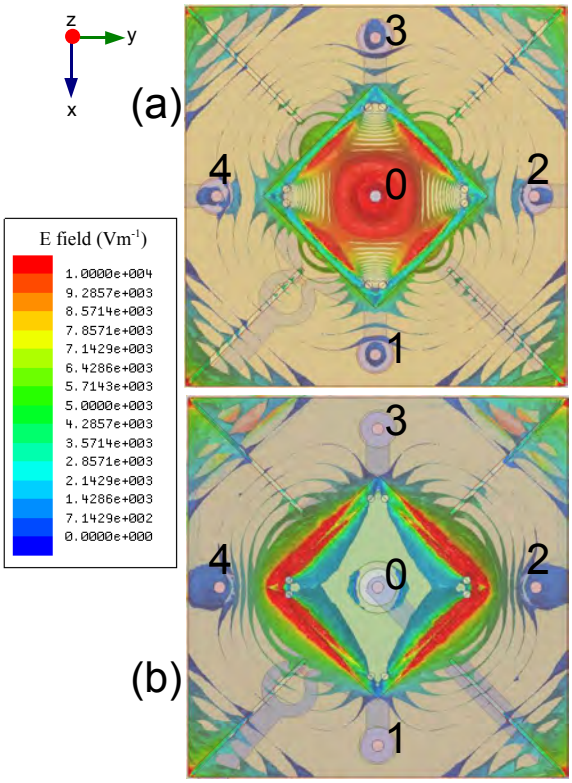

Figure 6.2. The two fundamental modes of operation of the proposed antenna. Shown in this figure are simulated instantaneous electric field magnitudes, as seen from the antenna topside: (a) magnetic current loop mode, or OLP radiation, excited by antenna port 0, (b) degenerated broadside radiation, excited by differential feeding of antenna port pairs numbered 1 and 3, or 2 and 4 as in this instance. Radiation of both modes is via the common radiative slot.

6.2.2 Specific Antenna Design

For demonstration of the concept, a specific realisation of the antenna is designed for operation at 5.89 GHz, in the allocated DSRC spectrum. The antenna is designed using the HFSS simulation tool. It is manufactured using Rogers RT Duroid® 5880 material, with a relative permittivity of 2.20, thickness h_1 of 3.18 mm, and is cladded with industry standard 17 μm of copper on either side. Optimised dimensions are given in Table 6.1. To provide high isolation between operation modes, an initial radial distance of one half of a guided wavelength, or 18.25 mm, is used between port 0 and ports 1 to 4. An initial slot length is one half of a guided wavelength, later optimised as l_3. An initial ground via radial distance, establishing the cavity for magnetic current loop mode operation, is one quarter of a guided wavelength, or 9.1 mm, later optimised as r_1. To

Table 6.1. Antenna Dimensions.

Reference	Dimension
l_1 (antenna side length)	41.20 mm
h_1 (antenna substrate height)	3.18 mm
l_2 (isolator cut length)	18.00 mm
w_1 (isolator cut width)	0.50 mm
l_3 (common slot length)	17.26 mm
l_4 (OLP port cavity length)	14.76 mm
d_1 (OLP port pin clearance)	2.84 mm ⊘
r_1 (via radial distance)	9.70 mm
α_1 (via angle offset)	4.50°
d_2 (via diameter)	0.85 mm ⊘
r_2 (port pin radial distance)	17.19 mm
d_3 (port pin hole diameter)	1.50 mm ⊘
d_4 (copper ground clearance)	4.10 mm ⊘

improve adjacent port isolation, in the instance of a non-differential feeding technique being used, four inward diagonal isolator slots are etched on the metallisation of the antenna upper surface. With the design optimised, including the uniform radiative slot width, tri-orthogonal overlapping frequency responses at the design frequency of the two orthogonal degenerated broadside modes and the magnetic current loop mode are achieved. Port matching of the OLP port to a 50 Ω characteristic impedance is achieved with an annular gap around the centre OLP port pin 0 on the antenna topside (Kaufmann and Fumeaux 2015). In effect, the capacitance of the annular gap compensates the inductive nature of the cavity coaxial feed. The LP port pins numbered 1 to 4 are matched to a 50 Ω characteristic impedance by varying their common radial distance r_2 from the antenna centre.

6.2.3 Feed Arrangement for Tri-Orthogonal Operation

Differential feed designs are able to provide polarisation purity through opposing port field cancellation (Zou and Fumeaux 2011), and hence reduce port coupling, as well as provide phase centring (Chiou and Wong 2002, Adamiuk *et al.* 2009a, Adamiuk *et al.* 2009b, Paryani *et al.* 2010, Li and Luk 2013, Xue *et al.* 2013, Zhu *et al.* 2014, Huang *et al.*

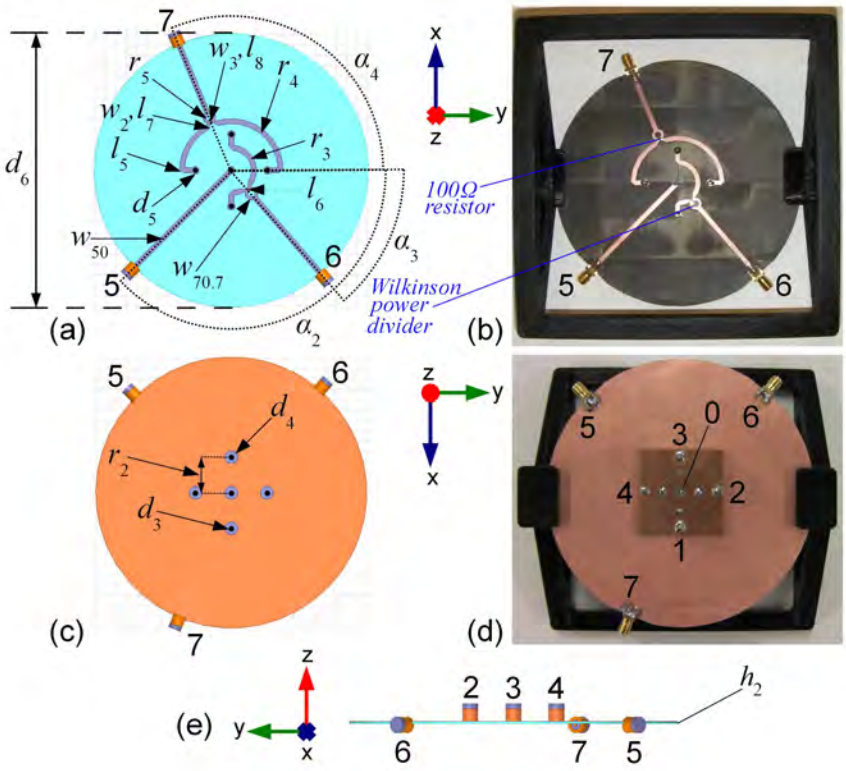

Figure 6.3. Tri-orthogonal feed design with port referencing. Refer to Tables 6.1 and 6.2 for reference descriptions: (a) Virtual tri-orthogonal feed backside view showing feed line detail, (b) manufactured feed backside view, (c) virtual feed ground or topside view showing copper ground clearances. These clearances align with those on the antenna backside, allowing for five port via pin connections to be inserted and soldered between feed backside and antenna topside, (d) manufactured feed with antenna mounted for tri-orthogonal operation. System operation is performed with the antenna facing skyward, in the positive z axis.

2015). It will be shown that this is an appropriate feeding technique if a third polarisation is to be included in a phase-centred tri-orthogonal design.

Figure 6.3 shows virtual and manufactured versions of a feed providing tri-orthogonal operation. Dimensions are given in Table 6.2. The feed copper ground clearances and port pin holes, in Figure 6.3(c), align with those of the antenna. Operation through antenna port excitation is achieved by five port via pins inserted and soldered through the port pin hole between feed backside and antenna topside. Port pins 1–4 provide a means of attachment for the antenna to the feed, which is suitable for testing purposes.

Table 6.2. Feed Dimensions.

Reference	Dimension
w_{50} (50 Ω line width)	2.43 mm
$w_{70.7}$ (70.7 Ω line width)	1.38 mm
h_2 (substrate height)	0.79 mm
α_2 (ports 5 and 8 connector angle)	135.00°
α_3 (port 6 connector angle)	48.50°
α_4 (port 7 connector angle)	113.00°
r_3 (polarisation in x direction feed line centre radius)	10.80 mm
r_4 (polarisation in y direction feed line centre radius)	23.60 mm
r_5 (Wilkinson divider internal radius)	1.70 mm
d_5 (port pin connection diameter)	3.70 mm ⊘
l_5 (external chamfer length)	2.72 mm
l_6 (resistor gap)	0.50 mm
w_2,l_7 (outer Wilkinson divider chamfer; width, depth)	5.36 mm, 2.60 mm
w_3,l_8 (inner Wilkinson divider chamfer; width, depth)	1.40 mm, 1.00 mm
d_6 (feed diameter)	130.00 mm ⊘
α_5 (port 9 connector angle)	30.00°
r_6 (CP feed line central radius)	39.70 mm

This feeding circuit is manufactured using Rogers RT Duroid® 5880 material, with a thickness h_2 of 0.79 mm. Both feeds are based on a 50 Ω characteristic impedance. Opposing ports are fed differentially i.e. in antiphase. This creates field cancellation, by exciting an anti-symmetric mode with a null, at the antenna centre and so provides high isolation between the OLP and LP modes. Wilkinson power dividers with 100 Ω resistors are placed at power splitting junctions to improve isolation between ports in the LP feed arms (Chiou and Wong 2002, Pozar 2011). This improves input return losses through reduction of unwanted voltage reflections.

For the tri-orthogonal system, the OLP feed to antenna port 0 is designated as port 5, while port 6 excites antenna ports 1 and 3 to provide polarisation in the x direction. Port 7 excites antenna ports 2 and 4 to provide polarisation in the y direction.

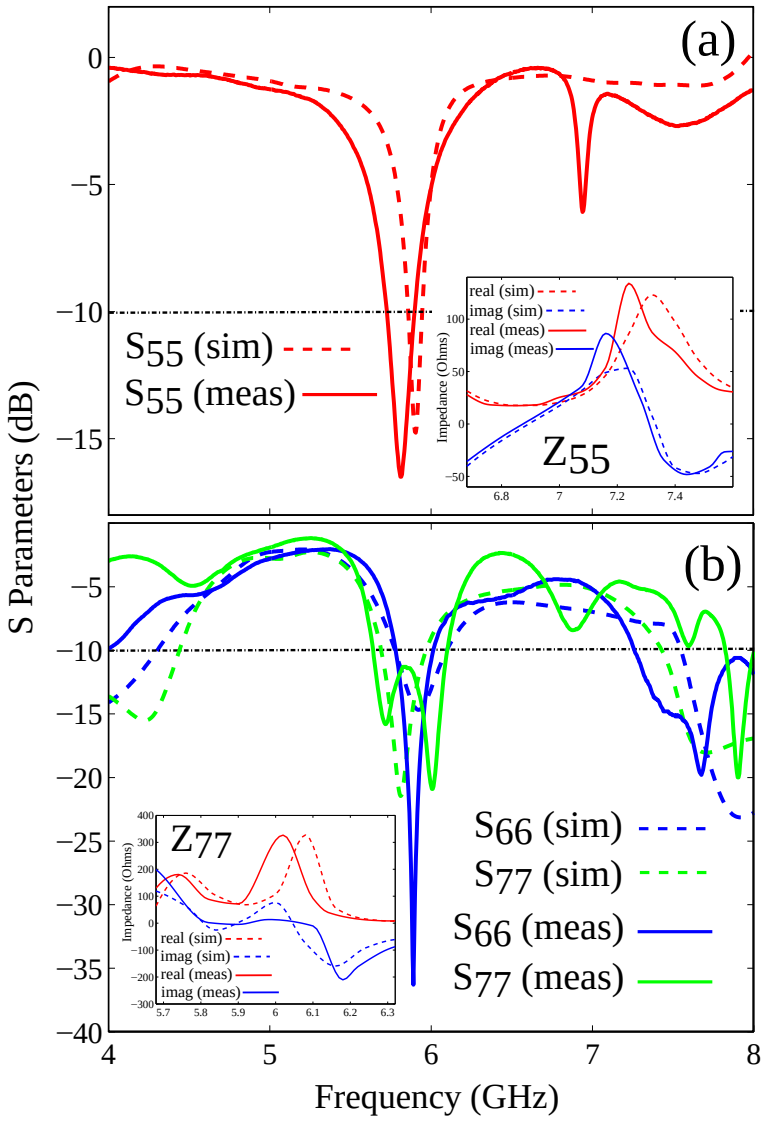

Figure 6.4. Simulated and measured port reflection coefficients of the LP system. The images shown are: (a) OLP feed (S_{55}), (b) broadside LP feeds (S_{66}, S_{77}). A reflection coefficient specification line of -10 dB is shown for convenience. Insets: Impedance matching causes the effects observed on measured S_{55} at 6.9 GHz, and on measured S_{77} at 5.7 GHz–6.2 GHz.

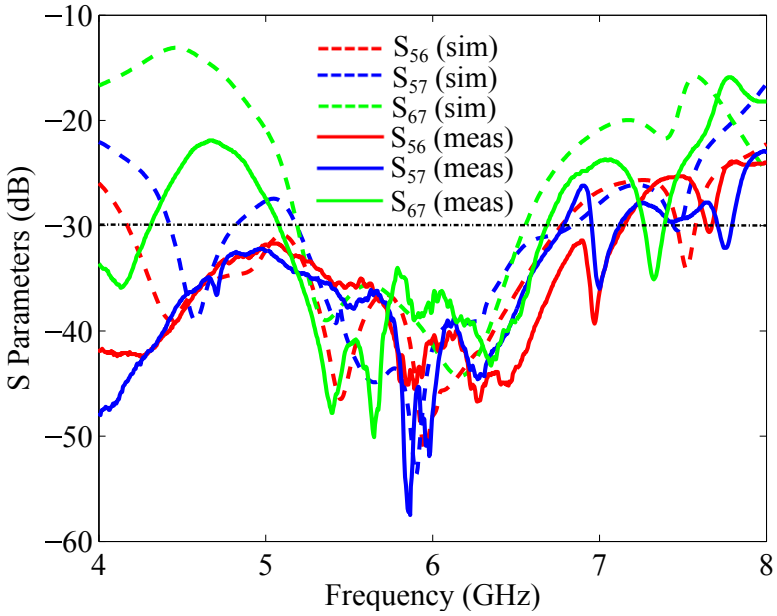

Figure 6.5. Simulated and measured port isolation coefficients of the LP system. The images shown are: S_{56}, S_{57}, and S_{67}. An isolation coefficient specification line of 30 dB is shown for convenience.

6.3 Results

The antenna backside and feeding circuit topside ground planes are brought together and connector holes aligned for port pin connections. A 50 Ω characteristic impedance is maintained through copper ground clearances of diameter d_4 at each connection point. Connections between feed and antenna are then soldered, resulting in a three-port tri-orthogonal system. For measurement, the system is supported by a 3D printed stand, shown in Figures 6.3(b), (d). The feed is larger than would be the case in an integrated solution in order to provide ease of rotation in measurement. Port 5 provides a feeding mechanism that avoids any potential coupling effects with port 6.

For ease of understanding, determination is made of three polarisation modes; x, y, and z, according to the feeding alignments shown in Figure 6.3. The third Ludwig definition of cross polarisation is used to determine LP performance (Ludwig 1973).

Figures 6.4(a), (b) illustrate the simulated and measured reflection coefficient of the OLP and broadside LP feeds. The measured resonance of S_{55} at 6.9 GHz is an effect of impedance matching Z_{55}, which is shown in the inset of Figure 6.5(a). A resonance is defined as where the imaginary component of impedance crosses the zero impedance line. The measured double resonance of S_{77} at 5.7–6.2 GHz is an effect of impedance

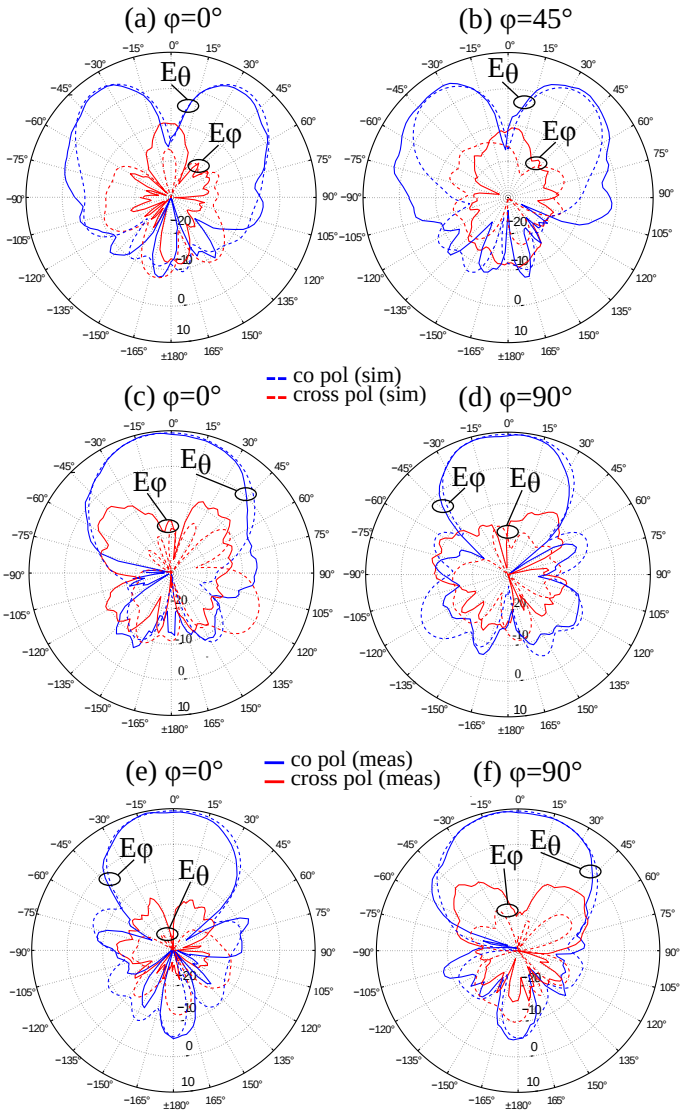

Figure 6.6. Radiation characteristics of the tri-orthogonal antenna and feed design. The images shown are: the OLP radiation characteristic achieved via excitation of port 5 of the LP feed and antenna combination (a), (b). Excitation of port 6 provides a LP radiation characteristic in the x direction (c), (d). Excitation of port 7 provides a LP radiation characteristic in the y direction (e), (f). Asymmetry in patterns results from the feeding interface and the measurement environment.

matching Z_{77}, which is shown in the inset of Figure 6.4(b). Figure 6.5 shows port isolation characteristics. The OLP resonance is measured as shifted downward in frequency to 5.81 GHz, or by an order of 1%, in comparison to that simulated. This phenomenon has been noted in previous work using the same design materials (Kaufmann and Fumeaux 2015), and is likely due to tolerances in a non-industrial manufacturing process. The OLP impedance bandwidth, defined as a reflection coefficient less than -10 dB, is measured as 185 MHz (5.72–5.91 GHz), or 3.18%.

Both LP modes, in the x and y directions, radiate at the design frequency, although polarisation in the y direction, fed by the outer feed radius via port 7, possesses a wider bandwidth of 495 MHz (5.64–6.13 GHz), or 8.41%, than polarisation in the x direction, fed by the inner feed radius via port 6, with bandwidth of 280 MHz (5.77–6.01 GHz), or 4.74%. The difference is observed in both simulation and measurement, and is an effect of the short line length to the inner feed pin exciting antenna port 3. Isolation of no less than 30 dB is measured from 5.10–6.70 GHz; 30 dB being a figure typical for mobile communications requirements (Barba 2008). The isolative effect of the Wilkinson power dividers is observed through S_{66} and S_{77}, the reflection coefficients of feed lines requiring isolation between fed antenna ports 1 and 3, and 2 and 4 respectively. The isolative effect of driving opposing ports in antiphase to create degenerated broadside mode field cancellation, or a null, at the antenna phase centre, where the OLP resonator is situated, is observed through S_{56} and S_{57}. Isolation between port 0, and antenna ports 1 and 3, and 2 and 4, driven by feed ports 5, 6 and 7 respectively is theoretically infinite. In reality, an isolation S_{57} up to 57 dB was achieved. The smallest overlapping tri-orthogonal operational bandwidth is measured as 135 MHz (5.77–5.91 GHz), or 2.3%.

Figure 6.6 provides OLP and LP gain profiles. To measure the gain of the prototype antenna, or device under test (DUT) the gain transfer method (Balanis 2005) is used in our anechoic chamber. The first step is to measure the power $P_{R,DUT}$ received by the antenna when illuminated by a transmitting broadband horn antenna (AEL H-1498, 2–18 GHz). In the second step, the antenna under test is replaced by a standard gain horn antenna (Narda 640) and the received power $P_{R,S}$ is recorded. The gain of the test antenna can then be calculated by Equation (6.1),

$$G_{DUT} = G_S + 10\log_{10}(P_{R,DUT}/P_{R,S}) \tag{6.1}$$

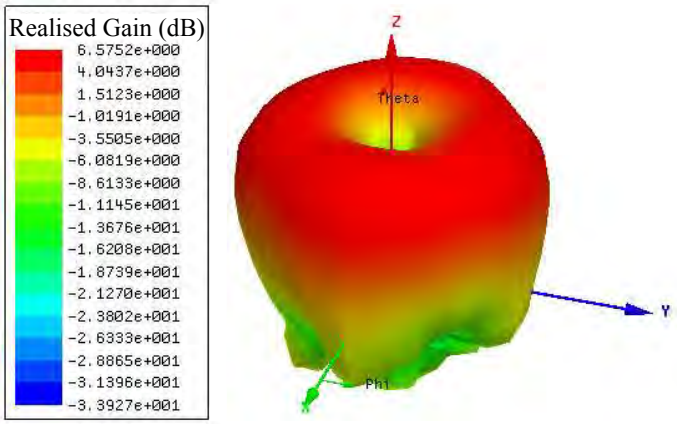

Figure 6.7. Simulated 3D OLP radiation pattern when the antenna is driven through port 5. The radiation pattern is slightly conical in nature, providing peak gain of 6.4 dB at $\theta = \pm 35°$.

where G_{DUT} and G_S are the gain of the test and standard gain horn antenna, respectively.

Figure 6.7 illustrates the simulated 3D OLP radiation mode pattern when the antenna is excited through port 5.

Figures 6.8(a), (b) illustrate the simulated 3D broadside mode L3X and L3Y radiation patterns when the antenna is excited through port 6. Figures 6.9(a), (b) illustrate the simulated 3D broadside mode L3Y and L3X radiation patterns when the antenna is excited through port 7.

Figures 6.6(a), (b) illustrate simulated and measured results for OLP radiation, excited through port 5, at azimuthal angles ϕ of 0° and 45° respectively. The OLP radiation pattern confirms the operation as a magnetic current loop. It is simulated and measured as conical, with absolute peak realised gain of 6.4 dB at $\theta = \pm 35°$. Antenna LP diversity in either the x or y direction is realised by differentially exciting port pair 1 and 3 through port 6, or 2 and 4 through port 7, respectively. This leads to excitation of either of the two orthogonal degenerated broadside modes, and radiation with peak gain in the z direction.

Figures 6.6(c), (d) illustrate simulated and measured results for LP in the x direction, fed by port 6. Absolute peak realised gain is measured as 9.3 dB. LP in the y direction, fed by port 7, is rotated about the z axis by 90° and its characteristics are shown in Figures 6.6(e), (f). Absolute peak realised gain is measured as 9.4 dB. A normalised

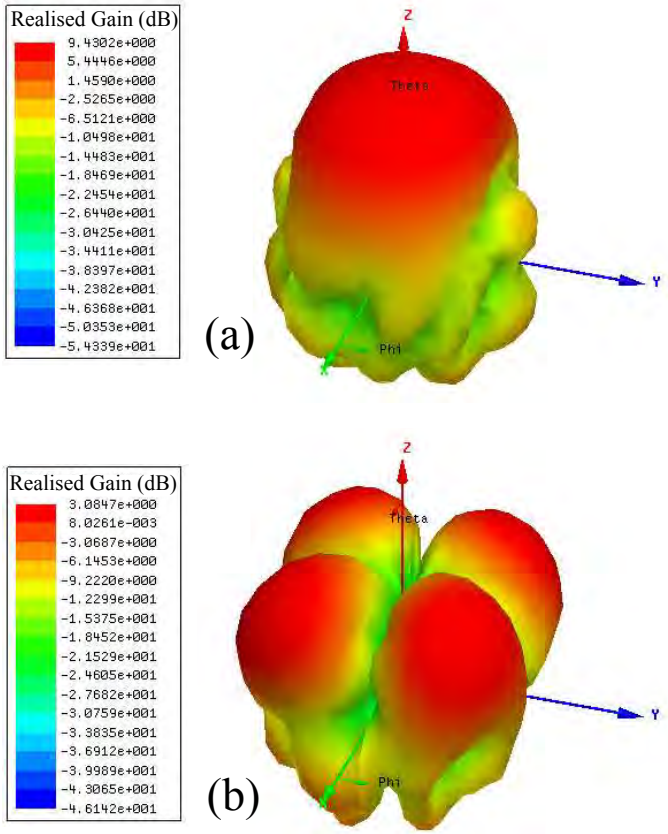

Figure 6.8. Simulated 3D (a) L3X (b) L3Y radiation patterns when the antenna is driven through port 6. In the direction of the z-axis, the orthogonal nature of the x and y polarisation modes, providing a high value of XPD greater than 30 dB, is readily observed through the respective realised gain profiles. After Ludwig (1973).

absolute gain of 8.8 dB is measured in the broadside direction. Simulated radiation efficiency is above 94%, with a worst case measured radiation efficiency of 86%.

Two commonly used criteria— i.e. the mean effective gain (MEG) (Taga 1990, Volakis 2007), and the envelope correlation (ECC) (Blanch *et al.* 2003, Brown *et al.* 2007)— are utilised to evaluate the antenna diversity performance. Both MEG and ECC metrics are calculated using spherical integration functions of the 3D far-field antenna patterns. For MEG, calculations are based on Equation (1) of Taga (1990). At the design frequency of 5.89 GHz, the MEGs as a function of θ in Figure 6.10 are reported, and as a function of solid angle in Table 6.3 in a LoS channel. Values of θ and solid angles from the antenna zenith, orthogonal to the antenna radiating surface, are measured. An ideal MEG will be -3 dBi in the case of 100% radiation efficiency, a cross polarisation ratio (XPR) of 0 dB at the transmitter and receiver, and it should be above -10 dBi

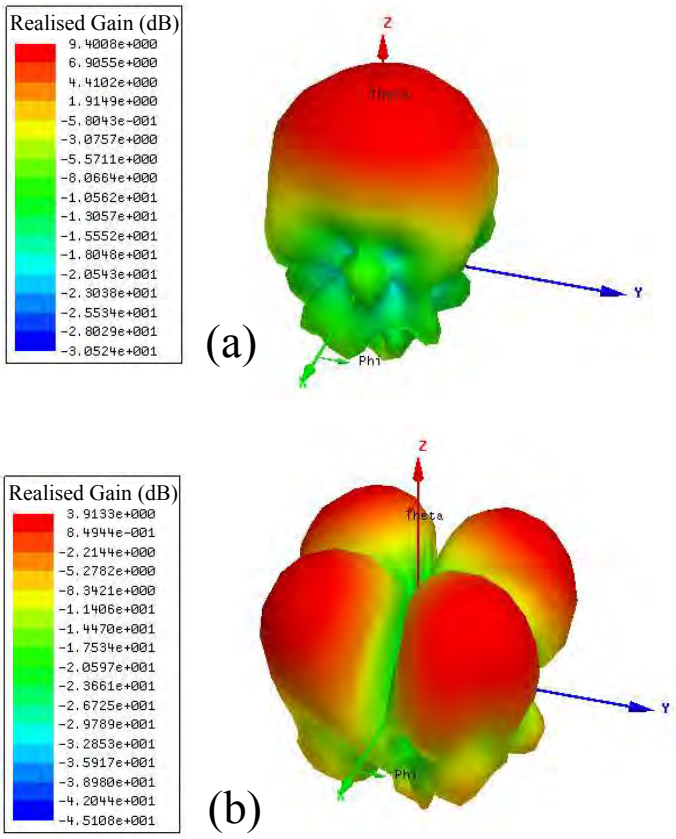

Figure 6.9. Simulated 3D (a) L3Y (b) L3X radiation patterns when the antenna is driven through port 7. In the direction of the z-axis, and in contrast, from an orthogonal perspective, to the port excitation observed in Figure 6.8, the orthogonal nature of the x and y polarisation modes, providing a high value of XPD greater than 30 dB, is readily observed through the respective realised gain profiles. After Ludwig (1973).

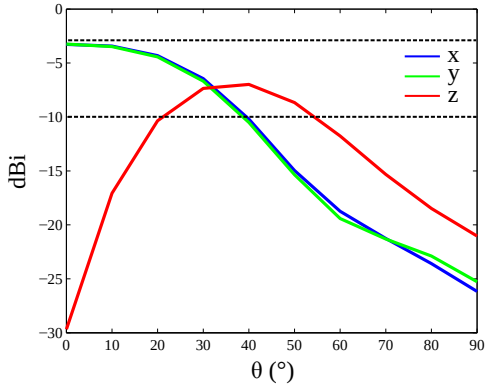

Figure 6.10. Mean effective gains (MEGs) for the three orthogonal polarisation modes. The MEGs of the polarisation modes of the antenna are presented in dBi as a function of θ from the zenith position, orthogonal to the antenna radiating surface, using simulated 3D radiation patterns and radiation efficiency. MEG limits of -3 dBi and -10 dBi are included for ease of data interpretation.

Table 6.3. Mean effective gains (MEGs) for the three orthogonal polarisation modes. The MEGs of the polarisation modes of the antenna are presented in dBi as a function of solid angle subtended from the zenith position, orthogonal to the antenna radiating surface (from simulated 3D radiation patterns and radiation efficiency).

	0°-30°	0°-60°	0°-90°	30°-60°	60°-90°
x	-4.19	-6.24	-7.75	-10.38	-21.61
y	-4.28	-6.35	-7.86	-10.65	-21.71
z	-11.29	-10.00	-11.24	-8.34	-15.30

Table 6.4. Envelope correlation coefficients (ECCs) (from simulated 3D radiation patterns). The ECCs are significantly lower than a commonly accepted upper diversity threshold of 0.5, highlighting low correlation between polarised modes due to the orthogonality and symmetry of the structure.

Frequency	Polarizations	ECC
5.77 GHz	xz	2e-02
	yz	1e-03
	xy	3e-02
5.89 GHz	xz	6.6e-04
	yz	6.9e-04
	xy	1e-03
5.91 GHz	xz	1e-02
	yz	1e-03
	xy	3e-02

for a practical antenna. According to the port isolation coefficients of Figure 6.5, polarisation coupling coefficients are introduced at the receiver into the diversity model in Chapter 3, and in Lawrence *et al.* (2015b), providing an upper bound on cross polarisation discrimination (XPD) values at the receiver. At the transmitter, interest is turned to the two polarisation modes that are aligned with the receiver at the FoV centre in the diversity model in Chapter 3, and in Lawrence *et al.* (2015b). A XPR of 0 dB is modelled between these polarisation modes at the transmitter through polarisation coupling coefficients of zero magnitude. As such, simulated data are output as

a function of the tri-orthogonal receive antenna uniquely. Simulated antenna radiation efficiency is above 94%, with a worst case measured radiation efficiency of 86%.

Figure 6.10 highlights that the MEGs of polarisation modes x and y are near optimal at -3.28 dBi and -3.25 dBi respectively when the antenna radiating surface is perfectly aligned with the transmitter. Polarisation z provides a MEG that is optimal at 40°, but that does not reach the optimal values of x and y. It does however provide a higher MEG than x and y for values of $\theta \geq 32°$.

For worst case measured radiation efficiency, and over the range of solid angles in Table 6.3, the values of MEG would drop by an additional -0.39 dB.

The ECCs shown in Table 6.4 over the antenna radiating hemisphere are also reported. An upper threshold of 0.5 is commonly held as acceptable, while a value of 0 would suggest no correlation between polarisation modes. According to Mikki and Antar (2015), the ECC may be calculated from the simulated far-field radiation patterns. The proposed antenna demonstrates low correlation between all three polarisation modes at the centre, and at the band edges, of the overlapping tri-orthogonal bandwidth. The antisymmetric-symmetric nature of distributed electric fields between x and z, and y and z polarisation modes, and the symmetry of the physical design, provides near zero correlation. The ECC between x and y polarisation modes is slightly higher but still low due to the orthogonal polarisation of the modes involved.

In order to provide evidence of the diversity performance of the antenna in a radiating direction that is furthest from orthogonality, the cross correlation at $\theta = 45°$ is examined at $\phi = 45°$. The value of cross correlation obtained at this specific radiating direction is then compared with singular values in orthogonal radiating directions of ($\theta = 45°$, $\phi = 0°$) and ($\theta = 45°$, $\phi = 90°$). The process begins by obtaining real and imaginary components of the E_ϕ and E_θ fields from simulated 3D radiation patterns in these specific radiating directions, and these are given in Table 6.5.

Cross correlation of the two broadside modes, excited by differential feeding of port pairs (1,3) and (2,4), yields the values denoted by polarisation modes xy in Table 6.6. It is observed that the cross correlation is above the threshold value of 0.5 for a diversity antenna in the ($\theta = 45°$, $\phi = 45°$) direction. This is a common characteristic of patch antennas, and more specifically those antennas which provide diversity. It is common practice to provide data in orthogonal directions. As such, the issue of performance in a radiating direction that is furthest from an orthogonal direction is avoided.

Table 6.5. Real and imaginary electric field components in specific radiating directions (from simulated 3D radiation patterns). Antenna port pairs in brackets are fed differentially.

Ports	$\theta(^\circ)$	$\phi(^\circ)$	E_θ (V)	E_ϕ (V)
(1,3)	45	0	10.4207-8.18895i	0.0858013+0.0041984i
(1,3)	45	45	0.636187-5.38073i	-11.0358+11.2246i
(1,3)	45	90	-0.0440687-0.0135517i	-3.98847+14.3287i
(2,4)	45	0	0.0112409-0.00214351i	14.1018+4.26349i
(2,4)	45	45	5.33914+0.665992i	11.1773+11.3668i
(2,4)	45	90	8.24338+10.4953i	-0.0105054-0.0560714i
0	45	0	6.60955-0.00803283i	-0.00803283-0.00246598i
0	45	45	4.79431-0.0227119i	-0.0227119-0.0269899i
0	45	90	6.63658+0.023885i	0.023885+0.0382212i

Table 6.6. Antenna cross correlation in specific radiating directions (from simulated 3D radiation patterns). Cross correlation is considered between two or more mentioned polarisation modes in each case.

Polarisations	$\theta(^\circ)$	$\phi(^\circ)$	Cross Correlation
xy	45	0	0.0072
xy	45	45	0.7918
xy	45	90	0.0064
xz	45	45	0.3323
yz	45	45	0.3130

For our antenna, the cross correlation in the ($\theta = 45^\circ, \phi = 45^\circ$) radiating direction may be reduced by introduction of the omnidirectional z radiation pattern. As a result, the value of cross correlation in this radiating direction in Table 6.6 is observed to drop below the upper threshold value of 0.5, from 0.7918 to values of 0.3323 and 0.3130. The values of cross correlation between xz and yz polarisation modes demonstrate the effect of introducing the omnidirectional mode in the ($\theta = 45^\circ, \phi = 45^\circ$) direction, as a means of providing diversity in this radiating direction.

The influence of the omnidirectional mode in improving the antenna performance for values of $\theta \geq 32^\circ$ has previously been bore out by the MEG values of Figure 6.10, and the values of Table 6.3.

Table 6.7. Antenna cross correlation at various values of elevation given by θ along a constant azimuthal angle of $\phi = 45^\circ$ (from simulated 3D radiation patterns). Cross correlation is considered between orthogonal polarisation mode pairs xy, xz and yz in each case.

$\theta(^\circ)$	$\phi(^\circ)$	Cross Correlation xy	Cross Correlation xz	Cross Correlation yz
0.1	45	0.0621	0.3431	0.9395
0.2	45	0.0624	0.5221	0.8527
5	45	0.0163	0.6938	0.7097
10	45	0.0621	0.6795	0.6904
20	45	0.2404	0.6123	0.6204
30	45	0.4891	0.5034	0.5075
40	45	0.7135	0.3812	0.3758
50	45	0.8461	0.2880	0.2669
60	45	0.9061	0.2311	0.2037
70	45	0.9426	0.1739	0.17
80	45	0.9601	0.1169	0.1672
90	45	0.6200	0.4239	0.4479

In Table 6.7, cross correlations are demonstrated at various values of elevation given by θ along a constant azimuthal angle of $\phi = 45^\circ$.

In Figure 6.11, derived from Table 6.7, the mitigating nature of tri-orthogonal polarisation diversity is evident. For a constant azimuthal angle of $\phi = 45^\circ$, and for low values of θ, polarisation modes xy provide low cross correlation. As the value of θ increases, so the effect of the omnidirectional mode in the form of polarisation z is observed to provide low cross correlation. In effect, the antenna provides diversity, measured by a cross correlation value of less than 0.5, in a worst case azimuthal radiating direction between orthogonal polarisation modes x and y for all elevations between antenna broadside and parallel to the antenna surface.

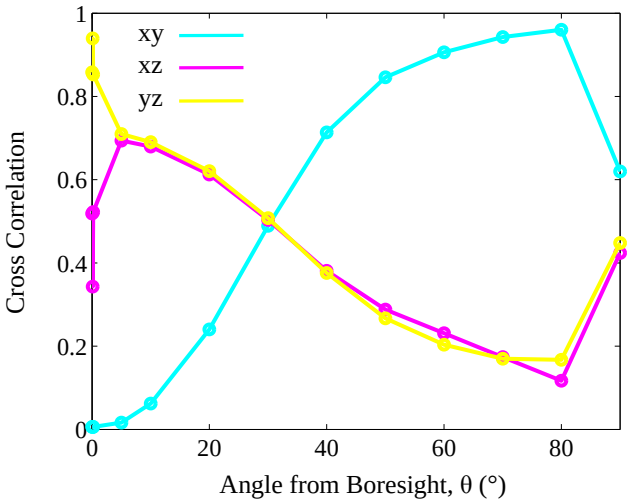

Figure 6.11. Cross correlation of the antenna. The cross correlation of the antenna at an azimuthal angle of $\phi = 45°$ as a function of θ from the zenith position, orthogonal to the antenna radiating surface, using simulated 3D radiation patterns and radiation efficiency is presented. The mitigating nature of tri-orthogonal polarisation diversity is evident as the omnidirectional mode proceeds to provide low cross correlation as deviation from boresight in the zenith direction, or θ, increases.

6.4 Mutual Coupling and Pattern Diversity

The low mutual coupling between polarisation branches x, y, and z provides active beam control through relative phasing techniques between polarisation modes. An example of this is shown in Figure 6.12. Through sequential 90° phasing of ports 1 to 4 of the antenna, a CP waveform may be established, propagating orthogonally to the radiating antenna surface, as shown in Figure 6.12(a). Polarisation modes x and y are associated with this radiation pattern. An omnidirectional radiation pattern, polarised orthogonally to the radiating surface, is provided through feeding of port 0 uniquely, as observed in Figure 6.12(b). Polarisation z is associated with this radiation pattern.

The application of simultaneous sequential 90° phase feeding of ports 1 to 4 and phased feeding of port 0 provides the radiation patterns of Figure 6.12(c)–(f). In effect, a combination of either x and z or y and z polarisation modes are associated with these radiation patterns. Radiation pattern gain is a combination of the gains of the x or y, and z radiation patterns. No asymmetry is observed in the patterns, as the design is phase-centred. As such, over an incrementally increasing phase argument of port 0

feeding from 0° to 360°, it is possible to sweep the radiation pattern over an entire azimuth about the radiating antenna surface. All three polarisation modes thus provide beam control through pattern diversity.

In this thesis, consideration is made of the role that a tri-orthogonal design may have on system performance, through a capacity metric.

In Wallace and Jensen (2004), the effect of mutual coupling on capacity is observed using two identically polarised dipoles that are intially spaced far apart, but are incrementally brought together. It is explained that when these dipoles are closely spaced, the effect of mutual coupling provides benefit to capacity, before providing detriment as the two dipoles merge into one. In effect, it is suggested that the proximity of the dipoles allows power scattered by one dipole to be recaptured by another. From a capacity point of view, some amount of mutual coupling appears useful.

In Chiu *et al.* (2007a), a reduction in mutual coupling is sought, as it is made clear that mutual coupling adversely affects antenna performance. Pattern asymmetry, directional radiation nulls, and deviation from expected performance are consequences of mutual coupling. Indeed, the pattern diversity observed in Figure 6.12 would not be possible without isolation existing between polarisation modes. Values of mutual coupling that typically exist for commercial antennas vary. In King and Stavrou (2007), a value of 20 dB is given at the transmitter, while a value of 15 dB is reported at the receiver. The latter value is suggested as detrimentally impacting the experiment. In this chapter, a design is provided with 35 dB isolation between ports. It is suggested that this value is high, and this is possible due to the symmetry and orthogonality of the design. As such, it provides the sharp definition required to provide the active beam control in Figure 6.12, in line with Chiu *et al.* (2007a).

Two points are summarised in regard to the design.

- The option to beamform is provided by the tri-orthogonal design through low mutual coupling. In effect, the orthogonality and symmetry of the design provides an extremely low amount of mutual coupling between polarisation modes. In Figure 6.12, phased feeding techniques are demonstrated that highlight the possibilities for beamforming to increase SNR, and hence link, performance in a direction of propagation.
- In Chapter 5, the performance of a tri-orthogonal receiver in a satellite channel is simulated and analysed. The proposed antenna in this chapter is scalable to

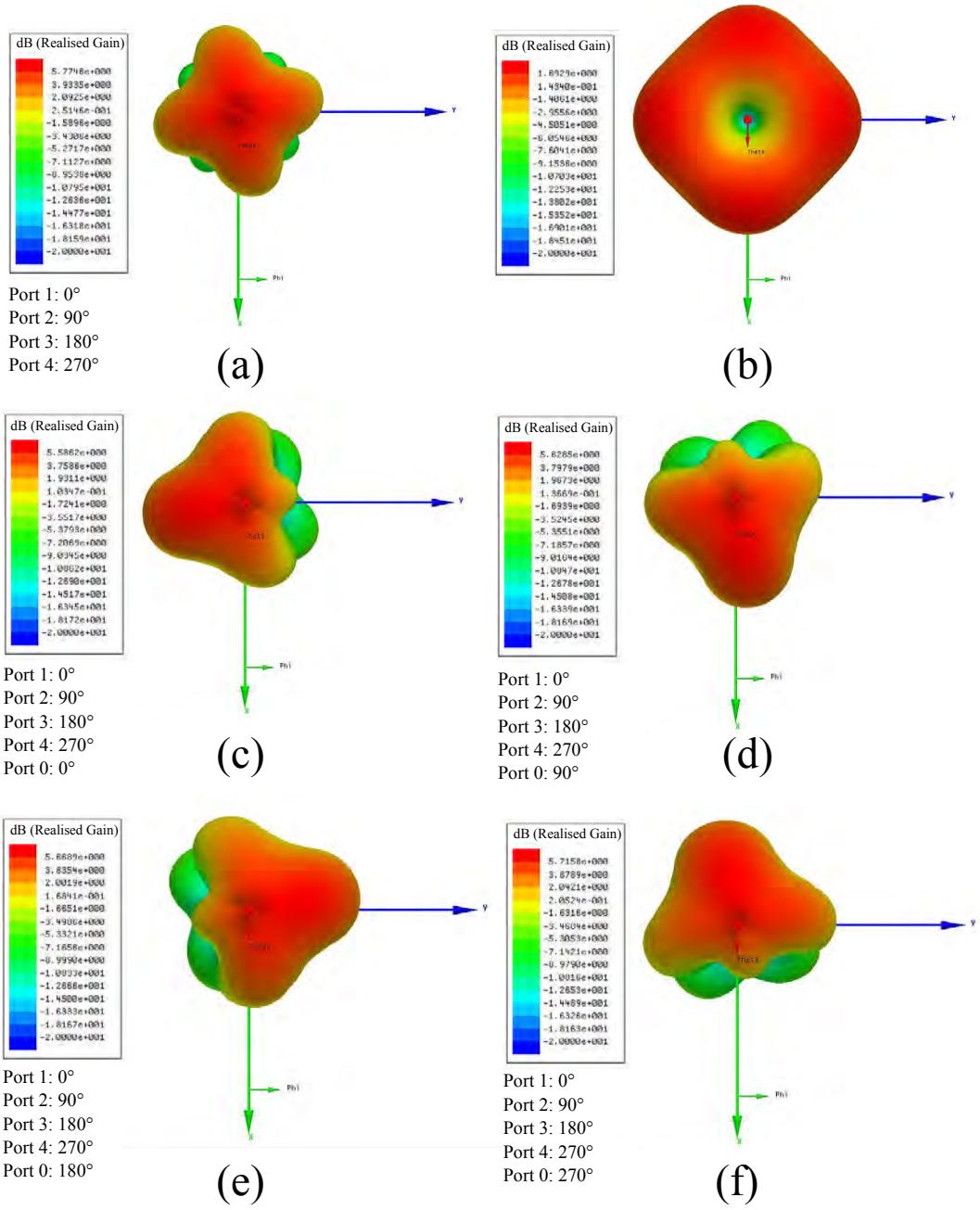

Figure 6.12. The tri-orthogonal design, due to low mutual coupling between the three orthogonal polarisation modes, provides pattern diversity through phased feeding techniques. The images shown are: (a) sequential 90° phased feeding of ports 1 to 4, (b) feeding of port 0 uniquely, (c)–(f) combination of the feeding in (a) with that in (b), where the phase of the feeding in (b) is altered as given.

operate at L-band satellite frequencies due to the symmetry and orthogonality of design. In Figure 6.12, it is possible to envisage the receiver scanning over a hemisphere through phase-cycling applied to port 0, and so polarisation z, which is represented by polarisation $\hat{\mathbf{r}}$ at R in Chapter 5. In effect, this would provide a MIMO scheme operation which could easily be altered to a beamforming operation in a unique link direction if required, once the most powerful satellite transmitter had been identified. The scanning technique would provide DP orthogonal modes for all propagation directions over a majority of the entire hemisphere, which would be enhanced to lower elevation levels by a large ground plane, providing a more monopole-like radiation pattern for polarisation z.

6.5 Chapter Summary

A planar slot antenna operating at 5.9 GHz and providing tri-orthogonal diversity operation is proposed in this chapter. Tri-orthogonal polarisation operation from a shared radiative slot on the top surface of the design is simulated, and subsequently confirmed through measurement. Radiation from three modes of operation, two orthogonal degenerated broadside modes and a magnetic current loop mode, is measured. The antenna provides 6.4 dB of OLP gain and 9.4 dB of LP gain at the design frequency, and operates with a minimum measured tri-orthogonal overlapping impedance bandwidth of 2.3% (5.77–5.91 GHz).

Isolation of no lower than 35 dB was measured between the three modes in the frequency band of operation, due to field cancellation of the two orthogonal degenerated broadside modes at the antenna centre, as a result of differential port feeding.

The antenna radiation pattern may be controlled in three orthogonal axes by combining feeding excitations to each of the antenna ports with varying relative phases, due to low mutual coupling of polarisation modes. As a consequence, the design may provide tri-orthogonal polarisation diversity, providing at least two polarisation modes in any one link direction, and thus mitigating the effects of antenna misalignment.

In Chapter 7, a specific feed providing the antenna described in this chapter with CP mode and OLP mode performance is described. The two-port feed design provides a ready method for obtaining all the modes that are presented in Figure 6.12.

Chapter 7

Multifunction Two-Port Slot Antenna with Omnidirectional and Circular Polarisation

THIS chapter demonstrates multifunction operation of a readily manufacturable two-port planar slot antenna. The antenna can radiate omnidirectional linearly polarised (OLP) and broadside circularly polarised (CP) radiation patterns through a common square slot in an overlapping frequency bandwidth at 5.9 GHz of 2.56%, with inter-port coupling below -45 dB. The antenna offers diversity in three dimensions through reconfigurable beamforming techniques.

7.1 Introduction

Mobile data traffic is anticipated to grow one thousand fold over the period 2010–2020. To cope with this increase, wireless resources need to be used efficiently (Rappaport *et al.* 2013b).

Transmission rate remains one of the main drivers of wireless communications technologies in the microwave region. Coverage is often degraded at the expense of an increase in rate. Circular polarisation techniques may mitigate performance issues as rate is driven higher, and where mobile wireless and satellite communications may stand together, such as in 5G proposed systems (Mak *et al.* 2014). Signal transmission in any direction without compromising link reliability would be highly desirable for mobile, and in particular vehicular, applications.

For mobile and vehicular applications, pattern diversity and low mutual coupling between ports using a single multiport antenna structure is one possible solution towards higher link reliability. Multiport printed diversity antennas or planar inverted-F antennas (PIFA) are often the focus of available literature, due to their compactness, low cost, and low profile (Diallo *et al.* 2006, Yang *et al.* 2008, Chebihi *et al.* 2008). However, a combination of a complicated structure, large size, poor radiation pattern symmetry, relatively low gain, and little consideration of polarisation orthogonal to the antenna surface often inhibit performance.

Transmission of a second orthogonally polarised signal is known to increase performance (Nabar *et al.* 2002, Erceg *et al.* 2006). In a small volume, polarisation diversity offers robustness provided mutual coupling between polarisation modes (Li *et al.* 2012) can be kept low, such as in an orthogonal system (Ramirez and De Flaviis 2003). Transmitter-receiver misalignment adversely affects robustness of dual-polarised systems.

To introduce orientation robustness in a rich scattering environment, the increase in capacity offered by colocated antennas in a tri-orthogonal arrangement has previously been demonstrated (Andrews *et al.* 2001, Mtumbuka *et al.* 2005, Mtumbuka and Edwards 2005, Getu and Janaswamy 2005, Getu and Andersen 2005, Yan *et al.* 2006, Chiu *et al.* 2007b, Gupta *et al.* 2008, Chiu *et al.* 2009, Yun and Vaughan 2010, Omote *et al.* 2015, Piao *et al.* 2015). Although realised configurations are typically voluminous, such

systems demonstrate the benefit of a third orthogonal antenna. For mobile applications, a compact design enabling emission and reception of three isolated and orthogonal polarisation modes would be highly desirable.

As a non-planar solution, a colocated tri-orthogonal antenna employing a dielectric resonator antenna (DRA) as an integrated solution to generate three orthogonally polarised signals, including one parallel to the direction of propagation, has been demonstrated (Zou and Fumeaux 2011). Design and implementation complexity, requiring dual-substrate manufacture (Zhong *et al.* 2009, Gao *et al.* 2010a), is often the result of placing a monopole at the centre of a tri-orthogonal antenna. Although a low profile tri-orthogonal design was presented in Tong *et al.* (2013), the asymmetric configuration led to pattern asymmetry in the far field.

In this chapter, a two-port planar slot antenna simultaneously capable of transmitting a OLP mode and CP mode signal, effectively providing radiation pattern diversity in three dimensions, and high inter-port isolation due to sequential feeding of ports providing the CP mode, is demonstrated. Two degenerated slot modes provide two broadside patterns with orthogonal polarisation modes that, with a 90° phase shift between them, can generate CP radiation through sequential feeding of CP mode ports (Hall *et al.* 1989, Hall 1989). The third polarisation, perpendicular to the antenna surface, is offered through inclusion of a low profile magnetic current loop electric monopole (Kaufmann and Fumeaux 2015).

A description of the demonstrated concept of the two-port slot antenna is provided in this chapter. As illustration, it describes a specific design at a frequency of 5.9 GHz, in the dedicated short-range communications (DSRC) allocated spectrum. To experimentally demonstrate the performance of OLP and CP modes, a purpose-built sequential feeding network is then combined with the antenna. The experimental results are found to validate the concept, in particular with measured coupling coefficients below - 45 dB. Further diversity patterns are then suggested as combinations of antenna port excitations. The design offers the option to beamform in three dimensions through phased feeding techniques (Razavizadeh *et al.* 2014).

7.2 Antenna Design and Feed Network

7.2.1 Concept

The antenna, in combination with a tri-orthogonal feed, is conceptually described in Chapter 6 and in the work of Lawrence *et al.* (2017b). The reader is referred to Chapter 6 for dimensional information. In this chapter, antenna operation is extended through combination with a OLP, CP feeding structure providing two-port reconfigurable beamforming options in three dimensions through phased feeding techniques.

In Figure 7.1, the structure may be considered as a square slot antenna allowing CP and OLP modes to radiate from the antenna upper surface. Figure 7.2 illustrates the modes of operation in the antenna, namely a magnetic current loop mode, for OLP radiation, and a sequentially fed degenerated broadside mode, for CP radiation. The radiative mechanism of both modes through the common radiative slot on the antenna upper surface is clearly shown.

Through sequential feeding, in other words a progressive 90° phase shift on ports numbered 1–4, broadside CP radiation is provided as observed in Figure 7.2(b)–(c). In effect, differential feeding of ports on opposite corners of the square slot (Paryani *et al.* 2010) is always maintained, providing high inter-port isolation.

The OLP radiation mode, provided through a substrate-integrated cavity with four radiating slots at its periphery, is described in Chapter 6 and in the work of Lawrence *et al.* (2017b). Due to its inclusion at the antenna centre, an additional degree of polarisation freedom is created through a OLP magnetic current loop mode, as compared to conventional CP mode antenna design.

The common radiative slot radiates the magnetic current loop mode, and also the CP radiation mode (Garg *et al.* 2001).

The antenna and feed design presented in this paper requires a high grade of mode symmetry to achieve high isolation between polarisation modes which is unlike uni- and dual-polarised designs that do not need to consider the implications of a slight break of symmetry about the centre of the design. As a standalone device, the antenna is coaxially probe fed in five positions from the backside of the substrate. Selected combinations of probe excitations provide diversity operation. Sequential feeding of ports of the square slot, with the antenna operating as a one-port device, provides CP radiation. The feeding network to provide CP radiation, as well as OLP radiation, is

described later in Section 7.2.3. Port 0 refers to the OLP port at the antenna centre, providing the magnetic current loop mode of operation, while ports 1 to 4 are labelled sequentially about the outer portion of the antenna, providing a broadside CP mode of operation. The design uses a 50 Ω characteristic, and so the antenna may be integrated with a variety of feeding networks, or be used as a standalone device with high frequency digital inputs.

7.2.2 Specific Antenna Design

A specific realisation of the antenna for operation at 5.89 GHz, in the allocated DSRC spectrum, is described in Chapter 6 and in the work of Lawrence *et al.* (2017b). The reader is referred to Chapter 6 for information regarding the design.

In this chapter, antenna operation is extended through combination with a OLP, CP feed design to introduce two-port reconfigurable pattern diversity in three dimensions.

7.2.3 Feed Arrangement for OLP, CP Operation

Polarisation purity through opposing port field cancellation (Zou and Fumeaux 2011), providing reduced port coupling and phase centring, may be offered through a differential feed design (Chiou and Wong 2002, Adamiuk *et al.* 2009a, Adamiuk *et al.* 2009b, Paryani *et al.* 2010, Li and Luk 2013, Xue *et al.* 2013, Zhu *et al.* 2014, Huang *et al.* 2015). For the OLP, CP mode design, a sequential feeding arrangement (Hall *et al.* 1989, Hall 1989), where a progressive 90° phase shift is maintained for ports 1–4, provides CP operation. This is an appropriate feeding technique if a third polarisation is to be included in a phase-centred OLP,CP mode design.

Virtual and manufactured versions of a sequential feed providing OLP, CP operation are found in Figure 7.3. Table 7.1 provides dimensioning detail.

In Figure 7.3(c), the feed copper ground clearances and port pin holes align with those of the antenna. Through insertion and soldering of five port via pins through the port pin hole between feed backside and antenna topside, operation through antenna port excitation is achieved. For testing purposes, port pins 1–4 provide a suitable means of attachment for the antenna to the feed.

The sequential feeding circuit is manufactured using Rogers RT Duroid® 5880 material, with a thickness h_2 of 0.79 mm, and is based on a 50 Ω characteristic impedance.

Sequential feeding with a progressive 90° phase shift on ports numbered 1–4 allows opposing ports to be fed differentially i.e. in antiphase. As a consequence, field cancellation is created through excitation of an anti-symmetric mode with a null at the antenna centre, providing high isolation between the OLP and CP modes. Power splitting junctions in the feed are equipped with Wilkinson power dividers with 100 Ω resistors. This improves isolation between ports in the CP feed arms (Chiou and Wong 2002, Pozar 2011) which improves input return losses through reduction of unwanted voltage reflections. In Figure 7.3(d), soldering of identically positioned port via pins and ground vias is observed. For the OLP, CP system, port 8 is the OLP feed while port 9 sequentially excites ports 1 to 4 in 90° phase increments.

By bringing together the antenna backside and feeding circuit topside ground planes, connector holes may be aligned for port pin connections. A 50 Ω characteristic impedance is maintained through copper ground clearances of diameter d_4 at each connection point. Soldering of connections between feed and antenna results in an OLP, CP system. The system is supported by a 3D printed stand, shown in Figure 7.3(d), for the purpose of measurement. Ease of rotation in measurement is provided through the feed being larger than would be the case in an integrated solution.

Table 7.1. Feed Dimensions.

Reference	Dimension
w_{50} (50 Ω line width)	2.43 mm
$w_{70.7}$ (70.7 Ω line width)	1.38 mm
h_2 (substrate height)	0.79 mm
α_2 (port 8 connector angle)	135.00°
α_3	48.50°
α_4 (port 9 connector angle)	30.00°
α_5	113.00°
r_3 (polarisation in x direction feed line centre radius)	10.80 mm
r_4 (polarisation in y direction feed line centre radius)	23.60 mm
r_5 (Wilkinson divider internal radius)	1.70 mm
d_5 (port pin connection diameter)	3.70 mm ⊘
l_5 (external chamfer length)	2.72 mm
l_6 (resistor gap)	0.50 mm
w_2,l_7 (outer Wilkinson divider chamfer; width, depth)	5.36 mm, 2.60 mm
w_3,l_8 (inner Wilkinson divider chamfer; width, depth)	1.40 mm, 1.00 mm
d_6 (feed diameter)	130.00 mm ⊘
r_6 (CP feed line central radius)	39.70 mm
r_2 (port pin radial distance)	17.19 mm
d_3 (port pin hole diameter)	1.50 mm ⊘
d_4 (copper ground clearance)	4.10 mm ⊘

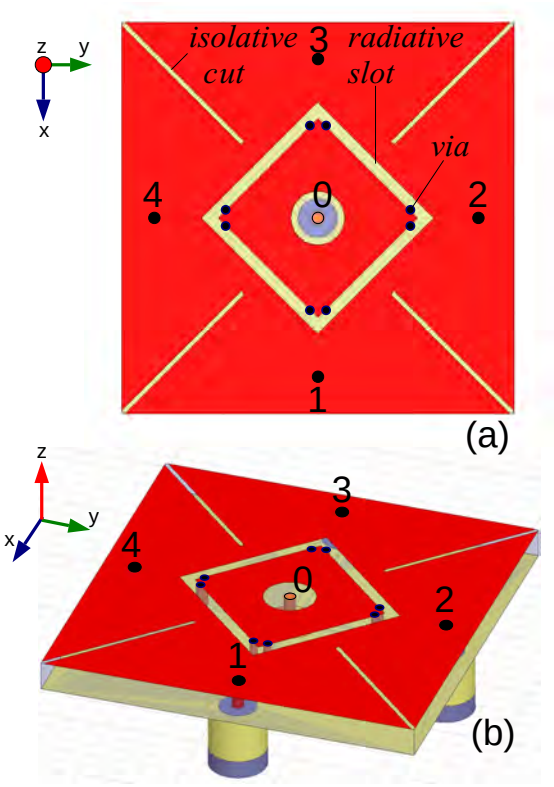

Figure 7.1. Antenna design with port referencing. A symmetrical design about the z axis includes a common radiative slot through which CP and OLP modes radiate. Views shown are: (a) antenna topside view showing the square slot and the position of the eight monopole cavity grounding via connections, and five coaxial probe feed connections, 0 to 4. As a result of its mode of operation, port 0 has topside clearance. The four isolative cuts are introduced to increase isolation between adjacent ports. Coaxial probe feeds are replaced with five via pin connections inserted and soldered between OLP, CP feed backside and the antenna topside, (b) antenna side view showing the passage of the grounding vias and port connections. Figure 7.1 (b) has dielectric material removed for convenience.

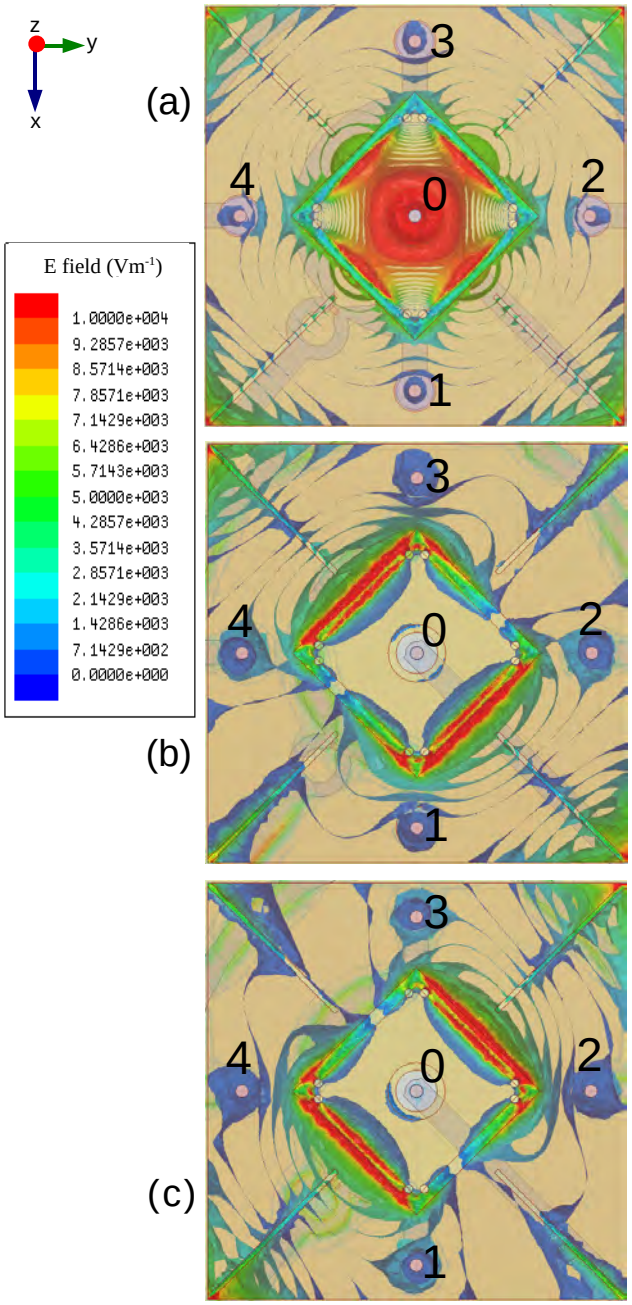

Figure 7.2. Mode radiation characteristics. The antenna radiates CP and OLP fundamental modes. Simulated instantaneous electric field magnitudes, as seen from the antenna topside are shown in this figure. The polarised modes are: (a) magnetic current loop mode, or OLP radiation, excited by antenna port 0, (b) broadside CP radiation, excited by sequential feeding of antenna ports (feed phase= 60°), (c) broadside CP radiation, excited by sequential feeding of antenna ports (feed phase= 150°). A common radiative slot provides a means of transmitting both modes.

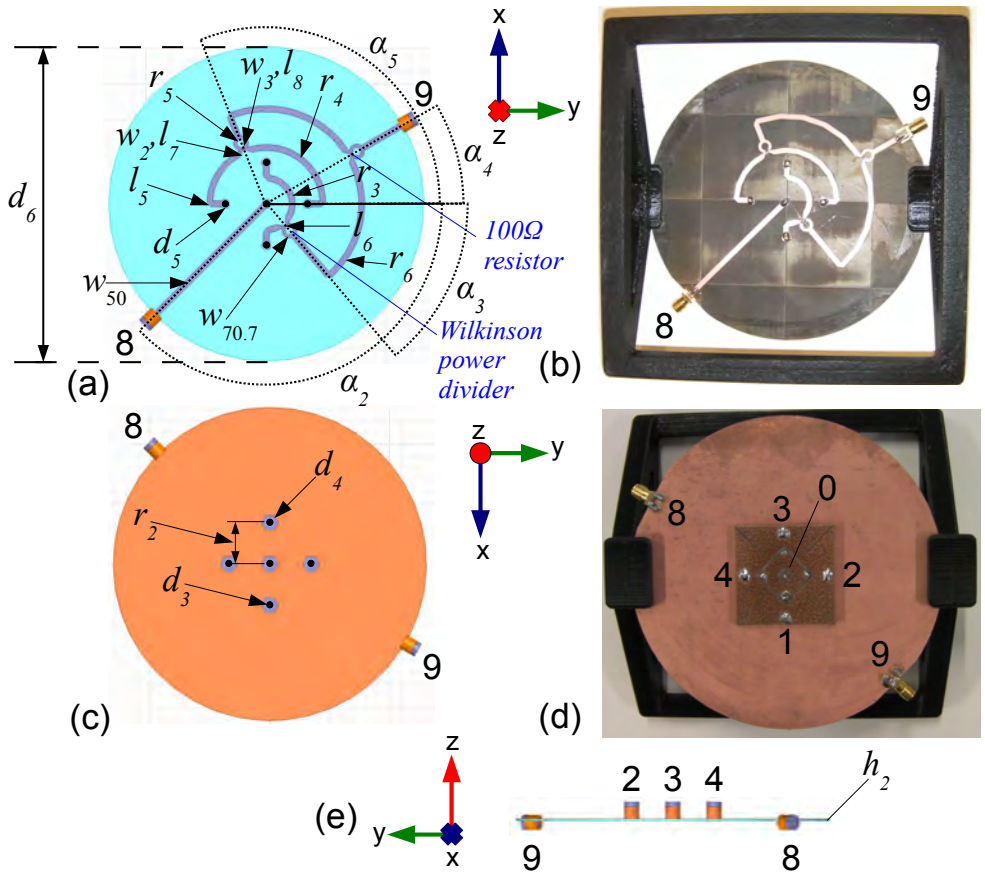

Figure 7.3. OLP, CP feed design with port referencing. Refer to Table 7.1 for reference descriptions. The images shown are: (a) Virtual OLP, CP feed backside view showing feed line detail, (b) manufactured OLP, CP backside view, (c) virtual OLP, CP ground or topside view showing copper ground clearances. These clearances align with those on the antenna backside, allowing for five port via pin connections to be inserted and soldered between feed backside and antenna topside, (d) manufactured feed with antenna mounted for OLP, CP operation, (e) Virtual feed frontside view. This image shows coaxial connections on the ground or topside, as references to show where the antenna is mounted. System operation is performed with the antenna facing skyward, in the positive z axis.

7.3 Results

Determination is made of three polarisation modes; x, y, and z, according to the feeding alignments shown in Figure 7.3. The third Ludwig definition of cross polarisation is used to determine CP performance (Ludwig 1973).

7.3.1 S-parameters

Simulated and measured S-parameters of the OLP, CP system are illustrated in Figure 7.4. Simulation and measurement are observed to provide good agreement. The OLP radiator provides a measured impedance bandwidth of 150 MHz, or 2.56%, centred at 5.87 GHz. A much larger CP mode impedance bandwidth is observed at 1.075 GHz (5.61–6.69 GHz), or 17.5%. The triple isolative effect of three Wilkinson dividers in the sequential feeding structure reduces unwanted reflections significantly, providing a wideband matching network. The Wilkinson divider network in the sequential CP feeding network and the driving of opposing ports in antiphase to create a null at the antenna phase centre, where the OLP radiator is situated, provide an isolative effect observed at the design frequency of 5.89 GHz through S_{88} and S_{89} respectively. Isolation of no less than 30 dB is measured from 4.10–6.80 GHz, peaking at 47 dB at the design frequency. The OLP mode operation limits the overlapping OLP, CP bandwidth to 150 MHz (5.79–5.94 GHz), or 2.56%.

7.3.2 Radiation Characteristics of OLP, CP System

Excitation of the magnetic current loop mode of antenna port 0, through port 8 of the OLP, CP feed, provides OLP mode radiation. Simulated and measured results for OLP radiation at azimuthal angles ϕ of 0° and 45° respectively are shown in Figures 7.5(a), (b). Simulation and measurement show OLP radiation to be conical, with absolute peak realised gain of 6.2 dB at $\theta = \pm 35°$.

A CP mode operation is achieved by driving antenna ports numbered 1 to 4, through CP feed port 9, to excite the two orthogonal degenerated broadside modes with a 90° sequential phase shift between them (Hall *et al.* 1989, Hall 1989).

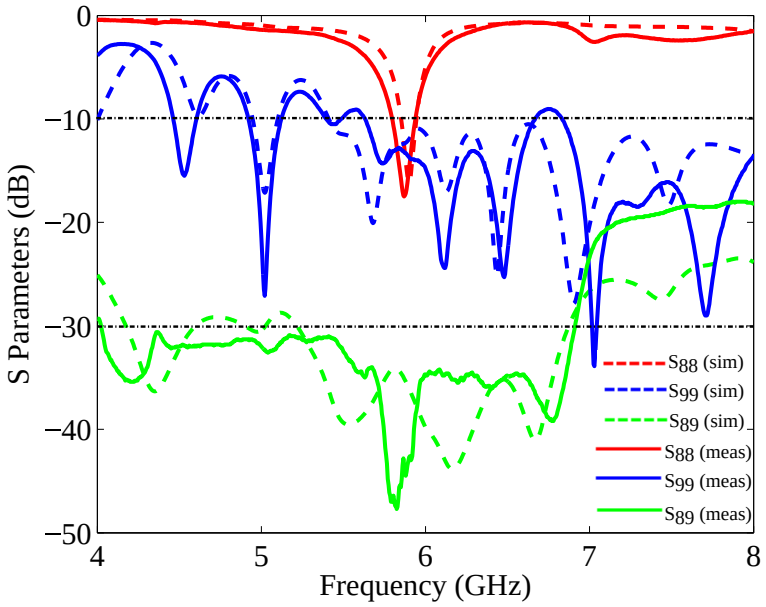

Figure 7.4. Simulated and measured port reflection coefficients and isolation coefficients of the OLP, CP antenna and feed system. The image includes the following S-parameters: S_{88}, S_{99}, and S_{89}. Port 8 is the OLP mode feed while port 9 is the CP mode feed, as shown in Figure 7.3. A reflection loss coefficient specification line of -10 dB and isolation coefficient specification line of 30 dB are shown for convenience.

Simulated and measured right-handed CP (RHCP) and left-handed CP (LHCP) characteristics of the sequentially fed CP system are illustrated in Figures 7.5(c), (d). Cross-polar levels of below 20 dB are observed in the broadside direction at the design frequency of 5.89 GHz. Absolute peak realised gain of 9.3 dBiC is measured.

A measure of CP performance through a measured 3 dB axial ratio bandwidth of 0.41 GHz, or 6.9%, centred at 5.96 GHz, is illustrated in Figure 7.6. An axial ratio of 0.26 dB, observed at 5.9 GHz (Toh *et al.* 2003), is determined by peak broadside CP mode performance. This performance, as shown by the notch bottom, is measured as being shifted upwards by 40 MHz, compared with simulation. Good agreement of CP performance is observed between measurement and simulation, with measurement slightly outperforming simulation both in terms of bandwidth and axial ratio.

In summary, the antenna and feed combination is able to generate radiation with OLP and CP mode patterns through a shared radiative slot on the top surface of the design. Gains of 6.4 dB in the case of magnetic current loop mode operation, and 9.3 dBiC in the case of degenerated broadside CP mode operation are measured, providing a

good match with simulation. Back radiation is minimised, and simulated radiation efficiency is above 96%, with a worst case measured radiation efficiency of 89%.

7.4 Diversity Characteristics

Two commonly used criteria— i.e. the mean effective gain (MEG) (Taga 1990, Volakis 2007), and the envelope correlation (ECC) (Blanch *et al.* 2003, Brown *et al.* 2007)— are utilised to evaluate the antenna diversity performance. Spherical integration functions of the 3D far-field antenna patterns are used to calculate both MEG and ECC metrics. For MEG, and at the design frequency of 5.89 GHz, the MEGs as a function of θ in Figure 7.7, and as a function of solid angle in Table 7.2 in a LoS channel are reported. Values are measured of θ and solid angles from the antenna zenith, orthogonal to the antenna radiating surface.

For conventional antenna designs, an ideal MEG will be -3 dBi in the case of 100% radiation efficiency, a cross polarisation ratio (XPR) of 0 dB at the transmitter and receiver, and it should be above -10 dBi for a practical antenna. In this instance, as examination of a CP mode and orthogonal OLP mode is made, the CP mode is treated as a single mode at the receiver, and so the MEG will be 0 dBi in the case of 100% radiation efficiency, and a cross polarisation ratio (XPR) of 0 dB at the transmitter and between the vertical OLP and CP modes at the receiver. According to the port isolation coefficients of Figure 7.4, polarisation coupling coefficients are introduced at the receiver into the diversity model in Chapter 3, and in Lawrence *et al.* (2015b), providing an upper bound on cross polarisation discrimination (XPD) values at the receiver. At the transmitter, interest is turned to the two polarisation modes that are aligned with the receiver at

Table 7.2. Mean effective gains (MEGs) for the OLP and CP modes. The MEGs of the polarisation modes produced by the antenna using the specific feed design of Figure 7.3 and Table 7.1 are given in dBi as a function of solid angle subtended from the zenith position, orthogonal to the antenna radiating surface (from simulated 3D radiation patterns and radiation efficiency).

	0°-30°	0°-60°	0°-90°	30°-60°	60°-90°
OLP	-11.29	-10.00	-11.24	-8.34	-15.30
CP	-1.17	-3.21	-4.73	-7.45	-18.57

the FoV centre in the diversity model in Chapter 3, and in Lawrence *et al.* (2015b). A XPR of 0 dB is modelled between these polarisation modes at the transmitter through polarisation coupling coefficients of zero magnitude. As such, simulated data are output as a function of the tri-orthogonal receive antenna uniquely. Simulated antenna radiation efficiency is above 96%, with a worst case measured radiation efficiency of 89%. Figure 7.7 highlights that the MEG of the CP mode is near optimal at -0.18 dBi when the antenna radiating surface is perfectly aligned with the transmitter. The OLP polarisation, aligned in the z direction, provides a MEG that is optimal at 40°, but that does not reach the near optimal MEG values of the CP mode. It does however provide a higher MEG than that of the CP mode for values of $\theta \geq 39°$.

For worst case measured radiation efficiency, and over the range of solid angles in Table 7.2, the values of MEG would drop by an additional -0.33 dB.

The ECC performance of the antenna over the radiating hemisphere is given in Figure 7.8. An upper threshold of 0.5 is commonly held as acceptable, while a value of 0 would suggest no correlation between polarisation modes. According to Mikki and Antar (2015), the ECC may be calculated from the simulated far-field radiation patterns, which is a preferred method to the less accurate method using S-parameters. The antenna demonstrates low correlation between CP and OLP modes at the centre, and at the band edges, of the overlapping tri-orthogonal bandwidth. The antisymmetric-symmetric nature of distributed electric fields between x and z, and y and z polarisation modes, where orthogonal x and y polarisation modes form the CP mode, and the symmetry of the physical design, provides near zero correlation. The ECC of the antenna is low due to the orthogonal polarisation of the modes involved.

To indicate the diversity performance of the antenna in a radiating direction that is furthest from orthogonality, the cross correlation at $\theta = 45°$ is examined at $\phi = 45°$. The value of cross correlation obtained at this specific radiating direction is then compared with singular values in orthogonal radiating directions of ($\theta = 45°$, $\phi = 0°$) and ($\theta = 45°$, $\phi = 90°$). The process begins by obtaining real and imaginary components of the E_ϕ and E_θ fields from simulated 3D radiation patterns in these specific radiating directions, and these are given in Table 7.3.

Cross correlation of the two broadside modes that form the CP mode, excited by sequential feeding of antenna ports 1–4, yields the values denoted by polarisation modes xy in Table 7.4. It is observed that the cross correlation is above the upper threshold value of 0.5 for a diversity antenna in the ($\theta = 45°$, $\phi = 45°$) direction.

Table 7.3. Real and imaginary electric field components in specific radiating directions (from simulated 3D radiation patterns). Antenna ports 1–4 are fed sequentially: port 1=0°, port 2=90°, port 3=180°, port 4=270°.

Ports	θ(°)	ϕ(°)	E_θ (V)	E_ϕ (V)
(1,3)	45	0	10.4207-8.18895i	0.0858013+0.0041984i
(1,3)	45	45	0.636187-5.38073i	-11.0358+11.2246i
(1,3)	45	90	-0.0440687-0.0135517i	-3.98847+14.3287i
(2,4)	45	0	0.0112409-0.00214351i	14.1018+4.26349i
(2,4)	45	45	5.33914+0.665992i	11.1773+11.3668i
(2,4)	45	90	8.24338+10.4953i	-0.0105054-0.0560714i
0	45	0	6.60955-0.00803283i	-0.00803283-0.00246598i
0	45	45	4.79431-0.0227119i	-0.0227119-0.0269899i
0	45	90	6.63658+0.023885i	0.023885+0.0382212i

Table 7.4. Antenna cross correlation in specific radiating directions (from simulated 3D radiation patterns). Cross correlation is considered between two or more mentioned polarisation modes in each case.

Polarisation modes	θ(°)	ϕ(°)	Cross Correlation
xy	45	0	0.0072
xy	45	45	0.7918
xy	45	90	0.0064
xyz	45	45	0.3179

For our antenna, the cross correlation in the ($\theta = 45°$, $\phi = 45°$) direction may be reduced by introduction of the omnidirectional z radiation pattern. As a result, the value of cross correlation in Table 7.4 is observed to drop below the threshold value of 0.5 in this direction.

The influence of the omnidirectional mode in improving the antenna performance for values of $\theta \geq 39°$ has previously been borne out by the MEG values of Figure 7.7, and the values of Table 7.2.

7.4.1 Excitation Port Diversity

In this chapter, performance metrics have been given for a specific feeding design, namely OLP mode and CP mode feeding, in combination with the tri-orthogonal slot antenna described in Chapter 6.

An attractive option of the antenna is the ability to beam steer radiation through the common radiative slot. Excitation of omnidirectional feed port 5 introduces a third dimension of diversity in two-port mode, or in five-port mode if the antenna is used as a standalone device. By presenting various excitations to the antenna ports, active control of the antenna radiation pattern is possible. Table 7.5 provides such information in the form of nine distinct feeding cases, I to IX, given in the form of total input power fraction and phase excitation for each antenna port, i.e. ports 0 to 4. Figures 7.9 and 7.10 illustrate the resulting simulated radiation pattern for each feeding case.

Cases I to IV, illustrated in Figures 7.9(a), (b), demonstrate how the radiation pattern may be aligned in the principal ϕ axes directions, with the antenna operating as a standalone device. The radiation pattern gain is maximised in the antenna zenith direction, or $\theta = 0^\circ$ direction. The pattern bcomes azimuthally asymmetric, due to excitation of port 0, with a null observed in the azimuthal, or ϕ, direction of the port fed in antiphase to the excitation of antenna port 0.

7.4.2 Excitation Phase Diversity

As well as providing separate OLP radiation orthogonal to that of CP radiation, the magnetic current loop mode, fed by port 0, is able to vary the elevation of the radiation beam, as given by case V, when compared with case I. Case V is illustrated in Figure 7.10(a), and employs a phase of 100° for the magnetic current loop mode excitation, while case I uses 0°. The beam deflection in this instance, as a standalone device, is -20° from $\theta = 0^\circ$, but can be increased with a large ground plane as the OLP radiation pattern becomes less conical and more monopole-like.

By increasing the magnetic current loop mode phase from 0° to 180°, it is possible to obtain pattern diversity ranging from case I to case II. From 180° to 360°, this diversity reverses, with the pattern reverting back to the original case I state at the end of the cycle. Case VI, shown in Figure 7.10(a), demonstrates this effect, as it is effectively case V, but with an additional 180° phase increment added to the magnetic current loop mode excitation state.

Table 7.5. Diversity Feeding. Port excitation information is provided in the form of nine distinct feeding cases, I to IX. Port excitations are given for each antenna port, numbered 0 to 4, in the form of total input power fraction and phase.

Case	Port 0	Port 1	Port 2	Port 3	Port 4
I	0.33, 0°	0.33, 180°	0	0.33, 0°	0
II	0.33, 0°	0.33, 0°	0	0.33, 180°	0
III	0.33, 0°	0	0.33, 0°	0	0.33, 180°
IV	0.33, 0°	0	0.33, 180°	0	0.33, 0°
V	0.33, 100°	0.33, 180°	0	0.33, 0°	0
VI	0.33, 280°	0.33, 180°	0	0.33, 0°	0
VII	0.50, 280°	0.25, 180°	0	0.25, 0°	0
VIII	0.80, 280°	0.1, 180°	0	0.1, 0°	0
IX	0.98, 280°	0.01, 180°	0	0.01, 0°	0

7.4.3 Excitation Magnitude Diversity

By altering the power distribution to antenna ports, while maintaining antenna total input power constant, it is possible to provide additional pattern diversity, as in cases VII to IX. These are power redistribution cases of case VI, and are shown in Figure 7.10(b). Comparing with case VI, the main lobe may be deflected by an additional 15°, to 35°, as a pure magnetic current loop mode is approached in case IX. The null observed in case VI may be deflected by an additional 65°, to $\theta = 0°$, as demonstrated by case IX. Through cases VI to IX, main lobe gain varies between 5 dB and 9 dB. The null varies between -18 dB and -30 dB.

Due to the symmetry of the design, it is possible to scan the radiation patterns in cases I to IX through all values of ϕ. For such operation, the antenna is in five-port standalone mode, or two-port mode using a OLP, CP feed.

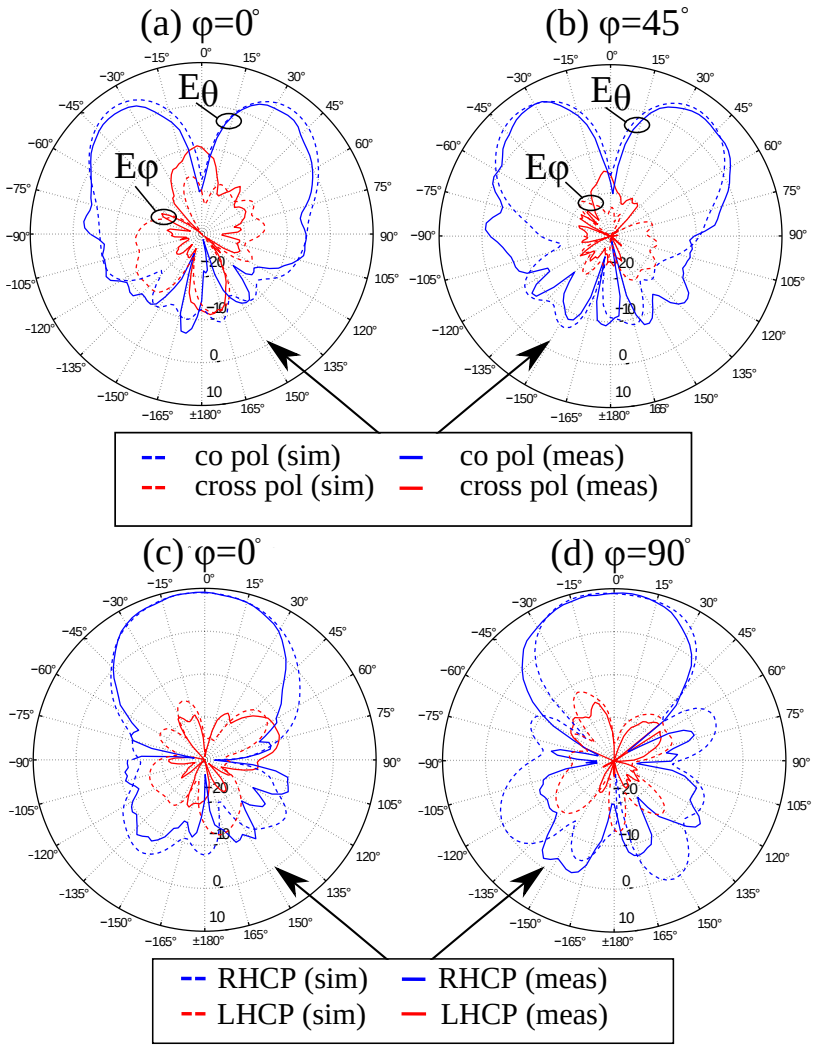

Figure 7.5. Radiation characteristics of the OLP, CP antenna and feed design. The images shown are: Excitation of port 8 of the CP feed and antenna combination provides an OLP radiation characteristic (a), (b). The right - handed and left - handed CP, or RHCP and LHCP respectively, radiation characteristic is achieved via excitation of port 9 of the CP feed and antenna combination (c), (d).

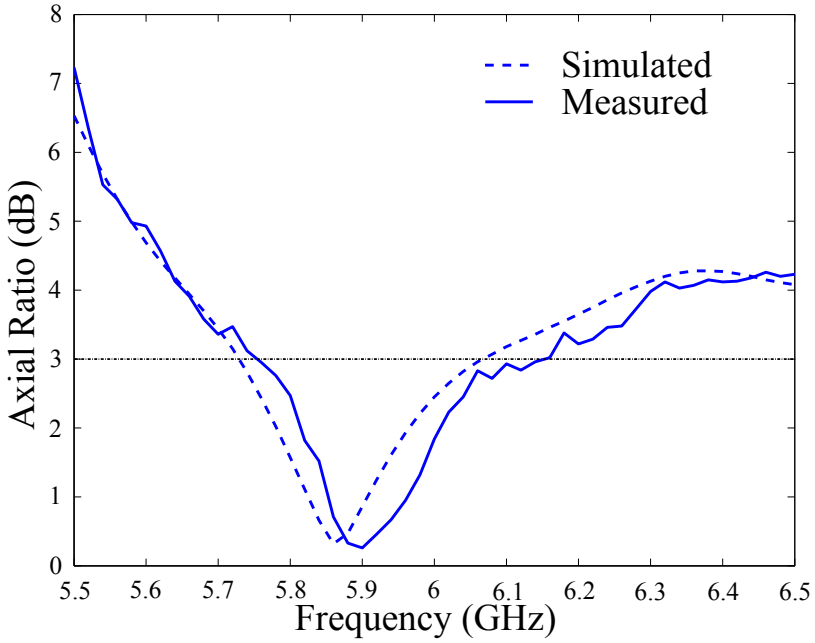

Figure 7.6. Measured and simulated axial ratio, showing CP performance over a bandwidth about the design frequency of 5.89 GHz. The 3 dB axial ratio specification line is shown for convenience.

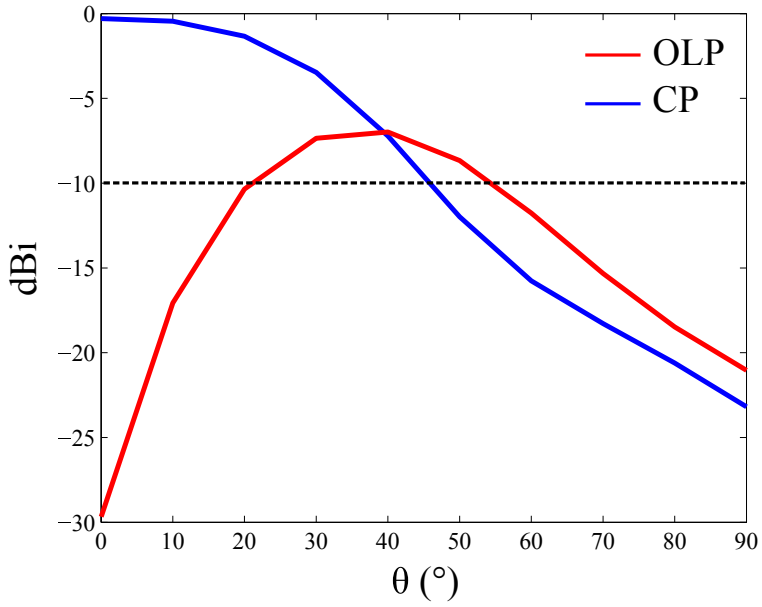

Figure 7.7. Mean effective gains (MEGs) for the OLP and CP modes. The MEGs of the polarisation modes produced by the antenna using the specific feed design of Figure 7.3 and Table 7.1 are given in dBi as a function of θ from the zenith position, orthogonal to the antenna radiating surface, using simulated 3D radiation patterns and radiation efficiency. A MEG limit of -10 dBi is included for ease of data interpretation.

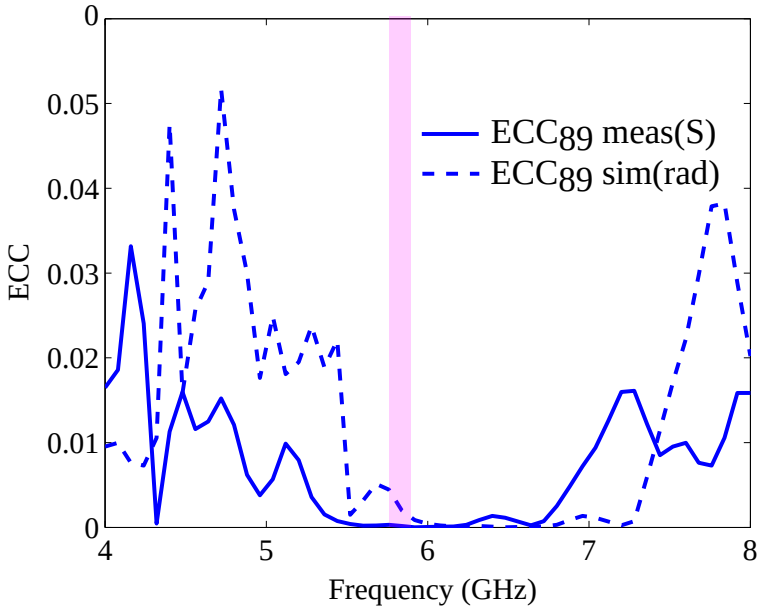

Figure 7.8. Measured and simulated envelope correlation coefficients (ECCs) of the OLP, CP mode antenna and feed system. Port 8 is the OLP mode feed while port 9 is the CP mode feed, as shown in Figure 7.3. For convenience, the overlapping impedance bandwidth (5.79–5.94 GHz) is shown. A value of 0.5 may be regarded as an upper limit on performance (Blanch *et al.* 2003, Brown *et al.* 2007). Low correlation between ports is suggested by values of the OLP, CP mode system.

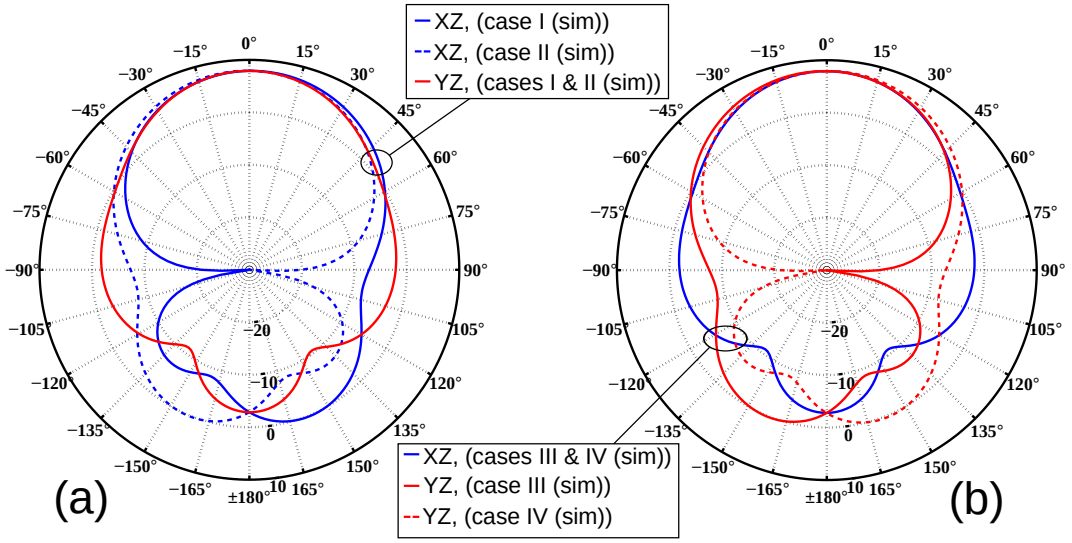

Figure 7.9. Port diversity operation of the antenna in the main orthogonal ϕ axes directions, according to antenna port excitations of cases I to IV in Table 7.5. Cuts are shown in the XZ ($\phi = 0°$) and YZ ($\phi = 90°$) planes for (a) cases I and II, (b) cases III and IV.

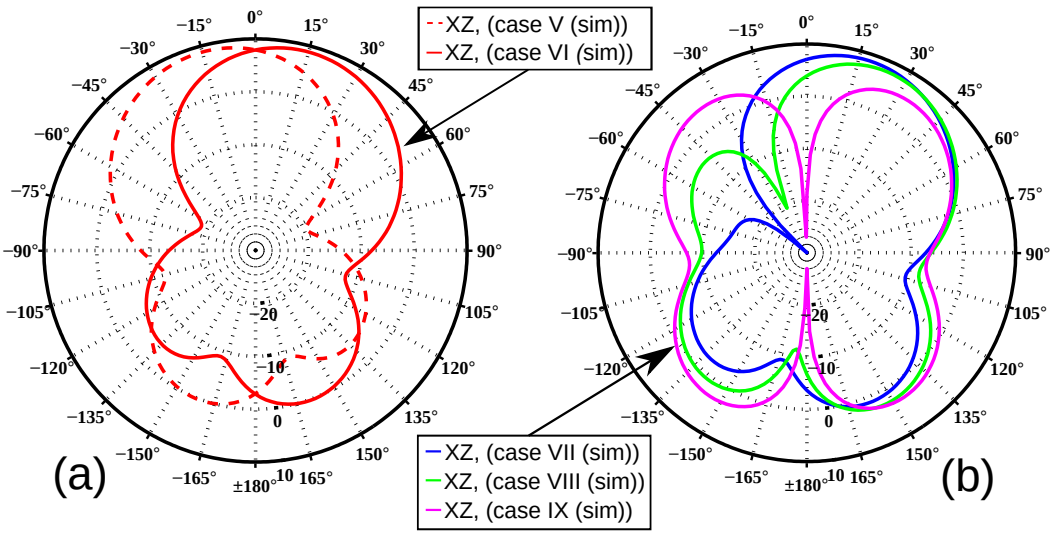

Figure 7.10. Phase and power diversity operation of the antenna. The images shown are: (a) illustration of phase adjustment of the magnetic current loop mode excitation (cases V and VI, Table 7.5), and its effect on the antenna radiation pattern, (b) illustration of antenna port power redistribution (cases VII to IX, Table 7.5), and its effect on the antenna radiation pattern. Cuts are shown in the XZ ($\phi = 0^\circ$) plane. The main lobe of the radiation pattern of cases VI to IX is in a positive θ direction as a result of introducing an additional phase increment of 180° to the magnetic current loop mode excitation of case V. In case IX, the pattern is near symmetric as a pure magnetic current loop mode of operation is approached.

7.5 Chapter Summary

A planar slot antenna operating at 5.9 GHz and providing simultaneous OLP and CP mode radiation is demonstrated in this chapter. Operation is simulated, and subsequently confirmed through measurement. A large ground plane would in effect provide a monopole-like magnetic current loop mode of operation, polarised orthogonally to the CP broadside mode. Sequential feeding of slot ports 1–4 provides two orthogonal degenerated broadside modes with a 90° phase shift between them, or CP mode radiation, and a magnetic current loop mode, provides OLP radiation. Measurement of these modes finds operation providing 6.4 dB of OLP gain, and 9.3 dBiC of CP gain at the design frequency. A minimum measured OLP mode, CP mode overlapping impedance bandwidth of 2.56% (5.79–5.94 GHz) is observed.

In the frequency band of operation, isolation of no lower than 45 dB is measured between the operational modes, due to field cancellation of the two orthogonal degenerated broadside modes, providing CP mode radiation, at the antenna centre, as a result of a sequential feeding arrangement.

Active control of the antenna radiation pattern, providing radiation pattern diversity, is possible in three orthogonal axes by varying feeding excitations to each of the antenna ports as a five-port standalone device. Nine distinct cases are given to illustrate the concept of beamforming in three dimensions through a combination of feeding excitations. As a two-port sequentially fed device, providing simultaneous OLP and CP polarisation modes as demonstrated in this chapter, the antenna is able to combine these modes to readily produce the radiation patterns observed in Figure 6.12 of Chapter 6.

Due to a complete ground plane, low profile and ready manufacture, the antenna may be integrated into various systems.

In Chapter 8, a low-profile electric monopole cavity antenna providing a wideband performance is demonstrated. The design is introduced in an effort to increase the narrow bandwidth performance of the OLP mode that is a feature of many readily manufacturable substrate-integrated cavity designs that operate using higher permittivity substrates.

Chapter 8

Wideband Low-Profile Electric Monopole

This chapter proposes a coaxial probe-fed wideband low-profile electric monopole cavity antenna with measured impedance bandwidth of 56% at a central operating frequency of 8 GHz. The design is compatible with applications requiring a vertically polarised signal with respect to the antenna surface, and provides the basis for a wider bandwidth tri-orthogonally polarised antenna design.

8.1 Introduction

Low-profile monopole antennas are becoming more relevant in an increasing number of technologies in the microwave region. Specific examples include the dedicated short-range communications (DSRC) band for vehicle-to-vehicle (v2v) safety systems (Biswas *et al.* 2006), aircraft applications (Sampigethaya *et al.* 2011), active (Marrocco *et al.* 2008) and passive (Mandel *et al.* 2011) sensor technologies, and unattended ground sensors (UGSs) (Nemeroff *et al.* 2001). For each of these applications, an antenna backed by a ground plane that can be integrated into an RF substrate appears very attractive. With such an antenna vertically mounted, one desired feature is an omnidirectional radiation pattern, making it useful for terrestrial applications, non-line-of-sight (NLoS) conditions, and situations where transceiver modules may be deployed randomly. A gain profile with maximum in or close to the substrate plane is possible; this being achieved by either a standalone device, or by mounting on a large metallic surface. Design architecture is varied, and includes a miniaturised cavity-backed composite slot loop antenna (CBCSLA) (Wonbin and Sarabandi 2008), and a multiple-element monopole design (Wonbin and Sarabandi 2009), as well as low-profile resonant cavities, with fringing fields from thin apertures forming equivalent magnetic currents (Lin and Row 2008).

Generally, low-profile monopole antennas can be split into two geometries: square (Row and Chen 2006, Abadi and Behdad 2014, Kaufmann and Fumeaux 2015) and circular (Economou and Langley 1997, Nakano *et al.* 2008, Al-Zoubi *et al.* 2009, Liu *et al.* 2013, Liu *et al.* 2014) cavities. More complex cross and conical geometries (Koohestani *et al.* 2014) may be employed to increase bandwidth. Circular designs tend to resonate with cylindrical TM_{01} and TM_{02} modes while square patches tend to resonate with TM_{11} and higher-order modes. Resonator height is largely influenced by the choice of cavity medium. Free space cavities generally lead to higher resonant frequencies for a given cavity size, and are often voluminous. Higher permittivity designs suffer from higher losses and decreased bandwidth.

For v2v and aircraft applications, the extended ground plane offered to the monopole in the form of large metallic outer surface renders the use of such an antenna an extremely attractive option. Such a surface offers the possibility of generating an omnidirectional radiation pattern with a maximum gain near the substrate plane. The ground plane shape influences the antenna radiation pattern.

For UGS and active and passive sensor applications, the standalone device may provide vertical polarisation with a radiation pattern that remains omnidirectional in a narrow bandwidth.

In this chapter, an easily manufacturable low-profile magnetic loop monopole antenna design is proposed, and demonstration is made of how a simple modification of the patch geometry, namely the introduction of concave curved edges, can significantly increase the operational bandwidth.

8.2 Design

Figure 8.1 illustrates the proposed antenna design, with dimensional information given in Table 8.1. The design is based on a Rogers Duroid® 5880 substrate with relative permittivity ϵ_r of 2.2, loss tangent $\delta = 0.0009$, and is cladded with 17 μm of copper on either side. Its geometry consists of an evolution of a square patch shorted at its corners, where the four radiating cavities are modified to curved concave shapes. This effectively forms a substrate-integrated cavity radiating as a magnetic current loop. This can be understood from the equivalence of a small constant magnetic current loop and an electric dipole, which is the dual case of a small loop of constant electric current being equivalent to a magnetic dipole.

Table 8.1. Antenna Dimensions.

Reference	Dimension
l_1 (antenna side length)	54 mm
h_1 (antenna side height)	6.35 mm
d_1 (circular copper diameter)	44.00 mm ⊘
r_1 (circular cutout centre point radius)	27.00 mm
r_2 (circular cutout radius)	18.50 mm
r_3 (radial via distance)	22.00 mm
d_2 (via diameter)	1.05 mm ⊘
d_3 (upper surface copper clearance diameter)	5.97 mm ⊘
d_4 (pin diameter)	1.27 mm ⊘
d_5 (coaxial feed copper clearance diameter)	4.1 mm ⊘

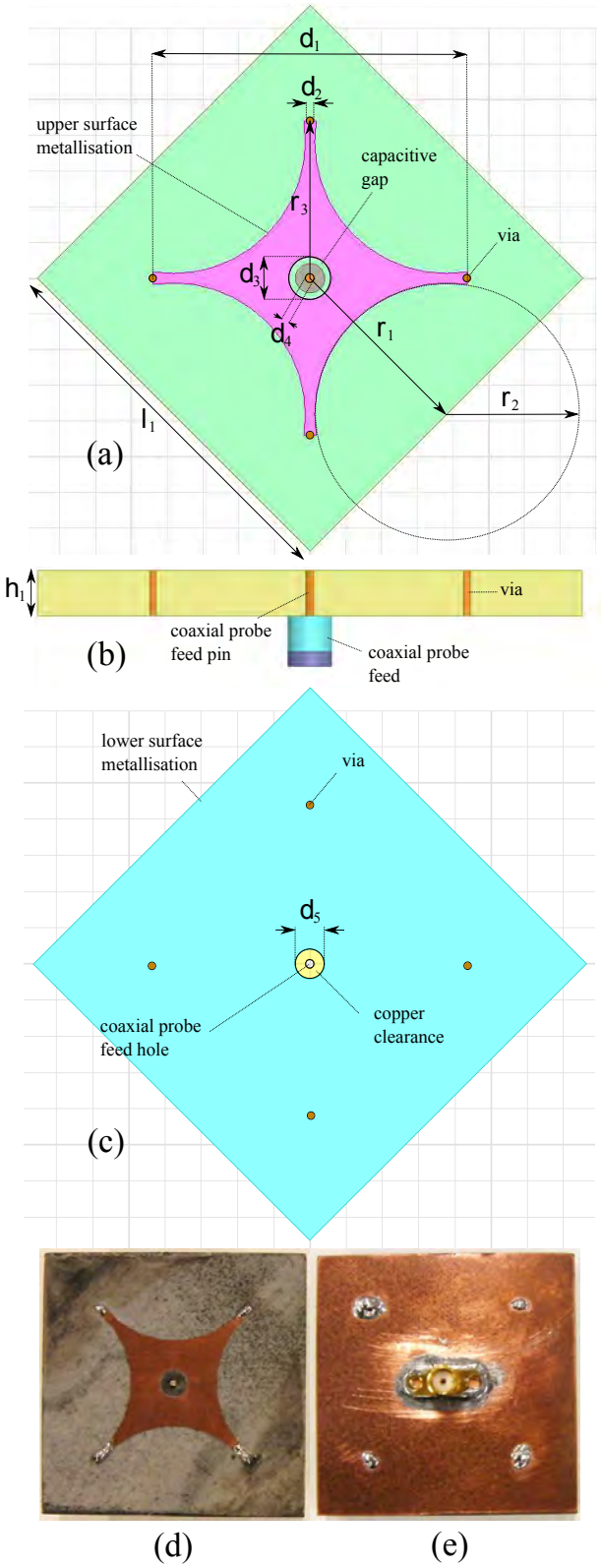

Figure 8.1. The antenna design. The antenna operates as a magnetic current loop via four concavely curved radiating slots, providing a symmetric radiation pattern through excitation of a magnetic current loop mode. Views shown are: (a) top view, (b) front view, (c) bottom view (with coaxial probe feed connection removed), (d) manufactured topside, (e) manufactured backside.

At the centre of the upper surface, the annular capacitive gap between the coaxial probe feed centre pin and the upper surface concave patch compensates the inductive nature of the cavity coaxial feed, providing control of impedance and input reflection coefficient of the antenna (Kaufmann and Fumeaux 2015).

The substrate height h_1 corresponds to a guided wavelength of $\lambda/5$ at 5.8 GHz, the lowest frequency of operation. While this can be considered high by some measures, this height enables the antenna bandwidth to significantly increase compared to a previous design using a substrate height of 3.2 mm (Kaufmann and Fumeaux 2015). This dependence of bandwidth on resonator height is consistent with observations of related microstrip patch antenna structures.

8.3 Results

Figure 8.2 shows the simulated and measured input reflection coefficient S_{11} of the optimised geometry. The measured impedance bandwidth is 56%, as per an input reflection coefficient criteria of $|S_{11}| \leq$ -10 dB with respect to a 50 Ω characteristic.

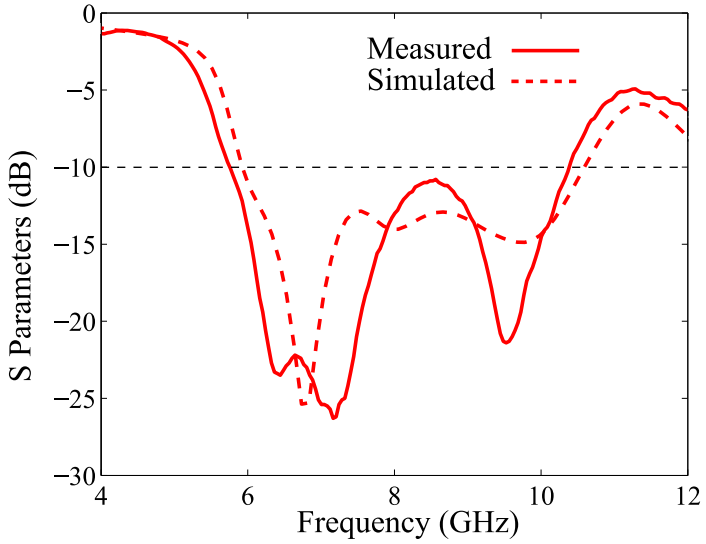

Figure 8.2. Reflection coefficient of the proposed antenna. The measured impedance bandwidth of the antenna, defined by an input reflection coefficient $|S_{11}| \leq$ -10 dB, is from 5.8 GHz to 10.3 GHz. The measured shift down in frequency has been previously observed with a similar structure (Kaufmann and Fumeaux 2015). Complex impedance matching results in the observed divergence between simulation and measurement at 6.3–7.2 GHz, and at 9.3 GHz.

Prior work has demonstrated a narrow bandwidth of 2.1% at a design frequency of 5.9 GHz for a design of comparable ground plane area, due to a reduced substrate height (Kaufmann and Fumeaux 2015). Figure 8.2 illustrates the bandwidth improvement that can be achieved by doubling the substrate height, and thus the monopole cavity height.

Simulated and measured antenna realised gain patterns are illustrated in Figure 8.3 at the low, mid- and upper bandwidth frequencies. As can be seen, patterns are symmetric and quasi-omnidirectional; consistent with similar reported structures. An extended ground plane, as in a v2v system, would provide a more omnidirectional pattern with a reduced maximum gain parallel to the planar antenna surface.

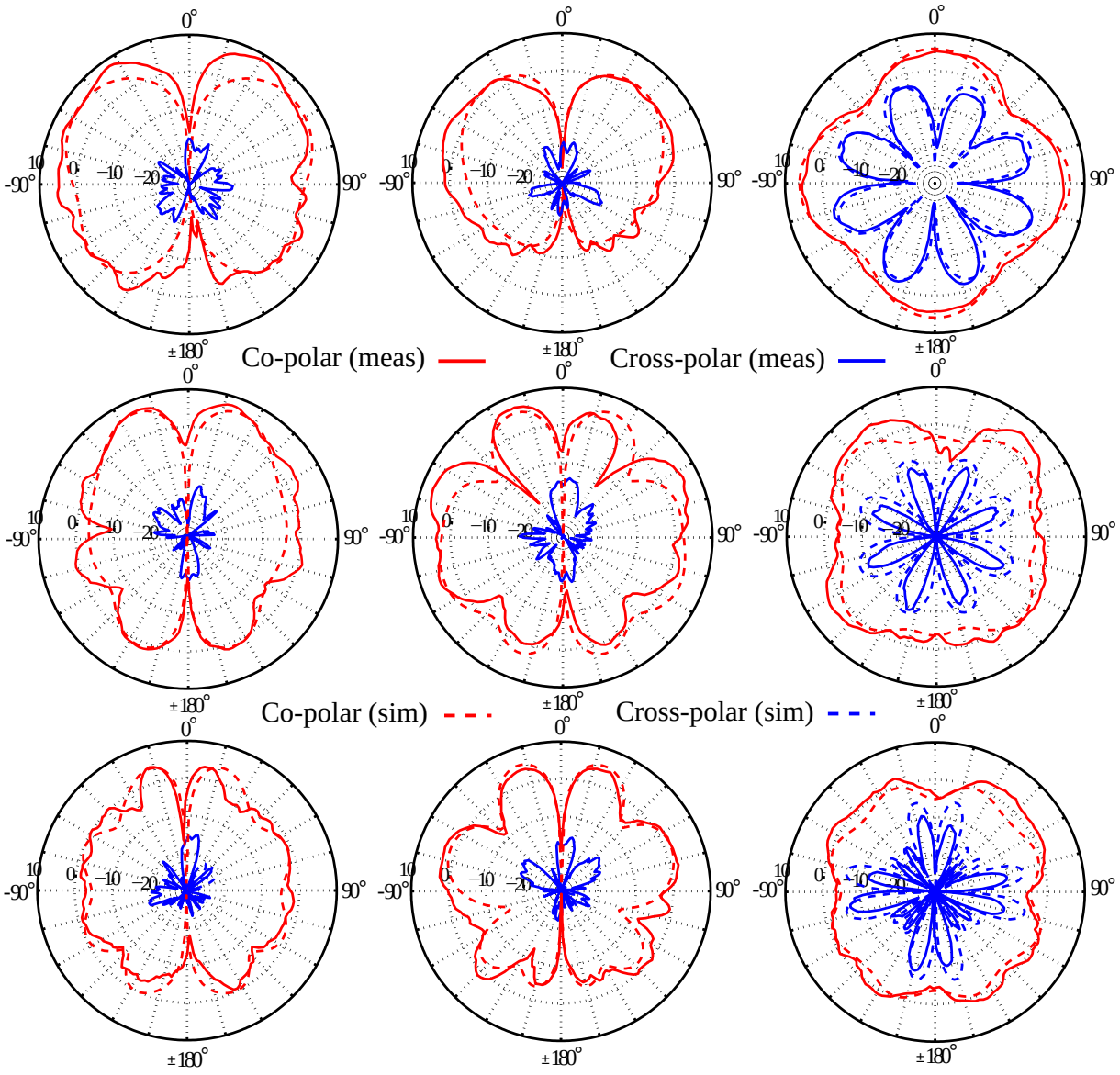

Figure 8.3. Antennna realised gain patterns. Images shown are: 5.9 GHz (top row), 8 GHz (middle row), and 10.3 GHz (bottom row). Sectional cuts of ϕ_{0° (left column), ϕ_{45° (middle column), and θ_{0° (right column) are shown.

8.4 Chapter Summary

Presentation has been made of a wideband low-profile monopole cavity substrate-integrated antenna, centred at 8 GHz, and with a 56% measured impedance bandwidth. The antenna extends the bandwidth of operation compared to prior design, and offers a possible direction to follow to increase the bandwidth of operation of the OLP mode that features in the tri-orthogonal antenna design demonstrated in Chapters 6 and 7.

Realised gain patterns illustrated at lower, mid- and upper bandwidth frequencies demonstrate vertical polarisation, as seen by a broadside null, and are symmetric and quasi-omnidirectional about an axis perpendicular to the antenna surface. The design proposes fewer components than prior work, suggesting less reliance on manufacturing tolerance.

The antenna may offer a more omnidirectional radiation pattern, with maximum gain near the substrate plane, when mounted onto a large metallic surface. As such, the design is particularly well suited to v2v systems and aircraft applications.

In Chapter 9, the original contributions contained within this thesis are highlighted. These contributions are both software and hardware-based. Future directions are suggested for the research that is presented in this thesis, and an outlook with regard to the possible role that tri-orthogonal polarisation diversity can play in the next generation of wireless system design is given.

Chapter 9

Contributions & Future Research Directions

THE research and contributions in this thesis are presented over a range of topics linked by tri-orthogonal polarisation diverse design. The thesis provides contributions in both software and hardware forms. This chapter summarises the main findings, conclusions and contributions of this thesis, and outlines possible directions for research into the future.

9.1 Introduction

The immediate future is heralded as a time of massive global digital data increase (Atzori *et al.* 2010, Rappaport *et al.* 2013b). In order to provide the systems able to cope with this increase, the telecommunication industry is undergoing a paradigm shift in its way of thinking. No longer can older technology be rejuvenated through coding algorithms to provide a solution. Instead, a whole new suite of technologies operating at higher frequencies and aimed at an increasingly mobile user is under research. Yet to achieve maximum benefit from this research, much of the old criteria used to improve performance of mobile technology needs adaptation. Conventional technologies operating at microwave frequencies have benefited from attributes including high power, high gain, multipath fading and spatial diversity. Conventional designs however all share a common disadvantage in that they are optimised to radiate in a single direction, typically broadside to the antenna surface. Spatial diversity techniques mitigate this issue by providing several diverse fixed antenna locations for communicating with a mobile user within a network cell. For satellite systems, the ground receiver tracks the satellite thus maintaining alignment. However, if technology is to deliver on an increase in data traffic in an evermore mobile world, then consideration must be made of misaligned systems, and how to mitigate for this issue. Polarisation diversity offers the potential of reducing antenna size as two or more orthogonal polarisation modes operate at a single frequency (Lee and Yeh 1972, Vaughan 1990, Turkmani *et al.* 1995, Gesbert *et al.* 2003, Erceg *et al.* 2004). This provides a useful starting point from which to tackle antenna misalignment.

This thesis considers the option of tri-orthogonal polarisation diversity (Andrews *et al.* 2001). Such a scheme offers increased data transfer rates (Mtumbuka *et al.* 2005, Chiu *et al.* 2007b), and of equal importance a possible mitigation of antenna misalignment. The thesis provides the reader with an insight into the advantages of tri-orthogonal polarisation diversity in both the context of a terrestrial channel and that of a non-geosynchronous satellite orbit channel. Where appropriate, a range of channel parameters is implemented in a model which considers all antenna alignments. The benefits of tri-orthogonal polarisation diversity are subsequently highlighted and discussed. In addition to this software component of the thesis, the ability to provide three orthogonal polarisation modes within a planar dielectric is demonstrated through design and test of a novel slot antenna. This hardware design is extended to provide

conventional CP mode patch antenna performance complemented by an omnidirectional vertical polarisation mode. Finally, extension of operational bandwidth of the omnidirectional vertical polarisation mode results in a design providing over 25 times the bandwidth of a prior comparable electric monopole substrate-integrated design.

The original contributions presented in the various chapters of this thesis, which extend the state-of-the-art in tri-orthogonal polarisation diverse modelling and design, are discussed in the following sections.

9.2 Part I: Software-Based Original Contributions

9.2.1 Tri-Orthogonal Approach Applied to Terrestrial Channel: (Chapter 3)

In this chapter, a fundamental approach to analysing the benefits of a tri-orthogonal antenna design operating at 60 GHz in a short range WLAN terrestrial channel is developed, based on an orthogonal arrangement of three colocated half-wavelength dipoles at both the transmitter and at the receiver. The benefits of a tri-orthogonal arrangement have been highlighted in prior research at lower frequencies (Andrews *et al.* 2001, Mtumbuka *et al.* 2005, Getu and Andersen 2005). Displacement of the receive antenna is generated in order to provide simulation of link performance over all antenna orientations at the receiver, while maintaining a fixed transmitter position. The displacement of the receive antenna over a spherical surface mimics the variation of antenna orientation in a mobile scenario. The results are introduced in a FoV format from the perspective of the transmitter. Performance of the tri-orthogonal arrangement at both ends of the link is compared to that of conventional patch antenna design. The results suggest that the enhancement offered by a tri-orthogonal arrangement is substantial over both extremes of a terrestrial channel, namely a channel devoid of scattering mechanisms and one in which scatterers abound. Orientational robustness through diversity of the tri-orthogonal antenna design is highlighted by the model. In subsequent research outside the thesis, the model is extended to both a relevant 5G network scenario and THz frequencies. The implication of polarisation purity (Ramirez and De Flaviis 2003) is considered for 5G networks.

Author works: (Lawrence *et al.* 2014a, Lawrence *et al.* 2014b, Lawrence *et al.* 2015b, Lawrence *et al.* 2016b, Lawrence *et al.* 2016c, Lawrence *et al.* 2017c)

9.2.2 Faraday Rotation and Path Delay in the Ionosphere: (Chapter 4)

The idea of a changing link geometry is not confined to just movement of a mobile handset in a terrestrial environment. A NGSO ionospheric channel provides a link geometry in which the satellite is constantly moving in relation to a ground receiver. To examine the benefits of a tri-orthogonal approach in such a channel, it is necessary to model the depolarising medium through which signal propagation occurs, namely the ionosphere. While ionospheric models are to be found in the literature, a limitation of these models is that they typically rely on single value data taken at the midpoint of a link propagation path (Mannucci *et al.* 1998). To model the ionosphere at a single point does not provide the ability to model ionospheric intricacies as a function of latitude, longitude and geodetic height (Smith *et al.* 2008). In order to model the ionosphere and incorporate these subtleties, a novel vectorised method of analysis is invoked. This provides a method to integrate ionospheric effects at multiple points along a propagation path, for all propagation paths within a FoV as observed from an orbiting satellite with a three dimensional spatial position that changes over time. The diurnal effect is subsequently added to simulate the varying nature of ionospheric layers as a function of solar excitation. Using realtime ionospheric data, the results of the integrated vectorised approach are compared with those generated through conventional trigonometrical methods. It is shown that the integrated vectorised representation of the ionosphere provides results of Faraday rotation and path delay that differ from those provided through a conventional singular value trigonometrical approach, although favourable magnitudinal and angular trend correlation is maintained.

Author works: (Lawrence *et al.* 2015a)

9.2.3 Tri-Orthogonal Approach Applied to Non-Geosynchronous Satellite Orbit Ionospheric Channel: (Chapter 5)

Chapter 4 provides the basis for analysing a tri-orthogonal polarisation diverse approach at the receiver applied to a NGSO ionospheric channel, as the main ionospheric effects on a signal propagating along a path are vectorially calculated over a NGSO FoV in realtime as a function of global position and geodetic height (Jehle *et al.* 2005, Jehle *et al.* 2009, Hunsucker and Hargreaves 2007, Kos *et al.* 2010). The tri-orthogonal polarisation diverse approach is only applied at the ground receiver, which is both financially and practicably plausible. Application of this approach at the satellite would

be onerous from both a cost and engineering perspective. Through vector analysis, and the application of the findings of Chapter 4, a resulting NGSO ionospheric channel model suggests that the communication link between a conventional CP mode antenna arrangement at both the satellite and ground receiver is enhanced through a tri-orthogonal arrangement applied at the receiver. Three operational satellite systems are investigated over their distinct orbits using a vectorial analysis, realtime ionospheric data, the ionospheric modelling of Chapter 4, and a range of NGSO channel environments. Statistical data is used in the case of the Iridium system to provide an analysis employing local scattering effects typically found in suburban and urban environments, in channels experiencing LoS, intermediate or deep shadowing effects (Fontan *et al.* 2001). For all systems, results are presented over an orbit in sequential FoV format from the perspective of the satellite transmitter. Through a capacity metric, comparison is made between a conventional CP mode patch antenna at the receiver, based on current commercial designs, and the application of a third polarisation mode at the receiver, orthogonal to the antenna radiating surface. For all three satellite systems, and over an entire orbit, link enhancement in the form of both an increase in capacity and diversity gain is shown to be provided by a third orthogonal polarisation mode at the receiver.

Author works: (Lawrence *et al.* 2013, Lawrence *et al.* 2016d)

9.3 Part II: Hardware-Based Original Contributions

9.3.1 Planar Tri-Orthogonal Diversity Slot Antenna: (Chapter 6)

Through the course of this research, prior tri-orthogonal polarisation diverse antenna design is scrutinised. Designs typically suffer from a lack of phase centring leading to asymmetric patterns (Tong *et al.* 2013), excessive volume as a third polarisation mode orthogonal to a conventional radiating surface requires an increase in the third dimension of the antenna (Getu and Andersen 2005, Chiu *et al.* 2007b), or complexity of design (Zhong *et al.* 2009). As a consequence of this scrutiny, in this chapter a readily manufacturable antenna design operating at 5.9 GHz providing three orthogonal polarisation modes in a phase-centred, planar solution is implemented. Furthermore, through differential phase feeding techniques, tri-orthogonality through pattern diversity is demonstrated. Pattern diversity is set to become more important over the next few years, as wireless communication design heads to higher operating frequencies

to provide increased data transfer rate. The ability to effectively beam steer radiated energy in a direction to enhance SNR over the link is set to beome a necessary component of the next wave of wireless technologies. Pattern diversity for the proposed design is made possible due to low mutual coupling between polarisation modes, as a consequence of the design being highly symmetric and orthogonal in nature. This symmetry and orthogonality renders the design scalable over a range of operating frequencies.

Author works: (Lawrence *et al.* 2017b)

9.3.2 Multifunction Two-Port Slot Antenna with Omnidirectional and Circular Polarisation: (Chapter 7)

Extending the research of Chapter 6, a sequentially phased feeding design (Hall *et al.* 1989) is implemented with the antenna that provides conventional CP mode performance that is supplemented by an omnidirectional vertically polarised monopole mode that is orthogonal to the radiating antenna surface. As such, the combined design provides the possibility of operating as a conventional CP mode patch antenna with the option to implement an omnidirectional electrical monopole mode providing radiated energy from a magnetic loop current (Kaufmann and Fumeaux 2015). The combined antenna and sequential feed design is able to drive both of these modes simultaneously, providing an option to beam steer radiated energy. The feeding technique is a specific design that complements the feeding used in Chapter 6, that provides an insight into the diversity of the antenna. As a five-port standalone device, the antenna is able to be fed to provide multiple radiation beam configurations, and these are highlighted in this chapter to further demonstrate the versatility of the antenna.

Author works: (Lawrence *et al.* 2017a)

9.3.3 Wideband Low-Profile Electric Monopole: (Chapter 8)

One of the fundamental drivers of a tri-orthogonal polarisation diverse approach to wireless communication is the provision of improved coverage in a channel. The channel may be of a depolarising nature or not. In a depolarising channel, the tri-orthogonal arrangement may enhance capacity simply due to providing an additional degree of freedom or diversity in the form of a third orthogonally polarised mode. In

a non-depolarising channel, the tri-orthogonal arrangement enhances signal transfer by mitigating polarisation mismatch between an incoming signal and the receive antenna. As a consequence, signal transfer is made more probable as a third orthogonal polarisation mode offers additional diversity to capture radiated energy of which the polarisation orientation would otherwise not be aligned with the polarisation modes of a conventional receive antenna. In the research contained in Chapters 6 & 7, that provides both general and specific detail on a low-profile planar antenna radiating three orthogonal polarisation modes through a common radiative slot, the third orthogonal polarisation is implemented as an electric monopole through the principle of a magnetic loop current (Razavi and Neshati 2013, Kaufmann and Fumeaux 2015). This provides a means of avoiding unwanted antenna growth in a third dimension, providing a design typically within the size constraints of a conventional CP mode patch design. The monopole operates over a narrow range of frequencies, curtailing the operational bandwidth of the proposed antenna and feed combinations in Chapters 6 & 7. In this chapter, the bandwidth of an electric monopole design is extended to 56% through an adjustment to the metallic upper surface.

Author works: (Lawrence *et al.* 2016a)

9.4 Part III: Future Research Directions

9.4.1 Wideband Planar Tri-Orthogonal Diversity Slot Antenna

The provision of communication links providing higher data transfer rate is a design goal for the next generation of wireless systems (Pi and Khan 2011, Ghosh *et al.* 2014). In this thesis, a proposed antenna design that provides a tri-orthogonal polarisation diverse solution in planar form is demonstrated. The introduction of a third polarisation mode, orthogonal to the radiating surface of the antenna, through an electric monopole reduces operational bandwidth of the overall design. An electric monopole, providing radiation polarised orthogonally to the radiating surface of an antenna, is separately demonstrated with a 56% operational bandwidth. A design that converges the idea of tri-orthogonal polarisation diverse operation and wide operational bandwidth in planar form would provide a high amount of flexibility in terms of operability. Indeed, in Mtumbuka *et al.* (2005), a tri-orthogonal arrangement of omnidirectional discone antennas providing ultra-wideband performance demonstrates a spectral efficiency of

17.5 bpsHz^{-1}, and a low value of correlation of polarisation modes of 0.3. High capacity of 130 Gbps and diversity apt for MIMO performance are offered as a result of a tri-orthogonal arrangement.

9.4.2 Millimetre-Wave Tri-Orthogonal Diversity Slot Antenna

A planar antenna design offering tri-orthogonal polarisation diversity at an operating frequency of 5.9 GHz is demonstrated in this thesis. Next generation wireless systems operating at mmWave frequencies have the possibility to use colocated antennas to provide pattern diversity through polarisation diverse operation. The advantage of such a technique is a compact antenna design and the ability to beam steer radiated energy, providing an increased SNR in a link direction, and thus extending wireless range. The idea of an array of colocated antennas leads to the concept of massive MIMO (Larsson *et al.* 2014, Boccardi *et al.* 2014, Lu *et al.* 2014), that applies adaptive techniques such as phase shifting in two dimensions to radiate energy efficiently. Massive MIMO designs are however complex and do not offer a three dimensional aspect to beam control. In addition, the designs are unexploited above frequencies of 5 GHz and so their adaptation to mmWave frequencies is largely unknown. While it is possible to have tri-orthogonal polarisation diversity in a planar antenna operating at 5.9 GHz, as shown in the thesis, it would be advantageous to provide a solution operating at mmWave frequencies. The proposed design in this thesis is scalable over a range of operating frequencies, due to the symmetry and orthogonality of the design. An investigation into the physical limitations of higher operating frequencies on a tri-orthogonally polarisation diverse design in planar antenna form provides an interesting avenue of further research.

9.4.3 Circular Polarisation Operation in Any Link Direction

The ability for a planar antenna to provide three colocated orthogonally polarised radiation patterns which are not prone to mutual coupling effects provides an additional degree of freedom beyond that of conventional CP mode patch design. From a conventional design perspective that accounts for CP mode patch design, radiated energy that is circularly polarised is typically offered in a link direction orthogonal to the radiating surface of the antenna. Elliptical polarisation is offered as the link direction

deviates from this direction, eventually becoming linear polarisation as the link direction approaches a direction parallel to the antenna surface. The advantage of circular polarisation is that the electric field vector tip revolves around the direction of propagation, providing a component of a transmitted signal at the receiver regardless of receiver orientation in the direction of alignment. A component of the signal may always be received, unless the receive antenna is polarised in an opposing direction of circular polarisation. A tri-orthogonal polarisation diverse solution, which does not suffer from mutual coupling, may offer the possibility of circular polarisation in any link direction through pattern diversity and combination, or beamforming and beam steering techniques. Such operation is of increasing relevance in the next generation of communication technologies (Rappaport *et al.* 2013b, Tercero *et al.* 2016). Pattern diversity is possible through amplitude and phase modulation on each polarisation mode. By providing such operation, the advantages of circular polarisation may be possible in any link direction. Tri-orthogonal polarisation diversity could provide the option of increased link range and performance through beamforming, together with the advantage of circular polarisation, as required.

9.5 Part IV: Outlook

Within the context of mobile antenna link performance, and more specifically the next generation of mobile communications, this thesis sets out to demonstrate to the reader the attributes that tri-orthogonal polarisation diversity can offer to high rate communication in any link direction. From the initial work of Andrews *et al.* (2001), the concept has been demonstrated (Mtumbuka *et al.* 2005, Getu and Andersen 2005, Chiu *et al.* 2007b), but never as a fully implementable tool to increase link performance. Yet, there can be little doubt that the concept is relevant with regard to the next generation of communication technology that is required to deliver the high data rate ubiquitous services that the service subscriber is anticipating (Gubbi *et al.* 2013, Rappaport *et al.* 2013b, Larsson *et al.* 2014). The ability to beamform and beam steer radiated energy efficiently to maintain link performance regardless of antenna alignment and link direction is now extremely pertinent (Nam *et al.* 2013, Rangan *et al.* 2014, Roh *et al.* 2014, Razavizadeh *et al.* 2014, Rappaport *et al.* 2013a). Tri-orthogonal polarisation diversity offers one possible option, and the option is further extended through this thesis by relevant and achievable outcomes via modelling and practical design.

In general, with the many efforts and initiatives that are currently being implemented to augment mobile communication performance, the field of tri-orthogonal polarisation diversity looks set to have a promising future. The ongoing research into the next generation of communication systems, coupled with the provision to maintain link performance in all directions is likely to lead to technologies that incorporate tri-orthogonal polarisation diverse measures that can be used in real-world applications in the near future.

Appendix A

Fundamentals Relative to this Research

THIS appendix provides a brief description of the fundamental theory behind electromagnetic wave propagation, wave polarisation and antenna principles encountered in this thesis. It is written as a reference tool for the thesis, as the reader is assumed to have a basic understanding of the principles contained herein.

A.1 Maxwell's Equations

A.1.1 In Vacuo

For a region of space devoid of charges and currents, the equations of Maxwell are given as a set of coupled, first order, partial differential equations for the electrical vector **E** and magnetic vector **B**. These equations form the foundation of classical electromagnetics and are given in the following form (Pozar 2011),

$$\nabla \cdot \mathbf{E} = 0 \qquad \text{(Faraday's Law)} \tag{A.1}$$

$$\nabla \cdot \mathbf{B} = 0 \qquad \text{(Ampère's Law)} \tag{A.2}$$

$$\nabla \times \mathbf{E} = -\frac{\partial \mathbf{B}}{\partial t} \qquad \text{(Gauss' Law)} \tag{A.3}$$

$$\nabla \times \mathbf{B} = \mu_0 \epsilon_0 \frac{\partial \mathbf{E}}{\partial t} \qquad \text{(Coulomb's Law).} \tag{A.4}$$

Applying a curl operation to Equations (A.3) and (A.4) yields the following expressions respectively,

$$\nabla \times (\nabla \times \mathbf{E}) = \nabla(\nabla \cdot \mathbf{E}) - \nabla^2 \mathbf{E} = -\nabla \times \frac{\partial \mathbf{B}}{\partial t} = -\frac{\partial}{\partial t}(\nabla \times \mathbf{B}) = -\mu_0 \epsilon_0 \frac{\partial^2 \mathbf{E}}{\partial t^2} \tag{A.5}$$

$$\nabla \times (\nabla \times \mathbf{B}) = \nabla(\nabla \cdot \mathbf{B}) - \nabla^2 \mathbf{B} = \nabla \times \left(\mu_0 \epsilon_0 \frac{\partial \mathbf{E}}{\partial t}\right) = \mu_0 \epsilon_0 \frac{\partial}{\partial t}(\nabla \times \mathbf{E}) = -\mu_0 \epsilon_0 \frac{\partial^2 \mathbf{B}}{\partial t^2} \tag{A.6}$$

where the permittivity of free space, ϵ_0 and permeability of free space μ_0, are constants that are respectively found in Coulomb's law and the Biot-Savart law. Since $\nabla \cdot \mathbf{E} = \mathbf{0}$ and $\nabla \cdot \mathbf{B} = \mathbf{0}$, so these expressions reduce to,

$$\nabla^2 \mathbf{E} = \mu_0 \epsilon_0 \frac{\partial^2 \mathbf{E}}{\partial t^2} \tag{A.7}$$

and

$$\nabla^2 \mathbf{B} = \mu_0 \epsilon_0 \frac{\partial^2 \mathbf{B}}{\partial t^2}. \tag{A.8}$$

This process generates separate equations for **E** and **B**, which are of second order. In a vacuum, each Cartesian component of **E** and **B** satisfies a three dimensional wave equation, or,

$$\nabla^2 f = \mu_0 \epsilon_0 \frac{\partial^2 f}{\partial t^2}. \tag{A.9}$$

The solution of this equation is a wave. Maxwell's equations suggest that a vacuum supports the propagation of an electromagnetic wave, travelling with a velocity of light, c, or 3×10^8 ms^{-1}.

A.1.2 Monochromatic Plane Waves

For a light wave, which is an electromagnetic wave, different frequencies in the visible range correspond to different colours. Different frequencies correspond to different wavelengths of electromagnetic waves, and these waves may collectively be referred to as monochromatic waves. Electromagnetic waves, travelling in a direction that we shall refer to as z, with no x and y dependence, are known as plane waves. Plane waves are made of fields that are uniform over every plane orthogonal to the direction of propagation, z. The coexisting electric and magnetic fields of such plane waves assume the following form (Pozar 2011),

$$\mathbf{E}(z,t) = \mathbf{E}_0 \exp^{\mathrm{i}(kz-\omega t)} \tag{A.10}$$

$$\mathbf{B}(z,t) = \mathbf{B}_0 \exp^{\mathrm{i}(kz-\omega t)}. \tag{A.11}$$

The vectors $\mathbf{E}_0$ and $\mathbf{B}_0$ are the electrical and magnetic complex amplitudes of the propagating electromagnetic wave. Through substitution of Equations (A.10) and (A.11) into Equations (A.7) and (A.8), we are led to,

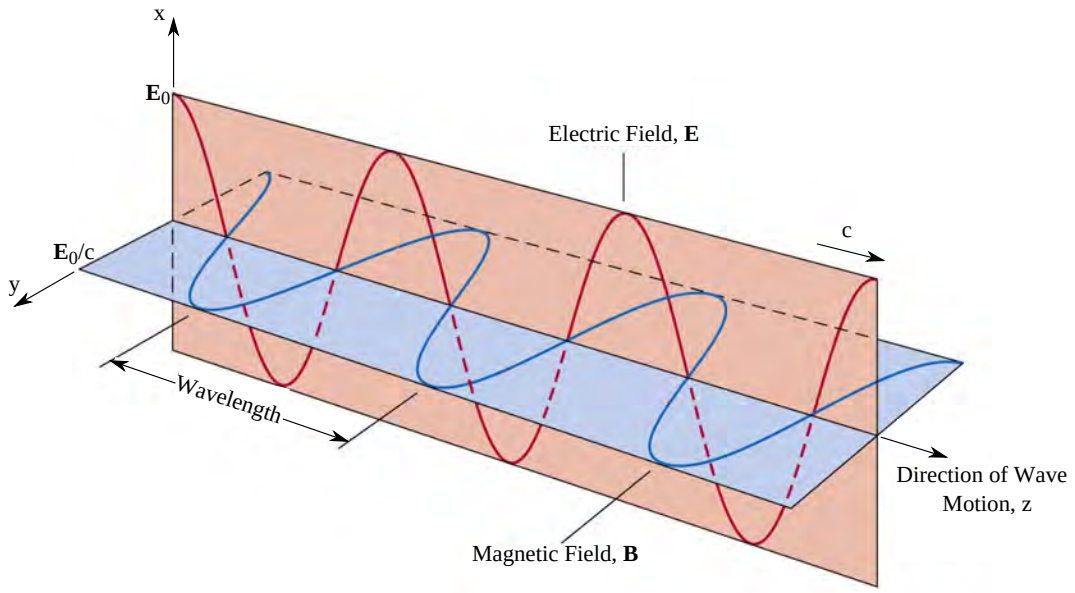

Figure A.1. An electromagnetic wave consists of a sinusoidal electric field distribution and associated sinusoidal magnetic field distribution. In this image, the electric field represented by the red wave, and the magnetic field represented by the blue wave, are orthogonal to each other and in phase with each other, and are both orthogonal to the direction of propagation. Adapted from Nanjing University (Accessed: 2016).

$$c = \frac{\omega}{k} \tag{A.12}$$

where c is the velocity of light and ω is the angular frequency of the electromagnetic wave. The wavenumber k is related to the wavelength of the wave by Equation (A.13),

$$\lambda = \frac{2\pi}{k}. \tag{A.13}$$

Classically, the direction of $\mathbf{E}$ is used to specify the polarisation of the electromagnetic wave. In empty space, the wave equations for $\mathbf{E}$ and $\mathbf{B}$ are derived from Maxwell's equations. Indeed, the wave equation must be obeyed by every solution to Maxwell's equations in empty space. Since $\nabla \cdot \mathbf{E} = 0$ and $\nabla \cdot \mathbf{B} = 0$, it follows that $E_{0z} = B_{0z} = 0$.

In other words, electromagnetic waves are transverse in nature. The electric and magnetic fields are orthogonal to the direction of propagation, as shown in Figure A.1. Equation (A.1), or Faraday's law, implies a relation between the dielectric and magnetic amplitudes. In compact form, this relationship may be given as,

$$\mathbf{B}_0 = \frac{k}{\omega}(\hat{\mathbf{z}} \times \mathbf{E}_0) = \frac{1}{c}(\hat{\mathbf{z}} \times \mathbf{E}_0). \tag{A.14}$$

The electric and magnetic vectors, **E** and **B**, are in phase and are orthogonal. We may introduce a wave vector, **k**, pointing in the direction of propagation z, with a magnitude equal to the wave number k. The scalar product $\mathbf{k} \cdot \mathbf{r}$, where **r** is a radial vector, is the appropriate generalisation of kz where,

$$\mathbf{E}(\mathbf{r}, t) = E_0 \mathbf{e} \exp^{\mathrm{i}(\mathbf{k}\cdot\mathbf{r}-\omega t)} \tag{A.15}$$

$$\mathbf{B}(\mathbf{r}, t) = \frac{1}{c} E_0(\mathbf{n} \times \mathbf{e}) \exp^{\mathrm{i}(\mathbf{k}\cdot\mathbf{r}-\omega t)} = \frac{1}{c}(\mathbf{n} \times \mathbf{E}) \tag{A.16}$$

The vector **n** is a unit vector in the direction of propagation, where $\mathbf{n} = \frac{\mathbf{k}}{k}$. The polarisation vector is given as **e**. As **E** is transverse, so $\mathbf{n} \cdot \mathbf{e}$=0.

A.1.3 Linear, Circular and Elliptical Polarisation

The plane wave with components given in Equations (A.15) and (A.16) is a wave with its electric field vector in the direction **e**. A wave of this nature is said to be linearly polarised and possess a polarisation vector $\mathbf{e}_1 = \mathbf{e}$.

We introduce a second linearly polarised wave with a polarisation vector $\mathbf{e}_2 \neq \mathbf{e}_1$. This wave is linearly independent of the first. As a consequence, we may write the two waves as (Orfanidis 2002, Pozar 2011),

$$\mathbf{E}_1(\mathbf{r}, t) = E_1 \mathbf{e}_1 \exp^{\mathrm{i}(\mathbf{k}\cdot\mathbf{r}-\omega t)} \tag{A.17}$$

and

$$\mathbf{E}_2(\mathbf{r}, t) = E_2 \mathbf{e}_2 \exp^{\mathrm{i}(\mathbf{k}\cdot\mathbf{r}-\omega t)}. \tag{A.18}$$

Coexisting magnetic waves may be given in the form,

$$\mathbf{B}_{1,2} = \frac{1}{c}(\mathbf{n} \times \mathbf{E}_{1,2}) \tag{A.19}$$

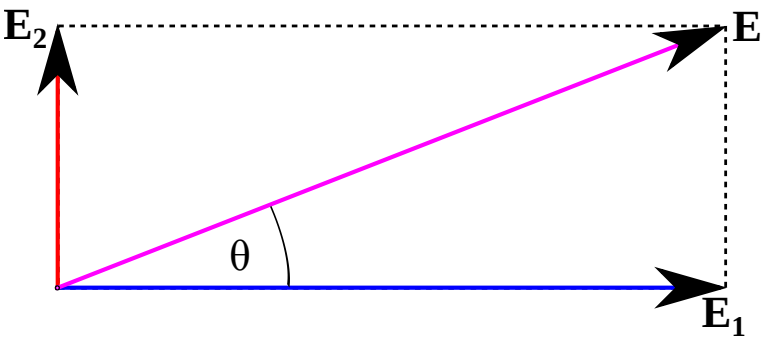

Figure A.2. The direction of polarisation of an electromagnetic wave is described according to the electric field vector. Two linearly polarised electric fields, described respectively by electric field vectors $\mathbf{E}_1$ and $\mathbf{E}_2$, that are in phase with each other and are travelling in the same direction of propagation, combine to form a resultant linearly polarised electric field distribution shown here by the electric field vector $\mathbf{E}$, or the magenta line. The resultant electric field vector may be described according to the angle theta between the resultant electric field vector $\mathbf{E}$ and the electric vector $\mathbf{E}_1$.

The two waves may be combined to provide a plane wave in general form propagating in the direction of $\mathbf{k} = k\mathbf{n}$,

$$\mathbf{E}(\mathbf{r},t) = \mathbf{E}_1(\mathbf{r},t) + \mathbf{E}_2(\mathbf{r},t) = (E_1\mathbf{e}_1 + E_2\mathbf{e}_2)\exp^{\mathrm{i}(\mathbf{k}\cdot\mathbf{r}-\omega t)}. \tag{A.20}$$

The amplitudes E_1 and E_2 are complex numbers, allowing the possibility of a phase difference between waves of different linear polarisation. Alternatively, a phase difference may be represented by an additional term in the complex exponent of one of the propagating waves. Three possibilities of plane wave exist:

- If E_1 and E_2 have the same phase then Equation (A.20) represents a wavefront demonstrating **linear polarisation**, as shown in Figure A.2. The polarisation vector of the resultant waveform is given by $\tan\theta = E_2/E_1$ with respect to $\mathbf{e}_1$, with a magnitude of $\sqrt{{E_2}^2 + {E_1}^2}$.

- If a 90° phase exists between E_1 and E_2, which are of the same magnitude, then Equation (A.20) represents a wavefront exhibiting **circular polarisation** of the form,

$$\mathbf{E}(\mathbf{r},t) = \mathbf{E}_1(\mathbf{r},t) + \mathbf{E}_2(\mathbf{r},t) = E_0(\mathbf{e}_1 \pm \mathrm{i}\mathbf{e}_2)\exp^{\mathrm{i}(\mathbf{k}\cdot\mathbf{r}-\omega t)} \tag{A.21}$$

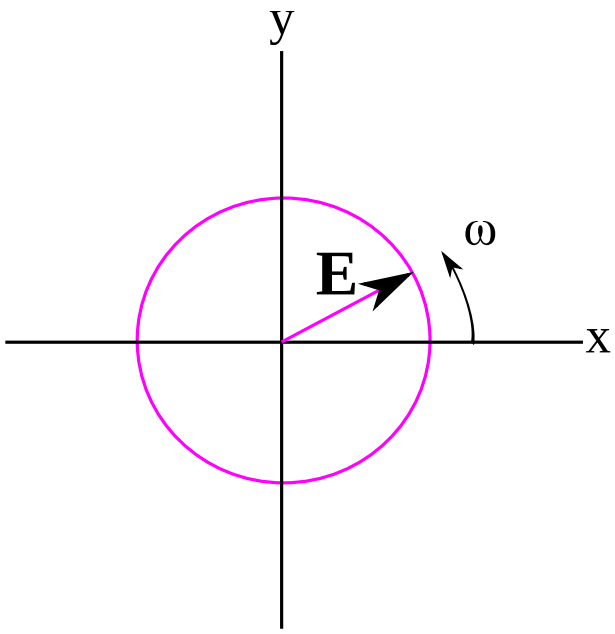

Figure A.3. Circular polarisation. Providing a relative phase difference of 90° between two orthogonal linearly polarised electric field distributions of the same magnitude, and travelling in the same direction of propagation, results in a circularly polarised electric field vector. The resultant wave polarisation, shown here by the magenta line, is observed to rotate with angular frequency ω about a fixed point as it propagates through a medium. The sense of rotation is dictated by the advancement or retardation of one of the linearly polarised electric field distributions with respect to the other.

with E_0 the common real amplitude. We imagine axes chosen so that the wave is propagating in the positive z direction, while $\mathbf{e}_1$ and $\mathbf{e}_2$ are in the x and y directions, respectively. By taking the real part of Equation (A.21), the components of the electric field are,

$$E_x(\mathbf{r},t) = \mathbf{E}_0 \cos(kz - \omega t) \tag{A.22}$$

and

$$E_y(\mathbf{r},t) = \mp \mathbf{E}_0 \sin(kz - \omega t). \tag{A.23}$$

At a given fixed point in space, the fields of Equations (A.22) and (A.23) provide a resultant electric vector with constant magnitude, sweeping around in a circle at an angular frequency ω, as shown in Figure A.3.

For the upper sign of Equation (A.21), the rotation is counterclockwise for an observer facing into the oncoming wave. The wave is deemed to be right-hand circularly polarised in antenna design. Conversely, for the lower sign in Equation (A.21), the rotation is clockwise, and so the wave is deemed to be left-hand circularly polarised.

- Two counter-rotating circularly polarised waves may form an equally acceptable basis for describing a general state of polarisation, known as **elliptical polarisation**, of which several cases may be observed in Figure A.4. Vertical linear polarisation is described by counter-rotating circularly polarised waves experiencing no relative phase shift between them, as shown in Figure A.4 (d). As a relative phase shift is introduced between the counter-rotating electric vector tips, so linear polarisation veers away from the vertical, becoming horizontal with a 180° relative phase shift. This is shown in Figure A.6.

  Using two counter-rotating circularly polarised waves, we may represent Equation (A.20) for a general state of polarisation through the introduction of complex orthogonal unit vectors,

$$\mathbf{e}_{\pm} = \frac{1}{\sqrt{2}}(\mathbf{e}_1 \pm i\mathbf{e}_2) \tag{A.24}$$

  to give,

$$\mathbf{E}(\mathbf{r}, t) = (E_{+}\mathbf{e}_{+} + E_{-}\mathbf{e}_{-}) \exp^{\mathrm{i}(\mathbf{k}\cdot\mathbf{r}-\omega t)}. \tag{A.25}$$

  In Equation (A.25), E_+ and E_- are complex amplitudes. If E_+ and E_- have different magnitudes, but the same phase, so Equation (A.25) represents an elliptically polarised wave with principal axes of the ellipse in the directions of $\mathbf{e}_1$ and $\mathbf{e}_2$, as shown in Figure A.4 (e). The ratio of semimajor to semiminor axis is $|(1+r)/(1-r)|$, where $r = E_-/E_+$. With a relative phase difference between the amplitudes, $E_-/E_+ = re^{\mathrm{i}\alpha}$, and the ellipse traced out by the vector has its axes rotated by an angle $(\alpha/2)$, as shown in Figure A.4 (f). A linearly polarised wave is obtained when $r = \pm 1$.

  By cycling the relative phase of two orthogonal linear polarised waves of identical magnitude, we may produce the elliptical polarisations observed in Figure A.5.

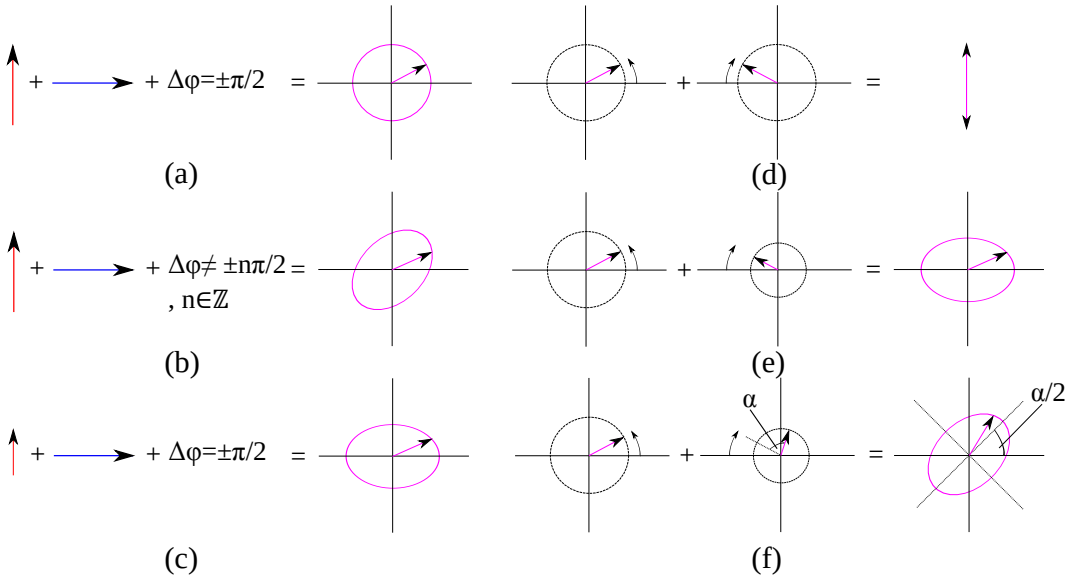

Figure A.4. Linear and circular polarisations are the extreme forms of the more general case of elliptical polarisation. The cases of elliptical polarisation are most simply understood when two orthogonal linearly polarised waves travelling in the same direction of propagation towards the observer combine with: (a) identical magnitudes and a phase difference of 90° to produce circular polarisation, (b) identical magnitudes and a phase difference that is non-zero and that is not a multiple of 90° to produce elliptical polarisation with 45° rotated semi-major and semi-minor axes, (c) a 90° phase difference but non-identical magnitudes to produce elliptical polarisation. Cases of elliptical polarisation may also be demonstrated by two counter rotating circularly polarised electric field vectors with: (d) identical phase and identical magnitudes to produce linear polarisation, (e) identical phases and non-identical magnitudes to produce elliptical polarisation, (f) the introduction of non-identical phases to (e) causing the axes of the ellipse to be rotated by an angle ($\alpha/2$), where the angle α represents the relative phase difference between the counter rotating electric field vectors.

In Figure A.7, various forms of linear, circular and elliptical polarisation are shown using combinations of linearly polarised waves travelling towards the observer. From observation of Figures A.4, A.5, A.6, and A.7, the interconnection of linear, circular, and elliptical polarisation is evident.

A.1.4 Electromagnetic Waves in Matter

In regions of matter devoid of free charges and free currents, Maxwell's equations become,

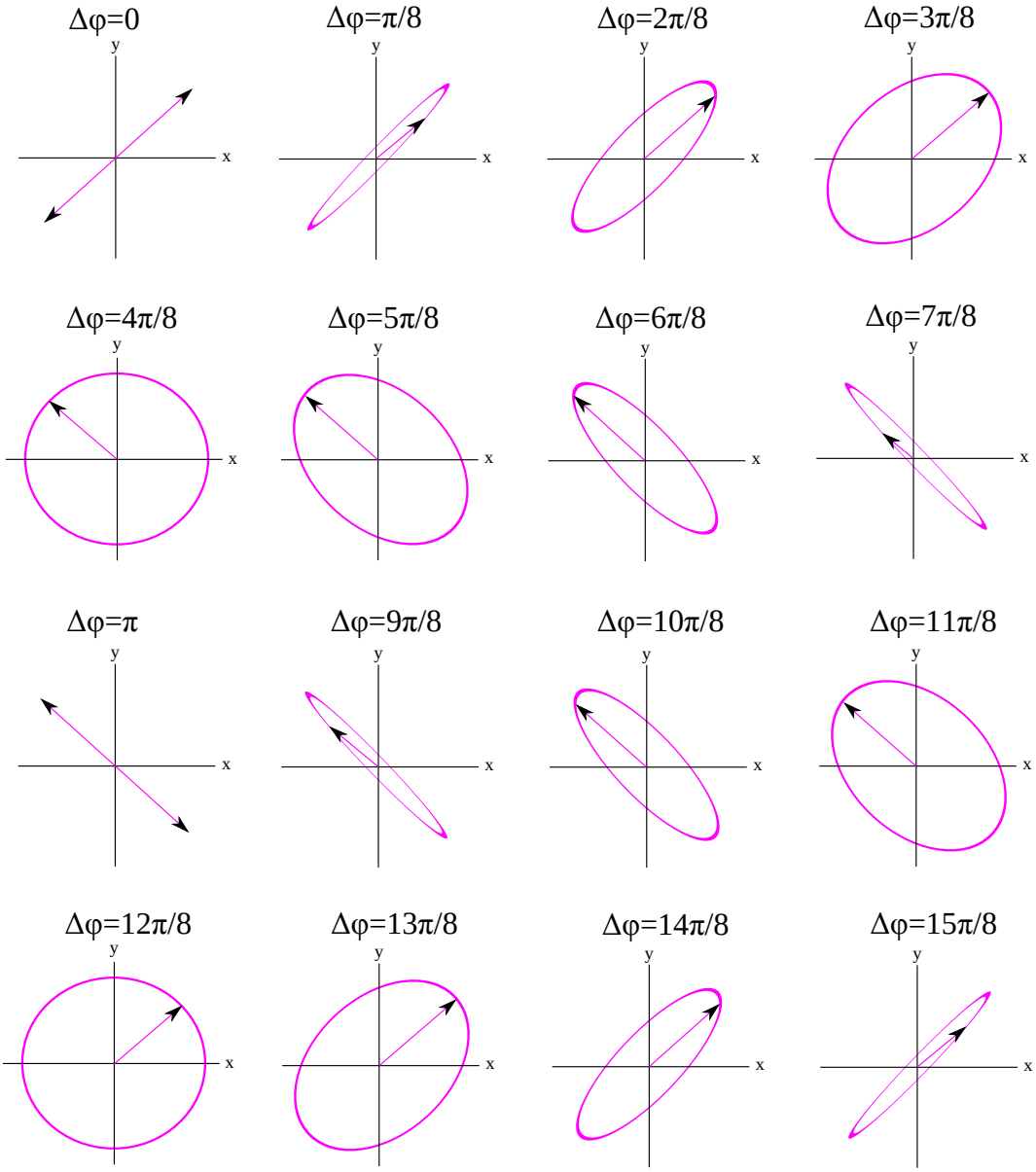

Figure A.5. The effect of relative phase on two orthogonal polarisation modes. By combining a vertically polarised electric field distribution with a horizontally polarised electric field distribution, of identical magnitude and both travelling in the same direction of propagation towards the observer, it is possible to cycle through resultant wave linear, elliptical and circular polarisations by altering the relative phase difference between the two waves. In this diagram, increments of $\pi/8$ radians are sequentially added to this relative phase difference, providing the cycling of resultant wave polarisations indicated. The ellipse axes are rotated by 45°, due to the identical magnitude of the vertically polarised and horizontally polarised electric field distributions.

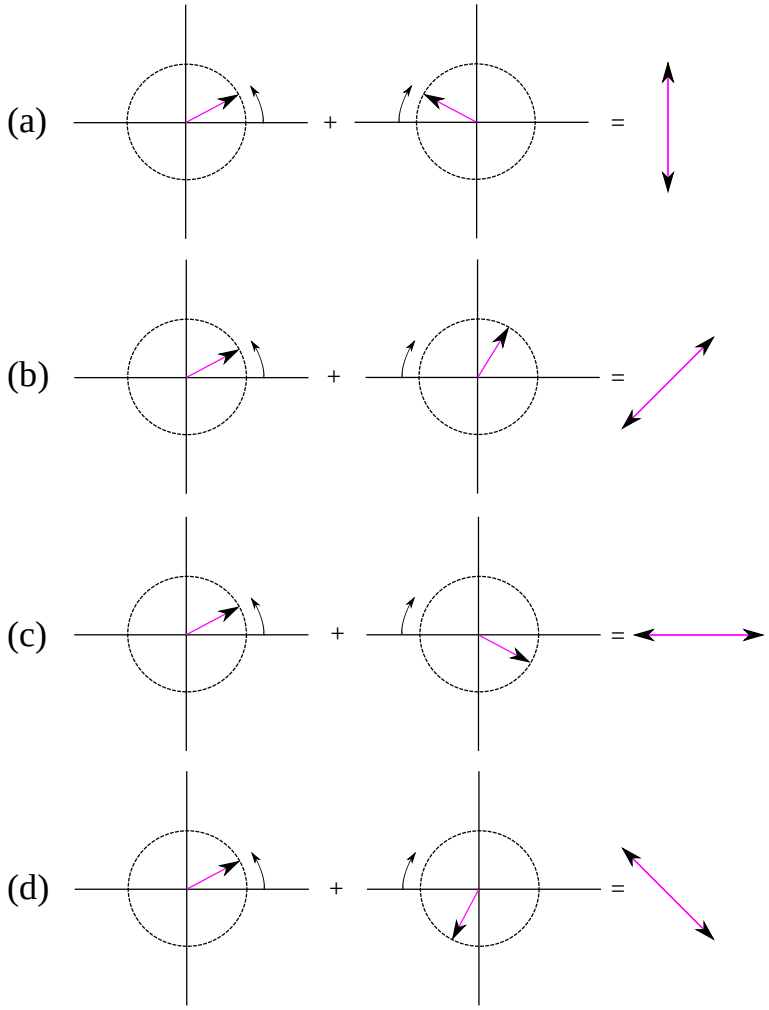

Figure A.6. Resultant polarisation through circular polarisation combination. Two counter-rotating circularly polarised electric field vectors of the same magnitude travelling in the same direction of propagation towards the observer may combine to form each of the four specific cases shown. The cases are: (a) relative phase difference of 0° results in a vertically polarised electric field distribution, (b) relative phase difference of 90° results in a slant polarised electric field distribution, (c) relative phase difference of 180° results in a horizontally polarised electric field distribution, (d) relative phase difference of 270° results in a slant polarised electric field distribution that is 90° rotated about the direction of propagation in relation to (b).

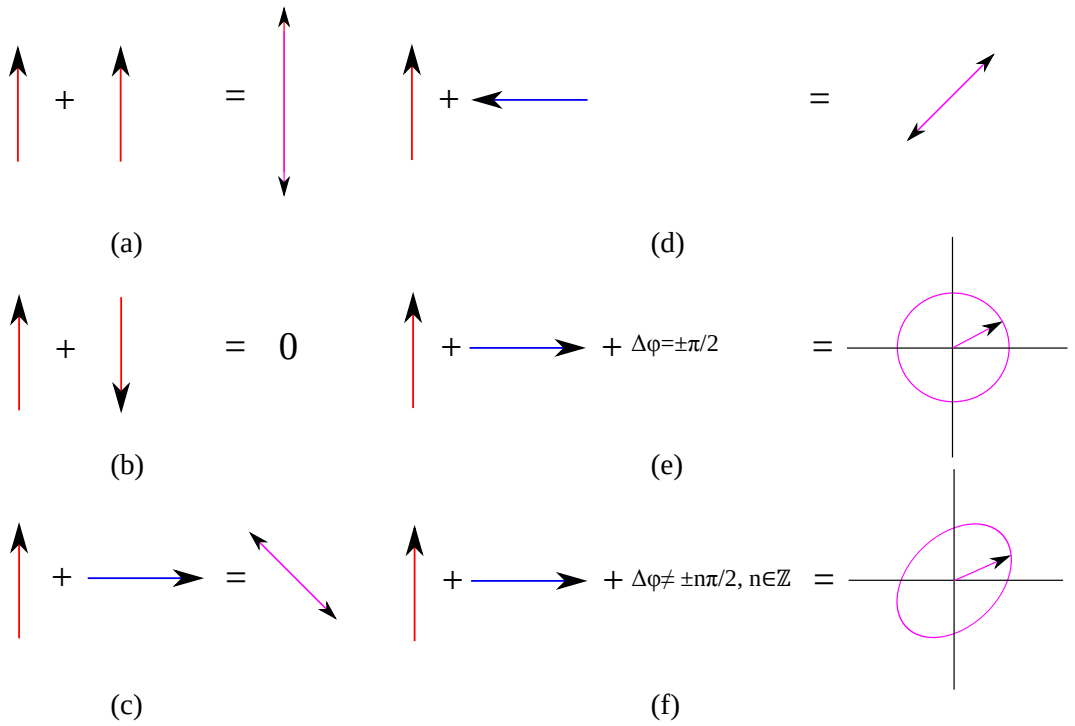

Figure A.7. Resultant polarisation through linear polarisation combination. Presented are general forms of polarisation resulting from the combination of two linearly polarised electric field distributions of identical magnitude travelling in the same direction of propagation towards the observer. Images shown are: (a) two vertically polarised in-phase electric vectors combine to form a vertically polarised electric field vector, (b) two vertically polarised electric vectors in anti-phase combine to form no electric field distribution, (c) vertically polarised and horizontally polarised electric field vectors that are in phase combine to form a slant polarised electric field vector, (d) vertically polarised and horizontally polarised electric field vectors that are in anti-phase combine to form a slant polarised electric field vector that is 90° rotated about the direction of propagation in relation to (c), (e) vertically polarised and horizontally polarised electric field vectors with a relative phase difference of 90° between them combine to form a circularly polarised electric field vector, (f) vertically polarised and horizontally polarised electric field vectors with a relative phase difference between them that is non-zero and that is not a multiple of 90° combine to form an elliptically polarised electric field vector with 45° rotated semi-major and semi-minor axes.

$$\nabla \cdot \mathbf{D} = 0 \qquad \text{(Faraday's Law)} \tag{A.26}$$

$$\nabla \cdot \mathbf{B} = 0 \qquad \text{(Ampère's Law)} \tag{A.27}$$

$$\nabla \times \mathbf{E} = -\frac{\partial \mathbf{B}}{\partial t} \qquad \text{(Gauss' Law)} \tag{A.28}$$

$$\nabla \times \mathbf{H} = \frac{\partial \mathbf{D}}{\partial t} \qquad \text{(Coulomb's Law) .} \tag{A.29}$$

For linear matter, $\mathbf{D} = \epsilon\mathbf{E}$ and $\mathbf{H} = \frac{1}{\mu}\mathbf{B}$. If the matter is also homogenous, then Maxwell's equations reduce to (Pozar 2011),

$$\nabla \cdot \mathbf{E} = 0 \qquad \text{(Faraday's Law)} \tag{A.30}$$

$$\nabla \cdot \mathbf{B} = 0 \qquad \text{(Ampère's Law)} \tag{A.31}$$

$$\nabla \times \mathbf{E} = -\frac{\partial \mathbf{B}}{\partial t} \qquad \text{(Gauss' Law)} \tag{A.32}$$

$$\nabla \times \mathbf{B} = \mu\epsilon\frac{\partial \mathbf{E}}{\partial t} \qquad \text{(Coulomb's Law).} \tag{A.33}$$

In effect, the difference between electromagnetic waves propagating in a linear homogenous medium and those propagating in a vacuum is the inclusion of relative permittivity and permeability into Coulomb's law in the former case. Through a linear homogenous medium, electromagnetic waves travel with a velocity,

$$v = \frac{1}{\sqrt{\mu\epsilon}} = \frac{c}{n} \tag{A.34}$$

where

$$n = \sqrt{\frac{\mu\epsilon}{\mu_0\epsilon_0}} \tag{A.35}$$

is the index of refraction. In the case of most non-ferromagnetic materials, μ is very close to μ_0. As a result of this, we may say that $n \approx \sqrt{\epsilon_r}$, where ϵ_r is the dielectric constant of the medium.

A.2 Transmitting and Receiving Antennas

A.2.1 Effective Area of an Antenna

In the model employed in this thesis, we consider linear antennas. The effective area of a linear antenna is not equal to the physical antenna area. This is in contrast to dish or horn antennas, where the effective area is typically 55–65% of the physical area for the former and 60–80% for the latter. Antennas typically fall into two classes: (i) fixed-gain antennas such as linear antennas where gain G is independent of frequency and (ii) fixed-area antennas where gain G increases quadratically with frequency f. In this thesis, our model primarily considers a half-wavelength dipole antenna, which is a linear antenna with a maximum gain given as 1.64, this being in a direction of propagation orthogonal to the dipole (Balanis 2005).

A.2.2 Antenna Noise Temperature

The received signal from a non-geosynchronous satellite is extremely weak due to the large free space path loss that it experiences during propagation. This loss is typically of the order of 150 dB or more, resulting in a received signal being of the order of pi-cowatts. Detection of such a weak signal requires the receiving system to maintain a noise level lower than the received signal. Several sources may introduce noise into the receiving system. As well as the desired signal, the receiving antenna may pick up noisy signals from the several sources including the sky, the weather, the ground, as

well as other natural or man-made noise sources. Noise signals, impingent on the receiver from various directions, may be weighted according to the antenna gain. From this weighting, a weighted average noise power for the receiver at the output terminals of the antenna may be calculated. As an example, for an antenna pointing in the zenith direction, noise will be picked up through its sidelobes due to thermal noise and reflected signals from the ground. Ohmic losses in the antenna provide an additional noise source. Any antenna output that propagates in a lossy feed line, such as a transmission line or waveguide, before arriving at the receiver circuits is attenuated by the feed line. In addition, the feed line will introduce additional thermal noise.

From the feed line, the output is then passed into a LNA, pre-amplifying the signal and introducing only a limited amount of thermal noise. Indeed, a critical property of the receiving system is the low-noise nature of the LNA. From the LNA, the output signal is then passed to system downconverters, IF amplifiers, and bandpass filters. These subsystems all introduce their own gain and thermal noise factors. Collectively, the system provides a cascade of receiver components. Receiver system performance can only be guaranteed by maintaining the sum total of all the noises introduced by these components at acceptably low levels, relative to the amplified desired signal. For a receiver system operating with a bandwidth of B Hz, the average power P_{N} (in Watts) of a noise source is given by means of an equivalent temperature T. The average power is defined as,

$$P_{\mathrm{N}} = kTB \tag{A.36}$$

where k is the Boltzmanns constant = 1.3803×10^{-23} W/Hz·K and T is in degrees Kelvin (Pozar 2011). A convenient way to express the noise power is through the temperature T. This temperature does not have to equal the physical temperature of the source. However, this temperature T is indeed the physical temperature for a thermal source.

A.3 Effective Length and Polarisation Mismatch

For an antenna, the polarisation properties of an electric field $\mathbf{E}$ depend on the transverse component of a radiation vector $\mathbf{F}_{\perp}$ where,

$$\mathbf{E} = -jk\eta \frac{e^{-jkr}}{4\pi r}\mathbf{F}_{\perp} = -jk\eta \frac{e^{-jkr}}{4\pi r}(F_{\theta}\hat{\boldsymbol{\theta}} + F_{\phi}\hat{\boldsymbol{\phi}}). \tag{A.37}$$

A.3 Effective Length and Polarisation Mismatch

An effective length vector $\mathbf{h}$ of an antenna may be defined in terms of the radiation vector $\mathbf{F}_\perp$, and the input current I_{in} to the terminals of an antenna,

$$\mathbf{h} = -\frac{\mathbf{F}_\perp}{I_{\text{in}}}. \tag{A.38}$$

In general, $\mathbf{h}$ is a function of (θ,ϕ). The electric field $\mathbf{E}$ may then be written as (Orfanidis 2002, Balanis 2005),

$$\mathbf{E} = -jk\eta \frac{e^{-jkr}}{4\pi r} I_{\text{in}}\mathbf{h}. \tag{A.39}$$

Motivation for the definition of $\mathbf{h}$ is provided by the case of a vertical Hertzian dipole antenna, which is shown to have $\mathbf{h} = I\sin\theta\hat{\boldsymbol{\theta}}$. As a consequence of the reciprocity principle, the open circuit voltage V at the terminals of a receiving antenna may be given in terms of the incident electric field $\mathbf{E}_i$ and the effective length $\mathbf{h}$ by,

$$V = \mathbf{E}_i \cdot \mathbf{h}. \tag{A.40}$$

The normal definition of the effective area A of an antenna and the resulting power gain $G = 4\pi A/\lambda^2$, where λ is the operating wavelength, depend on idealised assumptions. These assumptions are that a conjugate-match exists between the receive antenna and its load, as well as the antenna polarisation matching that of the incident wave.

Characterisation of the degree of polarisation mismatch that may exist between the incident field and the antenna is assisted by the effective length, ultimately leading to a modified area-gain relationship.

Polarisation and load mismatch factors may be defined by,

$$e_{\text{pol}} = \frac{|\mathbf{E}_i \cdot \mathbf{h}|^2}{|\mathbf{E}_i|^2|\mathbf{h}|^2}. \tag{A.41}$$

$$e_{\text{load}} = \frac{4R_{\text{L}}R_{\text{A}}}{|Z_{\text{L}} + Z_{\text{A}}|^2} = 1 - |\Gamma_{\text{load}}|^2 \tag{A.42}$$

where

$$\Gamma_{\text{load}} = \frac{Z_{\text{L}} - Z_{\text{A}}^*}{Z_{\text{L}} + Z_{\text{A}}}. \tag{A.43}$$

We include the load mismatch factor for completeness. In the thesis, the load mismatch factor is set to unity.

The effective area may then be written as,

$$A(\theta,\phi) = \frac{\eta|\mathbf{h}|^2}{4R_{\mathrm{A}}} e_{\mathrm{load}} e_{\mathrm{pol}}. \tag{A.44}$$

Finally, we may give the modified gain-area relationship as Equation (A.45),

$$A(\theta,\phi) = e_{\mathrm{load}} e_{\mathrm{pol}} \frac{\lambda^2}{4\pi} G(\theta,\phi) \tag{A.45}$$

where G is the power gain of the antenna under scrutiny, and λ is the operating wavelength. The assumption is made that the incident field originates at some antenna with its own effective length $\mathbf{h}_i$. By making this assumption, $\mathbf{E}_i$ will be proportional to $\mathbf{h}_i$, and hence the polarisation mismatch factor may be written as,

$$e_{\mathrm{pol}} = \frac{|\mathbf{h}_i \cdot \mathbf{h}|^2}{|\mathbf{h}_i|^2|\mathbf{h}|^2} = |\hat{\mathbf{h}}_i \cdot \hat{\mathbf{h}}|^2 \tag{A.46}$$

where

$$\hat{\mathbf{h}}_i = \frac{\mathbf{h}_i}{|\mathbf{h}_i|} \tag{A.47}$$

and

$$\hat{\mathbf{h}} = \frac{\mathbf{h}}{|\mathbf{h}|}. \tag{A.48}$$

For a load that is conjugate-matched, we have $e_{\mathrm{load}} = 1$. For an incident field that has matching polarisation with the antenna, or $\mathbf{h}_i = \mathbf{h}^*$, then $e_{\mathrm{pol}} = 1$. In this thesis, we assume the load to be conjugate-matched. We examine the mitigation of polarisation mismatch through tri-orthogonal polarisation diversity.

Bibliography

ABADI-S. M. A. M. H., AND BEHDAD-N. (2014). An electrically small, vertically polarized ultrawideband antenna with monopole-like radiation characteristics, *IEEE Antennas and Wireless Propagation Letters*, **13**, pp. 742–745.

ABOVE GROUND LEVEL MEDIA GROUP. (Accessed: 2015). FCC looks ever higher for spectrum to meet 5G wireless demand. Available at: http://www.aglmediagroup.com/fcc-looks-ever-higher-for-spectrum-to-meet-5g-wireless-demand/.

ADAMIUK-G., BEER-S., WIESBECK-W., AND ZWICK-T. (2009a). Dual-orthogonal polarized antenna for UWB-IR technology, *IEEE Antennas and Wireless Propagation Letters*, **8**, pp. 981–984.

ADAMIUK-G., WIESBECK-W., AND ZWICK-T. (2009b). Differential feeding as a concept for the realization of broadband dual-polarized antennas with very high polarization purity, *IEEE Antennas and Propagation Society International Symposium (APSURSI)*. DOI: 10.1109/APS.2009.5172047.

ADHIKARI-P. (2008). Understanding millimeter wave wireless communication, *Loea Corporation*. Available at: http://www.loeacom.com/pdf%20files/L1104-WP_Understanding%20MMWCom.pdf.

ADVE-R. (Accessed: 2013). Receive diversity. Available at: http://www.comm.toronto.edu/~rsadve/Notes/DiversityReceive.pdf.

AFRAIMOVICH-E. L., ASTAFYEVA-E. I., DEMYANOV-V. V., EDEMSKIY-I. K., GAVRILYUK-N. S., ISHIN-A. B., KOSOGOROV-E. A., LEONOVICH-L. A., LESYUTA-O. S., PALAMARTCHOUK-K. S., PEREVALOVA-N. P., POLYAKOVA-A. S., SMOLKOV-G. Y., VOEYKOV-S. V., YASYUKEVICH-Y. V., AND ZHIVETIEV-I. V. (2013). A review of GPS/GLONASS studies of the ionospheric response to natural and anthropogenic processes and phenomena, *Journal of Space Weather and Space Climate*. DOI: 10.1051/swsc/2013049.

ALI-I., AL-DHAHIR-N., AND HERSHEY-J. E. (1998). Doppler characterization for LEO satellites, *IEEE Transactions on Communications*, **46**(3), pp. 309–313.

ALI-I., BONANNI-P., AL-DHAHIR-N., AND HERSHEY-J. (2006). *Doppler Applications in LEO Satellite Communication Systems*, The Springer International Series in Engineering and Computer Science, Springer (US).

ALKHATEEB-A., MO-J., GONZALEZ-PRELCIC-N., AND HEATH-R. W. (2014). MIMO precoding and combining solutions for millimeter-wave systems, *IEEE Communications Magazine*, **52**(12), pp. 122–131.

AL-ZOUBI-A., YANG-F., AND KISHK-A. (2009). A broadband center-fed circular patch-ring antenna with a monopole like radiation pattern, *IEEE Transactions on Antennas and Propagation*, **57**(3), pp. 789–792.

ANDREWS-M. R., MITRA-P. P., AND DE CARVALHO-R. (2001). Tripling the capacity of wireless communications using electromagnetic polarization, *Nature*, **409**, pp. 316–318. DOI: 10.1038/35053015.

ANREDDY-V., AND INGRAM-M. (2006). Capacity of measured Ricean and Rayleigh indoor MIMO channels at 2.4 GHz with polarization and spatial diversity, *IEEE Wireless Communications and Networking Conference*. DOI: 10.1109/WCNC.2006.1683597.

ANTCOM CORPORATION. (Accessed: 2016). Combined Inmarsat/Iridium/GPS Thuraya antennas for ground and airborne applications. Available at: http://www.antcom.com/documents/catalogs/CombinedL-Band_Inmarsat_Thuraya_IridiumandGPSAntennas.pdf.

ANTENNA RESEARCH ASSOCIATES. (Accessed: 2016). Orbcomm antennas. Available at: http://www.ic72.com/pdf_file/a/187619.pdf.

ARAPOGLOU-P., BURZIGOTTI-P., BERTINELLI-M., BOLEA ALAMANAC-A., AND DE GAUDENZI-R. (2011a). To MIMO or not to MIMO in mobile satellite broadcasting systems, *IEEE Transactions on Wireless Communications*, **10**(9), pp. 2807–2811.

ARAPOGLOU-P. D., BURZIGOTTI-P., ALAMANAC-A. B., AND DE GAUDENZI-R. (2010a). Capacity potential of mobile satellite broadcasting systems employing dual polarization per beam, *Advanced Satellite Multimedia Systems Conference (ASMA) and the Signal Processing for Space Communications Workshop (SPSC)*. DOI: 10.1109/ASMS-SPSC.2010.5586911.

ARAPOGLOU-P.-D., BURZIGOTTI-P., ALAMANAC-A. B., AND GAUDENZI-R. D. (2012). Practical MIMO aspects in dual polarization per beam mobile satellite broadcasting, *International Journal of Satellite Communications and Networking*, **30**(2), pp. 76–87. DOI: 10.1002/sat.1008.

ARAPOGLOU-P.-D., ZAMKOTSIAN-M., AND COTTIS-P. (2010b). Dual polarization MIMO in LMS broadcasting systems: Possible benefits and challenges, *International Journal of Satellite Communications and Networking*, **29**(4), pp. 349–366. DOI: 10.1002/sat.986.

ARAPOGLOU-P., LIOLIS-K., BERTINELLI-M., PANAGOPOULOS-A., COTTIS-P., AND DE GAUDENZI-R. (2011b). MIMO over satellite: A review, *IEEE Communications Surveys Tutorials*, **13**(1), pp. 27–51.

ARAUJO-PRADERE-E. A., FULLER-ROWELL-T. J., SPENCER-P. S. J., AND MINTER-C. F. (2007). Differential validation of the US-TEC model, *Radio Science*. DOI: 10.1029/2006RS003459.

ASHTON-K. (2009). That internet of things thing, *RFiD Journal*, **22**(7), pp. 97–114.

ATZORI-L., IERA-A., AND MORABITO-G. (2010). The internet of things: A survey, *Computer Networks*, **54**(15), pp. 2787–2805.

BALANIS-C. A. (2005). *Antenna Theory: Analysis and Design*, Wiley-Interscience.

BARBA-M. (2008). A high-isolation, wideband and dual-linear polarization patch antenna, *IEEE Transactions on Antennas and Propagation*, **56**(5), pp. 1472–1476.

BASU-S., AND KELLEY-M. C. (2008). A review of recent observations of equatorial scintillations and their relationship to current theories of F region irregularity generation, *Radio Science*, **14**(3), pp. 471–485.

BETZ-J. (2015). *Engineering Satellite-Based Navigation and Timing: Global Navigation Satellite Systems, Signals, and Receivers*, Wiley-IEEE Press.

BIDAINE-B., AND WARNANT-R. (2010). Assessment of the NeQuick model at mid-latitudes using GNSS TEC and ionosonde data, *Advances in Space Research*, **45**(9), pp. 1122–1128. Special Issue: Recent Advances in Space Weather Monitoring, Modelling, and Forecasting.

BILITZA-D. (2001). International reference ionosphere 2000, *Radio Science*, **36**(2), pp. 261–275.

BISWAS-S., TATCHIKOU-R., AND DION-F. (2006). Vehicle-to-vehicle wireless communication protocols for enhancing highway traffic safety, *IEEE Communications Magazine*, **44**(1), pp. 74–82.

BLANCH-S., ROMEU-J., AND CORBELLA-I. (2003). Exact representation of antenna system diversity performance from input parameter description, *Electronics Letters*, **39**(9), pp. 705–707.

BOCCARDI-F., HEATH-R. W., LOZANO-A., MARZETTA-T. L., AND POPOVSKI-P. (2014). Five disruptive technology directions for 5G, *IEEE Communications Magazine*, **52**(2), pp. 74–80.

BOHAGEN-F., ORTEN-P., AND OIEN-G. E. (2005). Construction and capacity analysis of high-rank line-of-sight MIMO channels, *IEEE Wireless Communications and Networking Conference*. DOI: 10.1109/WCNC.2005.1424539.

BOIARDT-H., AND RODRIGUEZ-C. (2010). Low earth orbit nanosatellite communications using Iridium's network, *IEEE Aerospace and Electronic Systems Magazine*, **25**(9), pp. 35–39.

BOOKER-H. G. (1949). Application of the magneto-ionic theory to radio waves incident obliquely upon a horizontally-stratified ionosphere, *Journal of Geophysical Research*, **54**(3), pp. 243–274.

BRAASCH-M. S., AND VAN DIERENDONCK-A. J. (1999). GPS receiver architectures and measurements, *Proceedings of the IEEE*, **87**(1), pp. 48–64.

BRENNAN-D. G. (1959). Linear diversity combining techniques, *Proceedings of the IRE*, **47**(6), pp. 1075–1102.

BROWN-T. W. C., SAUNDERS-S. R., STAVROU-S., AND FIACCO-M. (2007). Characterization of polarization diversity at the mobile, *IEEE Transactions on Vehicular Technology*, **56**(5), pp. 2440–2447.

BUDDEN-K. G. (1965). Effect of electron collisions on the formulas of magneto-ionic theory, *Radio Sci. D*, **69**, pp. 191–211.

BUDDEN-K. G. (1985). *The Propagation of Radio Waves*, Cambridge University Press. Cambridge Books Online.

BUREAU INTERNATIONAL DES POIDS ET MESURES. (Accessed: 2016). International reference time scales. Available at: http://www.bipm.org/en/bipm-services/timescales/.

BURGIN-M., AND MOGHADDAM-M. (2014). Mitigation of Faraday rotation effect for long-wavelength synthetic spaceborne radar data, *IEEE Geoscience and Remote Sensing Symposium (IGARSS)*, pp. 2340–2342.

CANADIAN SPACE AGENCY. (Accessed: 2016a). RADARSAT-2. Available at: http://www.asc-csa.gc.ca/eng/satellites/radarsat2/.

CANADIAN SPACE AGENCY. (Accessed: 2016b). RADARSAT constellation. Available at: http://www.asc-csa.gc.ca/eng/satellites/radarsat/.

CELLULAR TELEPHONE INDUSTRIES ASSOCIATION. (Accessed: 2016). Wireless telecommunications bureau seeks comment on the state of mobile wireless competition. Available at: http://www.ctia.org/docs/default-source/fcc-filings/160531-filed-ctia-mobile-wireless-competition-report-comments.pdf.

CHANG-D. D., AND DE WECK-O. L. (2005). Basic capacity calculation methods and benchmarking for MF-TDMA and MF-CDMA communication satellites, *International Journal of Satellite Communications and Networking*, **23**(3), pp. 153–171.

CHEBIHI-A., LUXEY-C., DIALLO-A., LE THUC-P., AND STARAJ-R. (2008). A novel isolation technique for closely spaced PIFAs for UMTS mobile phones, *IEEE Antennas and Wireless Propagation Letters*, **7**, pp. 665–668.

CHEN-X., LIANG-J., LI-P., GUO-L., CHIAU-C. C., AND PARINI-C. G. (2005). Planar UWB monopole antennas, *Proc. Asia-Pacific Microwave Conference (APMC)*. DOI: 10.1109/APMC.2005.1606191.

CHIN-W. H., FAN-Z., AND HAINES-R. (2014). Emerging technologies and research challenges for 5G wireless networks, *IEEE Wireless Communications*, **21**(2), pp. 106–112.

CHIOU-T.-W., AND WONG-K.-L. (2002). Broad-band dual-polarized single microstrip patch antenna with high isolation and low cross polarization, *IEEE Transactions on Antennas and Propagation*, **50**(3), pp. 399–401.

CHIU-C. Y., CHENG-C. H., MURCH-R. D., AND ROWELL-C. R. (2007a). Reduction of mutual coupling between closely-packed antenna elements, *IEEE Transactions on Antennas and Propagation*, **55**(6), pp. 1732–1738.

CHIU-C.-Y., YAN-J.-B., AND MURCH-R. (2007b). Compact three-port orthogonally polarized MIMO antennas, *IEEE Antennas and Wireless Propagation Letters*, **6**, pp. 619–622.

CHIU-C.-Y., YAN-J.-B., MURCH-R. D., YUN-J. X., AND VAUGHAN-R. G. (2009). Design and implementation of a compact 6-port antenna, *IEEE Antennas and Wireless Propagation Letters*, **8**, pp. 767–770.

CHOI-M.-S., GROSSKOPF-G., AND ROHDE-D. (2005). Statistical characteristics of 60 GHz wideband indoor propagation channel, *Proc. IEEE 16th International Symposium on Personal, Indoor and Mobile Radio Communications (PIMRC)*. DOI: 10.1109/PIMRC.2005.1651506.

CHUAH-C.-N., TSE-D. N. C., KAHN-J. M., AND VALENZUELA-R. A. (2002). Capacity scaling in MIMO wireless systems under correlated fading, *IEEE Transactions on Information Theory*, **48**(3), pp. 637–650.

CIRAOLO-L., AZPILICUETA-F., BRUNINI-C., MEZA-A., AND RADICELLA-S. M. (2006). Calibration errors on experimental slant total electron content (TEC) determined with GPS, *Journal of Geodesy*, **81**(2), pp. 111–120.

CISCO INC.. (Accessed: 2014). The Internet of Things: How the next evolution of the internet is changing everything. Available at: https://www.cisco.com/c/dam/en_us/about/ac79/docs/innov/IoT_IBSG_0411FINAL.pdf.

COBHAM PLC. (Accessed: 2015). GPS antenna installation guidelines. Available at: https://www.cobham.com/media/5048/gpsantennainstallationguide.pdf.

COETZEE-L., AND EKSTEEN-J. (2011). The internet of things—promise for the future? An introduction, *IST-Africa Conference Proceedings*. Available at: http://ieeexplore.ieee.org/stamp/stamp.jsp?arnumber=6107386.

COLDREY-M. (2008). Modeling and capacity of polarized MIMO channels, *Proc. IEEE Vehicular Technology Conference (VTC)- Spring*. DOI: 10.1109/VETECS.2008.103.

COMPTON-R. (1981). The tripole antenna: An adaptive array with full polarization flexibility, *IEEE Transactions on Antennas and Propagation*, **29**(6), pp. 944–952.

CORAZZA-G. E., AND VATALARO-F. (1994). A statistical model for land mobile satellite channels and its application to nongeostationary orbit systems, *IEEE Transactions on Vehicular Technology*, **43**(3), pp. 738–742.

COSTER-A., AND KOMJATHY-A. (2008). Space weather and the global positioning system, *Space Weather*. DOI: 10.1029/2008SW000400.

COVERDALE-D. R. (1995). Potential applications of the Orbcomm global messaging system to US military operations, *Naval Postgraduate School, Monterey, California*. Available at: https://core.ac.uk/download/pdf/36724187.pdf.

COX-D. C. (1983). Antenna diversity performance in mitigating the effects of portable radiotelephone orientation and multipath propagation, *IEEE Transactions on Communications*, **31**(5), pp. 620–628.

COX-D. C., MURRAY-R. R., ARNOLD-H. W., NORRIS-A., AND WAZOWICZ-M. (1986). Cross-polarization coupling measured for 800 MHz radio transmission in and around houses and large buildings, *IEEE Transactions on Antennas and Propagation*, **34**(1), pp. 83–87.

DANDEKAR-K. R., LING-H., AND XU-G. (2002). Experimental study of mutual coupling compensation in smart antenna applications, *IEEE Transactions on Wireless Communications*, **1**(3), pp. 480–487.

DANIELS-R. C., AND HEATH-R. W. (2007). 60 GHz wireless communications: emerging requirements and design recommendations, *IEEE Vehicular Technology Magazine*, **2**(3), pp. 41–50.

DAO-M. T., NGUYEN-V. A., IM-Y. T., PARK-S. O., AND YOON-G. (2011). 3D polarized channel modeling and performance comparison of MIMO antenna configurations with different polarizations, *IEEE Transactions on Antennas and Propagation*, **59**(7), pp. 2672–2682.

DAVIDSON-M. (Accessed: 2016). SAOCOM-CS mission and ESA airborne campaign data. Available at: http://seom.esa.int/polarimetrycourse2015/files/SAOCOM_MDavidson.pdf.

DAVIS-L. M., COLLINGS-I. B., AND EVANS-R. J. (1997). Estimation of LEO satellite channels, *Proc. International Conference on Information, Communications and Signal Processing (ICICS)*. DOI: 10.1109/ICICS.1997.647048.

DEGLI-ESPOSTI-V., KOLMONEN-V., VITUCCI-E. M., AND VAINIKAINEN-P. (2011). Analysis and modeling on co- and cross-polarized urban radio propagation for dual-polarized MIMO wireless systems, *IEEE Transactions on Antennas and Propagation*, **59**(11), pp. 4247–4256.

DIALLO-A., LUXEY-C., LE THUC-P., STARAJ-R., AND KOSSIAVAS-G. (2006). Study and reduction of the mutual coupling between two mobile phone PIFAs operating in the DCS1800 and UMTS bands, *IEEE Transactions on Antennas and Propagation*, **54**(11), pp. 3063–3074.

DIETRICH-C. B., DIETZE-K., NEALY-J. R., AND STUTZMAN-W. L. (2001). Spatial, polarization, and pattern diversity for wireless handheld terminals, *IEEE Transactions on Antennas and Propagation*, **49**(9), pp. 1271–1281.

DING-Y., DU-Z., GONG-K., AND FENG-Z. (2007). A four-element antenna system for mobile phones, *IEEE Antennas and Wireless Propagation Letters*, **6**, pp. 655–658.

DONG-L., CHOO-H., HEATH-R. W., AND LING-H. (2005). Simulation of MIMO channel capacity with antenna polarization diversity, *IEEE Transactions on Wireless Communications*, **4**(4), pp. 1869–1873.

EARTH OBSERVATION PORTAL. (Accessed: 2016a). COSMO-Skymed second generation. Available at: https://directory.eoportal.org/web/eoportal/satellite-missions/c-missions/cosmo-skymed-second-generation.

EARTH OBSERVATION PORTAL. (Accessed: 2016b). Paz. Available at: https://directory.eoportal.org/web/eoportal/satellite-missions/p/paz.

EARTH OBSERVATION PORTAL. (Accessed: 2016c). TSX (TerraSAR-X) Mission. Available at: https://directory.eoportal.org/web/eoportal/satellite-missions/t/terrasar-x.

EARTH OBSERVATION RESEARCH CENTER. (Accessed: 2016). Advanced land observing satellite. Available at: http://www.eorc.jaxa.jp/ALOS/en/top/about_top.htm.

ECONOMOU-L., AND LANGLEY-R. J. (1997). Patch antenna equivalent to simple monopole, *Electronics Letters*, **33**(9), pp. 727–729.

EGGERS-P. C. F., TOFTGARD-J., AND OPREA-A. M. (1993). Antenna systems for base station diversity in urban small and micro cells, *IEEE Journal on Selected Areas in Communications*, **11**(7), pp. 1046–1057.

ERCEG-V., SAMPATH-H., AND CATREUX-ERCEG-S. (2006). Dual-polarization versus single-polarization MIMO channel measurement results and modeling, *IEEE Transactions on Wireless Communications*, **5**(1), pp. 28–33.

ERCEG-V., SOMA-P., BAUM-D. S., AND CATREUX-S. (2004). Multiple-input multiple-output fixed wireless radio channel measurements and modeling using dual-polarized antennas at 2.5 GHz, *IEEE Transactions on Wireless Communications*, **3**(6), pp. 2288–2298.

ERCEG-V., SOMA-P., BAUM-D. S., AND PAULRAJ-A. J. (2002). Capacity obtained from multiple-input multiple-output channel measurements in fixed wireless environments at 2.5 GHz, *IEEE International Conference on Communications*. DOI: 10.1109/ICC.2002.996883.

ERICKSON-W. C., PERLEY-R. A., FLATTERS-C., AND KASSIM-N. E. (2001). Ionospheric corrections for VLA observations using local GPS data, *Astronomy and Astrophysics*, **366**(3), pp. 1071–1080.

ERICSSON. (Accessed: 2015). Ericsson research blog: 5G challenges and research. Available at: https://www.ericsson.com/research-blog/5g/5g-challenges-research/.

EUROPEAN SPACE AGENCY. (Accessed: 2016a). ASAR. Available at: https://earth.esa.int/web/guest/missions/esa-operational-eo-missions/envisat/instruments/asar.

EUROPEAN SPACE AGENCY. (Accessed: 2016b). SAOCOM. Available at: https://earth.esa.int/web/guest/missions/3rd-party-missions/potential-missions/saocom.

EUROPEAN SPACE AGENCY. (Accessed: 2016c). Sentinel-1. Available at: http://www.esa.int/Our_Activities/Observing_the_Earth/Copernicus/Sentinel-1/Facts_and_figures.

EUROPEAN UNION. (Accessed: 2016). The 5G infrastructure public private partnership. Available at: https://5g-ppp.eu/5g-ppp-phase-1-projects/.

EVANS-B., ONIRETI-O., SPATHOPOULOS-T., AND IMRAN-M. A. (2015). The role of satellites in 5G, *Proc. IEEE 23rd European Signal Processing Conference (EUSIPCO)*, IEEE, pp. 2756–2760. DOI: 10.1109/EUSIPCO.2015.7362886.

EVANS-B., WERNER-M., LUTZ-E., BOUSQUET-M., CORAZZA-G. E., MARAL-G., AND RUMEAU-R. (2005). Integration of satellite and terrestrial systems in future multimedia communications, *IEEE Wireless Communications*, **12**(5), pp. 72–80.

FARKASVOLGYI-A., DADY-R., AND NAGY-L. (2009). Channel capacity maximization in MIMO antenna system by genetic algorithm, pp. 1119–1122. Available at: http://ieeexplore.ieee.org/stamp/stamp.jsp?tp=&arnumber=5067812?

FARSEROTU-J., AND PRASAD-R. (2000). A survey of future broadband multimedia satellite systems, issues and trends, *IEEE Communications Magazine*, **38**(6), pp. 128–133.

FEDERAL COMMUNICATIONS COMMISSION. (Accessed: 2015). Amendment of the commissions rules with regard to commercial operations in the 3550–3650 MHz band. Available at: https://apps.fcc.gov/edocs_public/attachmatch/FCC-12-148A1_Rcd.pdf.

FEDERAL COMMUNICATIONS COMMISSION. (Accessed: 2016). Fact sheet: Spectrum frontiers proposal to identify, open up vast amounts of new high-band spectrum for next generation (5G) wireless broadband. Available at: https://apps.fcc.gov/edocs_public/attachmatch/DOC-339990A1.pdf.

FEDERICI-J., AND MOELLER-L. (2010). Review of terahertz and subterahertz wireless communications, *Journal of Applied Physics*. DOI: 10.1063/1.3386413.

FELTENS-J. (2007). Development of a new three-dimensional mathematical ionosphere model at european space agency/european space operations centre, *Space Weather*. DOI: 10.1029/2006SW000294.

FLETCHER-P. N., DEAN-M., AND NIX-A. R. (2003). Mutual coupling in multi-element array antennas and its influence on MIMO channel capacity, *Electronics Letters*, **39**(4), pp. 342–344.

FONTAN-F. P., VAZQUEZ-CASTRO-M., CABADO-C. E., GARCIA-J. P., AND KUBISTA-E. (2001). Statistical modeling of the LMS channel, *IEEE Transactions on Vehicular Technology*, **50**(6), pp. 1549–1567.

FOSCHINI-G. J., AND GANS-M. J. (1998). On limits of wireless communications in a fading environment when using multiple antennas, *Wireless Personal Communications*, **6**(3), pp. 311–335.

FOWLES-G. R. (1989). *Introduction to Modern Optics (Second Edition)*, Dover Books on Physics.

FREEMAN-A. (2004). Calibration of linearly polarized polarimetric SAR data subject to Faraday rotation, *IEEE Transactions on Geoscience and Remote Sensing*, **42**(8), pp. 1617–1624.

FREEMAN-A., AND SAATCHI-S. (1998). Detection, estimation and correction of Faraday rotation in linearly polarized SAR backscatter signatures. Available at: https://trs.jpl.nasa.gov/bitstream/handle/2014/18962/98-0093.pdf?sequence=1.

FRIGYES-I., AND HORVÁTH-P. (2005). Polarization-time coding in satellite links, *IEEE Satellite and Space Newsletter*, **15**(2), pp. 6–8.

FRIIS-H. T. (1946). A note on a simple transmission formula, *Proceedings of the IRE*, **34**(5), pp. 254–256.

GAO-X., ZHONG-H., ZHANG-Z., FENG-Z., AND ISKANDER-M. F. (2010a). Low-profile planar tripolarization antenna for WLAN communications, *IEEE Antennas and Wireless Propagation Letters*, **9**, pp. 83–86.

GAO-Y., WANG-S., FALADE-O., CHEN-X., PARINI-C., AND CUTHBERT-L. (2010b). Mutual coupling effects on pattern diversity antennas for MIMO femtocells, *International Journal of Antennas and Propagation*. DOI: 10.1155/2010/756848.

GARG-R., BHARTIA-P., BAHL-I., AND ITTIPIBOON-A. (2001). *Microstrip Antenna Design Handbook*, Artech House.

GESBERT-D., BOLCSKEI-H., GORE-D. A., AND PAULRAJ-A. J. (2002). Outdoor MIMO wireless channels: Models and performance prediction, *IEEE Transactions on Communications*, **50**(12), pp. 1926–1934.

GESBERT-D., SHAFI-M., SHAN SHIU-D., SMITH-P. J., AND NAGUIB-A. (2003). From theory to practice: an overview of MIMO space-time coded wireless systems, *IEEE Journal on Selected Areas in Communications*, **21**(3), pp. 281–302.

GETU-B. N., AND ANDERSEN-J. B. (2005). The MIMO cube— a compact MIMO antenna, *IEEE Transactions on Wireless Communications*, **4**(3), pp. 1136–1141.

GETU-B. N., AND JANASWAMY-R. (2005). The effect of mutual coupling on the capacity of the MIMO cube, *IEEE Antennas and Wireless Propagation Letters*, **4**, pp. 240–244.

GHOSH-A., THOMAS-T. A., CUDAK-M. C., RATASUK-R., MOORUT-P., VOOK-F. W., RAPPAPORT-T. S., MACCARTNEY-G. R., SUN-S., AND NIE-S. (2014). Millimeter-wave enhanced local area systems: A high-data-rate approach for future wireless networks, *IEEE Journal on Selected Areas in Communications*, **32**(6), pp. 1152–1163.

GOLDSMITH-A. (2005). *Wireless Communications*, Cambridge University Press, Cambridge (UK).

GOLIO-M., AND GOLIO-J. (2007). *RF and Microwave Passive and Active Technologies*, The RF and Microwave Handbook, (Second Edition), CRC Press.

GUBBI-J., R.., MARUSIC-S., AND PALANISWAMI-M. (2013). Internet of things (IoT): A vision, architectural elements, and future directions, *Future Generation Computer Systems*, **29**(7), pp. 1645–1660.

GUO-H., LUO-B., REN-Y., ZHAO-S., AND DANG-A. (2010). Influence of beam wander on uplink of ground-to-satellite laser communication and optimization for transmitter beam radius, *Optics Letters*, **35**(12), pp. 1977–1979.

GUPTA-G., HUGHES-B. L., AND LAZZI-G. (2008). On the degrees of freedom in linear array systems with tri-polarized antennas, *IEEE Transactions on Wireless Communications*, **7**(7), pp. 2458–2462.

HAJJ-G. A., WILSON-B. D., WANG-C., PI-X., AND ROSEN-I. G. (2004). Data assimilation of ground GPS total electron content into a physics-based ionospheric model by use of the Kalman filter, *Radio Science*. DOI: 10.1029/2002RS002859.

HALL-P. (1989). Application of sequential feeding to wide bandwidth, circularly polarised microstrip patch arrays, *IEE Proceedings H—Microwaves, Antennas and Propagation*, **136**(5), pp. 390–398.

HALL-P., DAHELE-J., AND JAMES-J. (1989). Design principles of sequentially fed, wide bandwidth, circularly polarised microstrip antennas, *IEE Proceedings H—Microwaves, Antennas and Propagation*, **136**(5), pp. 381–389.

HASHEMI-H., AND RAMAN-S. (2016). *mm-Wave Silicon Power Amplifiers and Transmitters*, The Cambridge RF and Microwave Engineering Series, Cambridge University Press (UK).

HECHT-E. (2001). *Optics, Fourth edition*, Addison Wesley.

HERNÀNDEZ-PAJARES-M., JUAN-J., AND SANZ-J. (1999). New approaches in global ionospheric determination using ground GPS data, *Journal of Atmospheric and Solar-Terrestrial Physics*, **61**(16), pp. 1237–1247.

HERNÀNDEZ-PAJARES-M., JUAN-J. M., SANZ-J., ORUS-R., GARCIA-RIGO-A., FELTENS-J., KOMJATHY-A., SCHAER-S. C., AND KRANKOWSKI-A. (2009). The IGS VTEC maps: a reliable source of ionospheric information since 1998, *Journal of Geodesy*, **83**(3), pp. 263–275. DOI: 10.1007/s00190-008-0266-1.

HONG-W., BAEK-K. H., LEE-Y., KIM-Y., AND KO-S. T. (2014a). Study and prototyping of practically large-scale mmWave antenna systems for 5G cellular devices, *IEEE Communications Magazine*, **52**(9), pp. 63–69.

HONG-W., BAEK-K., LEE-Y., AND KIM-Y. G. (2014b). Design and analysis of a low-profile 28 GHz beam steering antenna solution for future 5G cellular applications, *Proc. IEEE MTT-S International Microwave Symposium (IMS)*. DOI: 10.1109/MWSYM.2014.6848377.

HORVÁTH-P., AND FRIGYES-I. (2006). Application of the 3D polarization concept in satellite MIMO systems, *Proc. IEEE Global Communications Conference (GlobeCom)*. DOI: 10.1109/GLOCOM.2006.481?

HORVÁTH-P., KARAGIANNIDIS-G. K., KING-P. R., STAVROU-S., AND FRIGYES-I. (2007). Investigations in satellite MIMO channel modeling: accent on polarization, *EURASIP Journal on Wireless Communications and Networking*. DOI: 10.1155/2007/98942.

HUANG-H., LIU-Y., AND GONG-S. (2015). A novel uniplanar differentially-fed UWB polarization diversity antenna with dual notch bands, *IEEE Antennas and Wireless Propagation Letters*, **14**(3), pp. 563–566.

HUNSUCKER-R. D., AND HARGREAVES-J. K. (2007). *The High-Latitude Ionosphere and its Effects on Radio Propagation*, Cambridge Atmospheric and Space Science Series, Cambridge University Press (UK).

ILČEV-S. D. (2005). *Global Mobile Satellite Communications: For Maritime, Land and Aeronautical Applications*, Springer (US).

INEVITABLE TECHNOLOGIES. (Accessed: 2016). Orbcomm antennas. Available at: http://www.inevtech.com/orbcomm-antennas.

INSTITUTE OF ELECTRICAL AND ELECTRONICS ENGINEERS. (Accessed: 2015). Draft standard for information technology–telecommunications and information exchange between systems–local and metropolitan area networks–specific requirements– part 11: Wireless LAN medium access control (MAC) and physical layer (PHY) specifications–amendment 3: Enhancements for very high throughput in the 60 GHz band. Available at: http://ieeexplore.ieee.org/xpl/mostRecentIssue.jsp?punumber=6242353.

INSTITUTE OF ELECTRICAL AND ELECTRONICS ENGINEERS. (Accessed: 2016). IEEE conference on standards for communications and networking. Available at: http://cscn2016.ieee-cscn.org/CFP/CSCN16-CFP.pdf.

INTERNATIONAL GNSS SERVICE. (Accessed: 2014). Available at: http://www.igs.org?

INTERNATIONAL TELECOMMUNICATIONS UNION (ITU-R). (1998). Ionosphere and its effects on radiowave propagation. Available at: http://www.itu.int/pub/R-HDB-32.

INTERNATIONAL TELECOMMUNICATIONS UNION (ITU-R). (Accessed: 2013). Ionospheric propagation data and prediction methods required for the design of satellite services and systems (Recommendation ITU-R P.531-11). Available at: https://www.itu.int/dms_pubrec/itu-r/rec/p/R-REC-P.531-11-201202-S!!PDF-E.pdf.

IRIDIUM COMMUNICATIONS INC.. (Accessed: 2014). Available at: http://www.iridium.com?

JACOB, M.AND HERRERO-P., AND SCHOEBEL-J. (2008). Low-cost omnidirectional planar antennas for the 122 GHz ISM frequency band, *IEEE Antennas and Propagation Society International Symposium*. DOI: 10.1109/APS.2008.4619478.

JAHN-A., AND LUTZ-E. (1995). Propagation data and channel model for LMS systems, *ESA*. Final Report, ESA Study 141742.

JAKES-W. J. (1974). *Microwave Mobile Communications*, New York:Wiley, New York (NY).

JANASWAMY-R. (2002). Effect of element mutual coupling on the capacity of fixed length linear arrays, *IEEE Antennas and Wireless Propagation Letters*, **1**(1), pp. 157–160.

JEHLE-M., RUEGG-M., SMALL-D., MEIER-E., AND NUESCH-D. (2005). Estimation of ionospheric TEC and Faraday rotation for L-band SAR, *Proc. SPIE*, **5979**, pp. 252–260.

JEHLE-M., RUEGG-M., ZUBERBUHLER-L., SMALL-D., AND MEIER-E. (2009). Measurement of ionospheric Faraday rotation in simulated and real spaceborne SAR data, *IEEE Transactions on Geoscience and Remote Sensing*, **47**(5), pp. 1512–1523.

JOHANNSEN-K. (1995). Mobile P-service satellite system comparison, *International Journal of Satellite Communications*, **13**, pp. 453–471. DOI: 10.1002/sat.4600130604.

JONES-M. (2008). A statistical comparison of vertical total electron content (TEC) from three ionospheric models. Available at: http://nldr.library.ucar.edu/repository/assets/soars/SOARS-000-000-000-174.pdf.

KAPLAN-E., AND HEGARTY-C. (2005). *Understanding GPS: principles and applications*, Artech house.

KATAYAMA-M., OGAWA-A., AND MORINAGA-N. (1992). Carrier synchronization under Doppler shift of the nongeostationary satellite communication systems, *Proc. Singapore ICCS/ISITA: 'Communications on the Move'*. DOI: 10.1109/ICCS.1992.254907.

KAUFMANN-T., AND FUMEAUX-C. (2015). Low-profile magnetic loop monopole antenna based on a square substrate-integrated cavity, *International Journal of Antennas and Propagation*. DOI: 10.1155/2015/694385.

KELLEY-M. C. (2009). *The Earth's Ionosphere: Plasma Physics & Electrodynamics*, Elsevier Science.

KENNEY-J. B. (2011). Dedicated short-range communications (DSRC) standards in the United States, *Proceedings of the IEEE*, **99**(7), pp. 1162–1182.

KERMOAL-J. P., SCHUMACHER-L., PEDERSEN-K. I., MOGENSEN-P. E., AND FREDERIKSEN-F. (2002). A stochastic MIMO radio channel model with experimental validation, *IEEE Journal on Selected Areas in Communications*, **20**(6), pp. 1211–1226.

KESKILAMMI-M., SYDÄNHEIMO-L., AND KIVIKOSKI-M. (2003). Radio frequency technology for automated manufacturing and logistics control. Part 1: Passive RFID systems and the effects of antenna parameters on operational distance, *The International Journal of Advanced Manufacturing Technology*, **21**(10), pp. 769–774.

KING-P. (2007). *Modelling and Measurement of the Land MIMO Satellite MIMO Radio Propagation Channel.*, PhD thesis, University of Surrey.

KING-P. R., AND STAVROU-S. (2006). Capacity improvement for a land mobile single satellite MIMO system, *IEEE Antennas and Wireless Propagation Letters*, **5**, pp. 98–100.

KING-P. R., AND STAVROU-S. (2007). Low elevation wideband land mobile satellite MIMO channel characteristics, *IEEE Transactions on Wireless Communications*, **6**(7), pp. 2712–2720.

KING-P. R., EVANS-B. G., AND STAVROU-S. (2005). Physical-statistical model for the land mobile-satellite channel applied to satellite/HAP-MIMO, *11th European Wireless Conference—Next Generation Wireless and Mobile Communications and Services (European Wireless)*. Available at: http://ieeexplore.ieee.org/stamp/stamp.jsp?arnumber=5755290.

KINTNER-P. M., AND LEDVINA-B. M. (2005). The ionosphere, radio navigation, and global navigation satellite systems, *Advances in Space Research*, **35**(5), pp. 788–811. Fundamentals of Space Environment Science.

KLEINE-OSTMANN-T., AND NAGATSUMA-T. (2011). A review on terahertz communications research, *Infrared Millmetre Terahertz Waves*, **32**(2), pp. 143–171.

KLOBUCHAR-J. A. (1996). Ionospheric effects on GPS, *Global Positioning System: Theory and Applications*, **1**, pp. 485–515. Available at: http://gauss.gge.unb.ca/gpsworld/EarlyInnovationColumns/Innov.1991.04.pdf.

KOMJATHY-A. (1997). *Global Ionospheric Total Electron Content Mapping Using the Global Positioning System*, PhD thesis, The University of New Brunswick (Canada). Available at: http://www2.unb.ca/gge/Pubs/TR188.pdf.

KOOHESTANI-M., ZÜRCHER-J.-F., MOREIRA-A. A., AND SKRIVERVIK-A. K. (2014). A novel, low-profile, vertically-polarized UWB antenna for WBAN, *IEEE Transactions on Antennas and Propagation*, **62**(4), pp. 1888–1894.

KOOI-J. E., FISCHER-P. D., BUFFO-J. J., AND SPANGLER-S. R. (2014). Measurements of coronal Faraday rotation at 4.6 $R_{\odot}$, *The Astrophysical Journal*, **784**(1), pp. 68–85. DOI: 10.1088/0004-637X/784/1/68.

KOS-T., MARKEZIC-I., AND POKRAJCIC-J. (2010). Effects of multipath reception on GPS positioning performance, *Proceedings ELMAR-2010*, pp. 399–402. Available at: http://ieeexplore.ieee.org/stamp/stamp.jsp?arnumber=5606130.

KOZONO-S., TSURUHARA-T., AND SAKAMOTO-M. (1984). Base station polarization diversity reception for mobile radio, *IEEE Transactions on Vehicular Technology*, **33**(4), pp. 301–306.

KWON-S.-C., AND STUBER-G. L. (2011). Geometrical theory of channel depolarization, *IEEE Transactions on Vehicular Technology*, **60**(8), pp. 3542–3556.

KYRITSI-P., COX-D. C., VALENZUELA-R. A., AND WOLNIANSKY-P. W. (2002). Effect of antenna polarization on the capacity of a multiple element system in an indoor environment, *IEEE Journal on Selected Areas in Communications*, **20**(6), pp. 1227–1239.

LANGLEY-R. B. (1997). GPS receiver system noise, *GPS world*, **8**(6), pp. 40–45.

LARSSON-E. G., EDFORS-O., TUFVESSON-F., AND MARZETTA-T. L. (2014). Massive MIMO for next generation wireless systems, *IEEE Communications Magazine*, **52**(2), pp. 186–195.

LAWRENCE-N., DAVIS-L. M., AND HALEY-D. (2013). A polarimetric line-of-sight channel model for MIMO satellite communications, *Proc. IEEE Australian Communications Theory Workshop (AusCTW)*. DOI: 10.1109/AusCTW.2013.6510052.

LAWRENCE-N. P., FUMEAUX-C., AND ABBOTT-D. (2016a). Wideband substrate-integrated monopole antenna, *Microwave and Optical Technology Letters*, **58**(8), pp. 1855–1857. DOI: 10.1002/mop.29925.

LAWRENCE-N. P., FUMEAUX-C., AND D.ABBOTT. (2017a). Planar slot antenna with circular and vertical polarization diversity, *Microwave and Optical Technology Letters*, **XX**(XX), pp. XXX–XXX. (in review).

LAWRENCE-N. P., FUMEAUX-C., AND D.ABBOTT. (2017b). Planar triorthogonal diversity slot antenna, *IEEE Transactions on Antennas and Propagation*, **65**(3), pp. 1416–1421. DOI: 10.1109/TAP.2016.2647719.

LAWRENCE-N. P., HANSEN-H., AND ABBOTT-D. (2016b). Tri-orthogonal polarization diversity for 5G networks, *Transactions on Emerging Telecommunications Technologies*. DOI: 10.1002/ett.3042.

LAWRENCE-N. P., HANSEN-H. J., AND ABBOTT-D. (2015a). 3-D low earth orbit vector estimation of Faraday rotation and path delay, *IEEE Access*, **3**, pp. 1684–1694. DOI: 10.1109/ACCESS.2015.2479247.

LAWRENCE-N. P., HANSEN-H. J., AND ABBOTT-D. (2016c). Implications of polarization impurity on diversity for 5G networks, *Proc. 41st International Conference on Infrared, Millimeter, and Terahertz waves (IRMMW-THz)*. DOI: 10.1109/IRMMW-THz.2016.7758493.

LAWRENCE-N. P., HANSEN-H. J., AND ABBOTT-D. (2016d). Tri-orthogonal polarization diversity reception for non-geosynchronous satellite orbit ionospheric channels, *International Journal of Satellite Communications and Networking*. DOI: 10.1002/sat.1203.

LAWRENCE-N. P., NG-B., HANSEN-H. J., AND ABBOTT-D. (2014a). Analysis of polarization diversity at terahertz frequencies, *Proc. 39th International Conference on Infrared, Millimeter, and Terahertz waves (IRMMW-THz)*. DOI: 10.1109/IRMMW-THz.2014.6956120.

LAWRENCE-N. P., NG-B. W.-H., HANSEN-H. J., AND ABBOTT-D. (2014b). Analysis of millimeter-wave polarization diverse MIMO capacity, *Proc. 39th International Conference on Infrared, Millimeter, and Terahertz waves (IRMMW-THz)*. DOI: 10.1109/IRMMW-THz.2014.6956121.

LAWRENCE-N. P., NG-B. W.-H., HANSEN-H. J., AND ABBOTT-D. (2015b). Analysis of millimetre-wave polarization diverse multiple-input multiple-output capacity, *Royal Society Open Science*. DOI: 10.1098/rsos.150322.

LAWRENCE-N. P., NG-B. W.-H., HANSEN-H. J., AND ABBOTT-D. (2017c). 5g terrestrial networks: Mobility and coverage—solution in three dimensions, *IEEE Access*. 10.1109/ACCESS.2017.2693375.

LEE-W. C. Y., AND YEH-Y. (1972). Polarization diversity system for mobile radio, *IEEE Transactions on Communications*, **20**(5), pp. 912–923.

LEVESON-I. (2006). Benefits of the new GPS civil signal, *Inside GNSS*, **1**(5), pp. 42–47.

LE VINE-D. M., AND ABRAHAM-S. (2002). The effect of the ionosphere on remote sensing of sea surface salinity from space: Absorption and emission at L band, *IEEE Transactions on Geoscience and Remote Sensing*, **40**(4), pp. 771–782.

LE VINE-D. M., AND UTKU-C. (Accessed: 2013). Estimation of Faraday rotation using SMOS full polarimetric mode data. Available at: http://earth.eo.esa.int/workshops/svrt10/Posters/Faraday_Rotation_D.Levine.pdf.

LE VINE-D. M., LAGERLOEF-G. S. E., AND TORRUSIO-S. E. (2010). Aquarius and remote sensing of sea surface salinity from space, *Proceedings of the IEEE*, **98**(5), pp. 688–703.

LEVINE-E. (2009). Overview of GPS antennas, *Proc. IEEE International Conference on Microwaves, Communications, Antennas and Electronics Systems*. DOI: 10.1109/COMCAS.2009.5386076.

LIBELLIUM COMUNICACIONES DISTRIBUIDAS. (Accessed: 2014). Smart World. Available at: http://www.libelium.com/libelium-smart-world-infographic-smart-cities-internet-of-things/.

LIEBE-H. J., MANABE-T., AND HUFFORD-G. A. (1989). Millimeter-wave attenuation and delay rates due to fog/cloud conditions, *IEEE Transactions on Antennas and Propagation*, **37**(12), pp. 1617–1612.

LI-M., AND LUK-K.-M. (2013). A differential-fed magneto-electric dipole antenna for UWB applications, *IEEE Transactions on Antennas and Propagation*, **61**(1), pp. 92–99.

LIN-S.-J., AND ROW-J.-S. (2008). Monopolar patch antenna with dual-band and wideband operations, *IEEE Transactions on Antennas and Propagation*, **56**(3), pp. 900–903.

LIOLIS-K. P., GOMEZ-VILARDEBO-J., CASINI-E., AND PEREZ-NEIRA-A. I. (2010). Statistical modeling of dual-polarized MIMO land mobile satellite channels, *IEEE Transactions on Communications*, **58**(11), pp. 3077–3083.

LIOLIS-K. P., PANAGOPOULOS-A. D., AND COTTIS-P. G. (2007). Multi-satellite MIMO communications at Ku-band and above: Investigations on spatial multiplexing for capacity improvement and selection diversity for interference mitigation, *EURASIP Journal on Wireless Communications and Networking*. DOI: 10.1155/2007/59608.

LI-Q. C., NIU-H., PAPATHANASSIOU-A. T., AND WU-G. (2014). 5G network capacity: key elements and technologies, *IEEE Vehicular Technology Magazine*, **9**(1), pp. 71–78.

LIU-J., XUE-Q., WONG-H., LAI-H. W., AND LONG-Y. (2013). Design and analysis of a low-profile and broadband microstrip monopolar patch antenna, *IEEE Transactions on Antennas and Propagation*, **61**(1), pp. 11–18.

LIU-J., ZHENG-S., LI-Y., AND LONG-Y. (2014). Broadband monopolar microstrip patch antenna with shorting vias and coupled ring, *IEEE Antennas and Wireless Propagation Letters*, **13**, pp. 39–42.

LI-X., GANI-A., SALLEH-R., AND ZAKARIA-O. (2009). The future of mobile wireless communication networks, *Proc. IEEE International Conference on Communication Software and Networks (ICCSN)*. DOI: 10.1109/ICCSN.2009.105.

LI-Y., ZHANG-Z., ZHENG-J., AND FENG-Z. (2012). Compact azimuthal omnidirectional dual-polarized antenna using highly isolated colocated slots, *IEEE Transactions on Antennas and Propagation*, **60**(9), pp. 4037–4045.

LOO-C. (1985). A statistical model for a land mobile satellite link, *IEEE Transactions on Vehicular Technology*, **34**(3), pp. 122–127.

LOUDET-L. (Accessed: 2014). Available at: http://sidstation.loudet.org/ionosphere-en.xhtml.

LUDWIG-A. (1973). The definition of cross polarization, *IEEE Transactions on Antennas and Propagation*, **21**(1), pp. 116–119.

LUKAMA-L. C., KONSTANTINOU-K., AND EDWARDS-D. J. (2001). Performance of a three-branch orthogonal polarization diversity scheme, *Proc. IEEE 54th Vehicular Technology Conference (VTC)-Fall*. DOI: 10.1109/VTC.2001.957101.

LU-L., LI-G. Y., SWINDLEHURST-A. L., ASHIKHMIN-A., AND ZHANG-R. (2014). An overview of massive MIMO: Benefits and challenges, *IEEE Journal of Selected Topics in Signal Processing*, **8**(5), pp. 742–758.

LUTZ-E. (1996). A Markov model for correlated land mobile satellite channels, *International Journal of Satellite Communications*, **14**(4), pp. 333–339.

LUTZ-E. (1998). Issues in satellite personal communication systems, *Wireless Networks*, **4**(2), pp. 109–124.

LUTZ-E., CYGAN-D., DIPPOLD-M., DOLAINSKY-F., AND PAPKE-W. (1991). The land mobile satellite communication channel- recording, statistics and channel model, *IEEE Transactions on Vehicular Technology*, **40**(2), pp. 375–386.

MACCARTNEY-G. R., AND RAPPAPORT-T. S. (2014). 73 GHz millimeter wave propagation measurements for outdoor urban mobile and backhaul communications in New York City, *Proc. IEEE International Conference on Communications (ICC)*, pp. 4862–4867. DOI: 10.1109/ICC.2014.6884090.

MAINE-K., DEVIEUX-C., AND SWAN-P. (1995). Overview of IRIDIUM satellite network, *WESCON/'95 Conference record. Microelectronics Communications Technology Producing Quality Products Mobile and Portable Power Emerging Technologies*. DOI: 10.1109/WESCON.1995.485428.

MAK-K. M., LAI-H. W., LUK-K. M., AND CHAN-C. H. (2014). Circularly polarized patch antenna for future 5G mobile phones, *IEEE Access*, **2**, pp. 1521–1529. 10.1109/ACCESS.2014.2382111.

MANDEL-C., KUBINA-B., SCHUBLER-M., AND JAKOBY-R. (2011). Passive chipless wireless sensor for two-dimensional displacement measurement, *41st European Microwave Conference (EuMC)*, pp. 79–82. Available at: http://ieeexplore.ieee.org/stamp/stamp.jsp?arnumber=6101801.

MANNUCCI-A. J., WILSON-B. D., YUAN-D. N., HO-C. H., LINDQWISTER-U. J., AND RUNGE-T. F. (1998). A global mapping technique for GPS-derived ionospheric total electron content measurements, *Radio Science*, **33**(3), pp. 565–582.

MARQUIS-W. A. (Accessed: 2014). The GPS block IIR/IIR-M antenna panel pattern. Available at: http://www.lockheedmartin.com.au/content/dam/lockheed/data/space/photo/gps/gpspubs/GPS%20Block%20IIR%20and%20IIR-M%20Antenna%20Panel%20Pattern,%20Marquis,%20Feb2014%20-%20publically%20releasable%20data.pdf.

MARQUIS-W. A., AND REIGH-D. L. (Accessed: 2015). The GPS block IIR and IIR-M broadcast L-band antenna panel: Its pattern and performance, *Navigation*, **62**(4), pp. 329–347.

MARROCCO-G., MATTIONI-L., AND CALABRESE-C. (2008). Multiport sensor RFIDs for wireless passive sensing of objects– basic theory and early results, *IEEE Transactions on Antennas and Propagation*, **56**(8), pp. 2691–2702.

MARZETTA-T. L. (2002). Fundamental limitations on the capacity of wireless links that use polarimetric antenna arrays, *Proc. IEEE International Symposium on Information Theory*. DOI: 10.1109/ISIT.2002.1023323.

MAUS-S., MACMILLAN-S., MCLEAN-S., HAMILTON-B., THOMSON-A., NAIR-M., AND ROLLINS-C. (2010). The US/UK world magnetic model 2010-2015, NOAA technical report (NESDIS/NGDC). Available at: http://www.ngdc.noaa.gov/geomag/WMM/data/WMM2010/WMM2010_Report.pdf.

MAZDA-F. (2014). *Telecommunications Engineer's Reference Book*, Elsevier Science.

MEYER-F. J., AND NICOLL-J. B. (2008). Prediction, detection, and correction of Faraday rotation in full-polarimetric L-band SAR data, *IEEE Transactions on Geoscience and Remote Sensing*, **46**(10), pp. 3076–3086.

MIKKI-S. M., AND ANTAR-Y. M. M. (2015). On cross correlation in antenna arrays with applications to spatial diversity and MIMO systems, *IEEE Transactions on Antennas and Propagation*, **63**(4), pp. 1798–1810.

MINTER-C. F., ROBERTSON-D. S., SPENCER-P. S. J., JACOBSON-A. R., FULLER-ROWELL-T. J., ARAUJO-PRADERE-E. A., AND MOSES-R. W. (2007). A comparison of Magic and FORTE ionosphere measurements, *Radio Science*. DOI: 10.1029/2006RS003460.

MISRA-P., AND ENGE-P. (2006). *Global Positioning System: Signals, Measurements and Performance, Second Edition*, Ganga-Jamuna Press (Lincoln, MA).

MITCH-R. H., PSIAKI-M. L., AND TONG-D. M. (2013). Local ionosphere model estimation from dual-frequency global navigation satellite system observables, *Radio Science*, **48**(6), pp. 671–684.

MIT HAYSTACK OBSERVATORY. (Accessed: 2014). Available at: http://www.haystack.mit.edu/atm/arrays/gps/.

MITTRA-R., YANG-R., ITOH-M., AND ARAKAWA-M. (1993). Microstrip patch antennas for GPS applications, *Antennas and Propagation Society International Symposium (AP-S) Digest*, Vol. 3, pp. 1478–1481. DOI: 10.1109/APS.1993.385474.

MONTENBRUCK-O., AND GILL-E. (2012). *Satellite Orbits: Models, Methods and Applications*, Springer (Berlin Heidelberg).

MORTON-Y. T., ZHOU-Q., AND VAN GRAAS-F. (2009). Assessment of second-order ionosphere error in GPS range observables using Arecibo incoherent scatter radar measurements, *Radio Science*. DOI: 10.1029/2008RS003888.

MOVABLE TYPE LTD.. (Accessed: 2014). Calculate distance, bearing and more between latitude/longitude points. Available at: http://www.movable-type.co.uk/scripts/latlong.html.

MTUMBUKA-M., AND EDWARDS-D. (2005). Investigation of tri-polarised MIMO technique, *Electronics Letters*, **41**(3), pp. 137–138.

MTUMBUKA-M. C., MALIK-W. Q., STEVENS-C. J., AND EDWARDS-D. J. (2005). A tri-polarized ultra-wideband MIMO system, *IEEE Symposium on Advances in Wired and Wireless Communications*, pp. 98–101. DOI: 10.1109/SARNOF.2005.1426521.

NABAR-R., BOLCSKEI-H., ERCEG-V., GESBERT-D., AND PAULRAJ-A. J. (2002). Performance of multi-antenna signaling techniques in the presence of polarization diversity, *IEEE Transactions on Signal Processing*, **50**(10), pp. 2553–2562.

NAKANO-H., IWAOKA-H., MORISHITA-K., AND YAMAUCHI-J. (2008). A wideband low-profile antenna composed of a conducting body of revolution and a shorted parasitic ring, *IEEE Transactions on Antennas and Propagation*, **56**(4), pp. 1187–1192.

NAM-Y.-H., NG-B. L., SAYANA-K., LI-Y., ZHANG-J., KIM-Y., AND LEE-J. (2013). Full-dimension MIMO (FD-MIMO) for next generation cellular technology, *IEEE Communications Magazine*, **51**(6), pp. 172–179.

NANJING UNIVERSITY. (Accessed: 2016). Waves in What? Available at: http://astronomy.nju.edu.cn/~lixd/GA/AT4/AT403/HTML/AT40302.htm.

NANZER-J. (2012). *Microwave and Millimeter-wave Remote Sensing for Security Applications*, Artech House Remote Sensing Library, Artech House.

NATIONAL OCEANIC AND ATMOSPHERIC ADMINISTRATION. (Accessed: 2014). Coupled thermosphere ionosphere plasmasphere electrodynamics model. Available at: http://www.swpc.noaa.gov/. (Accessed through research using http://helios.swpc.noaa.gov/ctipe/about.html).

NEMEROFF-J., GARCIA-L., HAMPEL-D., AND DIPIERRO-S. (2001). Application of sensor network communications, *IEEE Military Communications Conference MILCOM. Communications for Network-Centric Operations: Creating the Information Force*, Vol. 1, pp. 336–341. DOI: 10.1109/MILCOM.2001.985815.

NIKNEJAD-A. M., AND HASHEMI-H. (2008). *mm-Wave Silicon Technology: 60 GHz and Beyond*, Integrated Circuits and Systems, Springer (US).

OESTGES-C., CLERCKX-B., GUILLAUD-M., AND DEBBAH-M. (2008). Dual-polarized wireless communications: from propagation models to system performance evaluation, *IEEE Transactions on Wireless Communications*, **7**(10), pp. 4019–4031.

OMOTE-K., SATO-H., LI-K., HONDA-K., KOYANAGI-Y., AND OGAWA-K. (2015). Three-axis decoupling stub-loaded parallel dipole array with tri-orthogonal polarization directivity, *International Workshop on Electromagnetics: Applications and Student Innovation Competition (iWEM)*. DOI: 10.1109/iWEM.2015.7365037.

ORBCOMM INC.. (Accessed: 2014). Networks. Available at: http://www.orbcomm.com/networks.

ORBCOMM LLC. (Accessed: 2014). Orbcomm system overview A80TD0008 - revision G. Available at: http://www.m2mconnectivity.com.au/sites/default/files/more-information/System_Overview_Rev_G.pdf.

ORFANIDIS-S. J. (2002). *Electromagnetic Waves and Antennas Book*, Rutgers University, NJ. Available at: http://www.ece.rutgers.edu/faculty/orfanidis.

PADROS-N., ORTIGOSA-J. I., BAKER-J., ISKANDER-M. F., AND THORNBERG-B. (1997). Comparative study of high-performance GPS receiving antenna designs, *IEEE Transactions on Antennas and Propagation*, **45**(4), pp. 698–706.

PANTHER-G. (Accessed: 2015). Patch antennas for the new GNSS, *GPS World*. Available at: http://gpsworld.com/wirelesspatch-antennas-new-gnss-12552/.

PARKINSON-B. W., AND SPILKER-J. J. (1996). *Global Positioning System: Theory and Applications*, Progress in astronautics and aeronautics, American Institute of Aeronautics & Astronautics.

PARK-M., AND PAN-H. K. (2012). A spatial diversity technique for IEEE 802.11 ad WLAN in 60 GHz band, *IEEE Communications Letters*, **16**(8), pp. 1260–1262.

PARYANI-R. C., WAHID-P. F., AND BEHDAD-N. (2010). A wideband, dual-polarized, substrate-integrated cavity-backed slot antenna, *IEEE Antennas and Wireless Propagation Letters*, **9**, pp. 645–648.

PAULRAJ-A., GORE-D. A., NABAR-R., AND BOLCSKEI-H. (2004). An overview of MIMO communications- a key to gigabit wireless, *Proceedings of the IEEE*, **92**(2), pp. 198–218.

PAULRAJ-A., NABAR-R., AND GORE-D. (2003). *Introduction to Space-Time Wireless Communications*, Cambridge University Press (UK).

PIAO-D., YANG-L., GUO-Q., MAO-Y., AND LI-Z. (2015). Measurement-based performance comparison of colocated tripolarized loop and dipole antennas, *IEEE Transactions on Antennas and Propagation*, **63**(8), pp. 3371–3379.

PI-X., WANG-C., HAJJ-G. A., ROSEN-G., WILSON-B. D., AND BAILEY-G. J. (2003). Estimation of **exb** drift using a global assimilative ionospheric model: An observation system simulation experiment, *Journal of Geophysical Research: Space Physics*. DOI: 10.1029/2001JA009235.

PI-Z., AND KHAN-F. (2011). An introduction to millimeter-wave mobile broadband systems, *IEEE Communications Magazine*, **49**(6), pp. 101–107.

POZAR-D. (2011). *Microwave Engineering, 4th edition*, John Wiley and Sons.

POZAR-D. M., SCHAUBERT-D. H., AND ANTENNAS AND PROPAGATION SOCIETY-I. (1995). *Microstrip Antennas: The Analysis and Design of Microstrip Antennas and Arrays*, Electrical engineering, antennas and propagation, John Wiley & Sons, Ltd.

PROAKIS-J. G. (2001). *Digital Communications*, McGraw Hill, New York (NY).

QUALCOMM INC.. (Accessed: 2014a). The 1000x mobile data challenge. Available at: https://www.qualcomm.com/media/documents/files/1000x-mobile-data-challenge.pdf.

QUALCOMM INC.. (Accessed: 2014b). Rising to meet the 1000x mobile data challenge. Available at: https://www.qualcomm.com/media/documents/files/rising-to-meet-the-1000x-mobile-data-challenge.pdf.

QUALCOMM TECHNOLOGIES INC.. (Accessed: 2016). FCC vote will pave the path for 5G advancements to mobilize mmwave [UPDATED]. Available at: https://www.qualcomm.com/news/onq/2016/07/12/upcoming-fcc-vote-will-pave-path-5g-advancements-mobilize-mmwave.

QUITIN-F., OESTGES-C., HORLIN-F., AND DE DONCKER-P. (2009). Multipolarized MIMO channel characteristics: Analytical study and experimental results, *IEEE Transactions on Antennas and Propagation*, **57**(9), pp. 2739–2745.

QUOTIENT ASSOCIATES LTD. (Accessed: 2015). 5G candidate band study: Study on the suitability of potential candidate frequency bands above 6 GHz for future 5G mobile broadband systems. Available at: http://stakeholders.ofcom.org.uk/binaries/consultations/above-6ghz/qa-report.pdf.

RAMIREZ-R. R., AND DE FLAVIIS-F. (2003). A mutual coupling study of linear and circular polarized microstrip antennas for diversity wireless systems, *IEEE Transactions on Antennas and Propagation*, **51**(2), pp. 238–248.

RANGAN-S., RAPPAPORT-T. S., AND ERKIP-E. (2014). Millimeter-wave cellular wireless networks: Potentials and challenges, *Proceedings of the IEEE*, **102**(3), pp. 366–385.

RAPPAPORT-T. (Accessed: 2014). The coming renaissance of the wireless communications age. Available at: http://wireless.engineering.nyu.edu/presentations/NYSWAX.pdf.

RAPPAPORT-T. S. (1996). *Wireless Communications: Principles and Practice (Second Edition)*, Prentice Hall PTR (NJ).

RAPPAPORT-T. S., GUTIERREZ-F., BEN-DOR-E., MURDOCK-J. N., QIAO-Y., AND TAMIR-J. I. (2013a). Broadband millimeter-wave propagation measurements and models using adaptive-beam antennas for outdoor urban cellular communications, *IEEE Transactions on Antennas and Propagation*, **61**(4), pp. 1850–1859.

RAPPAPORT-T. S., MURDOCK-J. N., AND GUTIERREZ-F. (2011). State of the art in 60-GHz integrated circuits and systems for wireless communications, *Proceedings of the IEEE*, **99**(8), pp. 1390–1436.

RAPPAPORT-T. S., SUN-S., MAYZUS-R., ZHAO-H., AZAR-Y., WANG-K., WONG-G. N., SCHULZ-J. K., SAMIMI-M., AND GUTIERREZ-F. (2013b). Millimeter wave mobile communications for 5G cellular: It will work!, *IEEE Access*, **1**, pp. 335–349.

RATCLIFFE-J. A. (1972). *Introduction to the ionosphere and magnetosphere*, Cambridge University Press (NY).

RAZAVI-S. A., AND NESHATI-M. H. (2013). Development of a low-profile circularly polarized cavity-backed antenna using HMSIW technique, *IEEE Transactions on Antennas and Propagation*, **61**(3), pp. 1041–1047.

RAZAVIZADEH-S. M., AHN-M., AND LEE-I. (2014). Three-dimensional beamforming: A new enabling technology for 5G wireless networks, *IEEE Signal Processing Magazine*, **31**(6), pp. 94–101.

RIGNOT-E. J. M. (2000). Effect of Faraday rotation on L-band interferometric and polarimetric synthetic-aperture radar data, *IEEE Transactions on Geoscience and Remote Sensing*, **38**(1), pp. 383–390.

RODDY-D. (2006). *Satellite Communications, Fourth Edition (Professional Engineering)*, McGraw-Hill Professional.

ROH-W., SEOL-J. Y., PARK-J., LEE-B., LEE-J., KIM-Y., CHO-J., CHEUN-K., AND ARYANFAR-F. (2014). Millimeter-wave beamforming as an enabling technology for 5G cellular communications: theoretical feasibility and prototype results, *IEEE Communications Magazine*, **52**(2), pp. 106–113.

ROW-J.-S., AND CHEN-S.-H. (2006). Wideband monopolar square-ring patch antenna, *IEEE Transactions on Antennas and Propagation*, **54**(4), pp. 1335–1339.

ROYAL OBSERVATORY OF BELGIUM GNSS RESEARCH GROUP. (Accessed: 2014). Available at: http://www.gnss.be/Atmospheric_Maps/ionospheric_maps.php?

RYAN-M. (2003). *Principles of Satellite Communications*, Argos Press Series in Telecommunications Systems, Argos Press Pty. Ltd., Canberra, Australia.

SABAKA-T. J., OLSEN-N., AND PURUCKER-E. (2004). Extending comprehensive models of the Earth's magnetic field with Ørsted and CHAMP data, *Geophysical Journal International*, **159**, pp. 521–547. DOI: 10.1111/j.1365-246X.2004.02421.x.

SAKAMOTO-M., KOZONO-S., AND HATTORI-T. (1982). Basic study on portable radio telephone system design, *Proc. IEEE 32nd Vehicular Technology Conference (VTC)*, Vol. 32, pp. 279–284. DOI: 10.1109/VTC.1982.1623031.

SAMPIGETHAYA-K., POOVENDRAN-R., SHETTY-S., DAVIS-T., AND ROYALTY-C. (2011). Future e-enabled aircraft communications and security: The next 20 years and beyond, *Proceedings of the IEEE*, **99**(11), pp. 2040–2055.

SAMSUNG ELECTRONICS INC.. (Accessed: 2014). Samsung Electronics sets 5G speed record at 7.5 Gbps, over 30 times faster than 4G LTE. Available at: http://www.samsung.com/uk/news/local/samsung-electronics-sets-5g-speed-record-at-7-5gbps-over-30-times-faster-than-4g-lte.

SCHUSS-J. J., CARLSON-T., FRANCOIS-R., MALONEY-P., ROHWER-A., UPTON-J., WARDLE-L., AND SMITH-R. (1993). Design of the Iridium phased array antennas, *IEEE Antennas and Propagation Society International Symposium*, Vol. 1, pp. 218–221. DOI: 10.1109/APS.1993.385364.

SHAFI-M., ZHANG-M., MOUSTAKAS-A., SMITH-P., MOLISCH-A., TUFVESSON-F., AND SIMON-S. (2006). Polarized MIMO channels in 3-D: Models, measurements and mutual information, *IEEE Journal on Selected Areas in Communications*, **24**(3), pp. 514–527.

SHANNON-C. E. (1948). A mathematical theory of communication, *Bell System Technical Journal*, **27**(4), pp. 623–656.

SHANNON-C. E. (1949). Communication in the presence of noise, *Proceedings of the IRE*, **37**(1), pp. 10–21.

SHIU-D., FOSCHINI-G. J., GANS-M. J., AND KAHN-J. M. (2000). Fading correlation and its effect on the capacity of multielement antenna systems, *IEEE Transactions on Communications*, **48**(3), pp. 502–513.

SHKAROFSKY-I. (1961). Generalized Appleton-Hartree equation for any degree of ionization and application to the ionosphere, *Proceedings of the IRE*, **49**(12), pp. 1857–1871.

SIRIANUNPIBOON-S., HOWARD-S., CALDERBANK-A., AND DAVIS-L. (2009). Fully-polarimetric MIMO to improve throughput and reliability across propagation conditions, *Proc. IEEE 70th Vehicular Technology Conference (VTC)- Fall*. DOI: 10.1109/VETECF.2009.5379016.

SMART-W. M. (1960). *Textbook on Spherical Astronomy*, Cambridge University Press, Cambridge (UK).

SMITH-D. A. (2004). Computing unambiguous TEC and ionospheric delays using only carrier phase data from NOAA's CORS network, *Position Location and Navigation Symposium PLANS*, pp. 527–537. DOI: 10.1109/PLANS.2004.1309038.

SMITH-D. A., ARAUJO-PRADERE-E. A., MINTER-C., AND FULLER-ROWELL-T. (2008). A comprehensive evaluation of the errors inherent in the use of a two-dimensional shell for modeling the ionosphere, *Radio Science*. DOI: 10.1029/2007RS003769.

SMULDERS-P. (2002). Exploiting the 60 GHz band for local wireless multimedia access: prospects and future directions, *IEEE Communications Magazine*, **40**(1), pp. 140–147.

SPENCER-P. S. J., ROBERTSON-D. S., AND MADER-G. L. (2004). Ionospheric data assimilation methods for geodetic applications, *IEEE Position Location and Navigation Symposium (PLANS)*, pp. 510–517. DOI: 10.1109/PLANS.2004.1309036.

STAVROULAKIS-P. (2012). *Third Generation Mobile Telecommunication Systems: UMTS and IMT-2000*, Springer (Berlin Heidelberg).

STEYSKAL-H., AND HERD-J. S. (1990). Mutual coupling compensation in small array antennas, *IEEE Transactions on Antennas and Propagation*, **38**(12), pp. 1971–1975.

SUN-S., RAPPAPORT-T. S., HEATH-R. W., NIX-A., AND RANGAN-S. (2014). MIMO for millimeter-wave wireless communications: beamforming, spatial multiplexing, or both?, *IEEE Communications Magazine*, **52**(12), pp. 110–121.

SVANTESSON-T., AND RANHEIM-A. (2001). Mutual coupling effects on the capacity of multielement antenna systems, *Proc. IEEE International Conference on Acoustics, Speech, and Signal Processing (ICASSP)*, Vol. 4, pp. 2485–2488. DOI: 10.1109/ICASSP.2001.940505.

SVANTESSON-T., JENSEN-M. A., AND WALLACE-J. W. (2004). Analysis of electromagnetic field polarizations in multiantenna systems, *IEEE Transactions on Wireless Communications*, **3**(2), pp. 641–646.

TAGA-T. (1990). Analysis for mean effective gain of mobile antennas in land mobile radio environments, *IEEE Transactions on Vehicular Technology*, **39**(2), pp. 117–131.

TAOGLAS LTD. (2015). GPS patch integration application note. Available at: http://www.taoglas.com/images/product_images/original_images/TAOGLAS%20-%20GPS%20Patch%20Antenna%20Integration%20Application%20Note%28APN-12-8-002.B%29.pdf.

TELATAR-E. (1999). Capacity of multi-antenna gaussian channels, *European Transactions on Telecommunications*, **10**(6), pp. 585–595.

TELATAR-I. E., AND TSE-D. N. C. (2000). Capacity and mutual information of wideband multipath fading channels, *IEEE Transactions on Information Theory*, **46**(4), pp. 1384–1400.

TERCERO-M., SHARMA-S., COLDREY-M., AND KRONANDER-J. (2016). Coexistence between 5G and fixed services, *Proc. IEEE 83rd Vehicular Technology Conference (VTC)- Spring*. DOI: 10.1109/VTCSpring.2016.7504168.

THOMPSON-A. R., MORAN-J. M., AND SWENSON-G. W. (2008). *Interferometry and Synthesis in Radio Astronomy*, John Wiley & Sons, Ltd.

THURAYA TELECOMMUNICATIONS COMPANY. (Accessed: 2016). Available at: http://www.thuraya.com/.

TIRRÓ-S. (1993). *Satellite Communication Systems Design*, Springer (US).

TITHERIDGE-J. E. (1972). Determination of ionospheric electron content from the Faraday rotation of geostationary satellite signals, *Planet. Space Sci.*, **20**, pp. 353–369. DOI: doi:10.1016/0032-0633(72)90034-7.

TOH-B. Y., CAHILL-R., AND FUSCO-V. F. (2003). Understanding and measuring circular polarization, *IEEE Transactions on Education*, **46**(3), pp. 313–318.

TONG-K.-F., TANG-H.-J., AL-ARMAGHANY-A., AND HONG-W. (2013). Low-profile orthogonally tripolarized antennas, *IEEE Antennas and Wireless Propagation Letters*, **12**, pp. 876–879.

TONOUCHI-M. (2007). Cutting-edge terahertz technology, *Nature Photonics*, **1**(2), pp. 97–105.

TULINO-A. M., LOZANO-A., AND VERDU-S. (2005). Impact of antenna correlation on the capacity of multiantenna channels, *IEEE Transactions on Information Theory*, **51**(7), pp. 2491–2509.

TURCHINOVICH-D., KAMMOUN-A., KNOBLOCH-P., DOBBERTIN-T., AND KOCH-M. (2002). Flexible all-plastic mirrors for the THz range, *Journal of Applied Physics*, **A 74**, pp. 291–293.

TURKMANI-A. M. D., AROWOJOLU-A., JEFFORD-P. A., AND KELLETT-C. J. (1995). An experimental evaluation of the performance of two-branch space and polarization diversity schemes at 1800MHz, *IEEE Transactions on Vehicular Technology*, **44**(2), pp. 318–326.

UNITED STATES GOVERNMENT. (Accessed: 2015). GPS.GOV. Available at: http://www.gps.gov.

UNIVERSITY COLLEGE LONDON. (Accessed: 2016). Introduction to the Ionosphere. Available at: http://www.arm.ac.uk/summerschool2012/Aylward.pdf.

UNIVERSITY OF SHEFFIELD. (Accessed: 2016). Research Overview. Available at: http://gbailey.staff.shef.ac.uk/researchoverview.html.

UNIVERSITY OF SOUTH WALES. (Accessed: 2015). mmWave 28, 40 and 60 GHz RF modelling for small cells, 5G mobile networks and WiGig applications. Available at: http://woric.research.southwales.ac.uk/mmwave_model/.

UNIVERSITY OF SURREY. (Accessed: 2015). University-of-Surrey-achieves-5G-speeds-of-1Tbps. Available at: http://www.v3.co.uk/v3-uk/news/2396249/exclusive-university-of-surrey-achieves-5g-speeds-of-1tbps.

VALENZUELA-VALDES-J. F., AND SANCHEZ-HERNANDEZ-D. A. (2009). Increasing handset performance using true polarization diversity, *Proc. IEEE 69th Vehicular Technology Conference (VTC)-Spring*. DOI: 10.1109/VETECS.2009.5073600.

VALENZUELA-VALDES-J. F., GARCIA-FERNANDEZ-M. A., MARTINEZ-GONZALEZ-A. M., AND SANCHEZ-HERNANDEZ-D. A. (2009). Evaluation of true polarization diversity for MIMO systems, *IEEE Transactions on Antennas and Propagation*, **57**(9), pp. 2746–2755.

VAN TUYL-R. L. (1996). Unlicensed millimeter wave communications. a new opportunity for MMIC technology at 60 GHz, *Proc. IEEE 18th Annual Gallium Arsenide Integrated Circuit (GaAs IC) Symposium Technical Digest*, IEEE. DOI: 10.1109/GAAS.1996.567624.

VAUGHAN-R. G. (1990). Polarization diversity in mobile communications, *IEEE Transactions on Vehicular Technology*, **39**(3), pp. 177–186.

VERDONE-R., AND ZANELLA-A. (2012). *Pervasive Mobile and Ambient Wireless Communications: COST Action 2100*, Signals and Communication Technology, Springer (London).

VOLAKIS-J. (2007). *Antenna Engineering Handbook, 4th edition*, McGraw-Hill.

WALLACE-J. W., AND JENSEN-M. A. (2004). Mutual coupling in MIMO wireless systems: a rigorous network theory analysis, *IEEE Transactions on Wireless Communications*, **3**(4), pp. 1317–1325.

WANG-C., HAJJ-G., PI-X., ROSEN-I. G., AND WILSON-B. (2004). Development of the global assimilative ionospheric model, *Radio Science*. DOI: 10.1029/2002RS002854.

WANG-J., ZHANG-H., TINGTING-L., AND GULLIVER-T. A. (2012). Capacity of 60 GHz wireless communication systems over fading channels, *Journal of Networks*, **7**(1), pp. 203–209.

WATTEYNE-T., LANZISERA-S., MEHTA-A., AND PISTER-K. S. J. (2010). Mitigating multipath fading through channel hopping in wireless sensor networks, *IEEE International Conference on Communications*. DOI: 10.1109/ICC.2010.5502548.

WERNER-D. H., AND JIANG-Z. H. (2016). *Electromagnetics of Body Area Networks: Antennas, Propagation, and RF Systems*, John Wiley & Sons, Ltd.

WONBIN-H., AND SARABANDI-K. (2008). Low profile miniaturized planar antenna with omnidirectional vertically polarized radiation, *IEEE Transactions on Antennas and Propagation*, **56**(6), pp. 1533–1540.

WONBIN-H., AND SARABANDI-K. (2009). Low-profile, multi-element, miniaturized monopole antenna, *IEEE Transactions on Antennas and Propagation*, **57**(1), pp. 72–80.

WRIGHT-P. A., QUEGAN-S., WHEADON-N. S., AND HALL-C. D. (2003). Faraday rotation effects on L-band spaceborne SAR data, *IEEE Transactions on Geoscience and Remote Sensing*, **41**(12), pp. 2735–2744.

XUE-Q., LIAO-S. W., AND XU-J. H. (2013). A differentially-driven dual-polarized magneto-electric dipole antenna, *IEEE Transactions on Antennas and Propagation*, **61**(1), pp. 425–430.

YAMASHITA-F., KOBAYASHI-K., UEBA-M., AND UMEHIRA-M. (2005). Broadband multiple satellite MIMO system, *Proc. IEEE 62nd Vehicular Technology Conference (VTC)- Fall*, Vol. 4, pp. 2632–2636. DOI: 10.1109/VETECF.2005.1559026.

YAN-G., DU-Z., AND GONG-K. (2006). A compact orthogonal tripolarized multiantenna with low mutual coupling for MIMO channel measurements, *Microwave and Optical Technology Letters*, **48**(7), pp. 1358–1362.

YANG-S.-L. S., LUK-K.-M., LAI-H.-W., KISHK-A. A., AND LEE-K.-F. (2008). A dual-polarized antenna with pattern diversity, *IEEE Antennas and Propagation Magazine*, **50**(6), pp. 71–79.

YUEH-S. H. (2000). Estimates of Faraday rotation with passive microwave polarimetry for microwave remote sensing of earth surfaces, *IEEE Transactions on Geoscience and Remote Sensing*, **38**(5), pp. 2434–2438.

YUN-J. X., AND VAUGHAN-R. G. (2010). Slot MIMO cube, *IEEE Antennas and Propagation Society International Symposium (APSURSI)*. DOI: 10.1109/APS.2010.5560947.

ZHENG-L., AND TSE-D. N. C. (2003). Diversity and multiplexing: a fundamental tradeoff in multiple-antenna channels, *IEEE Transactions on Information Theory*, **49**(5), pp. 1073–1096.

ZHONG-H., ZHANG-Z., CHEN-W., FENG-Z., AND ISKANDER-M. F. (2009). A tripolarization antenna fed by proximity coupling and probe, *IEEE Antennas and Wireless Propagation Letters*, **8**, pp. 465–467.

ZHU-F., GAO-S., HO-A. T. S., ABD-ALHAMEED-R. A., SEE-C. H., BROWN-T. W. C., LI-J., WEI-G., AND XU-J. (2014). Ultra-wideband dual-polarized patch antenna with four capacitively coupled feeds, *IEEE Transactions on Antennas and Propagation*, **62**(5), pp. 2440–2449.

ZORBA-N., REALP-M., LAGUNAS-M. A., AND PEREZ-NEIRA-A. I. (2008). Dual polarization for MIMO processing in multibeam satellite systems, *Signal Processing for Space Communications*. DOI: 10.1109/SPSC.2008.4686702.

ZOU-L., AND FUMEAUX-C. (2011). A cross-shaped dielectric resonator antenna for multifunction and polarization diversity applications, *IEEE Antennas and Wireless Propagation Letters*, **10**, pp. 742–745.

List of Acronyms

AWGN Additive White Gaussian Noise

BER Bit Error Rate

BGSGMM British Geological Survey Global Magnetic Model

CP Circular Polarisation

CSI Channel State Information

DCP Dual Circular Polarisation

DP Dual Polarisation

DSRC Dedicated Short Range Communications

EoE Edge of Earth

ECC Envelope Correlation Coefficient

EGC Equal Gain Combining

EP Ellipitcal Polarisation

FoV Field of View

GNSS Global Navigation Satellite System

GPS Global Positioning System

IGRF International Geomagnetic Reference Field

IGS International GNSS Service

IID ZMCSSCG Independent and Identically Distributed Zero Mean Circular Symmetric Complex Gaussian

IRI Ionospheric Reference Model

LEO Low Earth Orbit

LHCP Left Handed Circular Polarisation

LMS Land Mobile Satellite

LNA Low Noise Amplifier

LoS Line of Sight

LP Linear Polarisation

MEG Mean Effective Gain

MEME Model of the Earth's Magnetic Environment

MEO Medium Earth Orbit

MIMO Multiple Input Multiple Output

mmWave Millimetre Wave

MP Multipath Power

MRC Maximal Ratio Combining

NGSO Non Geosynchronous Satellite Orbit

NLoS Non Line of Sight

OLP Omnidirectional Linear Polarisation

PTC Polarisation-Time Coding

RFID Radio Frequency IDentification

RHCP Right Handed Circular Polarisation

SAR Synthetic Aperture Radar

SISO Single Input Single Output

SNR Signal to Noise Ratio

TE Transverse Electric

TEC Total Electron Content

TM Transverse Magnetic

v2v Vehicle to Vehicle

VTEC Vertical Total Electron Content

WMM World Magnetic Model

WPAN Wireless Personal Area Network

XPD Cross Polar Discrimination

WMM World Magnetic Model

Biography

Nicholas (Nick) Paul Lawrence was born in Chichester, UK in 1972. In 1995, he graduated from the University of Leicester, UK, with a Bachelor's Degree with Honours in Physics with the second class rank. In 1997, he obtained his Master of Science in Microwave Solid State Physics with distinction, from the University of Portsmouth, UK. This course is prominent in the field of microwave physics due to the proximity of the Royal Navy and the European Aeronautic Defence and Space company (EADS). In 2002, Nick completed research into Brillouin sensing techniques, used in optical fibre maintenance, at the Optical Research Centre, University of Southampton, UK, and gained his Master of Philosophy.

In 1998, Nick joined Milmega Ltd., UK, a company specialising in high power solid state microwave amplifier design, as a RF & microwave engineer. During this period, Nick formed links with a sister company, Milmega SA., France, and represented Milmega on two occasions at the Microwave & RF Trade show, Paris. He represented Milmega in several negociations with French client companies.

In 1999, Nick qualified as a translator in French, and became a Chartered Member of the Institute of Linguists (now CIOL).

In 2002, he began work at Wood and Douglas Ltd., UK, a company specialising in radio telemetry, broadcast and security products, as a RF engineer specialsing in DVB-T hardware design.

In 2004, Nick was accepted as a Chartered Engineer and Member of the Institute of Electrical Engineers (now IET), following a process of academic scrutiny and professional mentorship.

In 2005, following the death of his brother, he qualified as a secondary science teacher before moving to France, where he designed and built single-handedly his family's house. During this time, Nick continued to work in the field of microwave power amplifiers, through links he had established prior with a company in south-west France.

In 2010, Nick and his family took the plunge and moved to Adelaide, Australia, where he continued to pursue interests in the fields of residential construction and microwave power amplifier design.

In 2013, Nick was awarded an Australian Postgraduate Award (APA) scholarship to pursue his PhD under Prof. Derek Abbott, Dr Hedley Hansen and Dr Brian Ng in the School of Electrical & Electronic Engineering, The University of Adelaide.

Nicholas Paul Lawrence
nicholas.lawrence@adelaide.edu.au

Scientifc Genealogy of

Nicholas Paul Lawrence

"If I have seen further it is by standing on the shoulders of Giants."
Isaac Newton